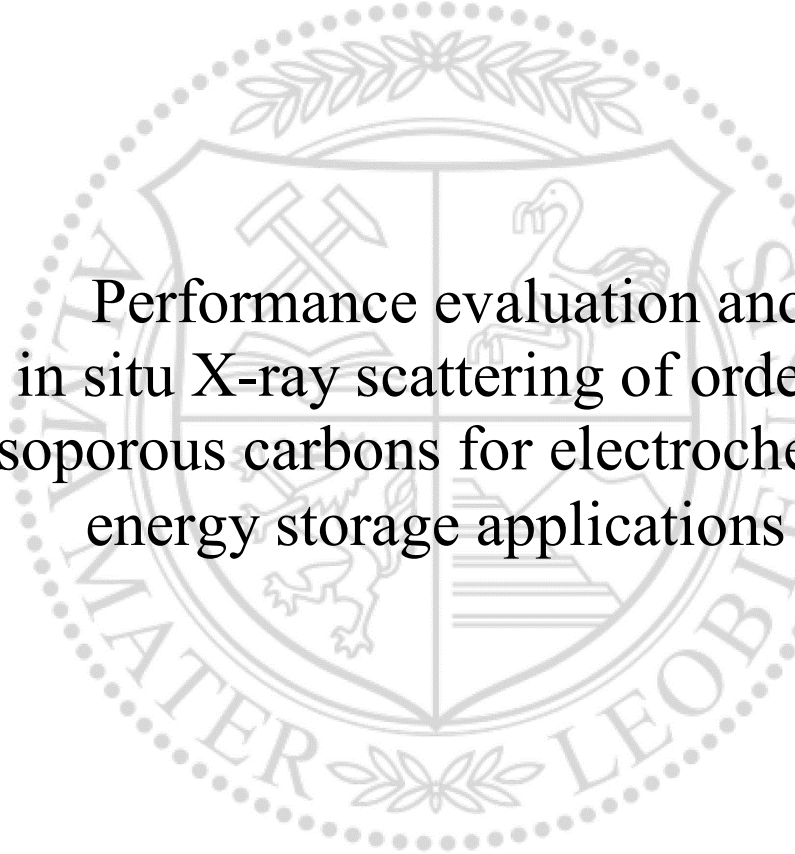




Institute of Physics

Doctoral Thesis



Performance evaluation and  
in situ X-ray scattering of ordered  
mesoporous carbons for electrochemical  
energy storage applications

Dipl.-Ing. Christian Koczvara

August 2019





## AFFIDAVIT

I declare on oath that I wrote this thesis independently, did not use other than the specified sources and aids, and did not otherwise use any unauthorized aids.

I declare that I have read, understood, and complied with the guidelines of the senate of the Montanuniversität Leoben for "Good Scientific Practice".

Furthermore, I declare that the electronic and printed version of the submitted thesis are identical, both, formally and with regard to content.

Date 29.08.2019

---

Signature Author  
Christian Koczwara  
Matriculation Number: 01035022



## Acknowledgements

At first, I want to thank my supervisor Oskar Paris not only for giving me the opportunity to work on such an interesting topic but also for giving me the chance to gather valuable teaching experience. He always found time for scientific discussions and provided guidance for working with the students. His enthusiasm for the scientific problems encouraged me to continue working on problems I otherwise would have given up.

Additionally, I want to thank Christian Prehal for the many days and nights we worked together, not only at the office, but also during all the synchrotron experiments we performed. I am grateful for all our discussions and for the many things he taught me.

Moreover, I want to thank Nicola Hüsing and Simon Rumswinkel, from the University of Salzburg, for providing the ordered mesoporous carbon used in this thesis. Without their commitment, this thesis would not have been possible.

I also want to thank the people working at the AustroSAXS beamline at ELETTRA for their support during the experiments we performed there. In particular, I want to thank Heinz Amenitsch for his scientific support and for making every trip to ELETTRA a scientific and culinary adventure.

Furthermore, I want to thank my colleagues and friends at the Institute of Physics for many on- and off-topic discussions. Especially I want to thank Rainer Lechner, Markus Kratzer, Gerhard Popovski, and Roland Morak for many discussions about how to motivate our students. Additionally, I want to thank Sebastian Stock and Lorenz Hammerschmidt for preparing electrodes and helping with measurements. I would also like to show my gratitude to Heide Kirchberger for helping with all the organizational work.

In addition, I thank my friends and my family for their support and for providing the right amount of distraction during this very busy time. Especially I want to thank my partner Sarah for being patient and supporting me during this stressful period.



# Abstract

Ongoing climate change is emerging to a global crisis. It is necessary to develop new environmentally friendly ways to satisfy the need for energy to reach the ambiguous goal of keeping global warming below 2°C. Not only the production is a big challenge, but also the storage systems need to be improved in order to reach a society that only relies on renewable energy sources.

Electrical double layer capacitors (EDLCs, also known as supercapacitors) can deliver a high power density and have a long lifetime, but suffer from a comparably low energy density. They are well suited for applications demanding very short charging and discharging times (e.g. frequency regulations in power grids). EDLCs usually consist of two porous (carbon) electrodes immersed in a liquid electrolyte. If a voltage is applied, an electrical double layer forms at each electrode, which causes the capacitive behavior. While the basic concept of the double-layer formation is well known, details of the ion rearrangement in microporous electrodes is still not fully understood.

The main goal of this thesis is to provide new insights on the ion movement (re-arrangement) and the volumetric change of the electrode during charging and discharging, as well as to study the influence of the pore structure on the charging process. To reach this goal, two different model materials with a hierarchically ordered mesopore structure were used. These materials provide a well-defined pore structure that can be adjusted by additional CO<sub>2</sub> activation treatment. This results in a hierarchically ordered macro/meso/microporous system. Additionally, the ordered structure results in Bragg peaks in the small-angle X-ray scattering regime, which allows additional analysis compared to (disordered) activated carbon materials.

Three different topics were investigated:

- Influence of the pore structure on the capacitance for elevated charging rates: An extensive structural and electrochemical characterization of nanocast (consisting of hexagonally ordered carbon nanorods) and soft-templated carbons (hexagonally ordered cylindrical pores) in order to study the influence of the pore structure on the electrochemical performance. It was shown that a hierarchical structure is beneficial, if they guarantee a three-dimensional access for the ions to the micropore network.
- Electrode swelling: The well-resolved Bragg peaks (in the small-angle scattering regime) originating from hexagonally ordered structure allow

new measurement concepts. It is shown that these materials allow us to track the deformation of a carbon based supercapacitor cell on the mesopore length scale, which is not possible with other (disordered) carbon materials.

- Proof of concept: Is in situ anomalous small-angle X-ray scattering suitable to study the rearrangement of individual ion species? Conventional small-angle X-ray scattering suffers from a major drawback: it is not element sensitive. These experiments rely on a simplification of the system and on data from additional measurements (e.g. overall charge accumulated) to link the measured changes to a single element or component. Anomalous small-angle X-ray scattering was evaluated as a tool to directly analyze the behavior of a single ion species without the need of additional data from other experiments.



## Kurzfassung

In Anbetracht des Klimawandels ist es notwendig, neue Technologien zu entwickeln, die es uns ermöglichen, den ständig steigenden Energiebedarf mithilfe erneuerbarer Energiequellen zu decken. Ohne eine drastische Reduktion der Treibhausgasemissionen wird es uns nicht gelingen, angepeilte Klimaziele zu erreichen. Dabei ist zu beachten, dass die (Weiter-)Entwicklung der Stromproduktion alleine das Problem nicht lösen kann. Leistungsfähige Speichersysteme sind ein wichtiger Faktor, ohne den das Erreichen der gesetzten Klimaziele in weite Ferne rückt.

Superkondensatoren können dabei einen wichtigen Beitrag leisten. Sie bestehen aus zwei porösen (Kohlenstoff-)Elektroden, eingetaucht in einen Elektrolyten. Diese Speichertechnologie zeichnet sich durch ihre hohe Leistungsdichte und Langlebigkeit (mehrere 100000 Ladezyklen) aus. Die Funktion basiert auf der Ausbildung einer elektrischen Doppelschicht an der Grenzfläche zwischen Elektrode und Elektrolyt. Das Grundkonzept dieser Doppelschicht wirkt auf den ersten Blick sehr simpel, bei genauerer Betrachtung wird allerdings klar, wie komplex die Prozesse beim Ladevorgang wirklich sind.

Im Zuge dieser Arbeit sollen genau diese Prozesse untersucht werden. Dazu wurde ein Kohlenstoff-Modell-Material mit hierarchisch geordneter Struktur verwendet. Dieses Material besitzt neben seiner gut definierten Porenstruktur auch noch einen weiteren großen Vorteil: die geordnete Struktur führt bei Kleinwinkel-Streuexperimenten zu Bragg-Reflexen. Dadurch ist es möglich Experimente durchzuführen, die mit den bisherigen (ungeordneten) Aktivkohlen nicht durchführbar waren.

Mit Hilfe dieser Materialien wurden folgende drei Fragestellungen behandelt werden:

- Welchen Einfluss hat die Porenstruktur auf die Kapazität bei erhöhten Laderaten? Dazu wurde eine umfangreiche Strukturanalyse und elektrochemische Charakterisierung zweier geordneter Kohlenstofftypen (geordnete Kohlenstoff-Nanozylinder und geordnete zylindrische Poren) durchgeführt. Diese Experimente haben gezeigt, dass eine hierarchische Struktur deutliche Vorteile gegenüber einer konventionellen rein mikroporösen Aktivkohle haben kann.
- Ausdehnung der Elektroden: Durch die Analyse der Positionsänderung der Bragg-Reflexe während des Lade-/Entlade-Vorgangs, war es möglich, auch kleinste Ausdehnung der Elektrode zu messen. Diese Effekte sind

bei Superkondensatoren deutlich kleiner als bei Li-Ionen-Akkus, sind aber trotzdem von Bedeutung.

- Es wurde bereits in mehreren Versuchen gezeigt, dass in situ Röntgenkleinwinkelstreuung eine geeignete Methode zur Analyse von Ionenbewegungen ist. Allerdings sind die gemessenen Signale immer eine Kombination aus allen Komponenten, die sich im Röntgenstrahl befinden, weshalb für die Auswertung dieser Messungen zusätzliche (elektrochemische) Daten notwendig sind. Hier wurde gezeigt, dass anormale Röntgenkleinwinkelstreuung eine Messmethode ist, die ohne zusätzliche Daten elementspezifische Auswertungen ermöglicht

## Abbreviations

AC	activated carbon
ACC	activated carbon cloth
AN	acetonitrile
ASAXS	anomalous small-angle X-ray scattering
BET	Brunauer-Emmett-Teller
CA	chronamperometry
CC	current collector
CDC	carbide derived carbon
CE	counter electrode
CNT	carbon nanotube
CPE	constant phase element
CV	cyclic voltammetry
DER	equivalent distribution resistance
DFT	density functional theory
EDLC	electrical double-layer capacitor
EFC	electrochemical flow capacitor
EIS	electrochemical impedance spectroscopy
ESR	equivalent serial resistance
ESRF	European Synchrotron Radiation Facility
GCPL	galvanostatic cycling with potential limit
GSA	gas (ad)sorption analysis
HF	hydrofluoric acid
IL	ionic liquid
LiC	lithium-ion capacitor
MOFs	metal organic frameworks
MWCNT	multi-walled carbon nanotubes
NCC	nanocast carbon
NLDFT	non local density functional theory
NMR	nuclear magnetic resonance
OMC	ordered mesoporous carbon
PANI	polyaniline
PC	propylene carbonate

PEEK	polyether ether ketone
PPy	polypyrrole
PSD	pore size distribution
PTFE	polytetrafluoroethylene
PVA	polyvinyl alcohol
PVDF	polyvinylidenedifluoride
PVP	polyvinylpyrrolidone
QSDFT	quenched solid density functional theory
RE	reference electrode
SAXS	small-angle X-ray scattering
SBU	secondary building unit
SSA	specific surface area
STC	soft-templated carbon
SWCNT	single-walled carbon nanotubes
TEM	transmission electron microscopy
WE	working electrode
XRD	X-ray diffraction

# Table of content

Acknowledgements .....	v
Abstract .....	vii
Kurzfassung.....	ix
Abbreviations .....	xi
1 Motivation .....	1
2 Fundamentals .....	7
2.1 Supercapacitors.....	7
2.1.1 Charge storage principle .....	8
2.1.2 Electrochemical flow capacitor.....	12
2.2 Electrochemical measurements .....	14
2.2.1 Two-electrode and three-electrode setup .....	14
2.2.2 Cyclic voltammetry .....	16
2.2.3 Galvanostatic cycling.....	19
2.2.4 Chronoamperometry .....	22
2.2.5 Electrochemical impedance spectroscopy .....	23
2.3 Scattering .....	29
2.4 Absorption of X-rays.....	30
2.5 Small-angle X-ray scattering .....	31
2.5.1 Particle scattering .....	31
2.5.2 SAXS on non-particular systems.....	33
2.6 Anomalous small-angle X-ray scattering (ASAXS).....	36
2.6.1 Data evaluation.....	40
2.7 Fluorescence.....	41
2.8 Specific surface area and pore size distribution.....	42
2.9 Electrolytes used in supercapacitors .....	44
2.9.1 Aqueous electrolytes.....	45
2.9.2 Organic electrolytes.....	45

2.9.3	Ionic liquids .....	46
2.10	Confinement effects .....	47
2.10.1	Ion desolvation .....	47
2.10.2	Solvents in confinement .....	48
2.10.3	Ion sieving .....	48
2.11	Materials for supercapacitor electrodes .....	49
2.11.1	Activated carbon .....	50
2.11.2	Carbide derived carbons .....	51
2.11.3	Metal organic frameworks .....	54
2.11.4	MXenes .....	56
2.11.5	Carbon nanotubes .....	59
2.11.6	Carbon onions .....	61
2.11.7	Summary .....	63
2.12	Templated carbon materials .....	64
2.12.1	Soft-templating .....	65
2.12.1	Hard-templating (nanocasting) .....	67
2.13	Pseudo-capacitance: the concepts .....	69
2.13.1	Pure EDLC .....	70
2.13.2	Pseudo-capacitance versus battery-like behavior .....	71
2.13.3	Capacitance versus capacity .....	72
2.14	Pseudo-capacitive materials .....	73
2.14.1	Transition metal oxides .....	73
2.14.2	Conductive polymers .....	74
2.14.3	Surface groups .....	74
2.14.4	Redox active electrolytes .....	75
2.15	Devices .....	75
2.15.1	Electrodes and binder .....	75
2.15.2	Hybrid devices .....	77
3	Experimental .....	79

3.1	Electrode preparation.....	79
3.2	Cell setups .....	79
3.3	Measurement setup for electrochemical testing.....	81
3.4	In situ SAXS setup .....	81
3.5	In situ ASAXS setup.....	82
3.6	Materials used.....	84
4	Influence of the pore structure on the rate handling capability.....	86
4.1	Motivation .....	86
4.2	Structural analysis .....	89
4.2.1	Sample preparation and measurement techniques .....	89
4.2.2	Structural analysis: results.....	90
4.2.3	Inhomogeneity in different NCC series.....	101
4.3	Electrochemical performance.....	103
4.3.1	Performance evaluation .....	103
4.3.2	STC sample without calcination .....	108
4.3.3	Electro-wetting.....	109
4.4	Discussion .....	111
4.5	Conclusion .....	115
5	Electrosorption induced electrode expansion.....	117
5.1	Motivation .....	117
5.2	Materials characterization .....	118
5.2.1	Gas adsorption analysis .....	118
5.2.2	Electrochemical characterization.....	120
5.2.3	In situ electrochemical dilatometry .....	120
5.3	In situ SAXS.....	121
5.3.1	SAXS data evaluation .....	121
5.3.2	Beam stability .....	122
5.3.3	Measurements with a lab source .....	123
5.3.4	Electrode wetting .....	125

5.4	Results .....	126
5.5	Discussion .....	128
5.6	Conclusion.....	129
6	Ion specific concentration change analyzed by ASAXS.....	130
6.1	Motivation .....	130
6.2	In situ ASAXS .....	131
6.2.1	Material characterization .....	131
6.2.2	In situ ASAXS .....	132
6.3	Data evaluation.....	133
6.3.1	Effective $f'$ and $f''$ values.....	133
6.3.2	Data separation .....	134
6.3.3	Radiation damage.....	137
6.4	Results and discussion .....	138
6.4.1	Fluorescence data .....	143
6.5	Conclusion.....	146
7	Summary and outlook.....	147
8	Bibliography.....	150
9	List of publications.....	175



# 1 Motivation

Climate change and its consequences are a major threat to societies all over the globe. It has been shown in different studies that many aspects of daily life could be affected by global warming. The influences can cause a reduction of food and drinking water quality/availability,<sup>1-3</sup> a decrease of biodiversity,<sup>4</sup> extinction of whole species,<sup>5</sup> and even an increase of infectious diseases.<sup>6-8</sup> To counteract these possible threats, humanity must work together to reduce global warming. This is now widely accepted and the Paris agreement signed by many countries in 2015 is a step in the right direction to keep global warming under a 2°C threshold compared to the pre-industrial level.

From model calculations, it is known that to keep global warming below the 2°C threshold, a drastic reduction of the emission of greenhouse gases is necessary. If the cumulative CO<sub>2</sub> emissions can be held below 1000 gigatons in the timespan from the year 2000 until 2050, there is a 75% chance to stay below 2°C, while the emission of 1440 gigatons will reduce the probability to 50%. To get a better understanding about these values, the cumulative CO<sub>2</sub> emissions between 2000 and 2006 have already reached 234 gigatons. As a result, the CO<sub>2</sub> emission budget to stay below a 25% chance to exceed the 2°C threshold would be reached in 2027, assuming an ongoing constant emissions. In addition, other gases, the so-called non-CO<sub>2</sub> Kyoto-gases (methane, nitrous oxide, hydrofluorocarbons, perfluorocarbons and SF<sub>6</sub>), are considered greenhouse gases also contributing to global warming. Depending on their CO<sub>2</sub> equivalent, calculated for each individual gas, these emissions have a certain impact that must also be taken into account. The urgency of reducing greenhouse gas emissions is even clearer when comparing forecasts from two different models: SRES A1FI and HALVED-BY-2050.<sup>9</sup> The SERS A1FI model predicts a world population of 9 billion people using mainly fossil fuel based technologies, while HALVED-BY-2050 is based on a reduction of Kyoto-gases, reaching 50% in 2050 relative to the emissions in 2000. The projected CO<sub>2</sub> concentration as well as the resulting anthropogenic radiative forcing are shown in Figure 1.1a for both models.<sup>9</sup> Even if the emission of greenhouse gases can be cut in half by 2050, there is still a possibility of exceeding the 2°C goal (Figure 1.1b). This fact should be alarming and calls for immediate actions to reduce emissions.

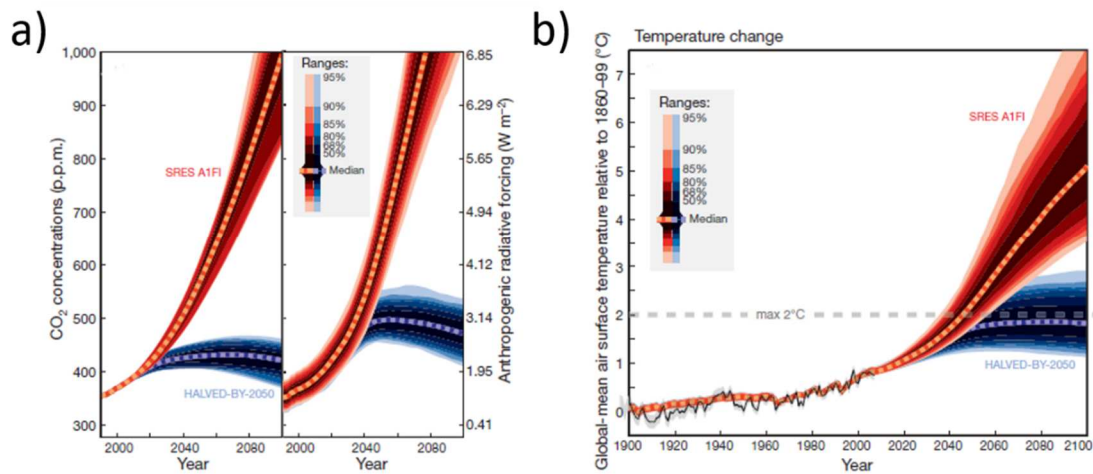


Figure 1.1: (a) Median of predicted evolution of CO<sub>2</sub> concentration in the atmosphere and anthropogenic radiative forcing using the SRES A1FI (red) and the HALVED-BY-2050 (blue) model. (b) Global-mean temperature relative to 1860-1899 for both scenarios. The dashed grey line indicates the 2°C threshold. Reproduced with permission from Ref.<sup>9</sup> © Nature Publishing Group

Climate change forces us to overthink established energy concepts. A transition from fossil based to renewable energy sources is essential in order to reach the goals established in the Paris agreement. Decarbonizing the electrical energy sector would be a major step in the right direction. Electricity production is responsible for about 40% of the global energy related greenhouse gas emissions,<sup>10</sup> despite ongoing efforts to increase the share of renewable energy sources. The transition to a carbon free energy production is not only influenced by new developments in the sector of renewable energy production, but also the long lifespan of state of the art fossil fuel powered electrical plants will influence the time frame. Nevertheless, calculations have shown that, although the electricity contribution to the overall energy mix is expected to increase, in 2050 photovoltaic power plants could cover about 16% of the predicted demands.<sup>10</sup> Since modern photovoltaic power plants have a CO<sub>2</sub> equivalent emission of less than 1/10 of the approximated global average (49.9 g vs. 532 g CO<sub>2</sub> per kWh), calculated over an average lifespan, they can substantially contribute to reach the set goals. The production costs of solar and wind plants have declined over the last years, while coal powered plants cost roughly the same. In terms of cost per gigajoule, wind energy can already compete with coal.<sup>10,11</sup>

The transition to renewable energy sources for electricity productions will also be accompanied by a change of the requirements for the electrical power grid and storage technologies. In contrast to the centralized production in conventional

power plants (nuclear power plants and coal, oil, or gas-powered plants) are renewable technologies (wind turbines and photovoltaic plants) smaller and lead to a decentralization of the energy production. This can result in a remodeling of the whole energy market.

Even though renewable technologies have experienced a boom over the last few years, there is one major challenge that has not been solved until now: the availability and intermittency of many renewable energy sources demand for flexible large-scale storage systems for electrical energy to guarantee security of supply. Fossil energy sources can be stock piled and used when needed, while wind and solar power can only be harvested when available. To be able to store energy in times of overproduction and deliver it when demand exceeds production is not only important to guarantee safety of supply, but the possibility to stockpile the produced energy is also important for the economics and ecology of power plants. Sophisticated storage systems allow the design of power plants for average consumption instead of peak demands, which influences construction costs and revenue of power plants. Additionally, storage systems can reduce the need for long-distance transmission lines as well as the fossil fuel based backup plants. Only by increasing the performance and lifetime of energy storage systems while simultaneously reducing their production cost, renewable energy sources can overcome their drawbacks.<sup>12-14</sup>

Storage systems used in power grids can be mainly divided into two groups: energy intensive and power intensive. For energy intensive applications (e.g. load shifting), systems with a high energy storage capability is needed, making Li-ion batteries or pumped-storage power plants promising technologies. Power intensive applications, like frequency regulations, demand for a high power output over a short time period as well as long cycle life.<sup>13</sup> Electrical double-layer capacitors (EDLCs, also called supercapacitors) fulfill these requirements.

Supercapacitors are high power density storage devices best suited for applications demanding for short charging and discharging times. In terms of specific power (Figure 1.2) and cycle lifetime, they clearly outperform conventional battery types.<sup>15</sup> EDLCs are used in a variety of different applications including backup systems for airplane doors and pitch control systems in wind turbines. They also play an important role in microelectronics, sensor applications, and can be used in storage systems for electrical vehicles.

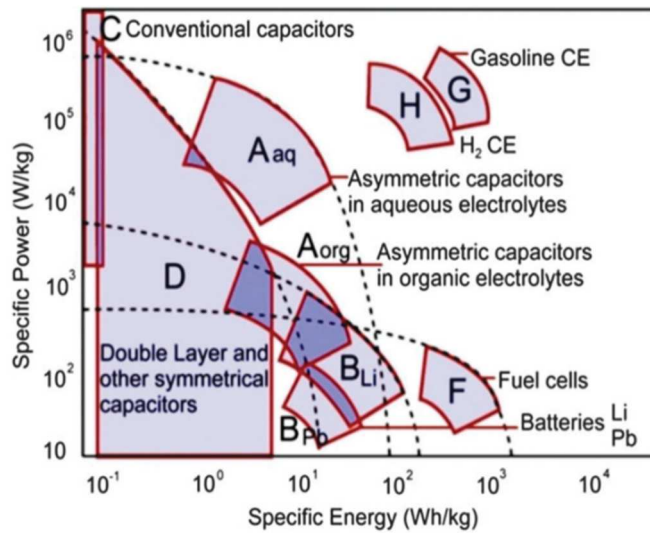


Figure 1.2: Ragone plot including different supercapacitor types as well as conventional batteries and fuel for combustion engines (CE). Reproduced from Ref.<sup>16</sup> with permission from The Royal Society of Chemistry

Due to the combination of the high power density and cycle stability, but lower energy density, supercapacitors will (in many cases) not replace other storage systems, but most probably be combined with other technologies. Applications like fuel cell powered vehicles can benefit from such a hybrid system.<sup>17,18</sup>

A supercapacitor consists of two porous electrodes immersed in an electrolyte. The charge is stored in an electrical double-layer at the electrode/electrolyte interface, which is formed when a potential is applied. As a result, the capacitance of a device is directly linked to the surface area of the electrode material. Activated carbon is the most used electrode material due to its high specific surface area, good electrical conductivity, low production costs and non-toxicity. The micropore structure in activated carbons is also beneficial in terms of shielding repulsive electrostatic forces, allowing a denser packing of ions, resulting in a high specific capacitance.<sup>15,19</sup>

When charging a supercapacitor, charge carriers (electrons or holes) accumulate at each electrode. As a result the above-mentioned double layer<sup>15</sup> is formed and a global ion flux ensures charge neutrality, which can be achieved in different ways: co-ions moving out of the electrode (co-ion expulsion), counter ions moving in (counter ion adsorption) and a combination of both (ion swapping or ion exchange).<sup>20</sup> The dominant mechanism depends on a variety of parameters like the electrolyte type and ion concentration, scan rate, cell design as well as the electrode material itself.<sup>21</sup> In addition to the global ion movement (ions moving in and out of the electrode), local ion rearrangement takes place, moving counter

ions towards the electrode (pore) surfaces forming the electrical double layer at the electrode/electrolyte interface.<sup>20-22</sup> To systematically improve the specific energy and power as well as the cycle stability of EDLCs it is crucial to understand these charging processes and their dependencies. This is much more complicated than it may look at first sight. The nanoporous nature of the used electrode for instance causes substantial changes of the electrolyte inside this confined system compared to its bulk behavior. The shift of the freezing point of aqueous solutions, the decreased permittivity and a changed mobility of ions are just a few of the parameters influenced by the confinement.<sup>23-25</sup> Naturally, these behavior changes will also influence the charging and discharging mechanisms of supercapacitor electrodes.

To increase the performance of a supercapacitor, different strategies are pursued. A higher cell potential, for instance, will increase the energy stored in a device. Due to the limitation of the potential window in aqueous electrolytes, organic electrolytes or ionic liquids can be used. The main drawback of both, ionic liquids and organic electrolytes is the reduced power density compared to aqueous electrolytes.<sup>26-28</sup>

The use of fast faradaic reactions is another concept to increase the capacitance and the specific energy. In recent years, hybrid devices have been developed with the goal of combining the high power density of an EDLC with the high energy density of a battery.<sup>16,29,30</sup>

All these strategies to improve the performance and stability of supercapacitor devices depend on a fundamental understanding of all processes taking place during charging and discharging of a device. Simulations and in situ techniques play an important role in improving the understanding of charging mechanisms. Over the last few years, different in situ techniques have been developed to track the behavior of ions, solvent and electrode materials in an operating device. The increasing computational power enabled the development of advanced simulations, and new methods to combine experimental studies with simulations.<sup>31-37</sup>

In this thesis, ordered mesoporous carbon (OMC) materials were used to study ion and electrode behavior in an operating supercapacitor device. These materials have a few key advantages: They exhibit a well-defined mesopore structure and their micropore content can be tuned without altering the mesopore system. Additionally their ordered structure results in Bragg peaks in the small-angle scattering regime, allowing new analysis methods compared to conventional

(disordered) activated carbon materials. Using these model materials three different studies were performed in this thesis:

1. A combination of electrochemical performance evaluation, gas sorption analysis and scattering techniques have been used to systematically study the influence of the pore structure on the storage capacitance for elevated charging and discharging rates. With these combined studies, it was possible to show that hierarchical pore structures can be beneficial for the electrochemical performance.
2. The deformation of the electrode itself was analyzed, as a function of the applied potential, by in situ small-angle X-ray scattering (SAXS). It was possible to show that the expansion behavior of the electrodes is influenced by the pore structure.
3. In situ anomalous small-angle X-ray scattering (ASAXS), has been evaluated as a technique to perform element specific analysis of ion specific equilibrium configurations. With this experiment, it was shown that ASAXS is in fact a powerful tool to track element specific changes in an operating supercapacitor device without the need of additional electrochemical data.

The thesis itself is divided into two main parts. The first part (Chapter 2) explains the basic principles of supercapacitors including a short overview of selected available electrode materials, electrolytes and characterization techniques. An additional short overview of the used X-ray scattering techniques will also be given. The second part (Chapter 3 to 6) is dedicated to the experiments and their results.

## 2 Fundamentals

Here the basic principles of supercapacitors and X-ray techniques necessary for the experiments performed in this thesis are explained. The focus of this chapter is on the basic principle of supercapacitors, the different electrode materials and electrolytes, as well as electrochemical characterization methods used for the characterization of supercapacitors. The description of the used X-ray techniques is presented in a much shorter and compact form, since these techniques are well established at the Institute of Physics (Montanuniversität Leoben) and have been explained in detail in previous theses.<sup>38-40</sup>

### 2.1 Supercapacitors

A supercapacitor, also called electrical double-layer capacitor (EDLC), is a high power density energy storage device. The concept of a supercapacitor made of metal electrodes coated with porous carbon was first patented in 1957, and commercially produced by the Japanese company NEC in 1971. Since then, enormous progress has been made in terms of electrode materials, electrolytes and production techniques. Supercapacitors do not reach the energy density of modern battery systems, but with their high power output, they can close the gap between batteries and conventional capacitors. Additionally, their high cycle life offers new and complementary applications to battery systems.<sup>22</sup> One example is the use of supercapacitors as an additional energy storage device in electric cars. Due to their low energy density they are not used as the main energy source, but as a supporting device to handle the high power demands during acceleration.<sup>41</sup>

EDLCs consist of two highly porous electrodes immersed in an electrolyte. A separator (e.g. glass filter) is located between the two electrodes to prevent short circuits of the electrodes and serves as an electrolyte reservoir. Therefore, the separator has to be stable in the liquid electrolyte and has to have a low electronic conductivity but high ionic conductivity. In terms of electrode materials, activated carbon is the most common one. The properties and applications of different electrode materials will be explained in Chapters 2.11 and 2.12.

### 2.1.1 Charge storage principle

The basic principle of an EDLC is based on the fact that a voltage applied between the electrodes leads to the formation of an electrical double-layer at each electrode/electrolyte interface, causing the capacitive behavior (Figure 2.1). Forming the electrical double-layer at the electrode/electrolyte interface is highly reversible, which is one of the reasons for the long cycle life of EDLCs. The fact that the charge is stored at the surface and not in the bulk of the electrode material, as it is the case in batteries, results in one of the major advantages of supercapacitors: The charge storage process is not limited by reaction kinetics or diffusion inside the electrode material, leading to a high power output as well as a coulombic efficiency (efficiency of charge transfer) typically above 95%. Additionally the volumetric changes of the electrode occurring during charging and discharging are small compared to storage devices using intercalation process. Therefore, aging processes in EDLCs are not as pronounced and they can easily stay operational for hundreds of thousands of charging and discharging cycles.<sup>15,22</sup>

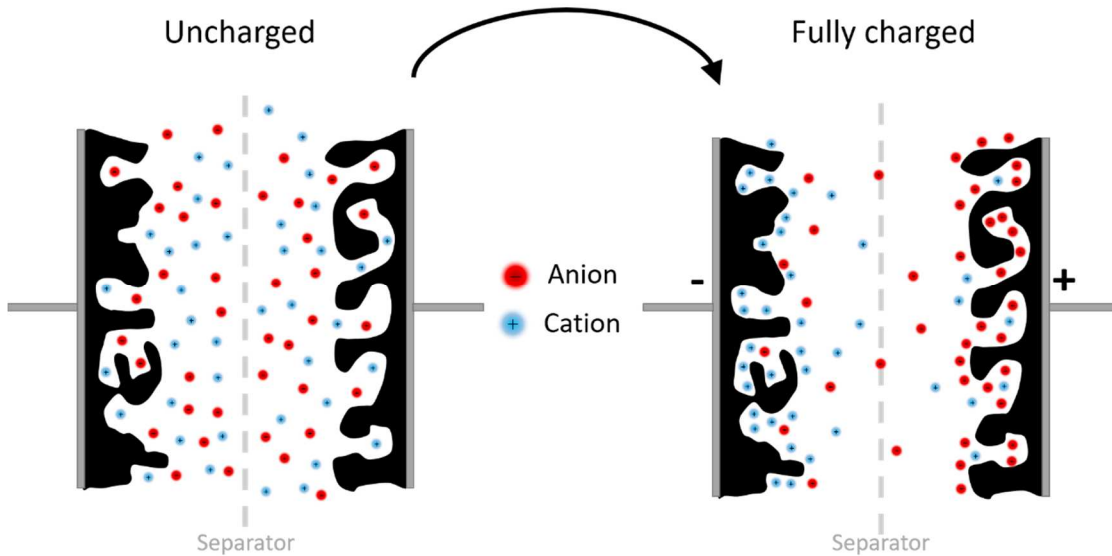


Figure 2.1: Schematic representation of the double layer formation in an EDLC made of two porous carbon electrodes.

In 1859 Helmholtz described the forming of a double-layer as a rigid layer of ions parallel to the surface (Figure 2.2a).<sup>15,22</sup> Analogous to conventional capacitors, the capacitance can be calculate by:

$$C_H = \varepsilon_r \varepsilon_0 \frac{A}{d} \quad (2.1)$$



where  $\varepsilon_0$  is the vacuum permittivity,  $\varepsilon_r$  is the relative permittivity of the electrolyte,  $A$  is the surface area, and  $d$  is the thickness of the Helmholtz layer. The combination of the enormous specific surface area (SSA) of microporous carbon materials (some studies claim over  $3000 \text{ m}^2 \text{ g}^{-1}$ )<sup>42</sup> and the few nanometers thick Helmholtz layer leads to a capacitance of  $10^2$ - $10^4 \text{ F}$  for EDLC devices compared to  $10^{-6}$ - $10^{-2} \text{ F}$  for conventional capacitors.<sup>43</sup>

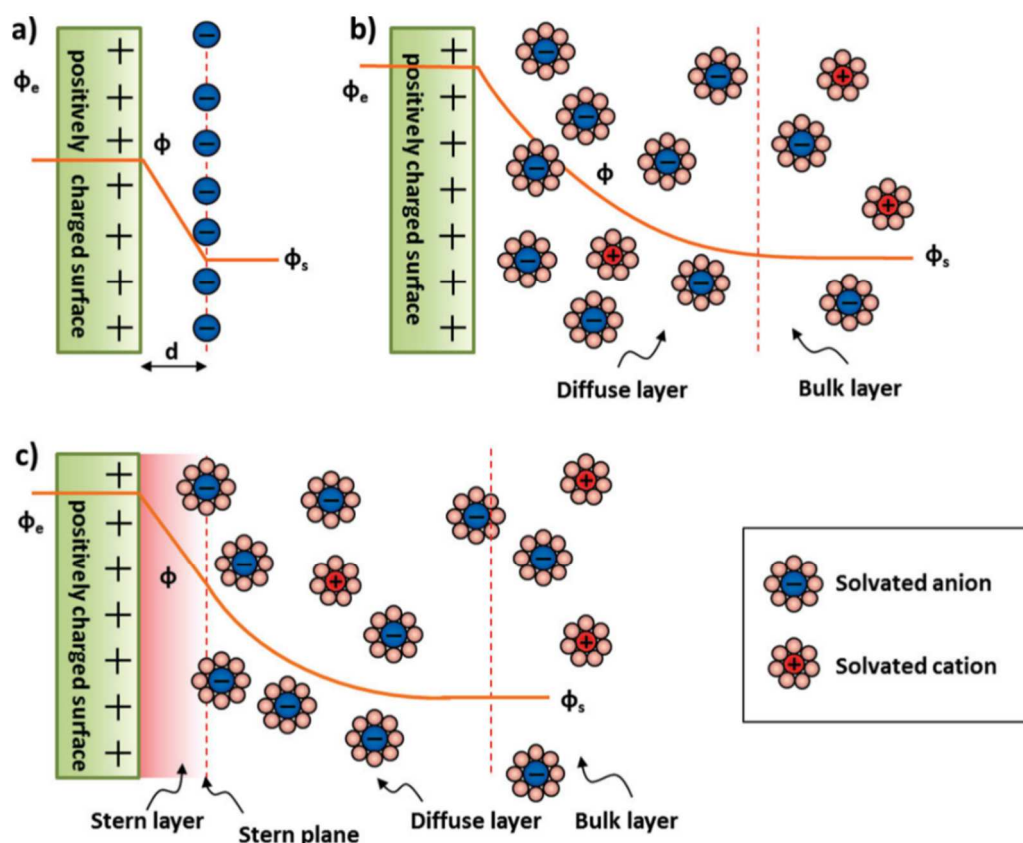


Figure 2.2: The Helmholtz model (a) describes the electrical double layer as a rigid layer of counter ions. No solvation shell or ion interactions are taken into account. The electrical potential  $\Phi$  decreases linear from the electrode potential  $\Phi_e$  to the bulk electrolyte potential  $\Phi_s$ . The Gouy-Chapman model (b) uses a diffuse layer with an exponential decay of the potential. The Stern model (c) combines both models. Reproduced with permission from Ref.<sup>15</sup> © WILEY-VCH

The Helmholtz model (Figure 2.2a) is the simplest way to explain the formation of a double-layer, but it fails to describe real systems. It neglects ion interactions, diffusion processes, dipole moment as well as the solvent. The Gouy-Chapman model proposes a diffuse layer of atoms, following a Boltzmann distribution of the ion concentration in the vicinity of the surface (Figure 2.2b) instead of the simple plane of ions. This model fails when highly charged layers are involved. Stern, therefore, proposed a combination of both previous models (Figure 2.2c), including

a strongly adsorbed layer (which cannot directly approach the surface) and a diffuse layer behind.<sup>15</sup> This results in an overall capacitance combined by the capacitance of the Stern layer  $C_H$ , which is equivalent to the Helmholtz layer, and the diffuse layer  $C_D$ :

$$\frac{1}{C_S} = \frac{1}{C_H} + \frac{1}{C_D} \quad (2.2)$$

These models are all developed for flat electrodes, which are not directly applicable for real porous materials with curved surfaces. For large pores (pore diameter  $\gg$  ion size), the curvature of the surface can be neglected and the Stern model for flat surfaces is sufficient to describe the formation of a double-layer.<sup>44</sup> For smaller pores, this is not the case. First, we look at capacitive behavior of cylindrical pores with a diameter of a few nanometers (mesopores) and below (micropores), where a double layer cannot be formed anymore (Figure 2.3). For small pore diameter, the formed double layer corresponds rather to a double cylinder capacitor with a capacitance described by:<sup>44</sup>

$$C_{cylinder} = \varepsilon_r \varepsilon_0 2\pi \frac{L}{\ln(\frac{r_a}{r_i})} = \varepsilon_r \varepsilon_0 2\pi \frac{L}{\ln(\frac{r_a}{r_a - d})} \quad (2.3)$$

with  $L$  being the pore length,  $r_a$  the pore radius and  $d = (r_a - r_i)$  the layer thickness (Figure 2.3a). If the pore diameter is further reduced, there is not enough space to form an inner cylinder. As a result, a “wire” of counter ions is accumulated in the center of the cylindrical pore. Therefore, the capacitance is determined by the size of the counter ion itself ( $a_0$ ) rather than the size difference of the inner and outer cylinder (Figure 2.3b):<sup>44,45</sup>

$$C_{wire} = \varepsilon_r \varepsilon_0 2\pi \frac{L}{\ln(\frac{r_a}{a_0})} \quad (2.4)$$

In many cases, pores are not cylindrically shaped, but exhibit a more slit like structure. For very small slit pores, Feng et al.<sup>46</sup> proposed a sandwich like model, where the two opposite pore walls are treated as electrodes with the same polarity. The charge of each electrode corresponds to half of the charge accumulated in the layer of counter ions in-between the two electrodes. This setup can be approximated by a combination of two parallel capacitors. leading to an overall pore capacitance of:<sup>46</sup>

$$C_{slit} = \varepsilon_r \varepsilon_0 \frac{2A}{\frac{d_{slit}}{2} - a_0} \quad (2.5)$$

with  $A$  being the electrode area and  $d_s$  the distance between the pore walls (Figure 2.3c).

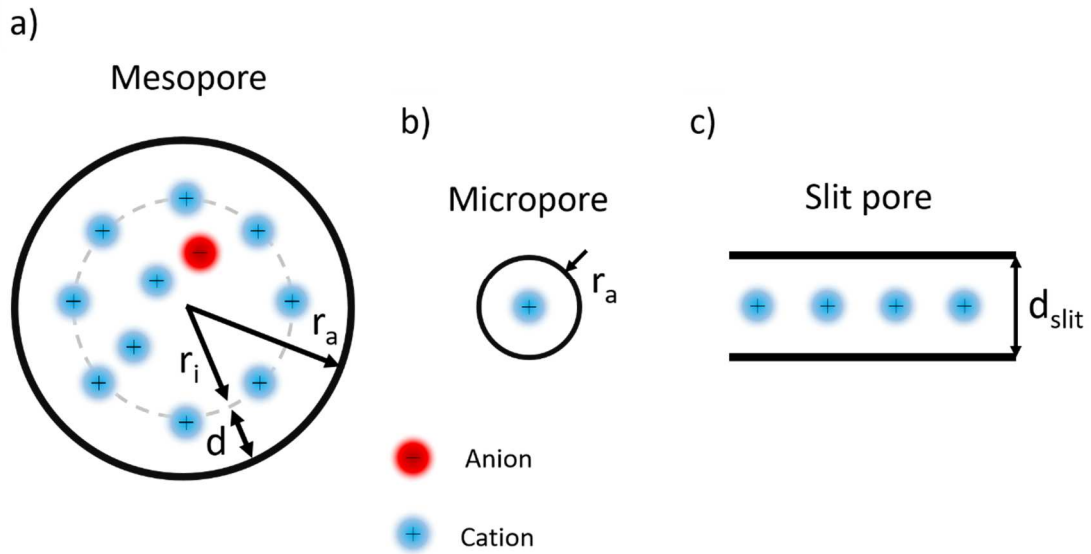


Figure 2.3: Schematic representation of the double layer formation in (a) cylindrical mesopores (pore diameter in the range of several ions) and (b) cylindrical micropores (pore diameter in the range of the ion size) as well as for a slit shaped micropore (c).

The two most important parameters for an EDLC device are the stored energy, defined by the capacitance  $C$  and the potential window  $U$ :

$$E = \frac{1}{2} CU^2 \quad (2.6)$$

and the maximum power, defined by the internal resistance  $R$  of the device:<sup>15</sup>

$$P = \frac{1}{4} \frac{U^2}{R} \quad (2.7)$$

The surface area of the electrodes and the electrochemical stability window of the electrode and the electrolyte limit the capacitance and the maximum potential, respectively. They are therefore the limiting factors for the achievable energy density.<sup>47</sup>

A conventional supercapacitor device consist of two separate electrodes (shown in Figure 2.1), resulting in an overall capacitance similar to two individual serial capacitors:

$$\frac{1}{C_{Device}} = \frac{1}{C_-} + \frac{1}{C_+} \implies C_{Device} = \frac{C_- C_+}{C_- + C_+} \quad (2.8)$$

where  $C_-$  and  $C_+$  correspond to the capacitance of negative and the positive electrode, respectively. In principle, there are two different possible cell setups: a symmetrical and an asymmetrical setup. The symmetrical cell design consisting of two electrodes made from the same material with the same size and capacitance. This leads to an overall capacitance of exactly half the value of each individual electrode. The potential at each electrode is half the overall cell voltage. The asymmetric cell setup can be achieved by using two electrodes produced from the same material but with different capacitance, or by using two different electrode materials. Because of the different capacitance of each electrode, the cell potential is not evenly divided between both electrodes. This can be used to adjust the potential at each electrode, which in some cases leads to an increase of the usable potential window because the cathodic and anodic stability windows are not necessary the same.

The main issue of a pure EDLC is the limited energy stored in each individual cell. Progress in material design, cell engineering and sophisticated systems like hybrid devices<sup>16</sup> can increase the capacitance of each cell, but cannot change the fact that a large portion of a deployable supercapacitor device not only consists of the active material and the electrolyte, but also needs additional components like the housing, electrical contacts, current collectors, etc. As a result, the active material can be as low as one fourth of the mass of the whole device.<sup>48</sup>

### 2.1.2 Electrochemical flow capacitor

The electrochemical flow capacitor (EFC) transfers the concept of a flow battery to supercapacitors.<sup>49</sup> In contrast to a regular EDLC, where the electrical charge is stored at the electrode/electrolyte interface of two solid electrodes, the EFC stores its energy in charged slurry containing both, the electrode material and the electrolyte. To charge or discharge the slurry, it is pumped through a cell containing the polarized current collectors (Figure 2.4). The charge itself is stored in a double layer in each of the carbon particles contained in the slurry (Figure 2.4b).<sup>48</sup>

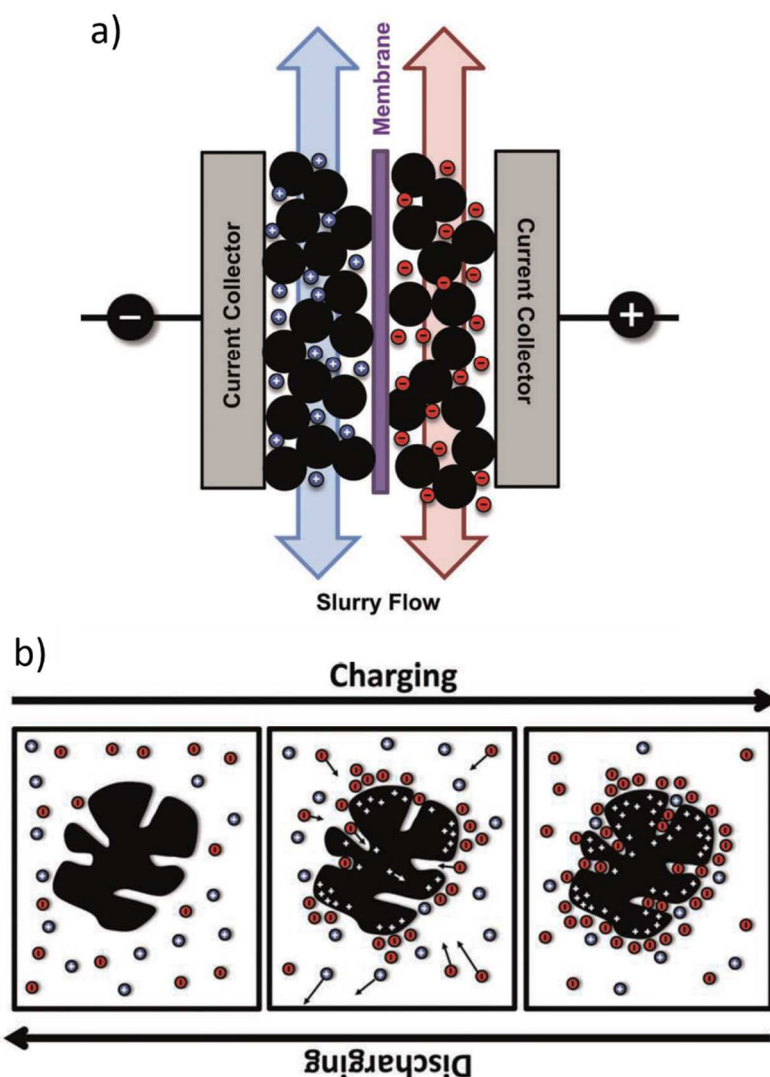


Figure 2.4: (a) Schematic representation of the setup of an EFC. The slurry (carbon-electrolyte mixture) is pumped through the polarized cell to charge/discharge the slurry. (b) Double-layer formation at each carbon particle in the slurry. Reproduced with permission from Ref.<sup>48</sup> © WILEY-VCH

This setup allows the decoupling of the cell size and the stored energy, since the electrolyte can be charged and stored in tanks outside the actual supercapacitor cell. The performance of an EFC strongly depends on the composition of the carbon/electrolyte mixture (slurry) and the cell design itself. The amount of carbon in the slurry has to be high enough to guarantee a physical contact between the individual particles, which is necessary for the electronic conductivity in the slurry. On the other hand, rheological properties of the slurry have to be optimized for a good performance. They depend on the amount and type of electrolyte, but also on the shape and size distribution of the carbon

particles. A narrow size distribution is preferred, since it reduces the particle size segregation. EFCs are primarily designed for stationary applications and could be used for example to stabilize power grid fluctuations. First proof of concept experiments have been done, but no commercial products are available until today.<sup>48</sup>

## 2.2 Electrochemical measurements

A comprehensive electrochemical characterization is essential to evaluate the performance of an electrode material for supercapacitor applications. From structural parameters (specific surface area or pore size distribution) alone, it is not possible to derive electrochemical performance parameters (e.g. the capacitance). Although, it is well accepted that a higher surface area leads to an increase in capacitance, other relations (e.g. pore size and shape) are not fully understood and it is not meaningful to draw any conclusion just from structural parameters, especially with redox active species present.<sup>15,47,50,51</sup> In addition, the performance of a supercapacitor is a system property: the use of different electrolytes, cell designs or scan rates can lead to different results.

A combination of extensive electrochemical characterization with structural and chemical analysis can help to increase the basic understanding of the charging mechanisms in a supercapacitor electrode.

In this chapter, the test cell setup as well as commonly used electrochemical measurement techniques are explained.

### 2.2.1 Two-electrode and three-electrode setup

A supercapacitor consists of two individual electrodes, resulting in an overall capacitance determined by both individual electrodes (Equation 2.8). As a result, the overall cell voltage is split between both electrodes ( $U_+$  and  $U_-$ ), depending on the corresponding capacitances  $C_+$  and  $C_-$ :

$$U_+ = U_{cell} \frac{C_-}{C_+ + C_-} \quad \text{and} \quad U_- = U_{cell} \frac{C_+}{C_- + C_+} \quad (2.9)$$

Understanding the dependency of electrode potential and capacitance is important for the interpretation of electrochemical measurements.

The measurement setup for the electrochemical characterization of a supercapacitor can be divided into two different designs: two-electrode cell and three-electrode cell. In a two-electrode cell, the setup is similar to an actual device. With such a setup is possible to build a symmetric or asymmetric device. This cell design is used to evaluate the performance parameters relevant for an actual device. It contains two electrodes with current collectors (CCs) and a separator. A three-electrode cell on the other hand is used to characterize just one electrode because only a single electrode determines the measured signal. This setup consists of a working electrode (WE), a counter electrode (CE), a reference electrode (RE), a separator and two CCs.<sup>52</sup> A schematic comparison of the different setups is shown in Figure 2.5

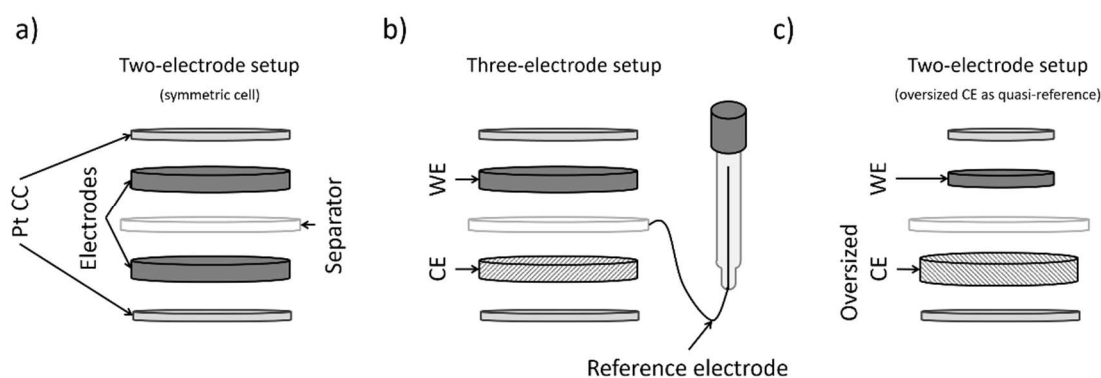


Figure 2.5: Comparison of different cell setups: (a) (symmetric) two electrode cell to evaluate device performance, (b) three-electrode setup for characterizing single electrodes, (c) two-electrode setup with an oversized CE as a quasi-reference

In a symmetric two-electrode cell, the potential is distributed between the two electrodes as described in Equation 2.9, while in a three-electrode cell the potential measured/applied corresponds to the potential between the WE and the RE.

In some cases, the use of a reference electrode is impracticable or even impossible due to limitations of the cell design. Additionally, the use of a reference electrode can also lead to inaccuracies when used with aqueous electrolytes.<sup>52</sup> Ag/AgCl electrodes and calomel electrodes both contain a 3M KCl solutions. During long term measurements, a contamination of the supercapacitor electrolyte with KCl can occur, which can influence the electrochemical measurements. To overcome these drawbacks, different quasi-reference electrodes (Pt-wire or oversized activated carbon (AC) electrode)<sup>53</sup> have been evaluated. It was shown that activated carbon materials can be used as a reliable quasi-reference for neutral aqueous electrolytes as well as for organic electrolytes and ionic liquids.

The use with electrodes containing redox active species requires a careful validation of the reference potential. In acidic aqueous electrolytes carbon, black is a better choice due to a reduced amount of surface groups compared to activated carbons.<sup>53,54</sup>

When using an oversized AC as a counter electrode, depending on its size, the CE still influences the measurements. The applied potential and the measured current are not fully determined by the WE (Equation 2.9). For example: a ten times higher capacitance of the CE will lead to a decrease of the measured capacitance by ~9% compared to the real value of the WE. Also the potential drop at the WE will be only ~91% of the overall cell voltage. It is worth noting that elevated charging and discharging rates can influence the accuracy of such a setup even further. If the (ten times oversized) activated carbon CE would experience a significant capacitance drop at higher rates, the actual capacitance ratio of WE/CE could be changed from the initial 1/10, leading to a change of the measured capacitance values. Another important factor is the used electrolyte, which can significantly influence the measured capacitance (see Chapter 2.9). Therefore, the electrochemical testing should be done with the electrolyte used for planned applications or experiments. Additionally, the use of electrodes with low mass (and a low capacitance) can also increase measurement errors due to an increased relative contribution of parasitic effects from other parts of the cell (wires, etc.).<sup>15,52</sup>

The symmetric two-electrode cell is often referred to as a full-cell setup and the three-electrode cell (or the two-electrode cell with an oversized CE as a quasi-reference) is also called half-cell setup.

### 2.2.2 Cyclic voltammetry

Cyclic voltammetry (CV) measurements are based on the linear increase and decrease of the potential with a predefined scan rate, resulting in a triangular potential signal between an upper and lower potential limit. The resulting current is measured and is directly proportional to the scan rate  $\nu$  for an ideal capacitor:<sup>55</sup>

$$I = C\nu = C \frac{dU}{dt} \quad (2.10)$$

with the proportional constant  $C$  representing the capacitance of a device. Figure 2.6 shows a schematic potential signal as well as the corresponding measured current. CV measurements are usually plotted in a cyclic



voltammogram, where the x-axis represents the applied potential and the y-axis shows the corresponding measured current or capacitance (Figure 2.6c and Figure 2.6d).

As shown in Equation 2.10, the measured current is proportional to the scan rate and the overall capacitance of the measured cell. For a better comparability between measurements performed with different materials at various scan rates, the measured current is normalized by the mass of the electrodes  $m$  as well as the used scan rate  $\nu$ , leading to units of specific capacitance ( $\text{F g}^{-1}$ ) instead of current plotted on the y-axis.

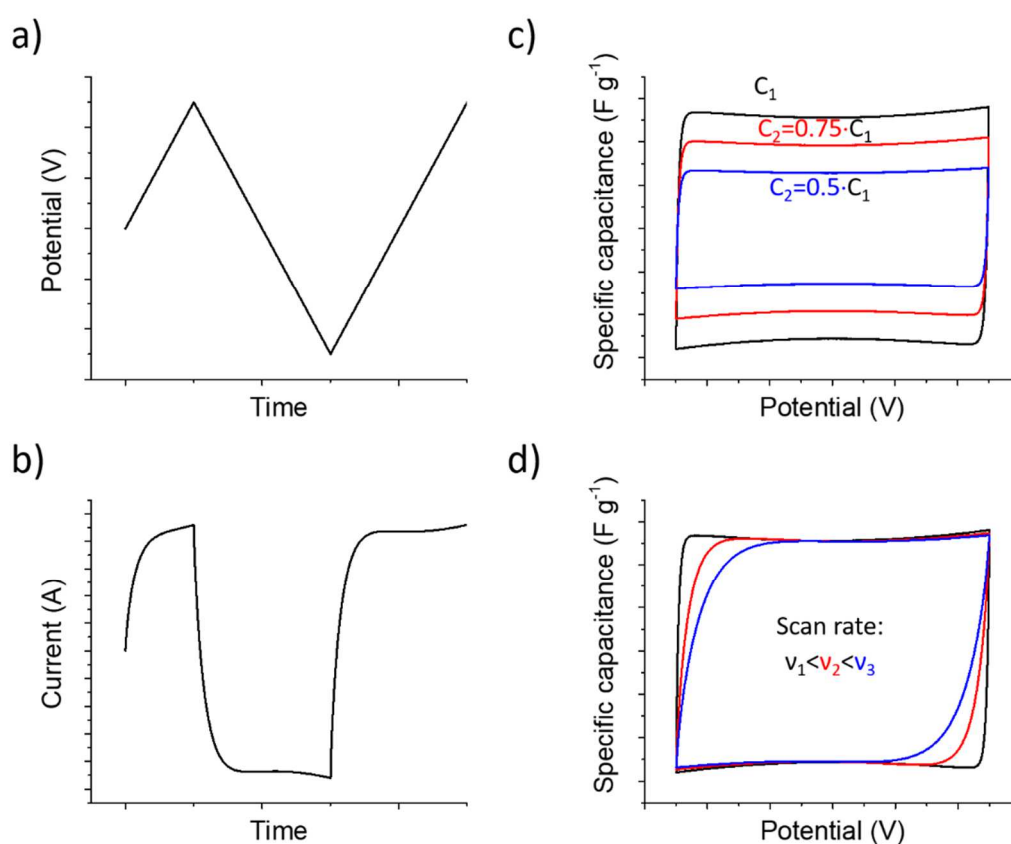


Figure 2.6: Applied potential during CV measurements (a) and measured current (b). Cyclic voltammogram (specific capacitance vs. applied potential) for cells with different capacitance (c) and for different scan rates (d).

For an ideal capacitor, a CV curve is rectangular. In a real device, effects like internal resistance or ion diffusion usually lead to a deviation from the ideal rectangular shape. Besides the cell setup and material properties (curves for different capacitances shown in Figure 2.6c), also measurement conditions can

affect the shape of the CV curve. Figure 2.6d shows the influence of the scan rate on the shape of a of the CV curve.<sup>56</sup>

The data evaluation from CV measurements depends on the cell design. In a three-electrode cell, the WE electrode alone determines the measured current. As a result, the specific capacitance of the electrode material  $C_{electrode}$  is equivalent to the capacitance calculated for the cell  $C_{cell}$ :

$$C_{electrode} = C_{cell} = \frac{\int_{t_1}^{t_2} I(t) dt}{\Delta U \cdot m} \quad (2.11)$$

where  $I(t)$  is the measured current,  $\Delta U$  the voltage window, and  $m$  the mass of the working electrode. Because of the constant scan rate, Equation 2.11 can be rewritten as:

$$C_{cell} = \frac{\int_{U_1}^{U_2} \frac{I(U)}{\nu} dU}{\Delta U \cdot m} \quad (2.12)$$

with  $\int_{U_1}^{U_2} \frac{I(U)}{\nu} dU$  being the area under the CV curve.

For a two-electrode cell, the calculated capacitance is a factor four lower compared to a three-electrode cell (or a two-electrode cell using an oversized CE):

$$C_{symmetric} = 4 \cdot C_{cell} = 4 \cdot \frac{\int_{t_1}^{t_2} I(t) dt}{\Delta U \cdot m_{total}} \quad (2.13)$$

where  $m_{total}$  is the total mass of both electrodes. This can be explained by the fact that a symmetric cell is basically a series of two individual capacitors. From Equation 2.8 it can be calculated, that a series of two serial capacitors of equal size lead to a measured capacitance only half the value of a single capacitor. The additional factor 2 results from the normalization to the combined mass of both electrodes. This has to be considered when comparing capacitance values obtained from two- and three-electrode setups.<sup>15,57,58</sup>

The measurements performed with two- and three-electrode cells can lead to large differences in the CV curves, especially when faradaic reactions are taking place. Figure 2.7 shows a the CV curves of a composition of carbon nanotubes with a pseudo capacitive conducting polymer (Polyaniline, PANI) measured with symmetrical two-electrode cell setup and a three-electrode cell using a Hg/Hg<sub>2</sub>SO<sub>4</sub> reference electrode. It can be clearly seen that the symmetric cell shows the typical rectangular shape of a supercapacitor, while the three-electrode setup shows

significant deviation from this ideal case. The difference can be explained by the fact that in the symmetric two-electrode setup the measured capacitance is similar to a serial combination of two individual capacitors, where the electrode with the smaller capacitance (Equation 2.8) limits the overall capacitance.<sup>59</sup>

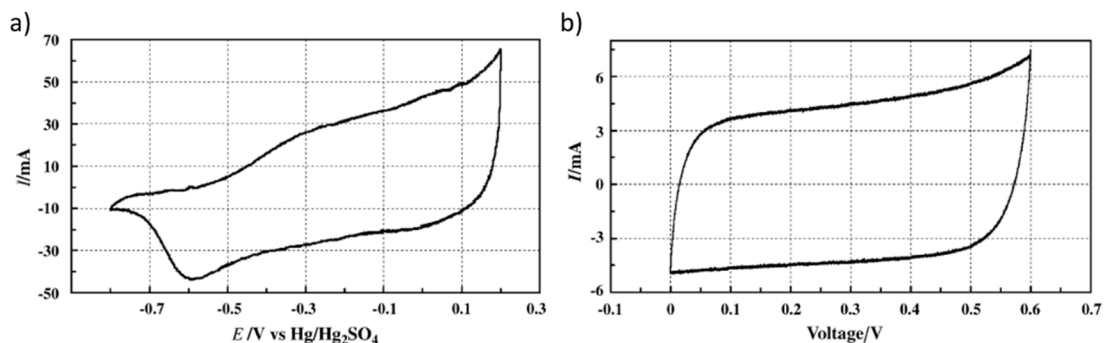


Figure 2.7: CV measurements of a PANI/multi-walled CNT electrode using a three-electrode cell (a) and a symmetric two-electrode setup (b). Both measurements were performed with a scan rate of  $5 \text{ mV s}^{-1}$ . Reproduced with permission from Ref.<sup>59</sup> © 2004 Elsevier Ltd.

The calculation of a capacitance using a three-electrode setup (Figure 2.7a) would strongly depend on the voltage window and is not comparable to the values obtained from the symmetrical cell. As a result, the three-electrode setup is suitable to investigate the electrochemical behavior of a single electrode, but not for determining the performance of an actual device. For comparing device relevant performance parameters, a two-electrode cell is recommended.<sup>52</sup>

### 2.2.3 Galvanostatic cycling

Galvanostatic cycling is also known as chronopotentiometry or GCPL (galvanostatic cycling with potential limit). This measurement technique is based on charging and discharging a test cell with a constant current between an upper and lower potential limit using a constant current, while measuring the resulting cell voltage. For an ideal capacitor with an internal resistance  $R_i$  and a capacitance  $C$  the potential changes linear with time:<sup>57</sup>

$$U(t) = IR_i + \frac{I}{C}t \quad (2.14)$$

resulting in a triangular shaped  $U$  vs.  $t$  curve shown in Figure 2.8. The sharp voltage drop occurring when changing from charging to discharging corresponds to the internal resistance  $R_i$  of the device:<sup>57</sup>

$$R_i = \frac{U_{dr}}{2I} \quad (2.15)$$

with  $U_{dr}$  being the voltage drop and  $I$  the charging/discharging current. The factor 2 originates from the fact that a change from charging ( $+I$ ) to discharging current ( $-I$ ) results in a current change of  $2I$ .

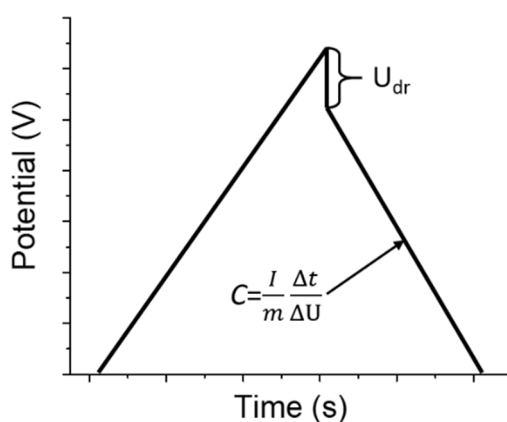


Figure 2.8: Schematic representation of a chronopotentiometry experiment.

From the slope of the curve, the capacitance can be calculated as following:<sup>58</sup>

$$C_{symmetric} = 4 \cdot C_{cell} = 4 \cdot \frac{I \Delta t}{m \Delta U} \quad (2.16)$$

The relation between the capacitance measured with (symmetric) two- and three-electrode cells has already been explained in the Chapter 2.2.2 (*Cyclic voltammetry*).

These calculations are only valid for an ideal linear behavior. If the measured curve deviates from the linear behavior (e.g. due to faradaic reactions), the calculated capacitance is not constant but depends on the voltage range used. Figure 2.9 illustrates the dependency of the calculated capacitance for a non-ideal system. Depending on the used potential window, the calculated slope (and capacitances) can differ significantly.

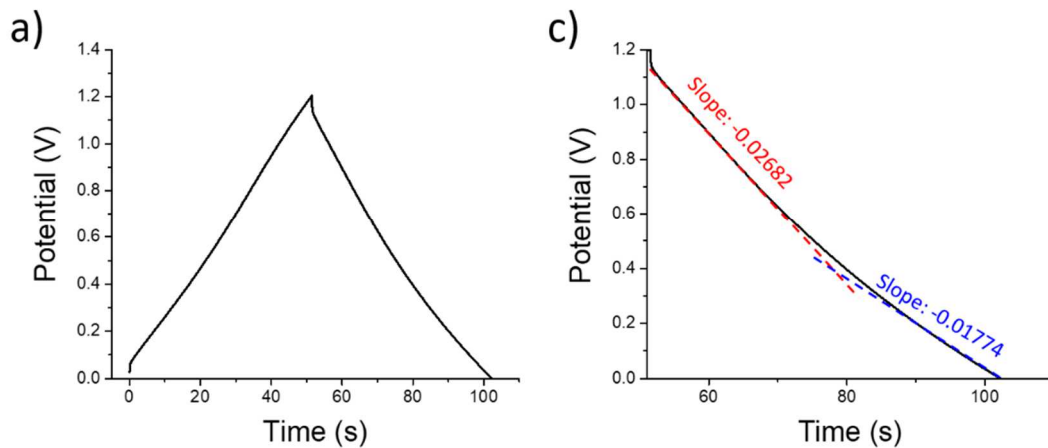


Figure 2.9: Galvanostatic cycling of a real two-electrode cell using an activated carbon as electrode material (a). Illustration of the different slopes in the discharging curve (b).

In the case of a not ideally linear behavior, it is recommended to calculate the capacitance via the overall energy in of a device. The specific capacitance can be calculated from Equation 2.6 leading to:<sup>58</sup>

$$C = \frac{E}{m} \frac{1}{2\Delta U^2} \quad (2.17)$$

with the energy density  $\frac{E}{m}$  calculated from:

$$\frac{E}{m} = \frac{I}{m} \int_{t_1}^{t_2} U(t) dt \quad (2.18)$$

Two additional parameter easily obtained from chronopotentiometry measurements are the coulombic efficiency  $\eta_c$  and the energy efficiency  $\eta_E$ . The coulombic efficiency represents the charge transfer ratio during charging and discharging, while the energy efficiency represents the ratio of energy delivered while discharging compared to energy needed for charging a device.  $\eta_c$  can be calculated just from the charging time  $t_c$  and discharging time  $t_d$ , since they are directly proportional to the accumulated charge if a constant current is used:<sup>58</sup>

$$\eta_c = \frac{Q_{discharge}}{Q_{charge}} = \frac{t_d}{t_c} \quad (2.19)$$

In an ideal system, coulombic efficiency and energy efficiency are identical, in a real system  $\eta_E$  can deviate from  $\eta_c$ , especially if faradaic reactions are involved. Therefore, the energy efficiency should be calculated in the following way:

$$\eta_E = \frac{E_{discharge}}{E_{charge}} \quad (2.20)$$

In an EDLC,  $\eta_c$  and  $\eta_E$  are typically above 95%.<sup>21,60,61</sup>

## 2.2.4 Chronoamperometry

For a chronoamperometry (CA) experiment the potential at the working electrode is changed stepwise and the resulting current is recorded as a function of time. This measurement technique is well suited to study equilibrium ion configuration.<sup>21</sup>

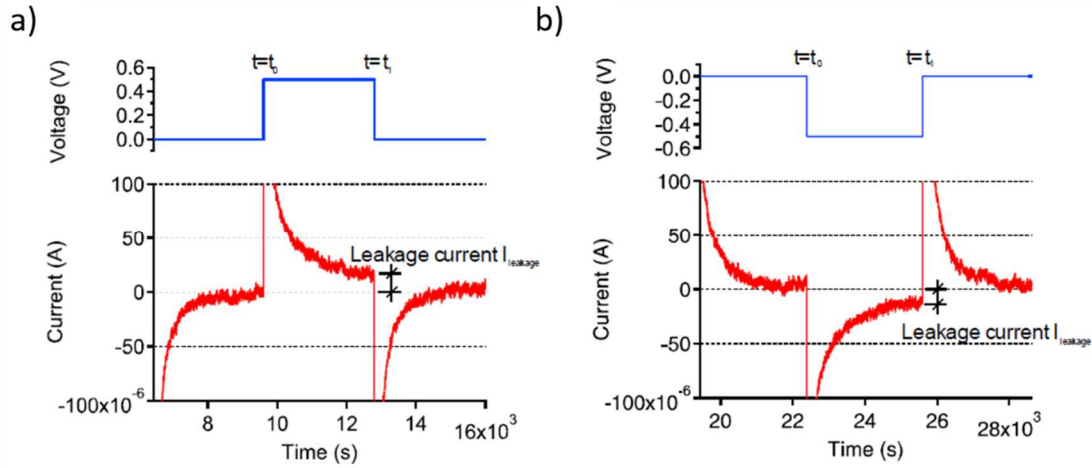


Figure 2.10: Chronoamperometry measurements for an EDLC using an aqueous 0.01M RbBr electrolyte at a positive (a) and negative (b) potential step. Reproduced with permission from Ref.<sup>21</sup> © 2018, Springer Nature

In addition to study the charging behavior of pure EDLC devices, CA can be used to analyze diffusion-controlled processes like redox reactions:<sup>62-64</sup>

$$I(t) = nFAc\sqrt{\frac{D}{\pi t}} \quad (2.21)$$

with  $n$  being the number of transferred electrons,  $F$  the Faraday constant,  $A$  the electrode area,  $c$  the bulk concentration and  $D$  the diffusion coefficient.

## 2.2.5 Electrochemical impedance spectroscopy

Electrochemical impedance spectroscopy (EIS) is a powerful tool to analyze (electrochemical) processes with a large range of time constants. For supercapacitors, this measurement technique can be used to study a broad range of effects: pseudo-capacitive behavior, ion diffusion characteristics, as well as faradaic processes in hybrid devices.<sup>65-68</sup>

EIS measurements are based on the fact that for a small enough excitation signal, the measured response becomes linear (Figure 2.11). Similar to Ohm's law, the potential  $U$  is proportional to the current  $I$  with the impedance  $Z$  as a proportional constant:<sup>57</sup>

$$U = Z \cdot I \quad (2.22)$$

EIS measurements can either be voltage or current controlled. All measurements in this thesis were done using a voltage controlled measurement protocol with a low amplitude ( $U_A$ ) sinusoidal alternating signal:<sup>57,69</sup>

$$\Delta U(\omega) = U_A e^{j\omega t} \quad (2.23)$$

resulting in a measured sinusoidal current signal with the amplitude  $I_A$ , shifted by the phase angle  $\varphi$  vs. the applied potential:

$$\Delta I(\omega) = I_A e^{j(\omega t + \varphi)} \quad (2.24)$$

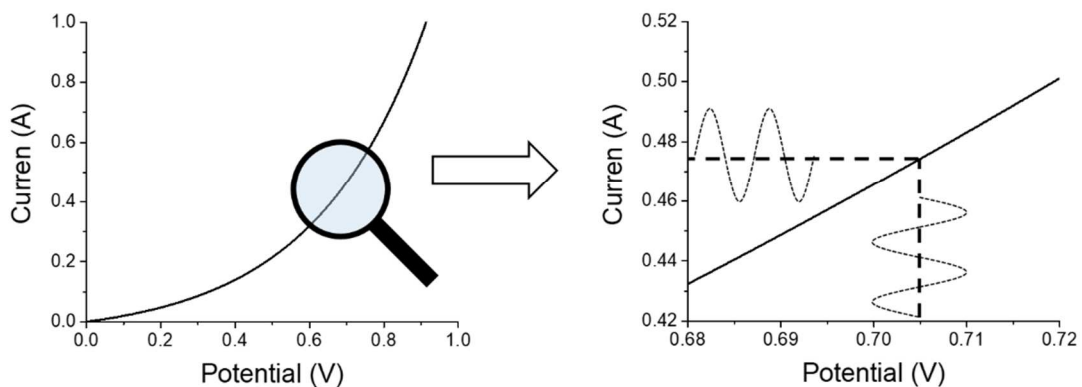


Figure 2.11: Schematic representation of a polarization curve with a nonlinear behavior (left). In a small range (right), the curve becomes linear. Therefore, a small excitation signal leads to a linear response.

Combining Equations 2.22 to 2.24 results in the complex impedance  $Z(\omega)$  with  $Z_{Re}$  and  $Z_{Im}$  being the real and imaginary part of impedance, respectively:<sup>57,69</sup>

$$Z(\omega) = \frac{\Delta U(\omega)}{\Delta I(\omega)} = |Z(\omega)|e^{-j\varphi} = Z_{Re} + jZ_{Im} \quad (2.25)$$

To analyze impedance data, it is important to understand the individual contributions in a supercapacitor. Figure 2.12 shows the simplified equivalent circuit for a pure EDLC with two serial RC modules. For the pseudo capacitive electrode, an additional faradaic impedance  $Z_{faradaic}$ , consisting of the charge transfer resistance  $R_{CT}$  and an additional (pseudo)capacitance  $C_{ps}$ , is necessary. These are the simplest equivalent circuits possible without considering leakage current, ion diffusion processes, or any other additional contributions.<sup>57</sup>

The interpretation of EIS measurements is not always an easy task. Electrochemical impedance spectroscopy is a suitable tool to find equivalent circuits (Figure 2.12) describing the processes taking place in a device or an electrode, with one major drawback: the results are not unique. It is possible to generate an equivalent circuit fitting the data perfectly while at the same time not representing any real processes occurring in the actual cell. Therefore, finding and developing a physics based model is a crucial part in the data analysis process.

For data visualization two different plots are common: the Nyquist plot ( $Z_{Im}$  vs.  $Z_{Re}$ ) and the Bode plot ( $|Z(\omega)|$  vs. frequency).<sup>57,70</sup> Figure 2.13 shows schematic Nyquist plots for different idealized capacitor types. An ideal capacitor just shows a vertical line, shifted by the internal resistance (Figure 2.13a). This real part of the impedance is also called the equivalent serial resistance (ESR), which originates from internal resistance of the electrode and electrolyte, wiring as well as contact resistance between the CC and the electrode. The equivalent circuit of such a system consist of only a capacitance and a resistor (Figure 2.12b). The equivalent circuit for an electrode also containing faradaic (pseudo-capacitive) contributions adds an additional parallel impedance  $Z_{faradaic}$  (Figure 2.12c). As a result, the Nyquist plot shows a vertical line combined with a characteristic semicircle due to the faradaic reactions (Figure 2.13b). The semicircle originates from the parallel RC module (Figure 2.12b) of the pseudo-capacitive (faradaic) contributions, with the charge transfer resistance defining the radius of this circle.<sup>57,70</sup>



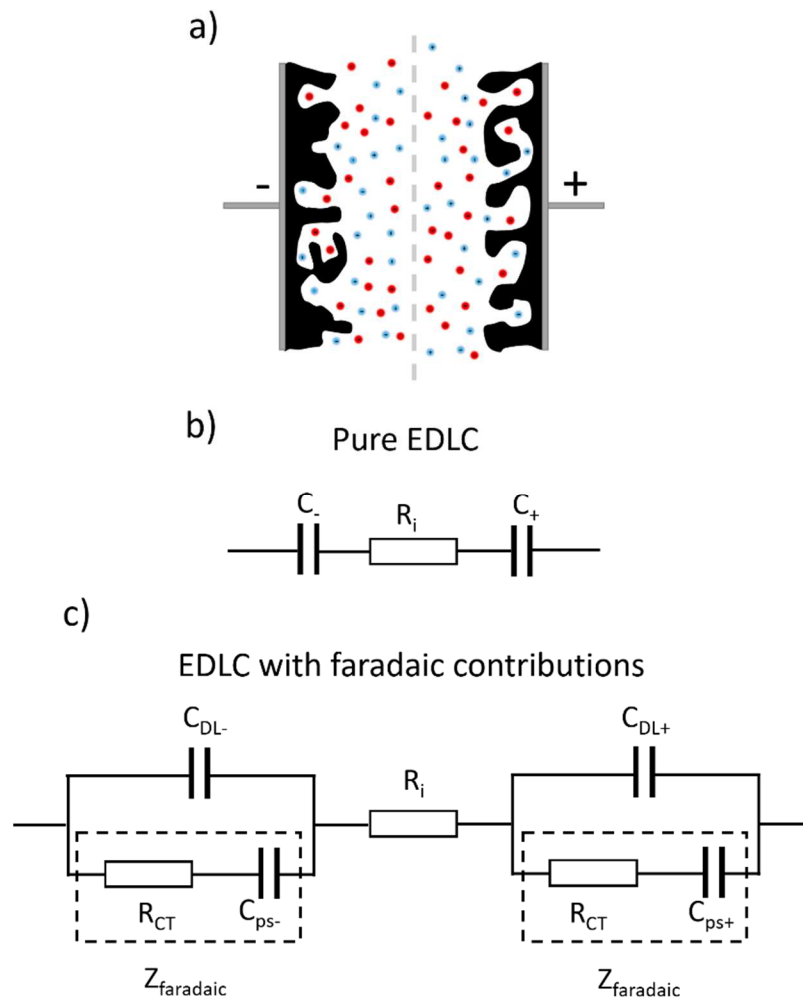


Figure 2.12: Schematic representation of a supercapacitor device (a) with a simple equivalent circuits for a pure EDLC (b) as well as an EDLC with faradaic contributions (c). In both setups, the serial resistance  $R_i$  (also called equivalent serial resistance, ESR) contributes for the resistance of the electrolyte as well as additional serial resistance in the cell (electrode/current collector contact resistance, wires, etc.). Faradaic contributions lead to an additional, parallel faradaic impedance  $Z_{faradaic}$  consisting of a charge transfer resistance  $R_{CT}$  and an additional (pseudo)capacitance  $C_{ps}$  at each electrode. Additional effects like ion diffusion are not considered here.

A real EDLC (Nyquist plot schematically shown in Figure 2.13c) can deviate from the ideal system and therefore not be described by the previous equivalent circuits. The most prominent difference can be seen in the high to medium frequency range where, instead of a vertical line, a line with a slope of  $\sim 45^\circ$  is present. This line is usually attributed to diffusion processes in the electrode. To

describe such a behavior in an equivalent circuit, an additional element is used: the constant phase element (CPE)  $Z_{CPE}$ :<sup>57,69,71</sup>

$$Z_{CPE} = \frac{1}{Y_0(j\omega)^\alpha} \quad (2.26)$$

$Y_0$  is the admittance and the exponent  $\alpha$  controls the slope of the line in the Nyquist plot. The constant phase element can be used to describe any behavior between a pure resistor, with the exponent  $\alpha = 0$ , and a pure capacitance with  $\alpha = 1$ . The most prominent version of a (CPE) is the so-called Warburg impedance (sometimes also called diffusion impedance) with  $\alpha = 1/2$ , leading to the characteristic  $45^\circ$  slope.<sup>57</sup>

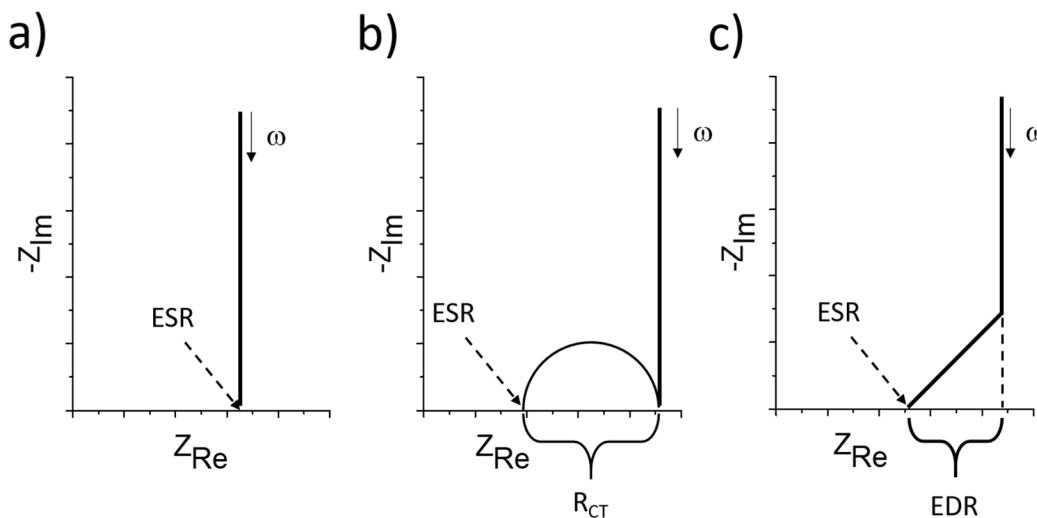


Figure 2.13: Schematic representation of (a) an ideal capacitor, (b) a combination of an ideal capacitor and an ideal pseudo-capacitance and (c) an AC based EDLC including diffusion contributions.

For a better understanding of the constant phase element, an equivalent circuit for an activated carbon based supercapacitor is shown in Figure 2.14. The left part shows a circuit as for the ideal EDLC, the right part is called a finite vertical ladder network. Each RC combination has a different time constant  $\tau$ , with an increasing value from bottom to top. This results in an asynchronous charging of each capacitance in the system, leading to the characteristic Warburg region ( $45^\circ$  slope) in the Nyquist plot. The finite ladder network can be used to model an activated carbon electrode, with each RC combination describing a set of pores with similar charging behavior. While dimensions of the pores and the time constant are related, it is not possible quantitatively relate them. The transition

frequency separating the Warburg region and the capacitive region is called knee frequency.<sup>72</sup>

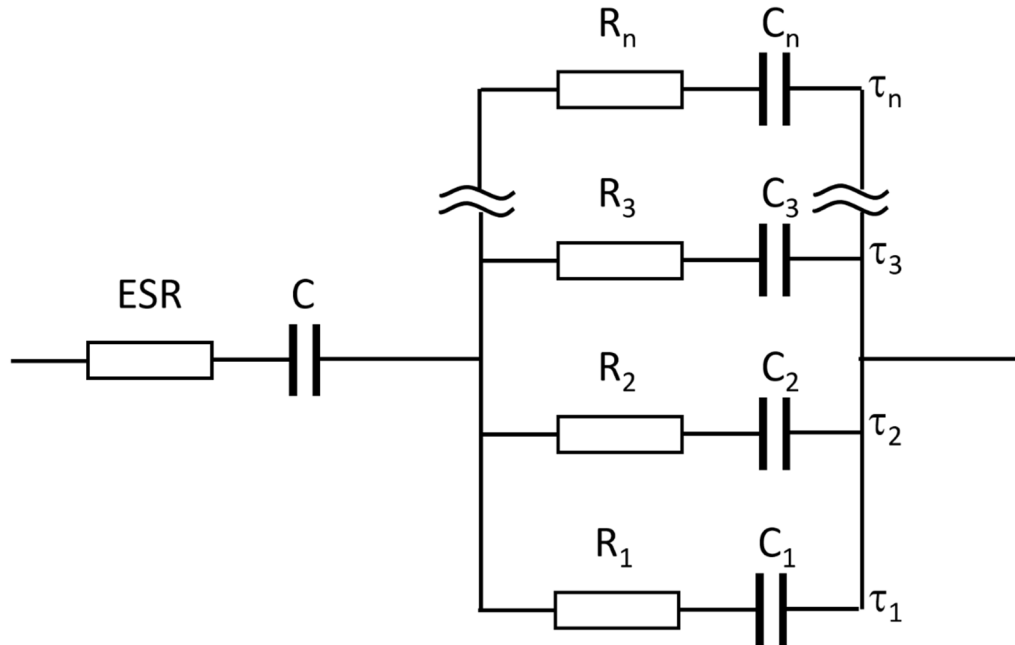


Figure 2.14: Equivalent circuit for a typical activated carbon based EDLC, representing the behavior shown in Figure 2.13c.

In addition to the frequency, a resistance associated with this transition change can be defined: the so-called equivalent distribution resistance (EDR).<sup>73,74</sup> As a result, a supercapacitor can be described by a nearly ideal capacitance and an ESR, which is increased by the EDR at lower frequencies (Figure 2.13c). The capacitance and resistance decrease with increasing frequencies, described by the slope of the CPE ( $45^\circ$  for a Warburg element), can be explained by a limitation of the accessible electrode area at higher frequencies. This effect can be caused by a (slow) diffusion of the ions in the porous electrode. The pore system of the electrode material can strongly influence the Warburg region and therefore the value of the EDR. This will be also discussed in Chapter 4. As a rule of thumb, an increase in pore length and a decrease of pore diameter of a cylindrical pore will lead to a higher EDR value.<sup>70,75</sup> The length and radius are not the only pore parameters influencing the Warburg region. Keiser et al.<sup>76</sup> have shown that the shape of the pore can influence the slope of the Warburg region (Figure 2.15).<sup>70,76</sup>

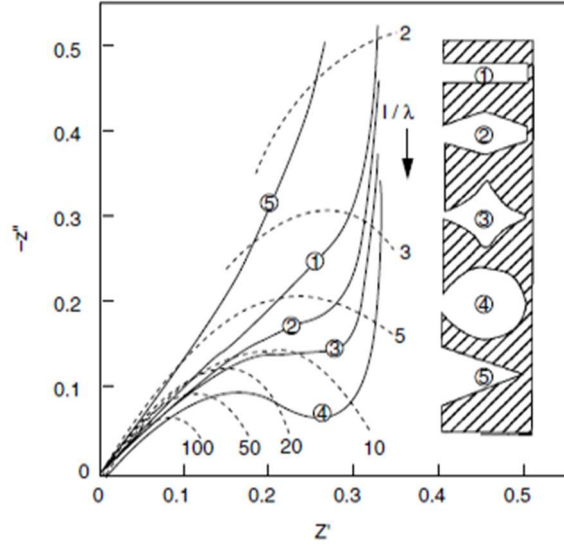


Figure 2.15: Influence of the pore shape on the behavior of the Warburg region in a Nyquist plot. Reproduced with permission from Ref.<sup>70</sup> © John Wiley and Sons

Using equivalent circuits is not the only approach to analyze impedance data. Alternatively, the investigated device can be treated as a single component with the capacitance being a complex quantity with the real part  $C_{Re}(\omega)$ :<sup>69,77</sup>

$$C_{Re}(\omega) = \frac{-Z_{Im}(\omega)}{\omega|Z(\omega)|^2} \quad (2.27)$$

and the imaginary part  $C_{Im}(\omega)$ :

$$C_{Im}(\omega) = \frac{Z_{Re}(\omega)}{\omega|Z(\omega)|^2} \quad (2.28)$$

combined to the overall capacitance  $C$

$$C = C_{Re} - jC_{Im} \quad (2.29)$$

Both, the imaginary and the real part of the capacitance are usually plotted against the frequency (Figure 2.16). From these curves the knee frequency  $f_{knee}$  can reliably be determined. The  $C_{Im}$  vs. frequency curve shows a maximum at the knee frequency, in the  $C_{Re}$  vs. frequency curve. The knee frequency also corresponds to the frequency where  $C_{Re}$  is reduced to half the value at low frequencies. The corresponding time constant  $\tau_0 = 1/f_{knee}$  is called the dielectric relaxation time.<sup>69</sup>

By separating the capacitance into a real and an imaginary part, it is also possible to distinguish between stored and dissipated energy in the system, which

is basically equivalent to a separation in a capacitive and a resistive behavior. While  $C_{Re}$  represents the “real” capacitance of the system,  $C_{Im}$  corresponds to the dissipated energy. As a result,  $f_{knee}$  represents the frequency where the coulombic efficiency reaches 50%.  $C_{Re}$  measured at low frequencies is similar to values obtained from chronopotentiometry.<sup>57,69</sup>

As an example, EIS measurements can be used to evaluate the influence of solvents on the power delivery of a supercapacitor device. Figure 2.16 shows the real and imaginary part of two supercapacitor cells using activated carbon electrodes and two different organic solvents (propylene carbonate (PC) and acetonitrile (AN) with  $NET_4BF_4$ ). It can clearly be seen that compared to the cell using PC, the AN containing cell shows a higher  $C_{Re}$  value (at a given frequency), as well as a shorter  $\tau_0$ . As a result the AN containing cell exhibits a higher maximum power. This can be explained by the better ionic conductivity in the AN solution.<sup>69</sup>

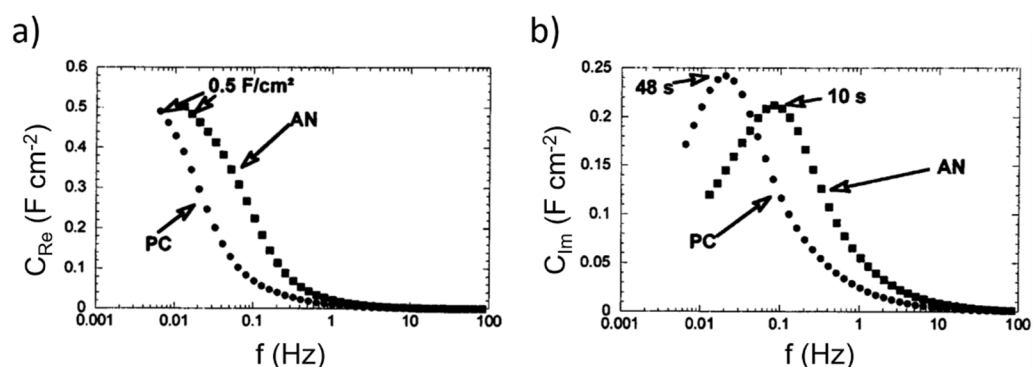


Figure 2.16: Real (a) and imaginary (b) capacitance vs. frequency for supercapacitors using AN and PC as a solvent. The PC based EDLC has a nearly five times higher relaxation constant  $\tau_0$  (PC: 48 s; AN: 10 s). Reproduced with permission from Ref.<sup>69</sup> Copyright 2003, The Electrochemical Society.

## 2.3 Scattering

In a scattering experiment, the scattered intensity is recorded as a function of the length of the scattering angle  $\theta$  (Figure 2.17). All experiments in this thesis were done using X-rays, but neutrons are an often-used alternative.

The primary X-ray beam can be scattered by the electrons in the sample in two different ways: elastically or inelastically. An inelastic scattering event involves an energy transfer between the photon and the sample. As a result, the energy of the scattered photon is different from the incident photon and has no fixed phase

relation leading to an incoherent background when a scattering experiment is performed. In an elastic scattering process on the other hand no energy is transferred from the photon, but a momentum transfer changes its direction (Figure 2.17), leading to:<sup>78,79</sup>

$$\hbar\vec{q} = \hbar(\vec{k}_s - \vec{k}_0) \longrightarrow \vec{q} = \vec{k}_s - \vec{k}_0 \quad (2.30)$$

with  $\vec{q}$  being the scattering vector and  $\vec{k}_s$  and  $\vec{k}_0$  being the wavevectors of the scattered wave and the primary wave, respectively. The energy of the scattered wave is similar to the energy of the primary beam, therefore, the magnitude of the scattered wavevector and the primary beam are equal:

$$|\vec{k}_s| = |\vec{k}_0| = \frac{2\pi}{\lambda} \quad (2.31)$$

with  $\lambda$  being the X-ray wavelength. The relation between the scattering angle and the length of the scattering vector  $q$  is given by (Figure 2.17):<sup>80,81</sup>

$$|\vec{q}| = q = \frac{4\pi}{\lambda} \sin(\theta) \quad (2.32)$$

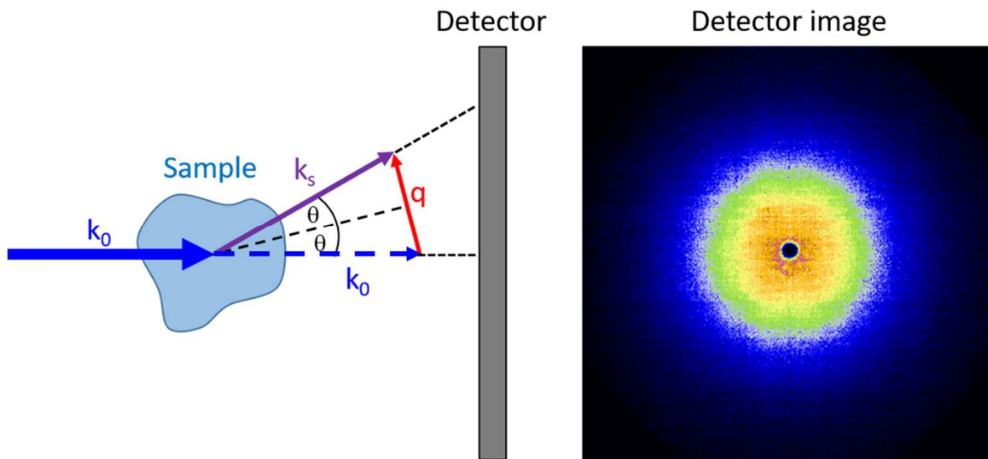


Figure 2.17: Schematic representation of the scattering process and a 2D detector image.

## 2.4 Absorption of X-rays

When an X-ray photon is absorbed by an atom in the sample, its energy is transferred to the atom by changing the electronic state of the atom. This can lead to different effects: the emission of photoelectrons or Auger electrons as well

as the emission of a fluorescence photon. These effects will not be discussed here, only a short description of fluorescence will be given later. The transmitted intensity (primary intensity - absorbed intensity) depends on the sample (in particular on the number of electrons) itself as well as the energy of the incident X-ray beam and follows Lambert-Beers law.<sup>78</sup>

$$I(x, E) = I_0 e^{-\mu(E)x} \quad (2.33)$$

with  $I_0$  being the intensity of the primary X-ray beam,  $E$  being the energy of the primary beam,  $\mu(E)$  being the energy depended attenuation coefficient and  $x$  the sample thickness. The absorption drastically increases when the energy of primary X-ray reaches an absorption edge.

## 2.5 Small-angle X-ray scattering

Small-angle X-ray scattering (SAXS) is a well-established method (based on elastic scattering of photons) to study particular systems as well as structural details of porous materials on the micro- and mesopore length scale. The description of small-angle X-ray scattering will be done in a very compact form, since this method and the underlying principles have been described in detail in previous theses written at the Institute of Physics.<sup>38-40</sup>

### 2.5.1 Particle scattering

The principles of SAXS will be explained assuming a diluted system of particles with no interaction between those particles. This is basically a two-phase system containing particles (phase 1) and the surrounding phase (e.g. a solvent).

In a SAXS experiment, the scattered intensity is measured as a function of the scattering vector at small angles. Using the scattering vector length instead of the scattering angle is advantageous especially when measurements are performed at different energies. The intensity measured with SAXS can be written as:<sup>78</sup>

$$I(q) \propto S(q)F(q)F^*(q)N \quad (2.34)$$

where  $S(q)$  is the structure factor,  $N$  is the number density of particles in the sample,  $F(q)$  and  $F^*(q)$  are the scattering amplitude and its complex conjugate of one isolated particle, respectively. The scattering intensity is proportional to the Fourier transform of the electron density distribution  $\rho(r)$  in the sample.<sup>78,80,82</sup>

The structure factor depends on particle interactions and the distribution function of the particles. For diluted systems with no particle interactions,  $S(q)$  is approximately 1 and does not have to be considered.<sup>83</sup> For a simple system of particles with a constant electron density in a solution,  $F(q)F^*(q)$  is a function of the electron density difference:

$$P(q) = F(q)F^*(q) \propto \Delta\rho^2 \quad (2.35)$$

where  $\Delta\rho^2 = (\rho_{Particle} - \rho_{Solution})^2$  is the squared electron density difference and  $P(q)$  is the form factor of a single particle, which is determined by the size and shape of the particle.  $P(q)$  has been calculated for a variety of different particle shapes.<sup>82,83</sup>

The use of SAXS is not limited to a system of diluted particles. If the particles are not diluted, the structure factor  $S(q)$  is not necessarily 1, but depends, as the name already suggests, on the structure of the analyzed samples. Depending on the structure, the separation in a structure factor and a form factor might not be valid. A short description of the scattering contributions of a hierarchical carbon material with (ideal) hexagonally ordered mesopore structure (used in this thesis) will be given here:

First, we look at a hexagonally ordered system of dense carbon nanorods. For such a system the separation of the intensity into a structure factor and a form factor is valid. The structure factor of a perfect hexagonal 2D lattice spherically averaged (i.e. powder samples) can be written as:<sup>84</sup>

$$S(q) = \frac{1}{q^2} \sum_{hk} M_{hk} S_{hk}(q) \quad (2.36)$$

with  $M_{hk}$  being the multiplicity factor and  $S_{hk}$  being a delta function at the peak positions (depending on the lattice type and lattice parameter). The form factor of a nanorod can be approximated by the form factor of an ideal (infinitely long) cylinder  $P(q)_{cylinder} = (F(q)_{cylinder})^2$  with:<sup>85</sup>

$$F(q)_{cylinder} = \frac{2J_1(qR)}{qR} \quad (2.37)$$

with  $R$  being the cylinder radius and  $J_1$  the Bessel function of first kind and order zero. In such a system, the scattering contrast is given by the electron density difference between the mesopores (void space) and the average electron density of the nanorods (again a two-phase system). The carbon nanorods are not a dense material with a uniform electron density distribution, but consist of a



(micro)porous structure. Therefore, an additional scattering contribution has to be taken into account.

## 2.5.2 SAXS on non-particular systems

For the microporous carbon material the separation into a form factor and a structure factor is not necessarily valid, if the pore structure is described as a percolating network instead of individual particles. The porous carbon nanorod again can be treated as an ideal two-phase system containing only pores (phase 1) and carbon matrix (phase 2), leading to a generalized scattering intensity of:<sup>82,86</sup>

$$I(q) = V(1 - \varphi)\varphi(\Delta\rho)^2 \int_0^\infty 4\pi r^2 \gamma_0(r) \frac{\sin(qr)}{qr} dr \quad (2.38)$$

with the total volume  $V$ , the porosity  $\varphi$ , the scattering contrast  $(\Delta\rho)^2$ , and the correlation function  $\gamma_0(r)$ . With an incoherent approximation, the scattering curve of the hexagonally ordered carbon nanorods represents a superposition of the microporous structure inside the rods and hexagonally ordered cylinders (Figure 2.18). There is also a third hierarchy level: the macropores between the carbon struts (see Chapter 4). This macropore system is responsible for the increasing intensity at low  $q$ -values. The concept of a superposition of the individual contributions is only valid if the incoherent approximation holds.

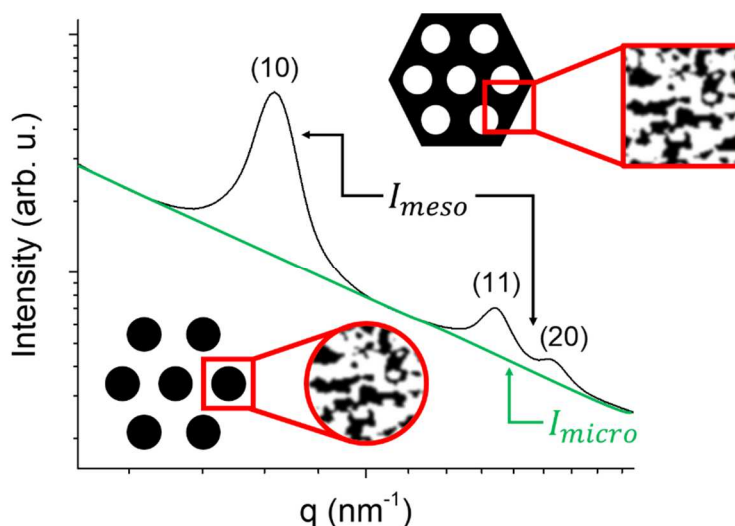


Figure 2.18: Schematic representation of the scattering pattern of ordered mesopore structures. Complementary structures exhibit the same scattering from the ordered structure. The scattering originating from the micropores on the other hand is different for the two ordered mesoporous sample types used in this thesis.

The samples investigated in this thesis have two inverse structures: the above explained carbon nanorods on a hexagonal lattice and a material with cylindrical pores on a hexagonal lattice (see Chapter 2.12). According to Babinet's principle (scattering pattern is not changed when contrast is inverted), those structures have the same scattering pattern (Figure 2.18).<sup>87</sup> As seen later, this is not entirely true because of the different micropore structure (see Chapter 4).

Obtaining accurate structural information from SAXS data can be challenging. Different approaches have been proposed to create a real space model from fitting the measured SAXS data.<sup>88,89</sup>

Another, more general approach is the use of so-called integral parameters, directly calculated from the measured SAXS curve. The most prominent is the integrated intensity. For a two-phase system the integrated intensity  $\tilde{I}$  is a function of the irradiated volume  $V$ , the porosity  $\varphi$  and the scattering contrast  $\Delta\rho^2$ .<sup>82</sup>

$$\tilde{I} = \int_0^{\infty} I(q)q^2 dq = 2\pi^2\varphi(1-\varphi)(\Delta\rho)^2V \quad (2.39)$$

The integrated intensity is not influenced by the shape or size of the pores, despite the fact that the intensity  $I(q)$  strongly depends on these structural parameter. For a system of diluted (dense) particles the invariant only depends on the scattering contrast and the particle volume  $V_p$  in the sample ( $\tilde{I} = 2\pi^2(\Delta\rho)^2V_p$ ).<sup>82</sup>

For an ideal two-phase system (porous material) with sharp interfaces the scattering intensity  $I$  decays, for large values of the scattering vector length  $q$ , according to Porod's law:<sup>82</sup>

$$I = Pq^{-4} \quad (2.40)$$

where the Porod constant  $P$  is related to the samples surface area:<sup>82,90</sup>

$$P = 2\pi(\Delta\rho)^2S \quad (2.41)$$

From the integrated intensity  $\tilde{I}$  (Equation 2.39) and the Porod constant  $P$  it is possible to calculate the surface area  $S$  per irradiate sample volume  $V$  as following:

$$\frac{\tilde{I}}{P} = \frac{2\pi^2\varphi(1-\varphi)(\Delta\rho)^2V}{2\pi(\Delta\rho)^2S} = \pi\varphi(1-\varphi)\frac{V}{S} \quad (2.42)$$

leading to

$$\frac{S}{V} = \pi\varphi(1 - \varphi) \frac{P}{\bar{l}} \quad (2.43)$$

This is only valid for a simple two-phase system with a sharp surface and a uniform electron density in each phase. A deviation from these ideal conditions can lead to a deviation from the  $q^{-4}$  decrease of the scattering intensity,<sup>91,92</sup> which is often observed for carbon materials.<sup>91,93,94</sup> This is also the case for the samples investigated in this thesis. The deviation from the ideal behavior may be explained by scattering contributions from density fluctuations in the carbon matrix, leading to an overall scattering intensity:<sup>95</sup>

$$I = I_{pore} + I_{fluct} + C \quad (2.44)$$

where  $I_{pore}$  represents the scattering of the porous system,  $I_{fluct}$  the contribution of the density fluctuations in the carbon matrix, and  $C$  a constant background. Before a detailed data analysis of the pore contribution can be performed, the fluctuation contribution has to be evaluated. In Ref.<sup>94</sup> the fluctuation term  $I_{fluct}$  was expressed by:

$$I_{fluct}(q) = \frac{Bl^2(18 + l^2q^2)}{(9 + l^2q^2)^2} \quad (2.45)$$

where  $l$  is the lateral correlation length of the carbon layers and  $B$  scales with the density fluctuations. For large values of  $q$  ( $ql \gg 1$ ) Equation 2.45 simplifies to  $I_{fluct}(q) = Bq^{-2}$  leading, together with Equation 2.44, to a modified asymptotic behavior of the SAXS intensity<sup>94,96,97</sup>

$$I(q) = Pq^{-4} + Bq^{-2} + C \quad (2.46)$$

After determining and subtracting these contributions, the scattering curves are treated as an ideal two-phase system.

In addition to the evaluation of the surface area, it is also possible to calculate average structural parameters of the material from integral parameters, e.g. the Porod length  $t$ . This parameter represents the average chord length of the two-phase system.<sup>90,98</sup>

$$t = \frac{4\tilde{I}}{\pi P} = 4\varphi(1 - \varphi)\frac{V}{S} \quad (2.47)$$

Another integral parameter is the so-called correlation length. The correlation length  $l_c$  represents the weight average of the chord length ( $l_0$  to  $l_n$ , Figure 2.19) through all points in all directions and is calculated by:<sup>82</sup>

$$l_c = \frac{\overline{l^2}}{\overline{l}} = \pi \int_0^\infty I(q)q dq \quad (2.48)$$

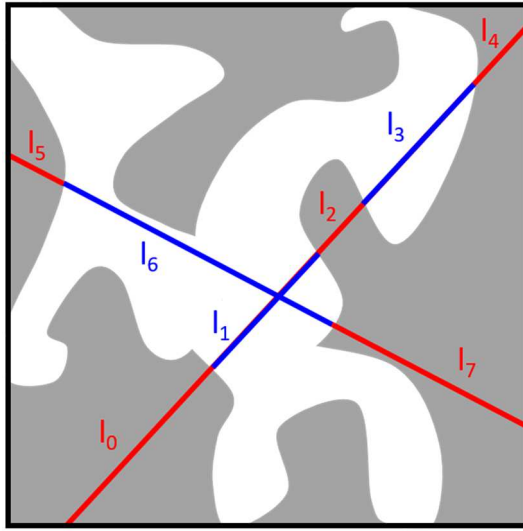


Figure 2.19: Schematic representation of the chord length in a two-phase system

## 2.6 Anomalous small-angle X-ray scattering (ASAXS)

SAXS is a well-established technique to study structural parameters of porous materials.<sup>89,96,97,99</sup> In situ SAXS has also been used to analyze ion movement in operating supercapacitor cells, leading to a better understanding of local ion rearrangement and de-solvation processes.<sup>20,34</sup> However, SAXS has a major drawback: for non-two-phase systems it is not easily possible to determine the scattering contribution of individual components in the sample because the measured intensity is always the sum of all components in the irradiated volume. For a simple two-phase system, this is not an issue, but for such a complex setup like a supercapacitor, containing the electrode material, two different types of ions as well as an aqueous or organic solvent, it is difficult to assign measured changes to certain components. In most experiments, the electrode material can be treated

as constant due to the small changes occurring during the charging and discharging process. The combination of SAXS experiments and simulations as well as contrast variation experiments can help to (at least partly) distinguish between changes caused by individual ion types. In a contrast variation experiment the scattering contrast between the individual phases in the multiphase supercapacitor device is changed. In a system with a defined electrode material and solvent, this can be achieved by exchanging ion species in the electrolyte. By using NaCl and CsCl, the number of electrons (Na<sup>+</sup>: 10, Cs<sup>+</sup>: 54) and therefore the scattering contrast of the cation changes, while the anion (Cl) is not changed. Comparing the scattering experiments of these two systems can now help to identify the contribution of each ion species.<sup>20,21,34</sup> In an in situ experiment it is important that these contrast changes do not influence the behavior of the system. Therefore, this approach is only valid under the assumption that the hydrated Cs<sup>+</sup> and Na<sup>+</sup> ions behave similar during charging and discharging. Using anomalous small-angle X-ray scattering (ASAXS) can overcome this drawback. While SAXS experiments are done at a fixed X-ray energy (resulting in a fixed scattering contrast), ASAXS is based on the fact that the atomic scattering factor  $f$  of an atom (or an ion) is a complex function which strongly changes in the vicinity of its absorption edge. Performing SAXS experiments at different energies near the absorption edge of an element in the sample consequently changes the scattering contribution of this element.

Generally, the scattering factor  $f(E)$  (the scattering factor also depends on the scattering vector:  $f(q, E)$ , for SAXS it is approximately independent from  $q$ ) of an atom is composed of an energy independent (also called non-resonant) term  $f_0$ , as well as the real ( $f'(E)$ ) and imaginary part ( $f''(E)$ ) of the energy dependent term:<sup>82,100</sup>

$$f(E) = f_0 + f'(E) + if''(E) \quad (2.49)$$

The non-resonant term  $f_0$  corresponds to the atomic number of the element (for SAXS experiments) and the imaginary part  $f''$  is proportional to the absorption cross section. Therefore,  $f''$  can be calculated from the linear attenuation coefficient  $\mu(E)$  and the atomic weight  $M$ :<sup>100</sup>

$$f''(E) = \frac{1}{4\pi} \frac{M}{N_A} \frac{mc}{\hbar e^2} E \mu(E) \quad (2.50)$$

$f'$  and  $f''$  are not independent from each other but are linked via the Kramers-Kronig relation:<sup>100</sup>

$$f'(E) = \frac{2}{\pi} \int_{E'=0}^{\infty} \frac{E' f''(E')}{E^2 - E'^2} dE' \quad (2.51)$$

These energy dependent values are tabulated for all elements.<sup>101,102</sup> Figure 2.20a shows the change of the real and imaginary part of the scattering factor (in units of electrons) as a function of the photon energy for Rb.

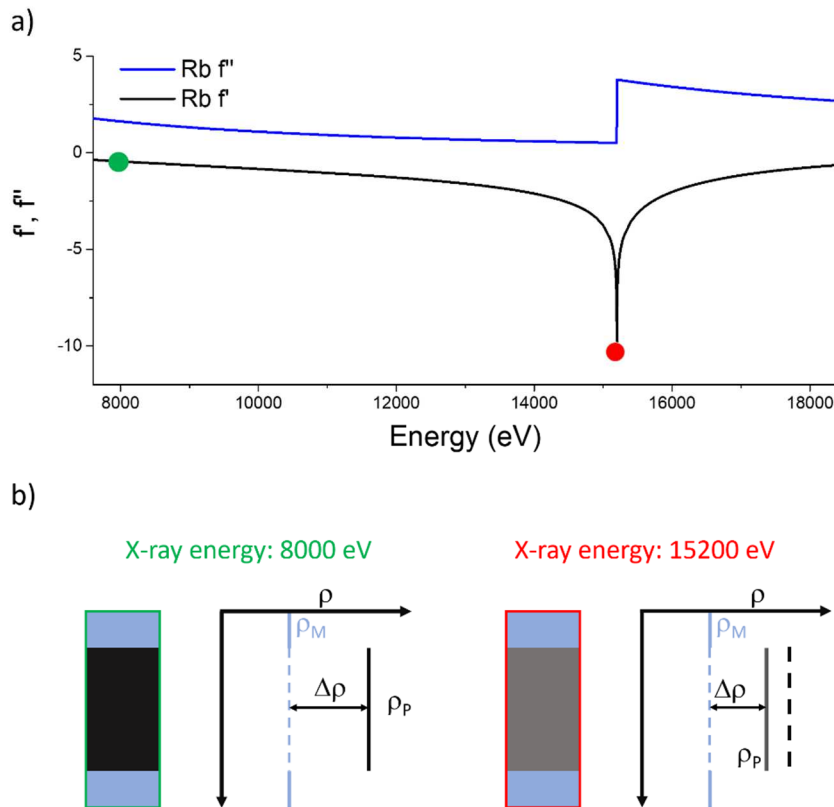


Figure 2.20: (a) Real  $f'$  and imaginary part  $f''$  of the scattering factor of Rb<sup>103</sup> as a function of the X-ray energy. (b) Change of the electron density contrast between a particle composed of the resonant element and a matrix (e.g. Carbon, no absorption edge between 8000 eV and 15200 eV) measured far away and directly at the absorption edge.

When performing scattering experiments at different photon energies, the effective number of electrons of the resonant element changes, leading to a change of the effective electron density. As a result, the scattering contrast between a particle composed of (or containing) the resonant element and an unaffected matrix (no absorption edge in the measured range) changes (Figure 2.20b).

Therefore, scattering experiments performed at different energies near the absorption edge correspond to a contrast variation experiment.

The changes of the scattering factor lead to an energy depending scattering length density profile  $\rho(\mathbf{r}, E)$ , which is also a complex function composed of the energy independent term  $\rho_0(\mathbf{r})$  and the number density distribution of the resonant species  $\nu(\mathbf{r})$ :<sup>100,104</sup>

$$\rho(\mathbf{r}, E) = \rho_0(\mathbf{r}) + \nu(\mathbf{r})r_e[f'(E) + if''(E)] \quad (2.52)$$

with  $r_e$  being the electron radius. As a result of the energy dependent scattering length density, the scattering amplitude  $F(\mathbf{q})$  contains a non-resonant contribution  $F_0(\mathbf{q})$  as well as a resonant part  $F_{res}(\mathbf{q})$ :

$$F(\mathbf{q}) = F_0(\mathbf{q}) + F_{res}(\mathbf{q}) \quad (2.53)$$

with the resonant contribution being a complex function:<sup>100,105</sup>

$$F_{res}(\mathbf{q}) = [f'(E) + if''(E)]F_R(\mathbf{q}) \quad (2.54)$$

By combining Equations 2.34, 2.53, and 2.54, the overall measured intensity  $I(\mathbf{q})$  near the absorption edge can therefore be written as:<sup>100</sup>

$$I(\mathbf{q}) = F_0^2(\mathbf{q}) + 2f'(E)F_0(\mathbf{q})F_R(\mathbf{q}) + (f'(E)^2 + f''(E)^2)F_R^2(\mathbf{q}) \quad (2.55)$$

$F_0^2(\mathbf{q})$  represents the non-resonant scattering intensity, similar to the intensity measured with SAXS experiments away from the absorption edge. The cross term  $F_0(\mathbf{q})F_R(\mathbf{q})$  is a combination of both, the resonant and the non-resonant scattering amplitude. The resonant scattering intensity  $F_R^2(\mathbf{q})$  contains only information about the resonant element in the system. This resonant intensity corresponds to an experiment where only resonant elements are “visible” to the X-ray beam. Therefore,  $F_R^2(\mathbf{q})$  contains the information about the spatial distribution of just the resonant species in the sample. As a result, ASAXS is a powerful tool to investigate the spatial distribution of individual elements in a variety of systems (soft matter, glass, metals).<sup>106–110</sup>

To perform ASAXS measurements the energy of the primary X-ray beam has to be varied with high precision during the experiment. Therefore, these experiments can only be performed at specialized beamlines (e.g. ID02 at the ESRF in Grenoble).

### 2.6.1 Data evaluation

As shown in Equation 2.55, the measured intensity in an ASAXS experiment at a certain energy contains the sum of a resonant term, a non-resonant term and a cross term. Having measured ASAXS data for at least three different energies, the separation into these three terms can be achieved by two methods: solving a set of linear equations or performing a quadratic fit.<sup>111</sup>

**System of linear equations:** A set of  $n$  measurements at different energies results in a set of linear equations from Equation 2.55:<sup>104,111</sup>

$$\begin{bmatrix} 1 & 2f'(E_1) & (f'(E_1)^2 + f''(E_1)^2) \\ \vdots & \vdots & \vdots \\ 1 & 2f'(E_n) & (f'(E_n)^2 + f''(E_n)^2) \end{bmatrix} \cdot \begin{bmatrix} F_0^2(q_i) \\ F_0(q_i)F_R(q_i) \\ F_R^2(q_i) \end{bmatrix} = \begin{bmatrix} I(E_1, q_i) \\ \vdots \\ I(E_n, q_i) \end{bmatrix} \quad (2.56)$$

By solving this set of linear equations for all measured  $q$ -values, the cross term  $F_0(q)F_R(q)$ , the non-resonant  $F_0^2$  and the resonant  $F_R^2$  scattering intensities can be obtained (Figure 2.21).

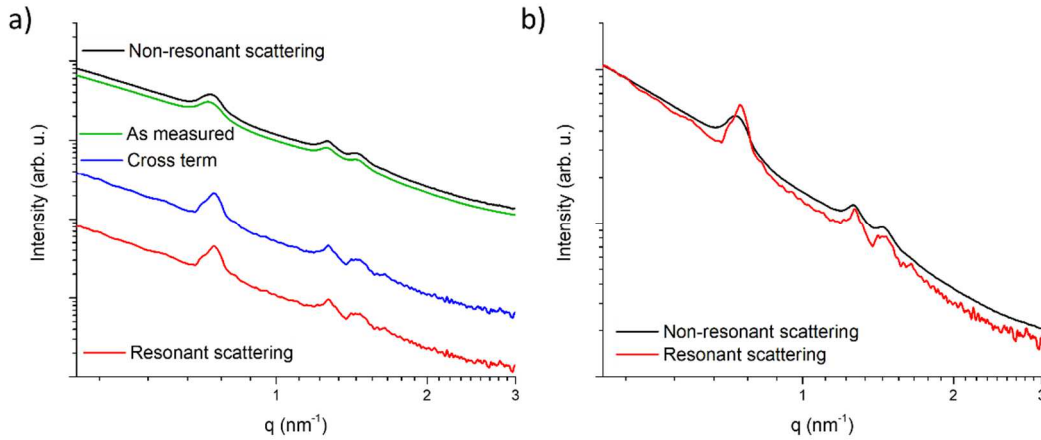


Figure 2.21: (a) Non-resonant (black), cross term (blue), resonant (red) scattering curves obtained from the solution of Equation 2.56 as well as the measured scattering curve (green). (b) Non-resonant and resonant scattering curves normalized to 1 at low  $q$ .

**Quadratic fit:** Ballauff and Jusufi<sup>112</sup> have proposed an alternative approach to extract the resonant scattering contribution from measurements below (but near) an absorption edge. In this region the value of  $f''$  is usually considerably smaller as compared to  $f'$  and therefore, Equation 2.55 simplifies to:



$$\begin{aligned}
 I_{(q)} &\approx F_0^2(q) + 2f'(E)F_0(q)F_r(q) + f'(E)^2F_R^2(q) \\
 &= (F_0(q) + f'(E)F_R(q))^2
 \end{aligned}
 \tag{2.57}$$

This is only valid for measurements close to the absorption edge (Figure 2.20a). To separate the non-resonant and resonant contributions, a quadratic fit of Equation 2.57 to the measured intensities is performed for each measured  $q$  value separately. As shown in Figure 2.22 the scattering curves obtained by this method lead to essentially the same result for the resonant scattering as Equation 2.56.

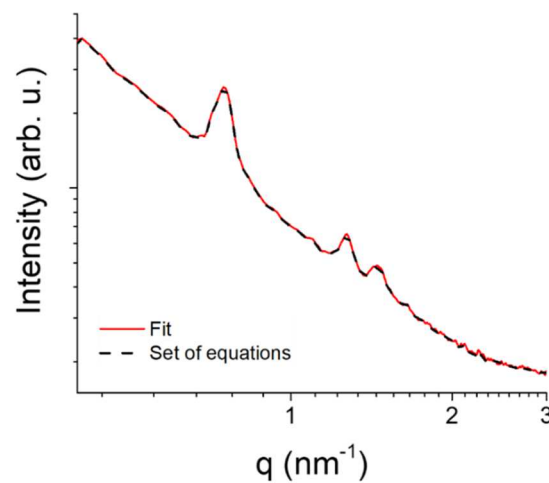


Figure 2.22: Comparison of the resonant scattering curve obtained from the quadratic fit using Equation 2.57 (red line) and from solving Equation 2.56 (dashed black line).

## 2.7 Fluorescence

If a photon has enough energy to remove an electron from an inner shell (e.g. K-shell), an electron from an outer shell (e.g. L-shell) fills the hole and a photon with the same energy as the energy difference between the two states is emitted (Figure 2.23).<sup>78</sup> The fact that the orbitals of different elements have characteristic energy levels results in element specific photon energies for the emitted fluorescence radiation. Because the incoming photon needs enough energy to kick out an electron, fluorescence radiation only occurs when the photon energy of the primary X-ray beam exceeds the energy of the absorption edge. The intensity of the fluorescence radiation reaches a maximum directly at the absorption edge and decreases with increasing energy of the primary beam.

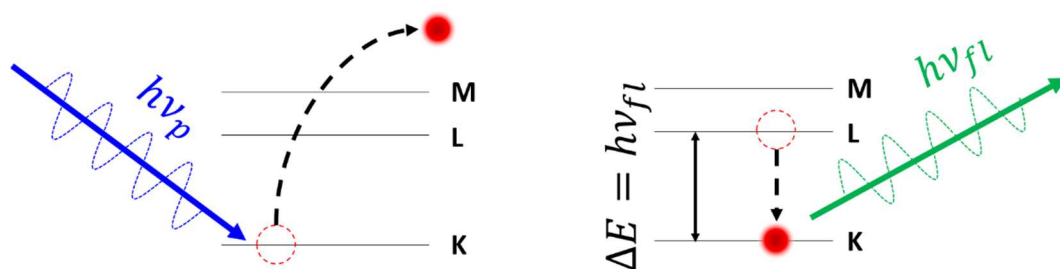


Figure 2.23: Schematic representation of producing fluorescence radiation

Fluorescence radiation leads to a constant (i.e.  $q$ -independent, but energy dependent) background when performing scattering experiments directly above the absorption edge. Since the energy width of the X-ray beam at a typical ASAXS beamline is not infinitely small, measurements performed very close to the absorption edge can lead to energy dependent fluorescence contributions. The presence of elements with an absorption edge somewhat lower than the investigated element can lead to the same issue (see Figure 6.2 in Chapter 6). The fluorescence background has to be considered when performing ASAXS data analysis.<sup>104,106</sup>

Besides these negative effects on the ASAXS experiments, the fluorescence radiation can be used to analyze ion concentration changes in a working supercapacitor (see Chapter 6).

## 2.8 Specific surface area and pore size distribution

The specific surface area (SSA), the pore size distribution (PSD) and the pore shape play an important role in the charge storage process. The specific surface area and the pore size distribution are usually determined from gas (ad)sorption analysis (GSA) measurement, but can also be calculated from small-angle scattering measurements. The use of SAXS to determine the SSA is explained in more detail in Chapter 4.

In a GSA experiment, the adsorbed amount of a probing gas is measured as a function of the relative pressure at a fixed temperature. The data obtained from such a measurement is called a gas (ad)sorption isotherm (Figure 2.24a). To calculate the specific surface area from a gas adsorption isotherm, different models are available. The Brunauer-Emmett-Teller (BET)<sup>113</sup> model and methods based on density functional theory (DFT) are widely used. DFT methods can also be used to calculate the pore size distribution (Figure 2.24b) from an adsorption isotherm. Both techniques are usually implemented in commercial software

packages. A detailed explanation and comparison of measurement techniques and data evaluation methods is not be part of this thesis and can be found elsewhere.<sup>114–117</sup>

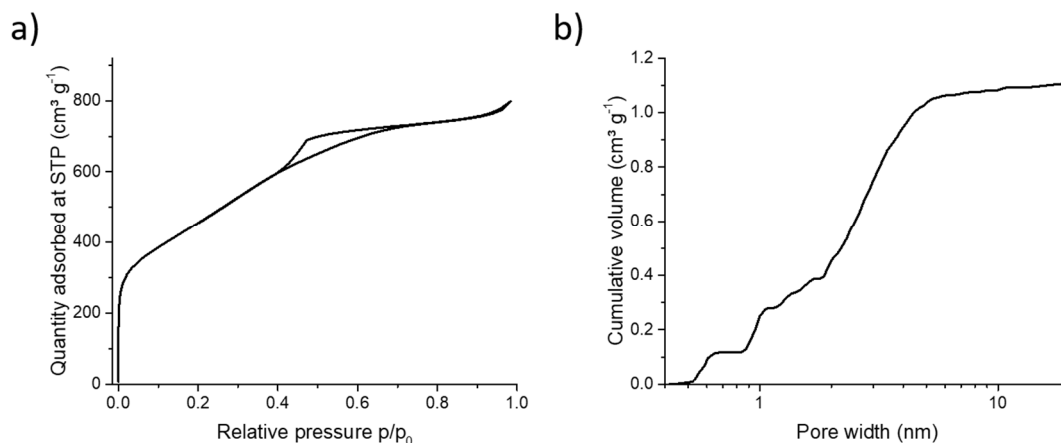


Figure 2.24: (a) N<sub>2</sub> isotherm of a micro- and mesoporous carbon powder. (b) Pore size distribution calculated with DFT (HS-NLDFT) from the N<sub>2</sub> isotherm shown in (a).

To be comparable to literature, in this thesis the IUPAC classification for different pore sizes is used, which defines three (size)classes of pores:<sup>114</sup>

- Micropores: pore size < 2 nm
- Mesopores: 2 nm ≤ pore size < 50 nm
- Macropores: pore size > 50 nm

Micropores can be further divided into ultramicropores (<0.7 nm) and supermicropores (0.7–2 nm). This classification is not arbitrary, but based on the different mechanisms occurring during adsorption of N<sub>2</sub> (a common probing gas used for GSA measurements). In macropores, multilayer adsorption is the dominant effect. Mesopores are classified by the size range in which capillary condensation is taking place, and in micropores the filling is continuously. The threshold between ultra- and supermicropores is twice the thickness of an adsorbed N<sub>2</sub> monolayer (0.354 nm).<sup>118</sup>

It should be mentioned that the BET is not suitable to calculate the SSA of microporous carbon materials because of its general overestimation of the SSA for such materials,<sup>114,115</sup> instead the use of DFT methods is suggested.<sup>116,119</sup> It has been shown that, depending on the used evaluation method, surface area normalized capacitance values show a different behavior. In Figure 2.25 the surface area normalized capacitance is shown as a function of the average pore size for different

materials in an organic electrolyte. Here a clear difference can be seen for the data obtained from BET and from DFT methods. BET-area normalized capacitance values show an anomalous increase with decreasing pore size, while DFT-area normalized capacitance values show no pronounced anomalous behavior.<sup>120,121</sup>

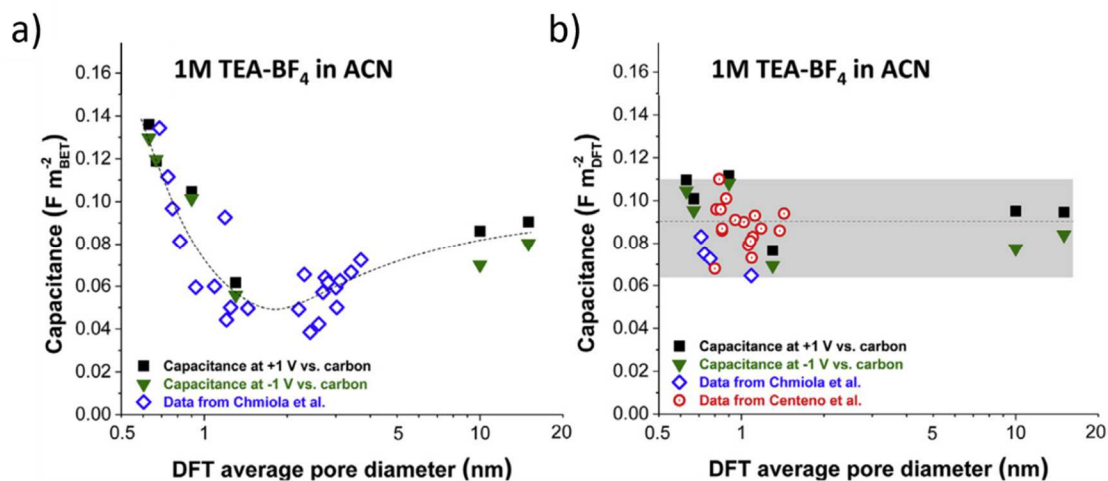


Figure 2.25: Area normalized capacitance value, using BET (a) and DFT (b) method for surface determination, as a function of the average pore size. Reproduced with permission from Ref.<sup>120</sup> © 2016 Elsevier B.V.

## 2.9 Electrolytes used in supercapacitors

The electrolyte plays an important role in terms of electrochemical performance (e.g. capacitance, maximum power output, capacitance at high scan rates, etc.) of a supercapacitor. The ionic conductivity and the electrochemical stability window are important parameters influencing the specific power and energy, respectively. A high ionic conductivity reduces the internal resistance of a device and, according to Equation 2.7, the specific power will increase. The specific energy increases quadratic with the voltage window (Equation 2.6), therefore, electrolytes with a wide stability window are of major interest for the development of high energy EDLCs. Besides the stability window and the internal resistance, also parameters like the ion concentration and viscosity influence the performance of a supercapacitor.<sup>42</sup> Toxicity, environmental friendliness, availability, and cost are not performance relevant but should also be kept in mind when choosing an electrolyte for a given application. In addition to the performance determining parameters of the electrode and electrolyte, also the stability of the non-active

components (current collector, separator and housing) in a device have to be taken into account. The used current collector for instance needs to be stable in the electrolyte, otherwise corrosion will lead eventually to device failure.

In Li-ion batteries, the electrolyte is also responsible for creating the solid-electrolyte interphase at the surface of the electrode, which limits potential electrolyte candidates. In an EDLC, such an interphase is not needed and therefore the range of possible electrolytes is wider than for Li-ion batteries.<sup>22</sup>

For supercapacitor applications there are three types of liquid electrolytes available: dissolved salts in aqueous and organic solvents, as well as ionic liquids. In addition to the aqueous electrolytes, also solid-state electrolytes can be used.<sup>123</sup> Each type has individual properties and is used for different applications.

### 2.9.1 Aqueous electrolytes

The big advantage of aqueous electrolytes is the high ionic conductivity, especially for acidic and alkaline electrolytes. Therefore, they are best suited for high power applications.<sup>15</sup> Salts used in aqueous electrolytes usually have small ions that can access smaller pores in the electrode, which leads to higher capacitance. Additionally, aqueous electrolytes are mostly non-toxic, environmentally friendly, easy to handle and cost efficient. Their main drawback is that the usable potential window is limited by the decomposition voltage of water (1.23 V). As a result, EDLCs using aqueous electrolytes only have a limited energy density. Overpotential (electrolyte decomposition-potential is shifted) can increase the usable voltage window: With optimized materials and cell setup, potential windows of 1.6 V for acidic ( $\text{H}_2\text{SO}_4$ ) and up to 2 V using neutral electrolytes were reported.<sup>15</sup> With the resulting increased energy density, EDLCs using aqueous electrolytes could substitute devices with organic solvents.<sup>22,42</sup> Aqueous electrolytes have been used for all experiments in this thesis.

### 2.9.2 Organic electrolytes

The higher stability window of organic electrolytes leads to a drastic increase of energy density compared to aqueous electrolytes (Equation 2.6). Organic electrolytes are the most used electrolyte type in commercial devices. Their major drawback is the reduced ionic conductivity, leading to a higher internal resistance and limiting the maximal power. In addition, flammability and toxicity are other possible disadvantages of this electrolyte type.<sup>22</sup> Propylene carbonate (PC) and

acetonitrile (AN) are two widely used organic solvents for EDLCs. PC is less toxic and has a higher flashpoint than AN, with the disadvantage of a lower ionic conductivity and a stronger temperature dependence of the conductivity. AN has an increased conductivity and therefore a higher maximum power. Besides that, also the performance at low temperatures is better.<sup>15</sup>

Organic electrolytes are usually more expensive than aqueous electrolytes, partly because of the purification and removal of water. A water content below 5 ppm is needed to guarantee a high usable potential window without degradation of the electrolyte. One of the most commonly used salts in organic electrolytes is tetraethylammonium tetrafluoroborate (TEA-BF<sub>4</sub>). The size of the bare and solvated TEA<sup>+</sup> and BF<sub>4</sub><sup>-</sup> are both larger than typical ions used in aqueous electrolytes, resulting in the inaccessibility of small micropores, which leads to a reduced capacitance (Figure 2.26).<sup>15,124</sup>

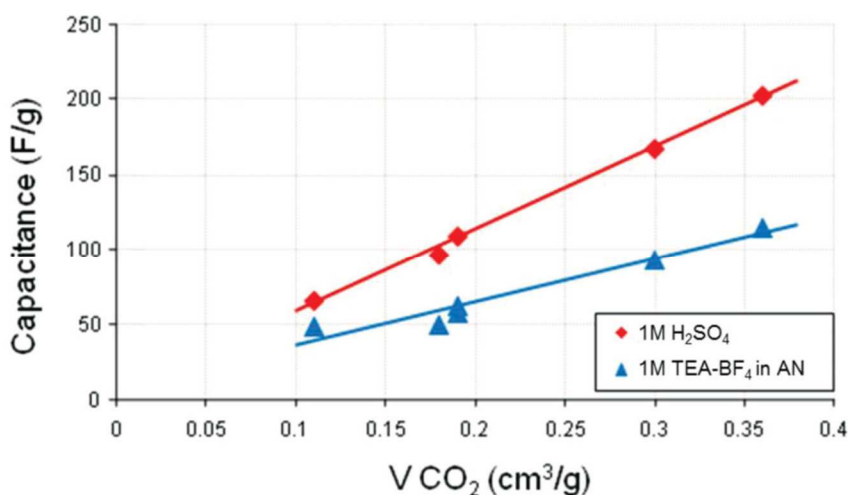


Figure 2.26: Specific capacitance vs. specific pore volume for pores smaller than 0.7-0.8 nm (calculated from CO<sub>2</sub> adsorption isotherms) using an aqueous (1M H<sub>2</sub>SO<sub>4</sub>) and an organic electrolyte (1M TEA-BF<sub>4</sub> in AN). With an increase of the volume of very small pores, the capacitance difference gets more pronounced because of the size difference of the used ions. Reproduced with permission from Ref.<sup>15</sup> © WILEY-VCH

### 2.9.3 Ionic liquids

Ionic liquids (ILs) are molten salts, which are liquid at room temperature. They have a high electrochemical stability window, leading to a high energy density. ILs typically suffer from a low ionic conductivity at room temperature. Because they have a very low vapor pressure and are badly flammable, ionic liquids are

considered safer than organic electrolytes. These properties, combined with the increasing ionic conductivity at elevated temperatures, results in a system ideal for high temperature applications.<sup>15</sup>

In contrast to salt solutions, ions in an IL do not have a solvation shell, leading to a well-defined size of each ion species in the system. These ions on the other hand are substantially larger than ions used in aqueous electrolytes, which influences the accessibility of micropores. The thickness of the double-layer in ionic liquid-based EDLCs was found to be in the range of the size of one ion. Therefore, the Helmholtz model describes the formation of the double-layer in this electrolyte type quite well.<sup>42</sup>

The two mainly used ionic liquids are imidazolium- and pyrrolidinium-based, with imidazolium having a higher ionic conductivity and pyrrolidinium having a higher potential window. To get a new electrolyte with properties tailored for a specific requirement, mixtures of individual molten salts, or even a combination with organic solvents can be used.<sup>15</sup> Due to the larger ion size, not the entire surface area of the commonly used mainly microporous activated carbon materials can be accessed by the ions. As a result, AC materials are not well suited to be used with ionic liquids. Therefore, to exploit the full potential of this electrolyte type, the material has to be tailored to the used electrolyte.<sup>15,42</sup>

## 2.10 Confinement effects

### 2.10.1 Ion desolvation

To produce aqueous and organic electrolytes, salts are dissolved in a solvent (water or organic solvent). Around each ion, there is a densified layer of solvent molecules, called a solvation shell. This solvation shell will lead to an increased effective size of the ion.<sup>125</sup> As a result, this can prevent the ions from entering pores that would be accessible for the bare ions, but are essentially smaller than the ion including the solvation shell. Nevertheless, it was shown that ions can anyway enter, to a certain extent, pores smaller than their solvated size, leading to the conclusion that ions can lose (at least in parts) their solvation shell.<sup>126</sup> The partial removal is not limited to small pores but can also be observed in pores bigger than the hydrated ion size. The local ion rearrangement during charging can cause the ions to approach the pore wall and cause the removal of solvent molecules from the solvation shell.<sup>34</sup>

### 2.10.2 Solvents in confinement

The performance of an EDLC is strongly linked to different solvent parameters. The capacitance for instance depends on the dielectric constant of the solvent (Equations 2.1 and 2.3 to 2.5). It is known that there are certain changes of solvent parameters in a confined system: The freezing temperature of water, as well as the eutectic temperature of a salt water mixture is shifted to lower temperatures in porous materials.<sup>24</sup> Molecular dynamics simulations revealed that also the mobility of water can be reduced by confinement effects in carbon.<sup>127</sup> Even a parameter like the dielectric constant of water is different when it is confined in a microporous material. A reduction of the dielectric constant of water by nearly 50% in a 1.2 nm pore was calculated.<sup>128</sup> As a result, the capacitance and therefore the energy density of an EDLC device can be strongly influenced by confinement effects when microporous materials are used as an electrode.

### 2.10.3 Ion sieving

Figure 2.26 shows that the larger ions and solvation shell in organic electrolytes can lead to a reduced capacitance when electrodes with small micropores (activated carbons) are used together with organic electrolytes. A similar effect can be observed using anions and cations with noticeable different ion sizes. A bigger ion cannot enter certain pores, leading to a capacitance difference for positive and negative potentials. This has been demonstrated using electrode materials with a well defined uniform pore size distribution (carbon molecular sieves).<sup>129-131</sup> The ion sieving phenomena can be observed when comparing cyclic voltammetry using electrolytes containing monovalent and divalent cations.<sup>129</sup> In Figure 2.27 it is shown that the specific capacitance drastically drops in the cation adsorption regime (negative potential) when changing from monovalent to divalent ( $\text{CaCl}_2$ ) cations. This results from the fact that the bigger divalent cations cannot access the pores and therefore, allowing the separation of different ion species. This effect can be used for capacitive water deionization, where it is beneficial to selectively extract different ion types.<sup>129,132-134</sup>



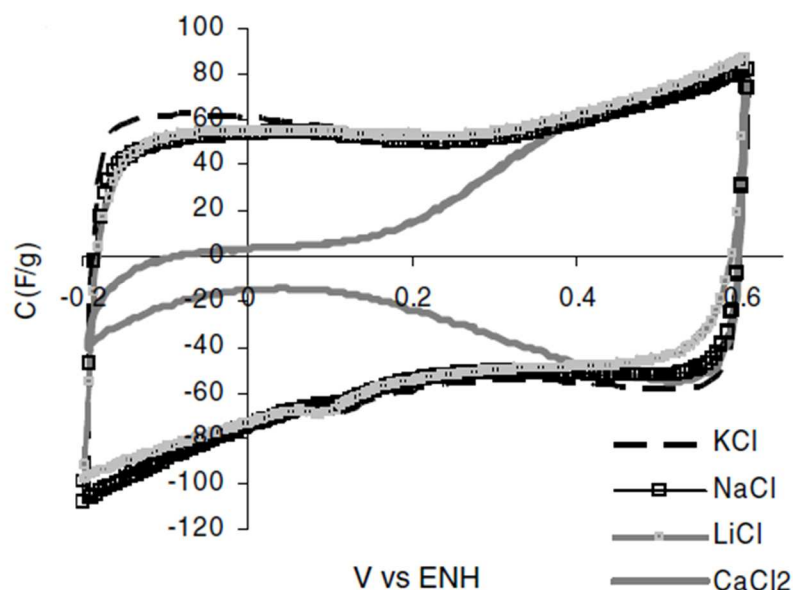


Figure 2.27: Cyclic voltammogram of a carbon molecular ion sieve with micropores mostly smaller than 0.48 nm. Capacitance drop for cation adsorption section when changing from electrolytes with monovalent cations (KCL, NaCl, LiCl) to a divalent cation ( $\text{CaCl}_2$ ). Reproduced with permission from Ref.<sup>129</sup> © 2007 Elsevier Inc.

## 2.11 Materials for supercapacitor electrodes

For EDLC electrodes, a wide range of possible materials is available. Carbon is used for most electrodes, the difference is mainly the (pore)structure and surface chemistry. For hybrid systems and electrodes with pseudo-capacitive behavior (see Chapter 2.14) also other materials, such as transition metal oxides and conductive polymers play an important role.

Carbon based materials have a reasonable thermal and electrical conductivity. Their production, depending on the type of material, is usually cost efficient and they are widely available in large amounts. They are non-toxic and environmentally friendly and can be produced as a highly porous material with a large specific surface area. A high SSA is beneficial for the electrochemical performance, since the capacitance principally scales with the surface area of the electrode (Equation 2.1). Carbon materials can be produced in many different ways leading to a variety of possible structures (fibers, powders, cloths, nanotubes, carbon onions, etc.). In this thesis, only experiments using activated carbon materials and templated carbons (see Chapter 2.12) were performed. Nevertheless, this chapter should provide a short overview of selected electrode materials and

help the reader to select/evaluate the right material for a certain experiment or application.

### 2.11.1 Activated carbon

Activated carbon (AC) materials can be produced cost efficiently on an industrial scale, making them an ideal basis for commercial supercapacitor devices. They can be derived from different organic precursors including renewable precursors (food waste, nutshells, coconut shells, etc.) and polymers. From carbonization of these precursors in inert atmosphere, a disordered carbon material is produced, which often results in a powder containing micron sized particles (Figure 2.28).

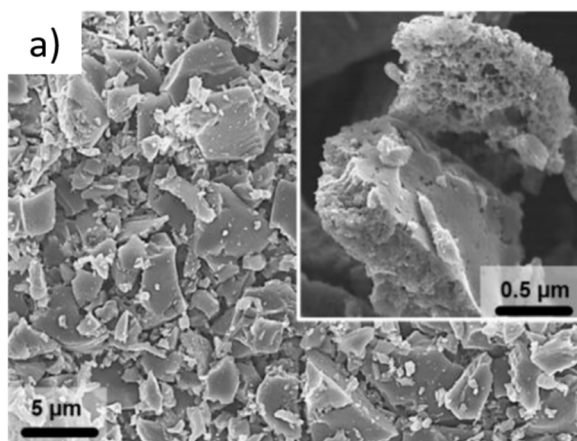


Figure 2.28: Activated carbon powder containing micron-sized particles. Reproduced with permission from Ref.<sup>135</sup> © 2014 Elsevier B.V.

An additional activation process can then be performed to tune the pore size distribution as well as increase the SSA of the carbon material. There are different types of activation: chemical activation using potassium hydroxide and physical activation at high temperatures using gases like CO<sub>2</sub> or steam. It should be kept in mind that a very high SSA leads to a high weight normalized capacitance, but on the other hand the volumetric energy and power can be reduced because of the decreasing density due to the activation process.<sup>136</sup>

### 2.11.2 Carbide derived carbons

The basis for the production of carbide derived carbon (CDC) materials is a precursor carbide (SiC, Mo<sub>2</sub>C, VC, TiC, ZrC, etc.), from which the metal is removed (Figure 2.29). The extraction process can be either physical or chemical.<sup>137</sup> Physical removal can be achieved by thermal decomposition in vacuum or an inert atmosphere and is based on the incongruent melting and evaporation of the carbide. During this process, the carbon layer is formed from the surface of the material inwards. As the carbon layer grows, the evaporated metal has to diffuse through this layer which turns out to be the rate limiting step in this synthesis method.<sup>137</sup>

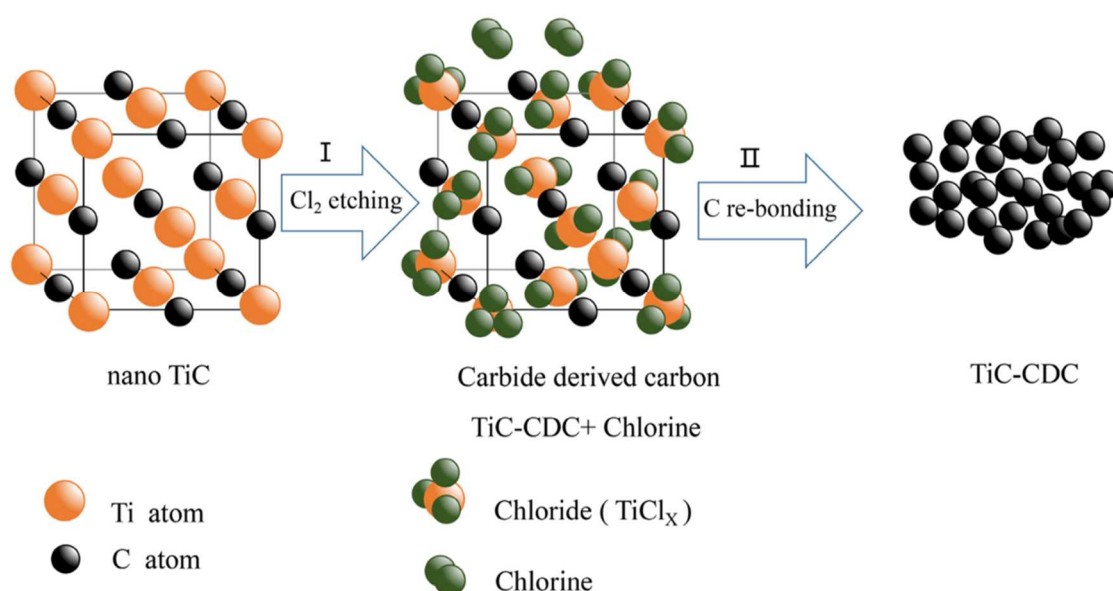
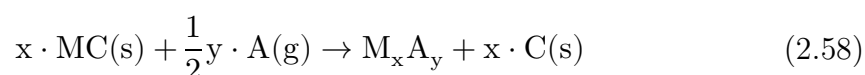


Figure 2.29: Schematic representation of the CDC synthesis from a TiC precursor. Ti is removed by Cl<sub>2</sub> etching. The gaseous Ti-Chlorides are removed from the material and the carbon atoms re-bond to form a highly porous carbon structure. Reproduced with permission from Ref.<sup>138</sup> © 2019, Springer

Halogenation is the most commonly used chemical method to extract the metal ion. This process can be described by the following equation:<sup>137</sup>



where M is the used metal, A a halogen gas (e.g. Cl<sub>2</sub>) or an etchant containing a halogen (e.g. HF) and M<sub>x</sub>A<sub>y</sub> is the gaseous reaction product which has to be removed. Chlorine is a widely used halogen gas for the metal extraction process.

After removing the metal atoms from the carbide, the carbon atoms form stable bonds and a porous carbon structure remains.<sup>50,137,138</sup>

One advantage of this method, compared to the production of activated carbon materials is that there is no organic precursor needed, which means that no organic residuals are present in the material.<sup>137</sup>

The structure of the resulting carbon material depends mainly on two parameters: the precursor type and the synthesis temperature. The halogenation process is usually done in a temperature range between 600°C and 1200°C. A higher temperature leads to an increased average pore size of the material, explained by the temperature dependent mobility of the carbon atoms. If the synthesis is done at lower temperatures, the carbon atoms are immobile and therefore form a more disordered structure with small pores in places where the metal atoms used to be. At elevated temperatures (above 1000 °C), the carbon atoms mobility is increased and formation of stable graphitic structures due to self-organization is favored.<sup>50,137</sup> Figure 2.30 shows the transmission electron microscopy (TEM) images of CDC materials based on two different carbides (TiC: Figure 2.30a-c; ZrC: Figure 2.30d-f) as well as structures obtained from quenched molecular dynamics<sup>139</sup> (Figure 2.30g-i). It can be seen that the CDC from both precursors show a completely amorphous structure when synthesized at 600°C (TiC: Figure 2.30a; ZrC: Figure 2.30d). By increasing the temperature to 1200°C (TiC: Figure 2.30c; ZrC: Figure 2.30f) the structure changes, and graphitic structures can be observed. The structures obtained from simulation are in good agreement with TEM images. The rearrangement of the carbon atoms leads to a reduction of the amount of very small micropores and the formation of larger pores, which results in an increased average pore size. Therefore, the pore size distribution and the specific surface area of CDC materials highly depend on the synthesis temperature and can to (some extent) be tuned rather precisely. After the chlorination process, especially at low temperatures, residual chlorine and metal chlorides can be trapped inside the material and block small pores, reducing the active surface area. These residuals can be removed by an additional annealing step. Another advantage is that during the CDC synthesis also the surface groups and conductivity (degree of graphitization) can be controlled and adapted.<sup>50,139</sup>

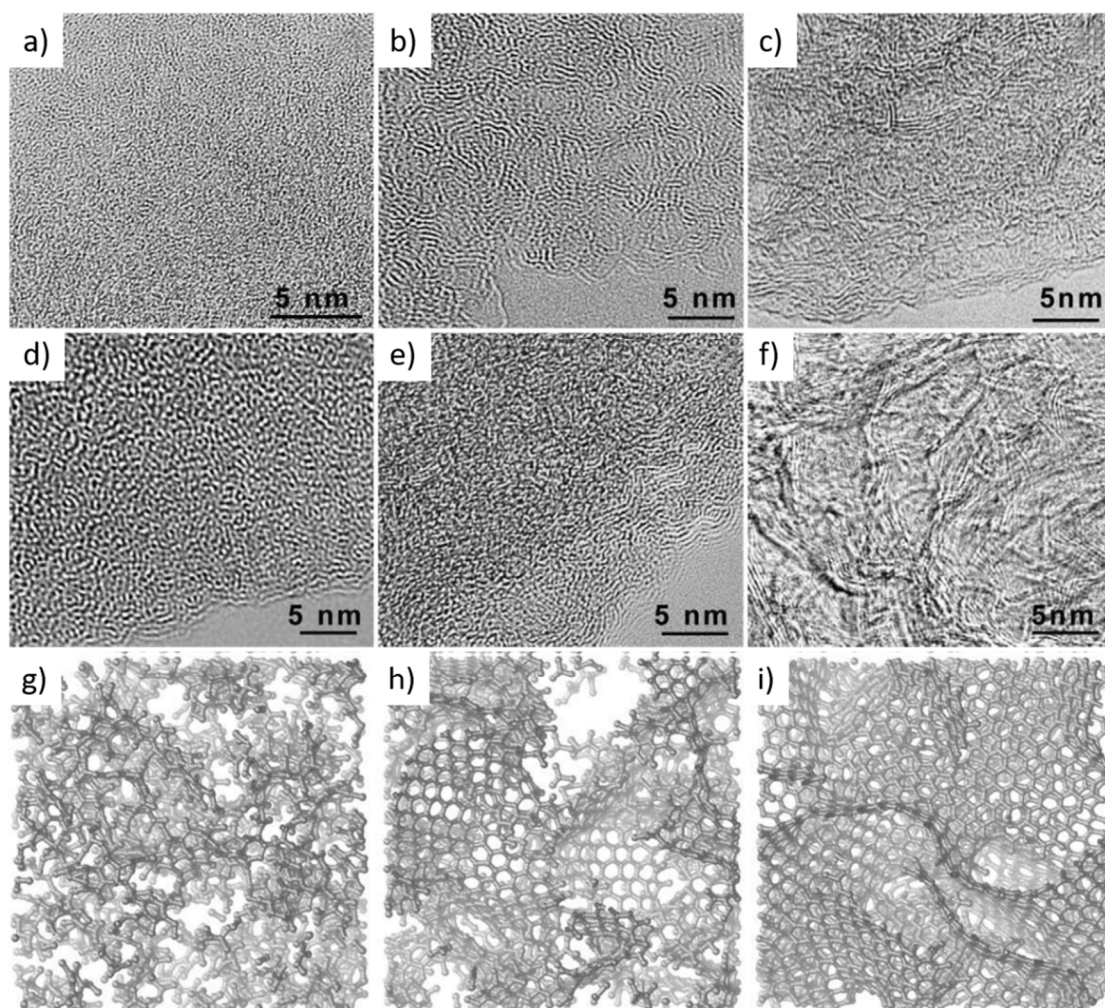


Figure 2.30: TEM images of CDC based on TiC precursor at (a) 600°C, (b) 800°C, (c) 1200°C and on ZrC precursor at (d) 600°C, (e) 800°C, (f) 1200°C. Carbon structures calculated from quenched molecular dynamics simulation at (g) 600°C, (h) 800°C, (i) 1200°C. (a) to (f) reproduced with permission from Ref.<sup>50</sup> © 2005 Elsevier B.V. (g) to (i) reproduced with permission from Ref.<sup>139</sup> © 2009 Elsevier Ltd.

The tunable properties of this carbon type provides a good model material to study the influence of different properties (e.g. porosity, pore size distribution, functionalities) on the electrochemical performance. Therefore, CDC materials can be designed to fit different scientific experiments. For example, the average pore size of TiC-based CDC materials is  $\sim 0.6$  nm if the chlorination is performed at 600°C and increases to  $\sim 2$  nm for a chlorination temperature of 1200°C.<sup>50</sup> CDC with different average pore sizes have been used to study ion sieving effects in solvent free environments (ionic liquids),<sup>140</sup> the influence of the pore size on the expansion behavior of EDLC electrodes during charging and discharging,<sup>141</sup> as well as ion rearrangement and desolvation.<sup>34</sup>

CDC materials can be produced using a variety of different precursor types and shapes ranging from bulk materials and fibers to carbon nanotubes. The shape of the precursor is usually not changed during the transition from the carbide precursor to the pure carbon. Due to the origin of the porosity, CDCs contain mainly open pores. In addition to their role as a useful model material, it is possible to upscale the production process to industrial quantities.<sup>50</sup>

### 2.11.3 Metal organic frameworks

Metal organic frameworks (MOFs) are a class of porous materials gaining a lot of interest over the last few years. They are made from inorganic metal containing units, the so-called secondary building units (SBUs), joined with organic linkers<sup>143</sup> (Figure 2.31). These building blocks form a three dimensional periodic structure and create a skeleton material with a large amount of pores and very high surface areas. Some reports claim a specific surface area (obtained from BET measurements) of over  $7000 \text{ m}^2 \text{ g}^{-1}$ .<sup>144</sup> It has to be mentioned that the BET method is not well suited to be used for microporous systems like MOFs. As a result, the calculated high values overestimate the real specific surface area. As a comparison, the theoretical SSA of a graphene sheet is  $2630 \text{ m}^2 \text{ g}^{-1}$ .<sup>145</sup>

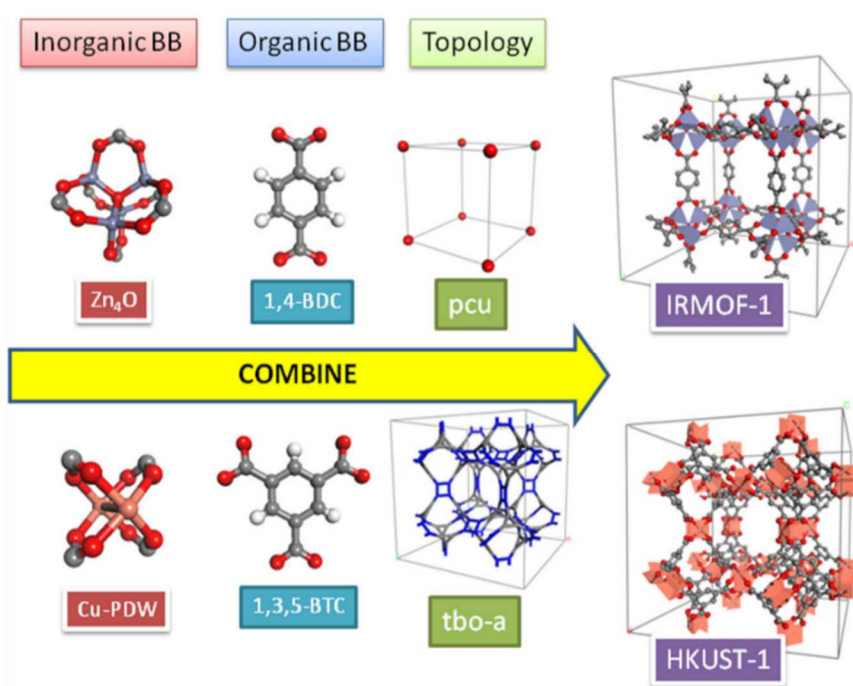


Figure 2.31: Schematic representation of organic and inorganic building blocks combined to metal organic frameworks. The large amount of building blocks and possible structures leads to over 20000 reported combinations. Reproduced with permission from Ref.<sup>143</sup> © 2017, Springer Nature

There are varieties of different inorganic SBUs as well as organic linkers and structural configurations that can be combined to form the actual material, leading more than 20000 different reported MOFs. To find the right material for a defined application, new screening methods have to be developed to accurately and efficiently preselect possible combinations from this database.<sup>143,144,146</sup> Machine learning technologies can help to improve this selection process.<sup>143</sup>

Due to the high surface area, variety of structures, tunable pore sizes and chemical functionalization, MOFs have a wide range of possible applications like gas separation and storage, sensors, drug delivery and electrode material for batteries and supercapacitors. There are three different ways to use MOFs in supercapacitor electrodes:<sup>146</sup>

1. *Using the pristine MOF to build supercapacitor electrodes:* In such an electrode, there are two contributions to the overall capacitance: the double layer forming at the high amount of surface area as well as possible pseudo-capacitive contributions from the containing metals. The main drawback of pristine MOFs is their low electronic conductivity (Cu:  $\sim 6 \cdot 10^5 \text{ S cm}^{-1}$ ; AC:  $10^{-3} \text{ Scm}^{-1} - 0.1 \text{ S cm}^{-1}$ ; MOFs:  $< 10^{-3} \text{ S cm}^{-1}$ ).<sup>147-149</sup>
2. *Metal oxides derived from MOFs:* MOFs are destroyed to get a porous structure of transition metal oxides exhibiting a pronounced pseudo-capacitive behavior (see Chapter 2.14 for details). The highly porous structure leads to a high accessible surface area and optimized ion diffusion, making MOFs promising templates for pseudo-capacitive electrodes. The limited conductivity is again a major drawback.
3. *Pyrolysis of MOFs:* MOFs can be used as a template to obtain a porous carbon material with a connected meso/microporosity. The organic components are carbonized leading to a porous carbon backbone.

Although, MOFs are a promising material class for high performance supercapacitor electrodes, they show significant drawbacks. The above-mentioned concepts suffer from either a low cycle stability, limited specific capacitance or a low electronic conductivity. To improve the performance, MOFs can be combined with other materials in hybrid electrodes. One example is the combination of high surface area MOFs with a conducting polymer. The polymer acts as a conductor for the MOFs, which results in a flexible electrode with a high double layer capacitance from the MOFs and an additional pseudo-capacitive contribution from the conducting polymer.<sup>143,146,150</sup>

### 2.11.4 MXenes

Because of their unique properties, two-dimensional materials (like graphene) gained a lot of interest over the last decades. MXenes are a new type of two-dimensional materials: exfoliated early transition metal carbides, produced from a so-called MAX phase. A MAX phase is a layered solid and conductive material with a chemical composition of  $M_{n+1}AX_n$ , where M is an early transition metal. A is an A group element (mostly group 13, boron group or group 14, carbon group), X is either carbon, nitrogen or a compound of both, and n is an integer in the range from one to three. The layers of transition metal carbides/nitrides are held together by an A element layer (Figure 2.32). There have been over 60 different MAX phases reported over the last few years.<sup>122,151</sup>

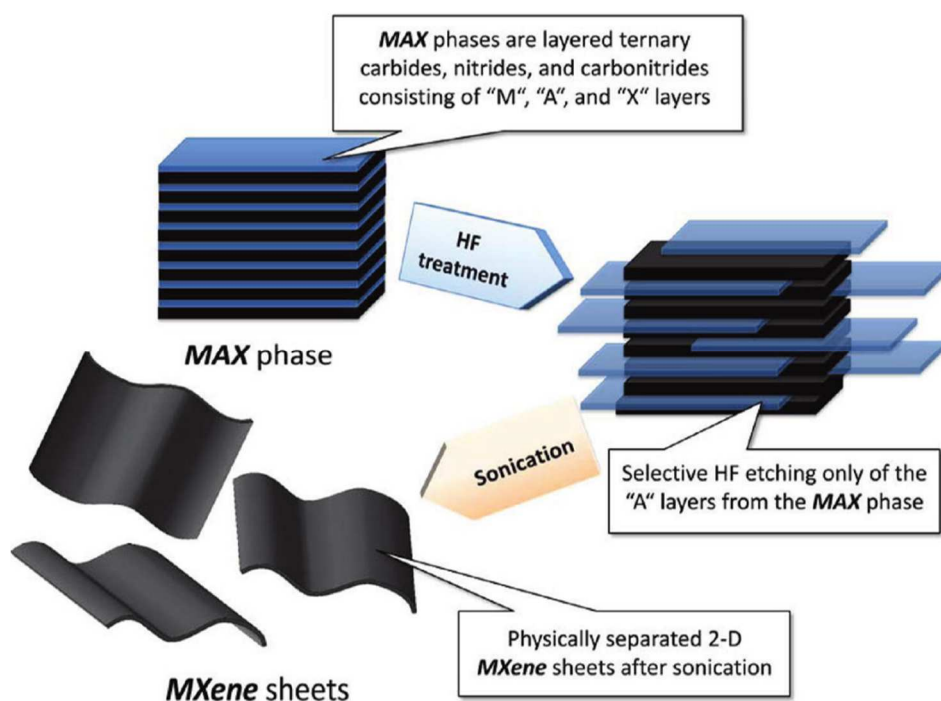


Figure 2.32: Schematic representation of the synthesis steps of MXenes. Reprinted with permission from Ref.<sup>122</sup> Copyright 2012 American Chemical Society

Due to the strong bonding between these layers it is not possible to separate them by mechanical shear, as it is done for graphene. A thermal decomposition would essentially be possible, but the high temperatures needed cause a recrystallization process, which would lead to a bulk material rather than a layered structure. Therefore, MXenes are produced by selectively etching the A phase from the MAX phase using HF at room temperature. The etching process replaces the A element with O, OH or F containing functional surface groups but



does not affect the M-X bonds. As a result, MXenes have a chemical composition of  $M_{n+1}X_nT_x$ , where T represents the mixed functional groups. After the etching process the MXene sheets stick together and form a layered structure (Figure 2.33).<sup>122,151,152</sup>

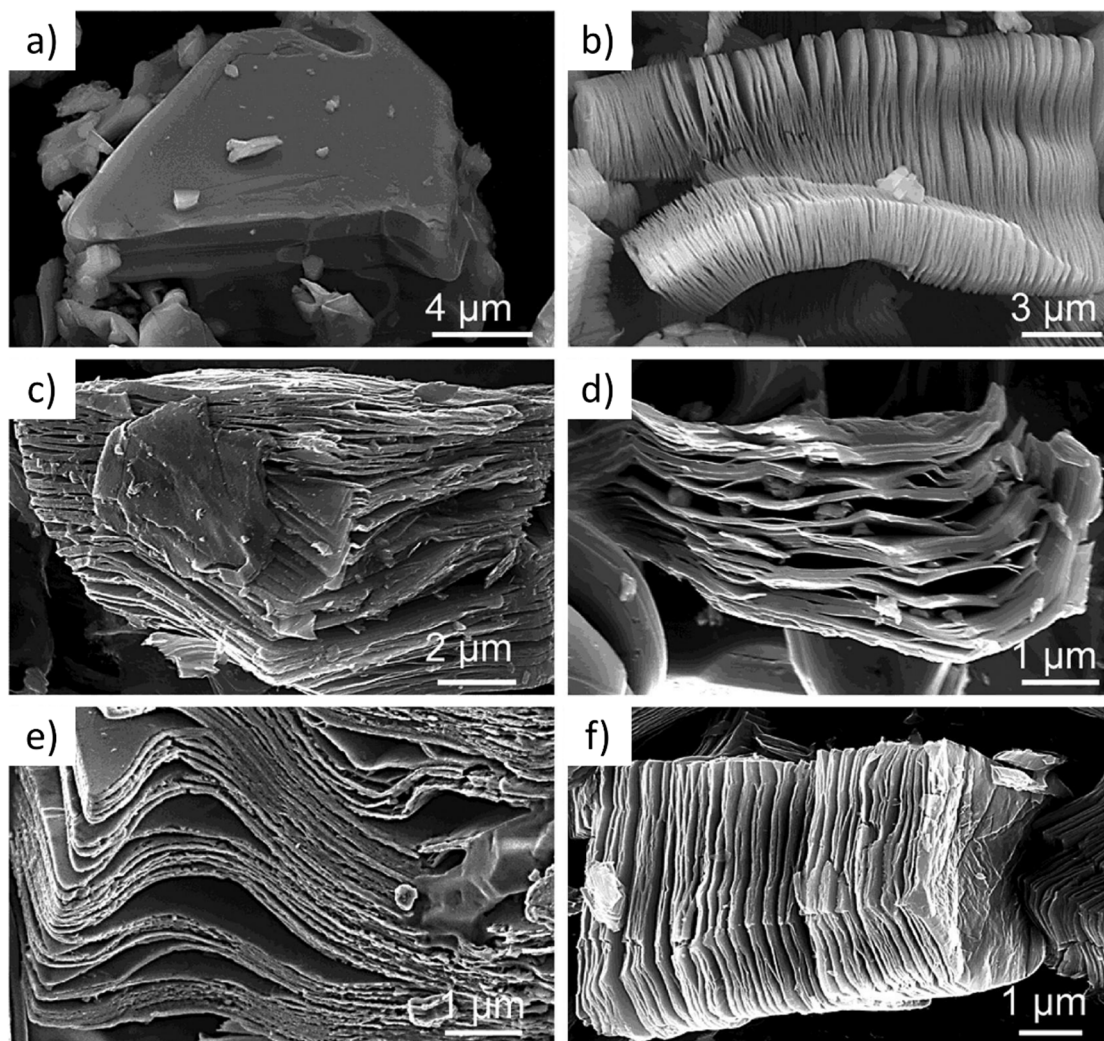


Figure 2.33: SEM images of an untreated  $Ti_3AlC_2$  MAX phase (a) and the layered structure of different MXenes after HF treatment: (b)  $Ti_3AlC_2$ , (c)  $Ti_2AlC$ , (d)  $Ta_4AlC_3$ , (e)  $TiNbAlC$ , and (f)  $Ti_3AlCN$ . Reprinted with permission from Ref.<sup>122</sup> Copyright 2012 American Chemical Society

To get single MXene sheets, a separating by ultrasonication is performed. The rough sonication needed to delaminate these structures leads to rather small MXene sheets. To minimize the damage, it is possible to intercalate certain species between the sheets to weaken their bonding. As a result, only weak sonication is needed to separate the sheets, which limits the damage and leads to increased sheet size. Intercalation is possible due to the layered structure and the

comparably weak bonding between the layers. Besides the improvement of the delamination process, intercalation could also be used for energy storage (similar to intercalation in Li-ion battery electrodes). MXene monolayers have metallic conductivity and the electronic properties and band structure of MXenes can be tuned by changing the composition of the MAX phase. It is also possible to produce ferromagnetic and antiferromagnetic MXenes. DFT simulations can help to predict properties and screen promising compositions to preselect the most promising for synthesis for a variety of possible applications.<sup>122,151</sup>

MXenes have already been used to produce high performance electrodes for supercapacitor applications. Due to the fact that they have a tendency to restack, pure MXene electrodes experience a significantly capacitance decrease during operation (reduced accessible surface area). It has been shown that by combining MXenes with graphene sheets the restacking can be prevented and binder free electrodes can be produced. Graphene sheets included between the MXene sheets not only prevent the restacking, but also act as a conductive spacer increasing the layer distance, leading to better ion diffusion. As a result, these hybrid electrodes show a high volumetric capacitance (but limited gravimetric capacitance due to higher density) and nearly no capacitance loss after 20000 cycles.<sup>152</sup> MXenes have also been used to increase the capacitance of pseudo-capacitive conductive polymer electrodes. Polypyrrole (PPy) is a conductive polymer used to produce flexible freestanding electrodes. PPy tends to dense packing, resulting in reduced accessible surface area and capacitance. By including MXenes, PPy electrodes show a more porous structure, leading to an increase of the capacitance by approximately 30%, while at the same time the cycling stability is strongly improved.<sup>153</sup>

Due to their layered structure, MXenes show a tendency for ion intercalation during charging. It has been shown that this can lead to reversible volumetric changes up to 12%. The actual expansion can be controlled by charging and discharging the supercapacitor (Figure 2.34). As a result, MXenes could also be used as electrochemical actuators. It has to be mentioned that intercalation not only occurs during charging and discharging processes, but also spontaneous ion intercalation can happen when electrode is immersed into an ionic liquid, even with no applied potential. This spontaneous intercalation has two effects: a volumetric expansion and an alignment of the MXene sheets (Figure 2.34).<sup>154</sup>

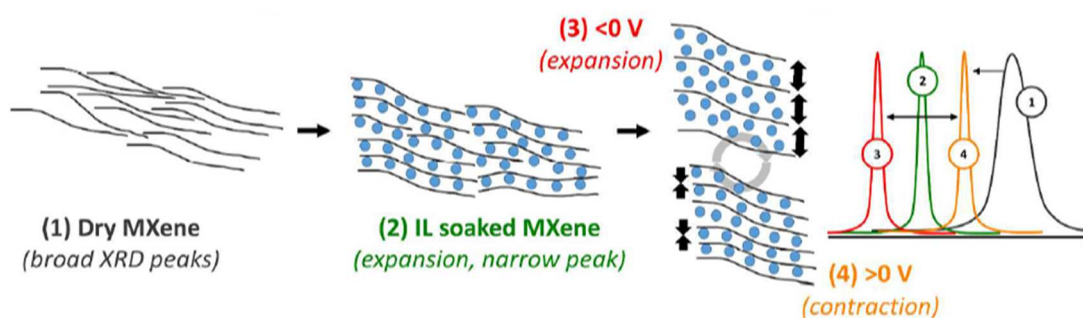


Figure 2.34: Changes of the MXene stacking peak during operation. When a dry (1) MXene electrode is filled, spontaneous intercalation occurs (2) and leads to an electrode expansion and an alignment of the MXene sheets indicated by the shifts of the Bragg peaks to smaller angles and narrower peak, respectively (schematic XRD measurement on the right side). Discharging (3) and charging (4) leads to an expansion and contraction, respectively. This can be seen from the peak shifts to higher and lower angles, respectively. Reprinted with permission from Ref.<sup>154</sup> Copyright 2016 American Chemical Society

### 2.11.5 Carbon nanotubes

Carbon nanotubes (CNTs) are cylindrical tubes of  $\text{sp}^2$  carbon, first discovered in 1991<sup>155</sup> and used as a material for supercapacitor electrodes since 1997.<sup>156</sup> CNTs can have either metallic or semiconductor behavior, depending on their chirality (Figure 2.35a):<sup>157</sup>

- Armchair
- Zigzag
- Chiral

and are divided into two different types: single-walled (SWCNT) and multi-walled (MWCNT) carbon nanotubes (Figure 2.35b). In a MWCNT each layer can exhibit a different chirality.<sup>158</sup> In addition to their good electrical conductivity, CNTs are also mechanical and chemically stable. The accessible surface area is located on the outside of the (mostly closed) nanotubes, leading to an open pore network.

Due to their good electrical conductivity and fast ion diffusion (caused by the open pore network) supercapacitor electrodes made from pure carbon nanotubes are well suited for applications demanding for a high maximum power output. The energy density of such devices on the other hand is limited due to the (compared to other carbon materials) lower specific surface area in the range of  $500\text{ m}^2\text{ g}^{-1}$ .<sup>159</sup>

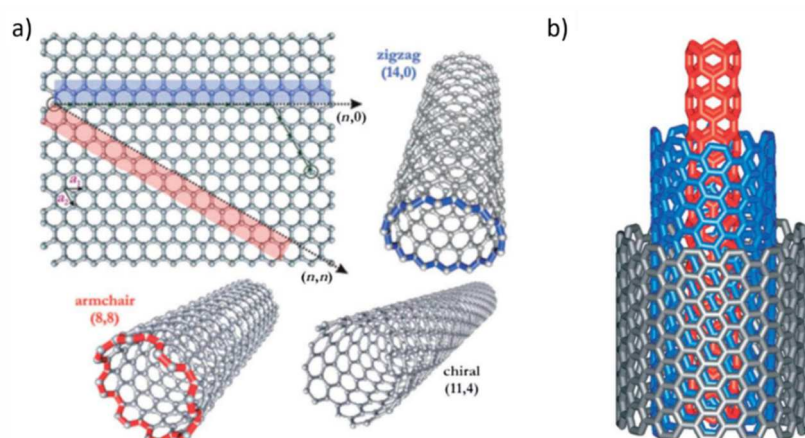


Figure 2.35: (a) Different types of chirality in a single-walled carbon nanotube. (b) Schematic drawing of a multi-walled carbon nanotube. Reproduced from Ref.<sup>160</sup> with permission from The Royal Society of Chemistry

To adjust the properties and widen the possible applications, CNTs can be modified in different ways: An increased specific surface area can be achieved by an additional chemical activation process. This will increase the microporosity (defects in the CNT walls), but simultaneously reduces the conductivity of the material. Adding functional surface groups or transition metal oxides with pseudo-capacitive behavior can also be used to increase the energy density of CNT based devices.<sup>160,161</sup> Deploying metal oxide nanoparticles on highly conductive CNTs helps to overcome two major drawbacks: the poor conductivity and the limited cycle lifetime of transition metal oxide based electrodes. The carbon nanotube skeleton acts as conductor and protects the metal oxides from degradation (see also Chapter 2.14.1).<sup>161,162</sup> This concept can also be applied to conductive polymers. PPy is a well-known pseudo-capacitive electrode material that suffers from low cycle lifetimes due to cracking from ongoing expansion and contraction during the charging process. It has been shown that a CNT/PPy composite electrode can lead to an increased lifetime.<sup>163,164</sup>

The actual performance is defined by the purity, functionalization, structural properties and modification of the CNT. Also the alignment of the individual CNTs can influence the performance: highly entangled CNTs can limit the ion diffusion and reduce the power density.<sup>159,165</sup> Although, carbon nanotubes could be an interesting material for high power application and hybrid electrodes, the production process is still very costly and cannot easily be upscaled to produce large quantities. Additionally, it is difficult to retain the properties of single CNTs when produced on a large scale.<sup>163,164</sup> Carbon nanofibers are a cheaper alternative. They also have an open pore network and can deliver a high maximum power output.<sup>166</sup>

### 2.11.6 Carbon onions

First discovered in 1980,<sup>167</sup> carbon onions (also known as onion-like carbons, carbon nano-onions and multi-walled fullerenes) have gained a lot of interest for the use in supercapacitor electrodes over the last decade. Carbon onions are  $sp^2$  hybridized concentric shells with a spherical or polyhedral closed shell (Figure 2.36) and an external surface area in the range of  $600 \text{ m}^2 \text{ g}^{-1}$ .<sup>168,169</sup>

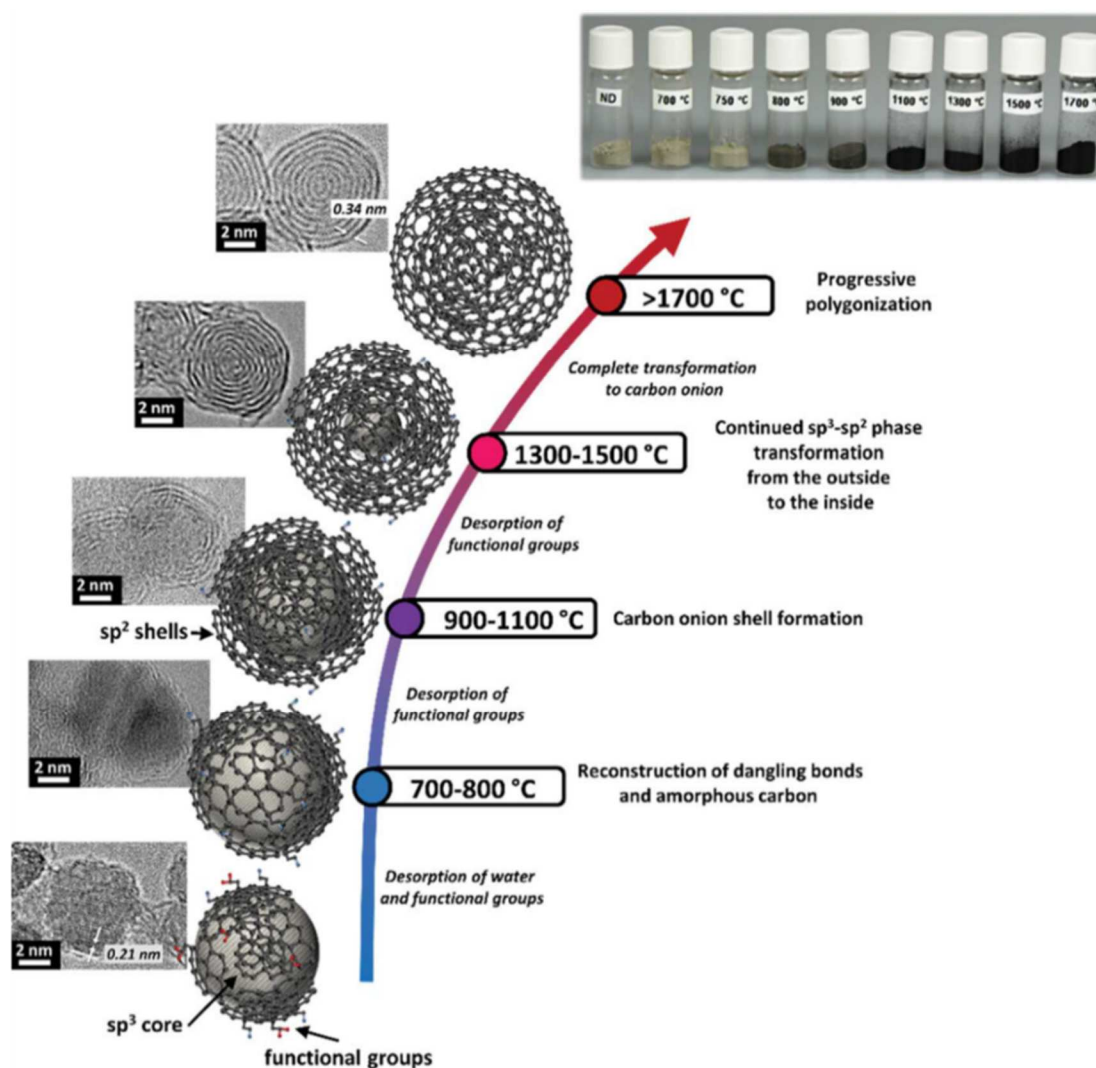


Figure 2.36: Synthesis steps of carbon onions for high temperature annealing of carbon nano-diamonds. Reproduced with permission from Ref.<sup>168</sup> published by The Royal Society of Chemistry

Thermal annealing of detonation nano-diamonds is one of the most common synthesis routes. It is a rather simple method and allows producing large amounts of carbon onions in one batch. In addition, detonation nano-diamonds have a narrow size distribution, which is beneficial for the production of carbon onions

as well as for their potential usage. The formation of carbon onions during the thermal annealing process is a transformation from a  $sp^3$  carbon in the diamond to a  $sp^2$  hybridized structure. This transformation is done in different steps, as shown in Figure 2.36. At first, physisorbed water is desorbed and surface groups (detonation nano-diamonds contain surface groups, e.g. anhydrides, carbonyl and quinone groups)<sup>170</sup> are removed, leading to the formation of dangling bonds. At 800-900°C,  $\pi$ -bonds are formed and graphitization starts, causing the formation of a  $sp^2$  carbon shell around the nano-diamond. With a further increased temperature, the shells show a more ordered structure. For a full transformation of nano-diamonds to highly ordered carbon onions, temperatures of at least 1800°C are required. The annealing process can be performed either in vacuum or in an inert atmosphere.<sup>168,171</sup> The physical and chemical properties of the produced onions strongly depend on the synthesis conditions as well as the precursor. A higher temperature leads to reduced defects in the shells, resulting in an increased conductivity. The high temperatures on the other hand reduce the surface area of the material. The highest specific surface area has been found with synthesis temperatures of ~1500°C. High heating rates can be used to counteract the surface reduction for high temperatures.<sup>168,169</sup>

Carbon onions have a significantly lower specific surface area compared to activated carbons or CDC materials. They have mainly external surfaces, while the surface area of other carbon materials, for the most part, originates from micro and mesopores. Additionally, the electronic conductivity of carbon onions is (because of their conducting shell) superior to most other carbon materials used for supercapacitor electrodes. From these unique properties, the following applications can be derived:

1. *Carbon onions as an active material for supercapacitor electrodes:* The high conductivity and the external surface area of carbon onions make them an ideal material for the use in devices requiring very high charging and discharging rates. Carbon onion electrodes have shown nearly no capacitance decrease over 10000 cycles. The main drawback is the limited energy density due to the comparably small SSA. An additional activation process can increase the surface area, but not to a value comparable to other activated carbon materials. For the production of freestanding electrodes, the amount of binder needed also exceeds activated carbon materials due to the very small particle size of ~10 nm. Carbon onions could also be used as an intercalation electrode.<sup>168,171,172</sup>

2. *Carbon onions as a conductive additive:* Due to their good conductivity and small particle size, carbon onions are well suited to be used as a conductive additive for carbon based supercapacitor electrodes. The conductivity, depending on the synthesis conditions, of carbon onions is comparable to carbon black ( $4 \text{ S cm}^{-1}$ ), which is commonly used as a conductive additive. With their smaller size of  $\sim 10 \text{ nm}$ , carbon onions are able to access small spaces between particles better than carbon black (particle size  $\sim 40 \text{ nm}$ ) and therefore increase the particle-particle contact. This reduces the sheet resistance of the electrode and increases the performance.<sup>168,171</sup>
3. *Carbon onions as a substrate for pseudo-capacitive materials:* Redox active metal oxides suffer from a poor conductivity. To overcome this issue, a hybrid electrode with carbon onions as a substrate coated with metal oxide nanoparticles can be produced. The high external surface of carbon onions also guarantees a good accessibility of the pseudo-capacitive particles. In activated carbon electrodes, the introduction of metal oxides can lead to a pore blocking effect, which is not the case for carbon onions.<sup>168</sup>

### 2.11.7 Summary

To sum up this chapter Table 2.1 compares a few important properties of the discussed materials: there is not a best electrode material, rather than an optimum combination of material and electrolyte for each individual application.

Table 2.1: Comparison of different performance parameters

Material	Conductivity	Surface area	Tunable PSD	Rate handling
Activated carbon	+	++	+	~
CDCs	+	++	++	~
MOFs	-	++	+(+)	~
MXenes	++	+	~	+
Carbon nanotubes	+(+)	-	~	++
Carbon onions	++	-	~	++
Templated carbons	+	+(+)	++	+(+)

## 2.12 Templated carbon materials

In this chapter, the synthesis and application of mesoporous carbon materials produced by hard-templating (nanocasting) as well as from soft-templating routes are explained. The focus will be on (hexagonally) ordered mesoporous systems, since they are the basis for the experiments described in Chapters 4 to 6 of this thesis.

Supercapacitor devices built from purely microporous activated carbons or CDCs exhibit a high specific capacitance, but suffer from a limited rate handling capability (rate handling capability: remaining capacitance at higher charging and discharging rates) and power density. While the microporous system governs an efficient screening of the counter ion charge and therefore allows a dense packing of the ions,<sup>34,173</sup> the ion dynamics is limited in such a system. In situ nuclear magnetic resonance (NMR) studies, using organic electrolytes, have shown a decrease of ion diffusion rates by two orders of magnitude in microporous activated carbon materials compared to bulk behavior.<sup>174</sup> As a result, the limited rate handling capability of purely microporous electrodes originates from the reduced ion dynamics. To overcome this issue, electrode materials with a hierarchical macro/meso/micropore structure can be used. In these materials the micropores are connected to the bulk electrolyte reservoir via macro- and mesopores. These pores provide an increased ion diffusion rate (diffusion rate in porous material is influenced by confinement effects, ion-ion and ion-carbon interactions<sup>174</sup>), leading to a better rate handling performance compared to purely microporous electrodes. Such hierarchical pore structures can be produced via different templating routes.<sup>175-177</sup>

Using a templating based synthesis, a carbon material with a structure related to the used template can be produced. There are a variety of different methods and templates available to obtain such hierarchical carbon materials. From a variety of studies it is known that these materials provide a specific capacitance comparable to microporous activated carbon materials, while simultaneously preserving a better rate handling capability.<sup>175,178-180</sup> This confirms the concept of mesopores acting as “highways” for ions moving from the bulk electrolyte through the macro- and mesopores into the micropores. The influence of the pore structure will be discussed in more detail in Chapter 4.



### 2.12.1 Soft-templating

The soft-templating synthesis route is based on the self-assembly and phase separation of a block-copolymer/carbon-precursor mixture. The block copolymer consist of a hydrophilic and a hydrophobic part (Figure 2.37).

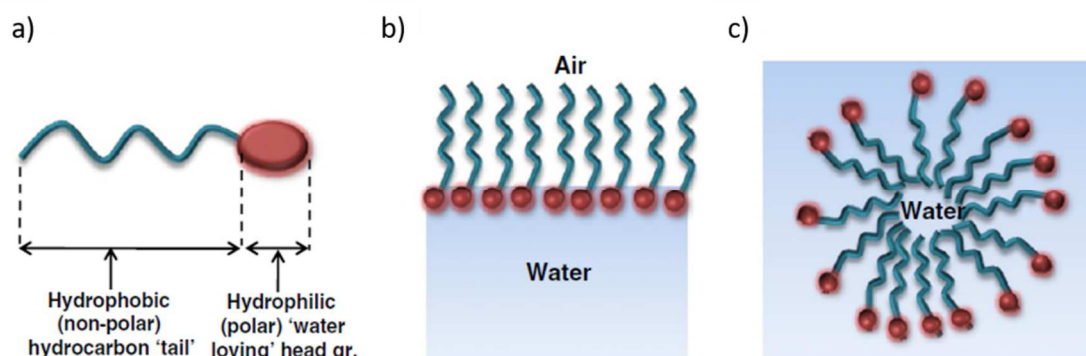


Figure 2.37: (a) Composition of the block copolymer consisting of a hydrophilic head and a hydrophobic tail. (b) Arrangement at an interface between a polar liquid (e.g. water) and a non-polar liquid (or air). (c) Forming of a micelle in a polar solvent. Reproduced with permission from Ref.<sup>181</sup> © 2012 Elsevier B.V.

The hydrophilic part interacts with the OH groups of the precursor (resorcinol-formaldehyde was used as a precursor for all samples in this thesis), leading to a formation of rod like micelles. The micelles self-organize on a two-dimensional hexagonal lattice, causing the formation of a liquid crystal template. The macroporosity in the system is a result of a phase separation due to spinodal decomposition.<sup>177,181–183</sup> After solidification and drying, an additional calcination step (nitrogen atmosphere with  $\sim 2\%$  oxygen<sup>177</sup>) is necessary to remove the surfactants from the sample, resulting in a polymer structure with cylindrical mesopores, ordered on a two-dimensional hexagonal lattice, which subsequently is carbonized. The product of this synthesis route (Figure 2.38) is an ordered mesoporous carbon with essentially the same structure as SBA-15 silica.<sup>184</sup> An additional CO<sub>2</sub> activation process can be performed to adjust the amount of micropores as well as the micro-pore size distribution. This activation process mainly introduces and widens micropores while leaving the ordered mesopore structure intact. Due to the fact that no individual (hard)template is needed, the soft-templating route can be performed as a one-pot synthesis.<sup>177,185</sup> In combination with the omission of an etching step (also needed in a hard templating synthesis route), upscaling of the soft-templating can done in a more cost efficient way than

nanocasting (see Chapter 2.12.2).<sup>185</sup> Figure 2.38 illustrates the synthesis route for ordered mesoporous material via soft templating.

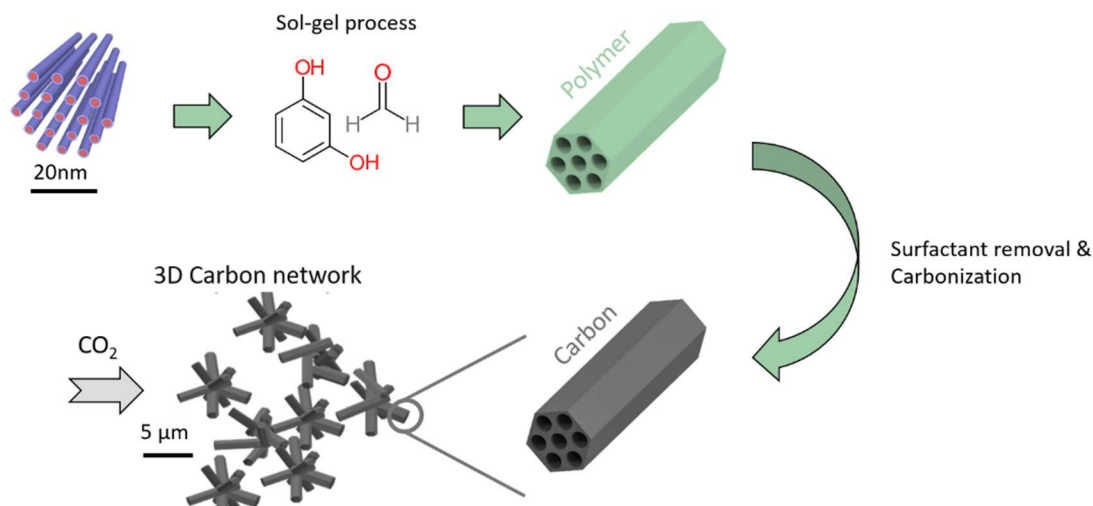


Figure 2.38: Schematic representation of the soft-templating synthesis route for ordered mesoporous carbons. In a sol-gel process the polymer precursor is formed. After calcination and carbonization, an additional CO<sub>2</sub> activation process can be performed to adjust the micropore size distribution within the mesopore walls and increase the surface area. Simon Rumswinkel, University of Salzburg (Austria), synthesized the material.

The carbon monoliths produced via this soft templating synthesis route consist of a three-dimensional network of micron-sized struts containing hexagonally ordered cylindrical pores (Figure 2.39).

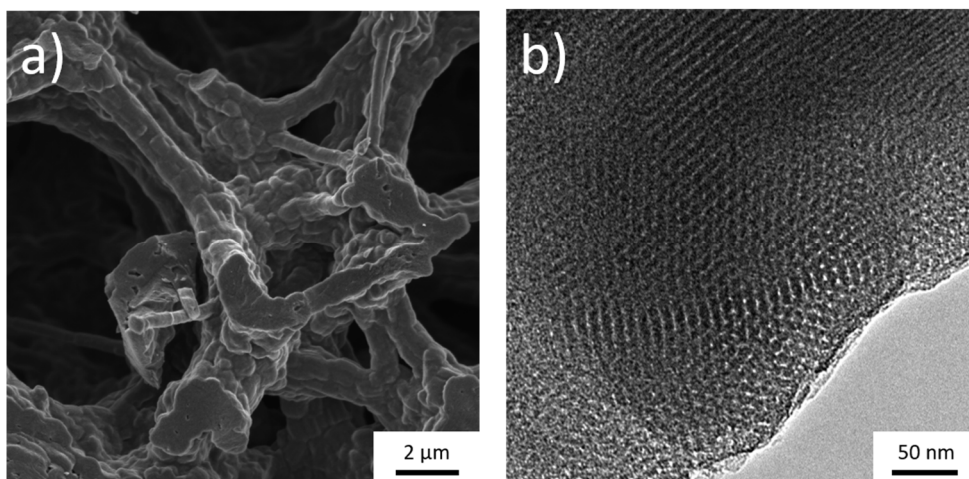


Figure 2.39: (a) SEM image of the three-dimensional strut network. (b) TEM image of the hexagonally ordered pore system. Reprinted with permission from Ref.<sup>142</sup> Copyright 2019 American Chemical Society

### 2.12.1 Hard-templating (nanocasting)

The synthesis of nanocast carbon materials is based on a rather simple concept: a stable (hard) template is infiltrated with an organic carbon precursor. The carbonization of this precursor leads to a carbon/template composite. To obtain the pure carbon material, the template has to be removed by an etching procedure. (Figure 2.40).

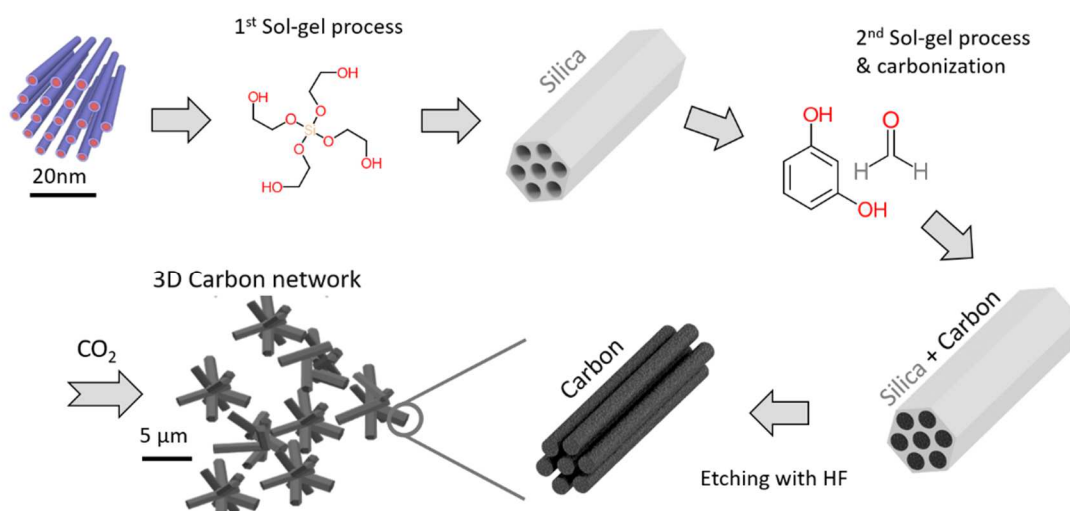


Figure 2.40: Synthesis route for nanocast carbon materials used in this thesis. In the first step, the silica template is synthesized. The resulting silica monoliths are filled with resorcinol formaldehyde, acting as a carbon precursor. After carbonization, the silica template is removed by HF etching. To adjust the micropore size distribution within the carbon nanorods, an additional CO<sub>2</sub> activation step is performed. Simon Rumswinkel, University of Salzburg (Austria), synthesized the material.

There are many possible inorganic frameworks available to act as a template and produce hierarchical structures. Zeolites are a widely used material to produce high specific surface area hierarchical carbon materials with a narrow pore size distribution.<sup>176,179,187,188</sup> Due to the variety of different Zeolite structures, the pore structure can be adjusted for different applications. Ordered silica materials are another possible template for the synthesis of ordered mesoporous carbon structures. The most prominent example is the so-called CMK-3 carbon, which uses SBA-15 silica as a template.<sup>189</sup> The result is a mesoporous carbon material consisting of carbon nanorods located on a hexagonal lattice. The drawbacks of this method is its costly multiple step character and that the etching process permanently destroys the template, produced in the first step.<sup>190,191</sup>

For synthesis of the materials used in this thesis, a custom made silica template was produced via surfactant self-assembly according to Brandhuber et al.<sup>192</sup> and Putz et al.,<sup>193,194</sup> which is comparable to the synthesis of the soft templated material. The carbon material for all nanocast materials used in this thesis is produced with a resorcinol formaldehyde solution acting as carbon precursor. The schematic representation of this synthesis is shown in Figure 2.40. As a result, a monolithic carbon material consisting of hexagonally ordered carbon nanorods is obtained. The nanorods form macroporous network of sub-micron sized struts (Figure 2.41). A detailed description of the synthesis procedure is given in Ref.<sup>142</sup> The carbon material produced via this particular templating route can be produced in a monolithic form.

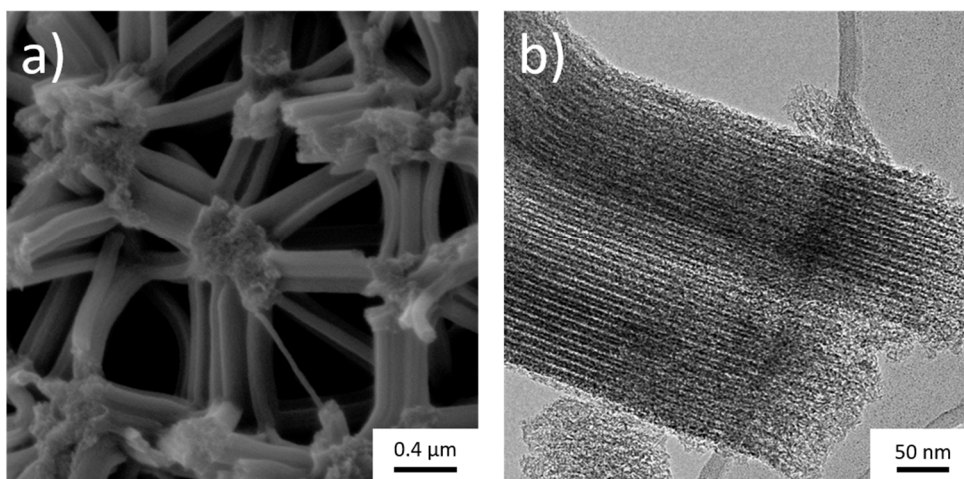


Figure 2.41: (a) SEM image of the three-dimensional strut network. (b) TEM image of the hexagonally ordered carbon nanorods. Reprinted with permission from Ref.<sup>142</sup> Copyright 2019 American Chemical Society

Besides their well-defined pore structure and improved electrochemical performance at elevated charging and discharging rates, ordered structures are beneficial for a variety of experiments. Due to the ordered nanorods or cylindrical pores, these materials show sharp Bragg peaks in the small-angle scattering region (Chapter 2.5). Figure 2.42 illustrates the comparison between a commercially available AC material and an ordered mesoporous carbon (OMC) produced via a soft templating route. In situ small-angle X-ray scattering (experimental setup explained in Chapter 3.4) experiments on activated carbon materials have been proven to be a powerful tool to study ion movement in an operating supercapacitor device.<sup>20,21,34,173</sup> Due to the Bragg peaks of OMC materials, additional experiments and data analysis techniques are possible. Chapter 5 and

6 focus on the use of ordered mesoporous carbon materials to study electrode expansion and ion concentration changes with in situ small-angle X-ray scattering.

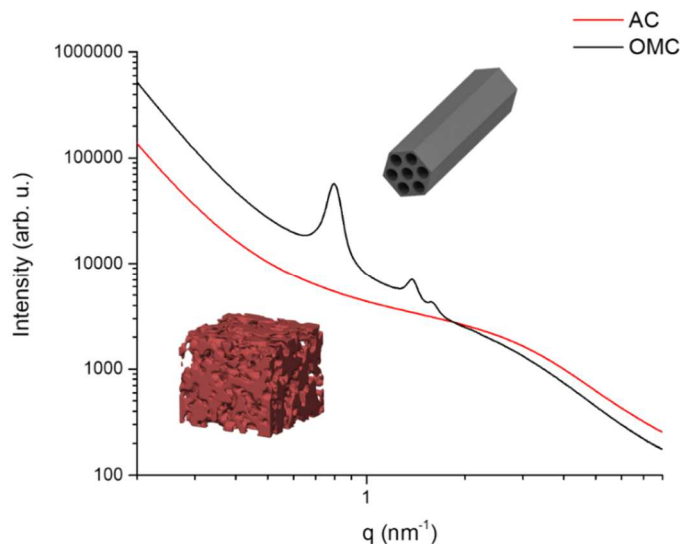


Figure 2.42: Small-angle X-ray scattering curve of a commercially available activated carbon (red) and an ordered mesoporous carbon (black) produced via soft-templating synthesis route. The Bragg peaks seen from the hexagonally ordered cylindrical mesopores.

## 2.13 Pseudo-capacitance: the concepts

The main drawback of EDLCs is the limited charge stored in the electrical double layer and the resulting low energy density compared to modern batteries. The capacitance scales with the surface area of an electrode and can therefore not be increased infinitely. In addition to the high surface area, carbon materials have only a low density resulting a high weight normalized capacitance and energy, but a rather low volumetric energy. In many applications, like mobile devices and electric cars, the size is the limiting factor. To overcome this issue and increase the gravimetric and volumetric energy, the development of new high surface area carbon materials alone will not be enough. The two main concepts to resolve this issues are: hybrid devices, consisting of a battery type and a conventional EDLC electrode, as well as the use of so called pseudo-capacitive reactions.<sup>19,30,195</sup> Before going into detail about the different materials and device types, it is mandatory to explain a few basic terms and concepts.

### 2.13.1 Pure EDLC

An ideal EDLC stores charge at the electrode/electrolyte interface by adsorbing ions and forming a double-layer (Chapter 2.1). The polarization (charge separation) is not limited by diffusion into the electrode material. Therefore, a (nearly) rectangular shape is observed when CV measurements are performed (Figure 2.43). The voltage changes linear with time when an EDLC is charged using a constant current, leading to a triangular-shaped curve for galvanostatic cycling experiments.<sup>195</sup>

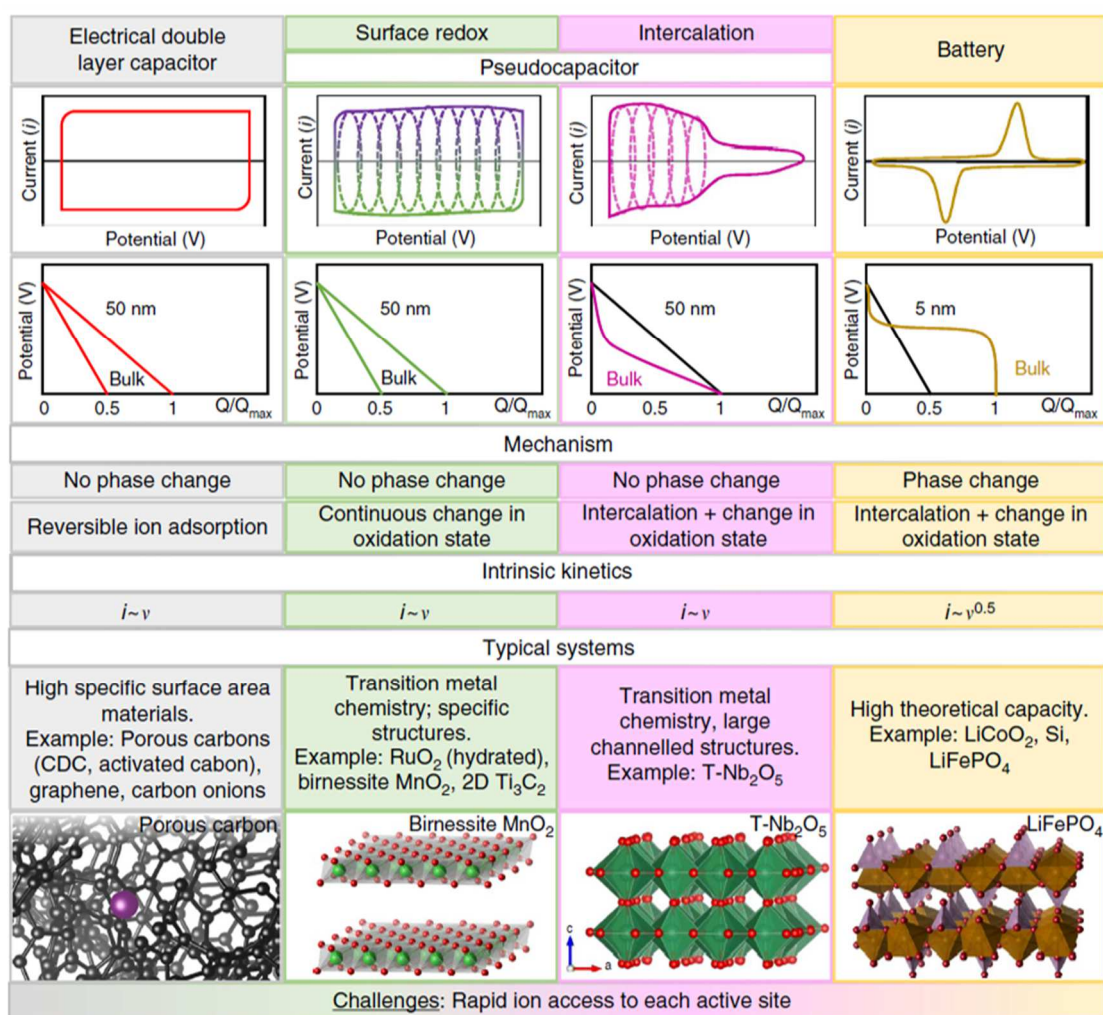


Figure 2.43: Comparison of different charge storage mechanisms. The first row shows schematic CV curves. The second row shows galvanostatic measurements comparing bulk quantities and small (nanometer sized) particles. Reproduced with permission From Ref.<sup>195</sup> published by Springer Nature

### 2.13.2 Pseudo-capacitance versus battery-like behavior

Although pseudo-capacitive reactions and battery type reactions utilize faradaic reactions to store charge, there is a big difference between a pseudo-capacitive and a battery type behavior. Electrochemical measurements (cyclic voltammetry, galvanostatic cycling) can be used to distinguish between these two types. Pseudo-capacitive reactions are fast, reversible faradaic-reactions showing a capacitor like behavior. The idea behind utilizing those reactions is to increase the energy density to reach battery-like values while at the same time maintaining the high power of EDLCs. Pseudo-capacitive reactions are based on changes of the oxidation state over a large range of the used potential window and on intercalation reactions. When performing cyclic voltammetry, pseudo-capacitive electrodes have an almost rectangular shape and show a mostly linear voltage increase/decrease when charged/discharged with a constant current (similar to a pure EDLC). Battery electrodes on the other hand show distinct redox peaks in the CV curves and a plateau region when galvanostatic experiments are performed.<sup>195</sup> An overview of the different charging mechanisms and electrochemical responses is shown in Figure 2.43.

Besides the shape of measured curves, also the intrinsic kinetics can determine the difference between a battery-like and a pseudo-capacitive material. Performing CV measurements at different scan rates  $v = \Delta U / \Delta t$  leads to a current response  $I$  according to:<sup>19</sup>

$$I \propto v^b \tag{2.59}$$

The exponent  $b$  determines if the behavior is capacitive or battery-like. If  $b = 1$  the current is directly proportional to the scan rate, resulting in a capacitive behavior with the proportionality constant describing the capacitance of the device. In battery electrodes, a diffusion process into the bulk electrode (e.g. semi-infinite diffusion) defines the peak current leading to  $b = 1/2$ . The optimization of electrode structure can help to increase the battery performance at elevated charging rates. The use of small battery-active particles on a conductive backbone instead of a bulk electrode for instance can increase the maximum power output for battery type electrodes, but they still show typical battery-like behavior in electrochemical measurements, meaning they are not pseudo-capacitive.<sup>19</sup>

There are only a limited number of real pseudo-capacitive materials (e.g.  $\text{RuO}_2$  or  $\text{MnO}_2$ ) with several different oxidation states in the usable potential window.<sup>195</sup> However, it is worth noting that under certain circumstances battery-type

materials can show capacitive behavior too. A miniaturization of battery-active particles in an electrode below a critical size (in the range of 10 nm) can lead to a capacitive behavior of such materials (e.g.  $\text{LiCoO}_2$ ), although their bulk properties are battery-like (yellow column in Figure 2.43).<sup>29,196</sup> It was proposed to call such a material “extrinsic” pseudo-capacitive, since their pseudo-capacitive behavior depends on particle size and structure, while intrinsic pseudo-capacitive materials show now dependence on structural parameters. The distinction between a pseudo-capacitive or battery-like behavior should always be done using a three-electrode setup because the use of a hybrid two-electrode device containing an EDLC and a battery type electrode will also show a capacitive behavior.<sup>30</sup>

### 2.13.3 Capacitance versus capacity

The capacitance  $C$  of an electrical charge storage device is the proportionality constant for the accumulated charge  $Q$  in a certain potential window  $\Delta U$ . The unit of the capacitance is Farad (F; Coulomb/Volt). Capacity on the other hand corresponds to the overall charge accumulated in a device. The unit of the capacity is Coulomb (C), which is equivalent to current-time, leading to the often-used milliampere-hours (mAh).

Therefore, capacitance is only meaningful for devices with a (nearly) capacitive behavior, which is not the case for a battery-type electrode material. Using the capacitance term for such electrodes would be misleading.<sup>30</sup> This will be explained in more detail using Figure 2.44 where an EDLC and a schematic battery-type electrode are compared.

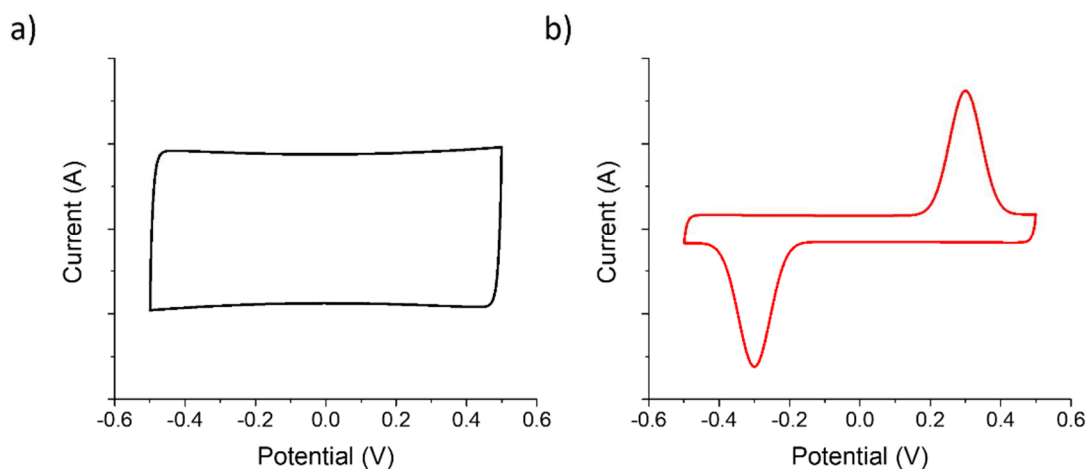


Figure 2.44: Schematic representation of a CV curve of a pure EDLC with a nearly rectangular shape (a) and a battery-type material showing distinct redox peaks (b).



A constant current response over the whole potential window (Figure 2.44a) leads to a capacitance value independent from the measurement or data evaluation range. The CV curve in Figure 2.44b on the other hand has two redox peaks in the shown potential range. Obviously, the calculated capacitance depends on the range used for its calculation. If the calculation is done in the range just before the onset of the redox peak, the calculated capacitance value would be very low. If done just in the range of the peak, a high value would be the result. If the calculation is done over the whole potential range, an average capacitance would be the result, which also strongly depends on the measured range: a wider range leads to a lower average capacitance. Therefore, calculating a capacitance value is not representative for such a device and capacity should be used instead. The use of battery-like electrode materials can be beneficial for the performance of electrical energy storage devices, but their true potential can only be determined if the characterization is done properly. Test conditions have to be comparable to future application conditions: determining storage capacity at very low charging and discharging rates might lead to an overestimation of the true capabilities of the device.<sup>19,30</sup>

Understanding the difference between battery-type and pseudo-capacitive behavior is mandatory to accordingly test electrode materials and evaluate their performance as well as to determine their suitability for certain applications.

## 2.14 Pseudo-capacitive materials

There is a variety of different battery type and pseudo-capacitive materials available. On the following pages a short overview of selected pseudo-capacitive material types is given.

### 2.14.1 Transition metal oxides

Some transition metal oxides exhibit a pseudo-capacitive behavior.  $\text{RuO}_2$  and  $\text{MnO}_2$  are the most prominent members of this group. Due to three oxidation states in the potential window of aqueous electrolytes, as well as a reasonable conductivity and cyclic stability,  $\text{RuO}_2$  is a well-suited pseudo-capacitive electrode material. The high production costs and toxicity on the other hand prevent a large-scale use in commercial devices.  $\text{MnO}_2$  also shows an oxidation state change in aqueous electrolytes and is a low-cost alternative for  $\text{RuO}_2$ .<sup>47</sup> The main

drawback here is the drastically reduced conductivity compared to  $\text{RuO}_2$ , resulting in just a small layer at the surface actively responsible for the charge storage. Therefore, the specific capacitance is significantly lower. This issue can be overcome by adjusting the structure of the electrode as well as placing metal oxide nanoparticles or thin film on a porous and conductive (carbon) backbone.<sup>15,29,195</sup> Other available pseudo-capacitive oxides also suffer from a limited conductivity and cyclic stability due to volumetric changes during charging and discharging.<sup>15</sup>

### 2.14.2 Conductive polymers

In conductive polymers, such as polypyrrole (PPy), redox reactions can occur at the polymer backbone chain. PPy is a conjugated (alternating double and single bonds at backbone chain) organic polymer with conjugated  $\pi$ -electrons, which can be delocalized and enable the redox reaction.<sup>42,197</sup> A big drawback of this material class is the limited lifetime due to volumetric changes during the redox reactions. Composite electrodes using carbon materials as a framework for PPy have shown promising results in terms of enhanced cyclic stability as well as an increased electrode conductivity compared to pure PPy films.<sup>150,195</sup>

### 2.14.3 Surface groups

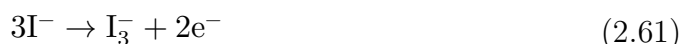
Redox active surface groups can be attached to the surface of the electrode material during the synthesis. These groups exhibit fast faradaic reactions with nearly no volumetric changes, resulting in a long lifetime. A prominent example is the use of quinone/proton reaction involving the transfer of two electrons:<sup>15,195</sup>



To exploit the full potential of such surface groups, it is necessary to use a suitable electrolyte and properly balance the electrode masses: oxygen-containing groups work best in acidic environment at a positive electrode, nitrogen-containing groups should be used at the negative electrode with alkaline electrolytes.<sup>15</sup>

### 2.14.4 Redox active electrolytes

In a conventional EDLC, the ions in the electrolyte have a quite simple purpose: ionic conductivity and storage of charge by forming the electrical double-layer at the electrode/electrolyte interface. Some ions can also exhibit a change of the oxidation state in the potential window of aqueous and organic electrolytes. This change of the oxidation state is a faradaic process contributing to the overall charge stored. Iodine for instance has different oxidation states in the potential range of aqueous electrolytes and can form an  $I_3^-$  complex:<sup>15,195</sup>



It is important to mention, that the actual available oxidation states also depend on the pH value of the electrolyte.<sup>15</sup>

## 2.15 Devices

### 2.15.1 Electrodes and binder

Carbon materials are often produced as powders, which are mixed with a binder to produce a stable electrode. The binder has to be stable in the used electrolyte (and potential window) and should not degrade during operation. Additionally, pore blocking by the binder has to be minimized to avoid a significant drop in specific capacitance. The content of the used binder is usually in the range of a few mass% and should be as low as possible to avoid the inclusion of a large amount of nonporous and nonconductive material into the electrode.<sup>135</sup>

Polyvinylidenedifluoride (PVDF) is a binder used for directly spraying or casting the binder carbon mixture onto the current collector, while polytetrafluoroethylene (PTFE) is an often-used particle binder to produce freestanding supercapacitor electrodes. Both binders contain fluorine, which can lead to the formation of volatile fluorocarbons when burned. PVDF also requires toxic additives during the production process of the electrode. Therefore, the development of new “greener” binder materials is a big step towards supercapacitors composed entirely of environmentally friendly components. Polyvinylpyrrolidone (PVP) is a possible green substitute for PVDF for producing electrode films directly cast on the current collector. The major drawback of PVP is that it is limited to be used in devices with non-aqueous electrolytes because it

dissolves in water. For the production of freestanding electrodes, adequate substitutes are still under investigation.

Due to fiber morphology of PTFE (Figure 2.45a) pore blocking is not a major issue. Additionally it leads to a good contact between the carbon particles and therefore increases the electrical conductivity over the whole electrode.<sup>135,198</sup> Polyvinyl alcohol (PVA) has been proposed as an environmentally friendly alternative, but it cannot compete with PTFE due to an increased electrode resistance and a reduced SSA because of pore blocking effects (Figure 2.45b), which results in a reduction of the overall performance of the device.<sup>135,198</sup>

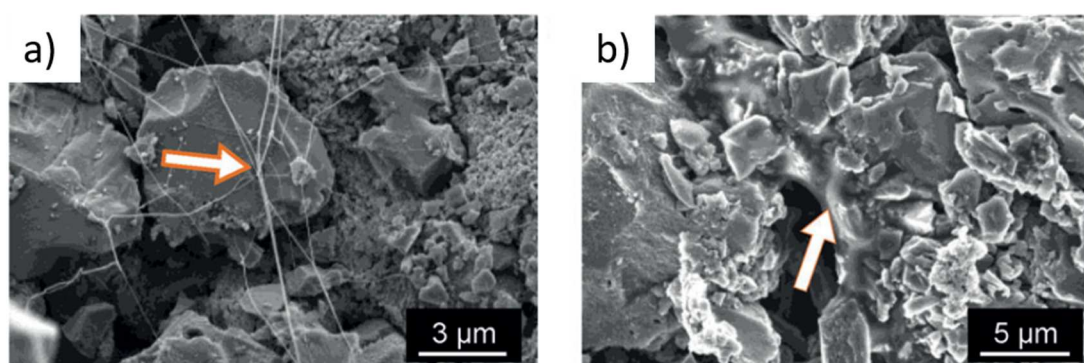


Figure 2.45: Electrode made out of activated carbon powder using PTFE (a) and a PVAc/polyisoprene blend (b) as binder. The white/orange arrows mark the binder phase. PTFE with its fiber morphology only limits the SSA by a small margin while the PVAc/polyisoprene blend can cause substantial pore blocking. Reproduced with permission from Ref.<sup>198</sup> © WILEY-VCH

To avoid these negative effects, binder free electrodes are developed. One example is the use of activated carbon cloth (ACC). By combining chemical impregnation, carbonization and activation of a low cost viscose rayon cloth, a highly porous carbon cloth can be produced. In Figure 2.46 it is shown that the woven structure of the cellulose based starting material is still present after carbonization and activation, resulting in a mechanically stable and flexible cloth that can be directly used as an EDLC electrode, without the need of an additional polymer binder. The ACC electrode has a capacitance comparable to commercial activated carbon powder materials.<sup>60,200</sup>

Activated carbon materials can also be used for some rather progressive applications like smart textiles. Wearable electronics suffer from a lack of availability of non-toxic, lightweight and flexible energy storage devices. EDLCs based on activated carbon materials using aqueous or solid electrolytes could be able to help to overcome this issue. It has to be mentioned that for commercial success of supercapacitors as storage devices in smart textiles it is important to

implement their production into established textile production methods. Slurries made from activated carbon powders are well suited for coating techniques like dip coating and screen-printing, which can be easily implemented in modern textile production routes. Due to the limited surface area of a human body (in the range of  $1.5 \text{ m}^2$ ), the areal capacitance is an important factor for this type of application. It is possible to coat cotton and polymer fabrics with an AC based slurry to create a flexible and durable EDLC electrode.<sup>201,202</sup>

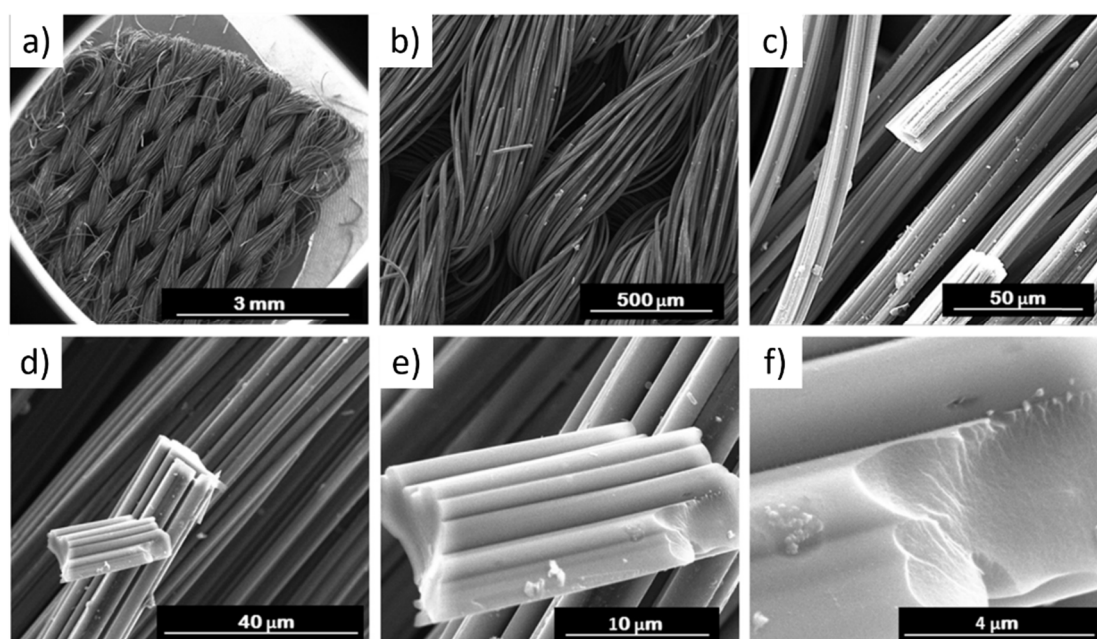


Figure 2.46: SEM image of an ACC electrode at different magnifications. (a) ACC electrode, (b) woven structure, (c-e) carbon fiber fragments, and (f) single carbon fiber with fractured surface. Reproduced with permission from Ref.<sup>60</sup> © 2017 Elsevier Ltd.

### 2.15.2 Hybrid devices

First, it is necessary to distinguish between a hybrid electrode and a hybrid device. A hybrid electrode combines multiple materials or charging mechanisms in one electrode,<sup>16,203</sup> a hybrid device contains two electrodes using different charging mechanisms (e.g. one EDLC electrode and a battery-type electrode). In such hybrid devices the electrode potential can be adjusted, leading to an increased voltage window (Figure 2.47). As a result, the energy density can be significantly improved compared to conventional EDLCs.<sup>16,204</sup>

The most prominent hybrid device is a so-called Li-ion capacitor (LiC), which is already commercially produced. A LiC consists of a positive EDLC electrode

and a negative graphite electrode, similar to a Li-ion battery. A LiC exhibits an increased energy density, but still suffers from reduced cycle stability and power handling. To overcome this issue, new high power electrodes (e.g. nano-structured and composite electrodes) have to be developed.<sup>47</sup>

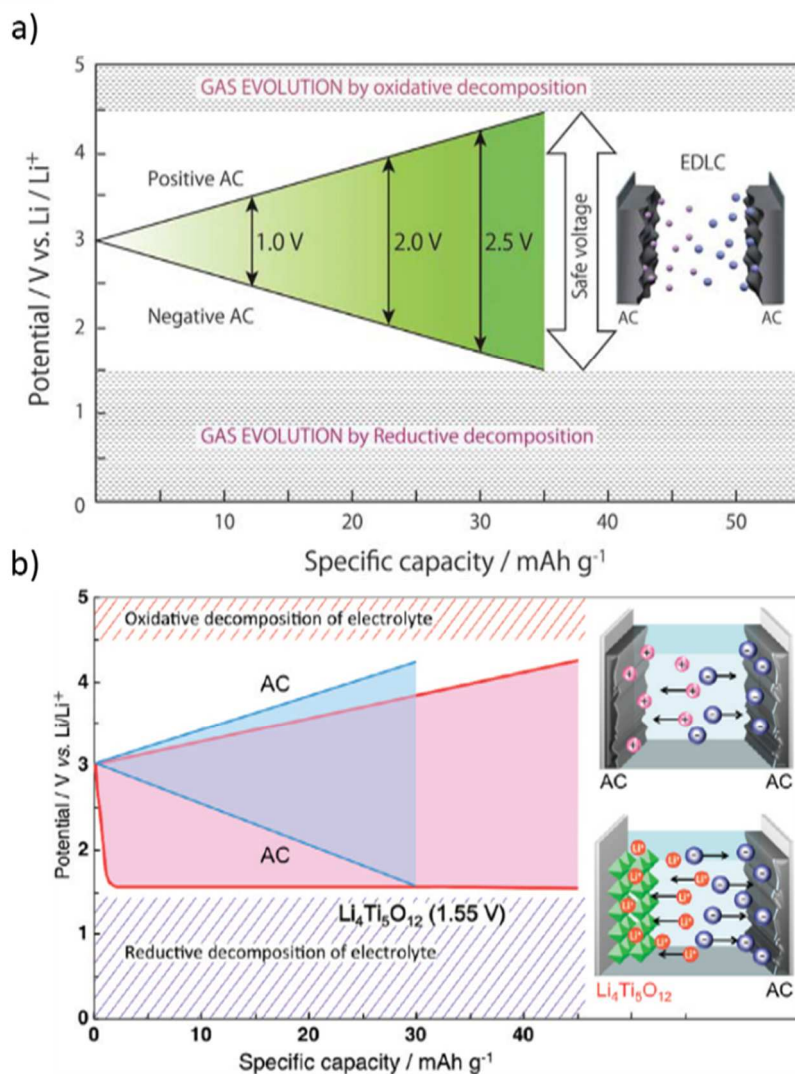


Figure 2.47: Comparison of a symmetric carbon/carbon supercapacitor (a) and a hybrid device using a battery type negative electrode (b). (a) Reprinted from Ref.<sup>205</sup> with permission from The Royal Society of Chemistry. (b) Reprinted with permission from Ref.<sup>204</sup> Copyright 2013 American Chemical Society

## 3 Experimental

### 3.1 Electrode preparation

For the preparation of electrodes, the carbon monoliths were manually ground in a mortar to a fine powder. This grinding is only necessary for the ordered mesoporous carbon material, the AC material was already delivered as a powder. The powder was then mixed with ethanol and 60 mass% polytetrafluoroethylene dispersion (PTFE in water, Sigma-Aldrich) as a binder. This mixture resulted in a slurry with 10 mass% of PTFE binder in the dry electrode. The slurry was rolled with a MSK-HRP-MR 100A (MTI Corporation) rolling press to a thickness of 300  $\mu\text{m}$  and dried at 393 K and 5 mbar for 24 h. A detailed step by step description of the electrode preparation can be found in Ref.<sup>206</sup>

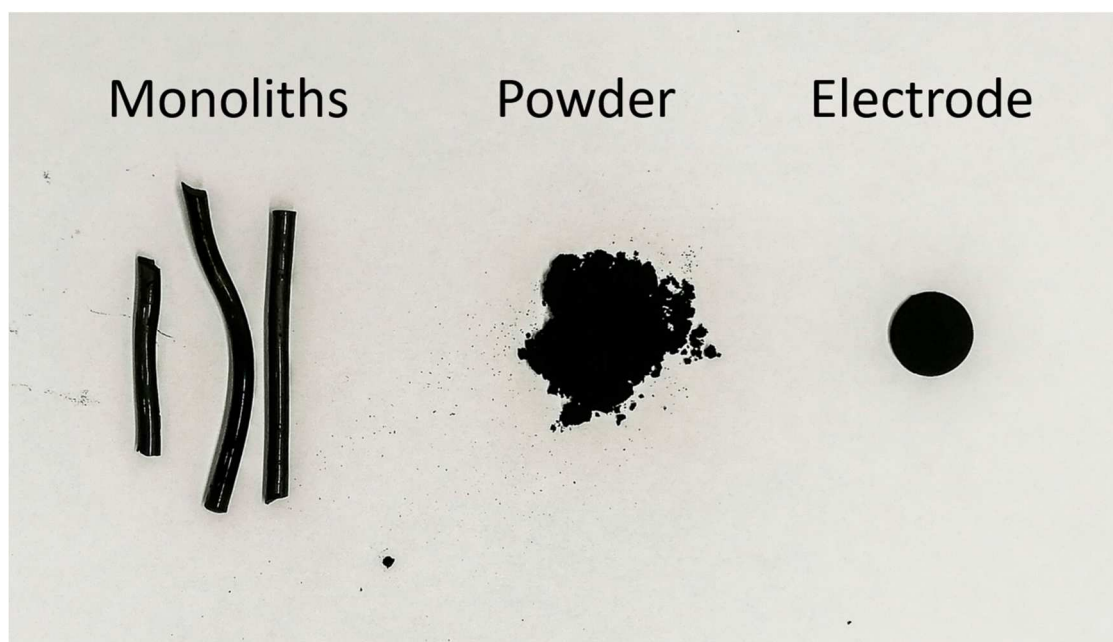


Figure 3.1: Photograph of the as synthesized monoliths, the powder and the ready to use electrode containing 10 mass% PTFE

### 3.2 Cell setups

In this thesis, two different two-electrode cells were used: one for the ex situ electrochemical characterization and one for in situ small-angle X-ray scattering experiments. A picture of the two cells and a schematic representation of their

setup is shown in Figure 3.2. The cell for electrochemical characterization (Figure 3.2a and Figure 3.2b) was used in two different setups: a symmetric two-electrode setup (or full cell setup) and an asymmetric two-electrode setup using an oversized counter electrode as a quasi-reference (half-cell setup). The cell has a polyether ether ketone (PEEK) housing and two titanium pistons connected to brass electrical contacts. It is custom made and similar to the one described in Ref.<sup>207</sup> The spring-loaded pistons guarantee a similar force on the operating supercapacitor cell for each experiment. The in situ cell is specially designed to perform in situ small angle X-ray scattering experiments. It is optimized for an asymmetric two-electrode setup with an oversized CE as quasi reference.

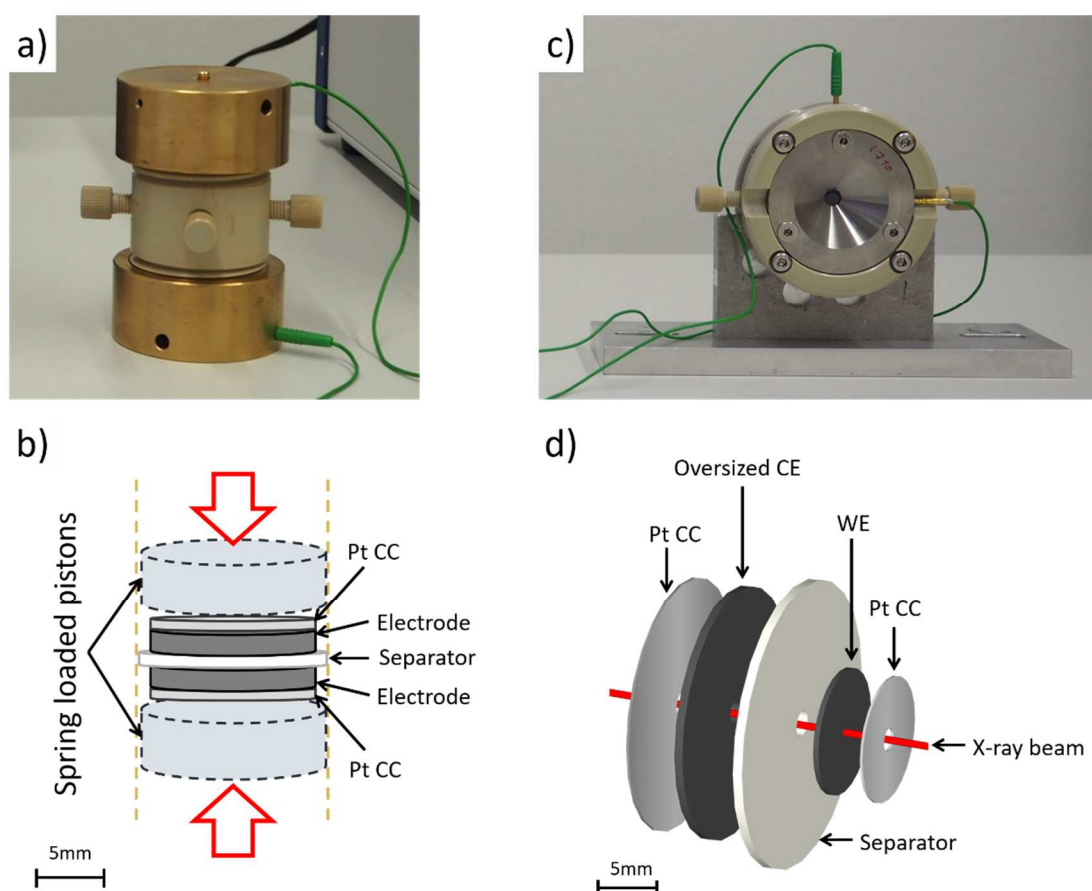


Figure 3.2: Photograph (a) and schematic setup (b) of the cell used for electrochemical characterization. The spring-loaded pistons guarantee a constant pressure for all experiments. Photograph (c) and schematic setup (d) of the cell used for the in situ small-angle X-ray scattering experiments (in situ cell). A reference electrode cannot be used in this cell. Therefore, an oversized CE has been used as a quasi-reference for all measurements. (d) Reproduced with permission from Ref.<sup>20</sup> Published by The Royal Society of Chemistry



The actual cell setup is shown in Figure 3.2c and Figure 3.2d. For in situ scattering experiments it is necessary that each component, except the WE, has a hole in it. This is necessary to guarantee that only the WE is irradiated during the experiment. Without these holes, the recorded signal would be a sum of both electrodes and the separator. Changes in the signal can therefore not be associated with the working electrode, which makes data interpretation impossible since both electrodes are at different potentials.

### 3.3 Measurement setup for electrochemical testing

Electrochemical testing was performed using a Reference 600 potentiostat (Gamry) and a custom-built cell (Figure 3.2).

The symmetric cell setup used in this thesis consists of two equally sized electrodes made from the same material (10 mm diameter,  $300\pm 20$   $\mu\text{m}$  thick) separated by a glass filter (Whatman GF/A) and electrically connected via platinum current collectors.

The asymmetric setup contains two platinum CC, a working electrode, a glass filter separator, and an oversized counter electrode. The oversized ( $\sim 8$  times) CE was used quasi-reference<sup>53</sup> and made from a commercial activated carbon (YP80F, Kuraray Chemical Co) with a reduced amount of PTFE binder (5 mass%). The WE for all investigated samples had a diameter of 6 mm and a thickness of  $300\pm 20$   $\mu\text{m}$ .

### 3.4 In situ SAXS setup

In situ SAXS measurements (discussed in Chapter 5) were performed at the Austrian SAXS beamline at the synchrotron radiation facility Elettra in Trieste (Figure 3.3).<sup>208</sup> A monochromatic X-ray beam with a wavelength of 0.077 nm was used. SAXS data were recorded with a Pilatus3 1M (Dectris) area detector. The transmitted intensity was determined with an X-ray sensitive photodiode mounted on the beamstop in front of the detector. The supercapacitor cell was built inside the custom-made housing shown in Figure 3.2b. The hole through all layers, except the working electrode, had a diameter of 3 mm. The size of the X-ray beam was  $\sim 1$  mm. While applying cyclic voltammetry at different scan rates (1  $\text{mV s}^{-1}$  to 20  $\text{mV s}^{-1}$ ), 2D SAXS patterns as well as corresponding transmission values were continuously recorded every 5 s.

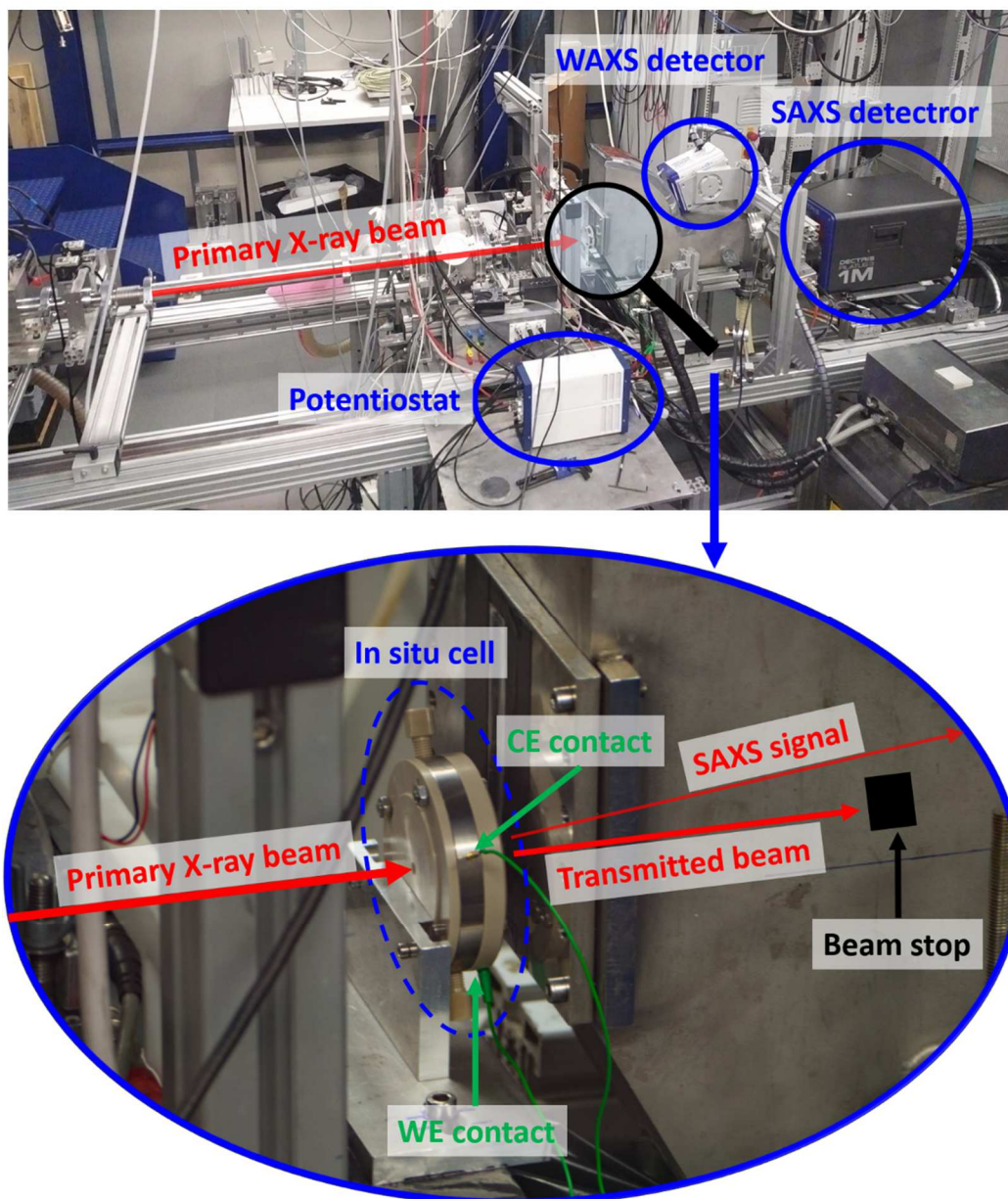


Figure 3.3: Picture of the in situ SAXS measurement setup at the Austrian SAXS beamline at Elettra (Trieste, Italy).

### 3.5 In situ ASAXS setup

ASAXS measurements were performed at the ID02 beamline at the European Synchrotron Radiation Facility (ESRF) in Grenoble, France.<sup>209</sup> 2D SAXS pattern were recorded with a Rayonix MX170 detector. A photodiode mounted on the beamstop in front of the detector was used to measure the X-ray transmission

during the scattering experiments. Chronoamperometry measurements were performed at 0 V and  $\pm 0.6$  V, using a Reference 600 Potentiostat (Gamry). 2D Scattering patterns were recorded at four different energies near the absorption edges of Br ( $E=13474$  eV) and Rb ( $E=15200$  eV) for each applied voltage after an equilibration time of approximately 2000 s after each voltage step. After correcting the data for detector specific imperfections (dark image, flat field, distortion), the 2D scattering patterns were normalized to the spherical angle, normalized to the recorded transmitted intensity and azimuthally averaged.<sup>209,210</sup> The energy depending efficiency of the detector was taken into account by normalizing the measured intensity to the scattering intensity of an energy independent standard sample (glassy carbon). In addition to the ASAXS/chronoamperometry experiments, a combination of cyclic voltammetry and fluorescence measurements was performed with an additional VORTEX-EX90 (Hitachi) fluorescence detector was mounted. In Figure 3.4 the setup for the fluorescence experiment is shown.

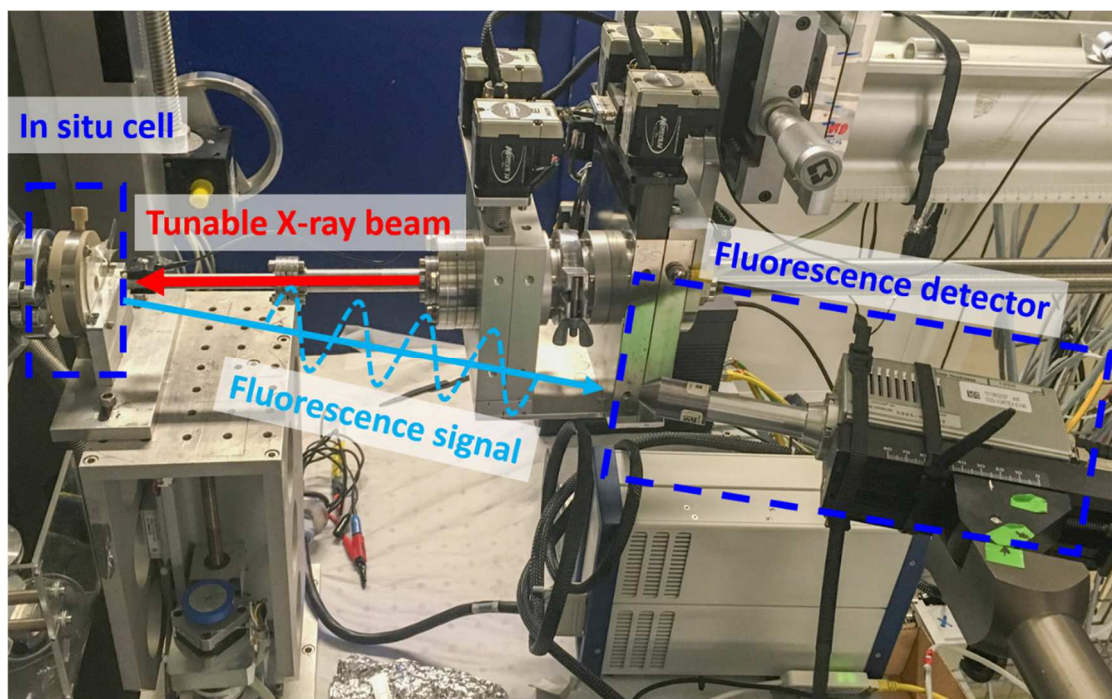


Figure 3.4: Measurement setup for fluorescence measurements

The cell design prevents the usual setup for fluorescence measurements where the fluorescence detector is placed facing the sample in  $90^\circ$  to the incoming X-ray beam. Therefore, the detector was mounted behind the cell. It is important that the fluorescence detector has a free line of sight to the point where the fluorescence signal originates (place where the X-ray beam hits the sample). To guarantee an

ideal fluorescence measurement it is necessary to minimize the shadow produced by the housing. (Figure 3.5).

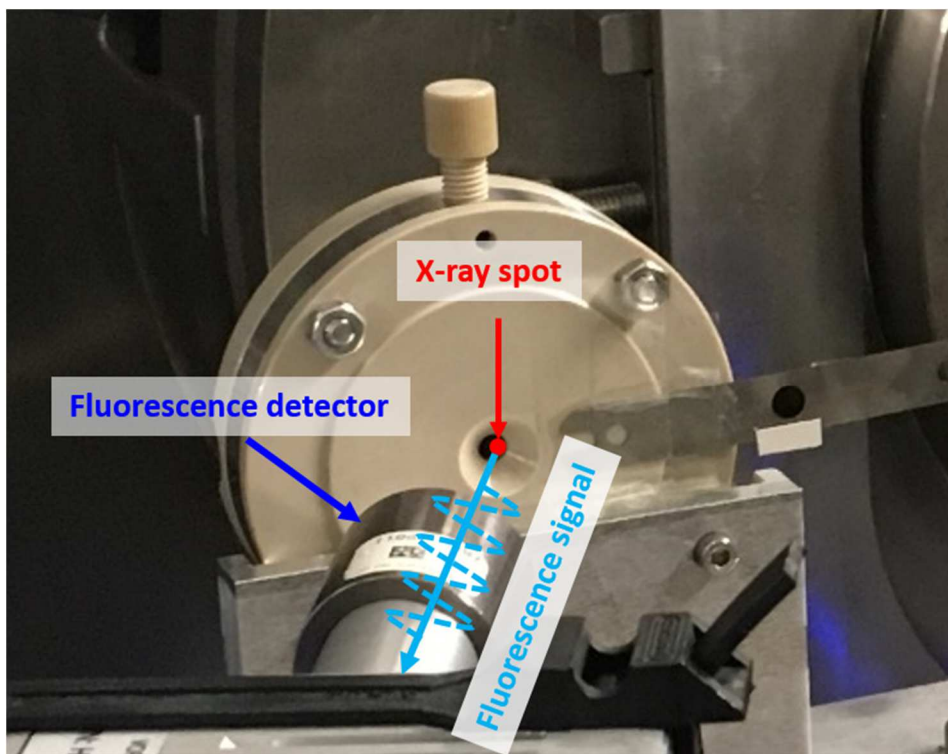


Figure 3.5: Detail of the backside of the in situ supercapacitor cell. The red spot indicates where the X-ray beam hits the electrode, which is the origin of the fluorescence signal.

It has to be mentioned the experimental setup was not optimized for fluorescence measurements and the fluorescence detector was not synchronized with the X-ray detector or the beamline shutter. Therefore, the normalization of the fluorescence signal to the intensity of the primary X-ray beam could not be done easily. As a result, the use of the data obtained from the fluorescence measurements was limited and could not be used to determine the fluorescence background during the ASAXS experiment.

### 3.6 Materials used

For this thesis three different material types were used: nanocast (hard-templated) and soft-templated ordered mesoporous carbon as well as a commercial activated carbon (YP80F, Kuraray Chemical. Co, Japan). The synthesis of the ordered mesoporous carbon materials is described in detail in Ref.<sup>199</sup> Table 3.1 lists all the samples used in this thesis.

Table 3.1: Samples used in this thesis. Values obtained from electrodes containing 10 mass% PTFE binder

Sample	Activation time (h)	$V_{\text{micro}}^{(a)}$ ( $\text{cm}^3 \text{g}^{-1}$ )	$V_{\text{meso}}^{(a)}$ ( $\text{cm}^3 \text{g}^{-1}$ )	S ( $\text{m}^2 \text{g}^{-1}$ )	$d_{50}$ ( $d_{25}$ - $d_{75}$ ) <sup>(b)</sup> (nm)	C <sup>(c)</sup> ( $\text{F g}^{-1}$ )
NCC 0.0	0.0	0.20	0.35	558 <sup>(d)</sup>	2.44 (1.61-3.99)	53
NCC 0.5	0.5	0.25	0.48	744 <sup>(d)</sup>	2.54 (1.67-3.91)	82
NCC 2.0	2.0	0.35	0.55	1072 <sup>(d)</sup>	2.40 (1.24-3.40)	92
NCC 4.0	4.0	0.46	0.70	1364 <sup>(d)</sup>	2.44 (1.21-3.50)	109
STC 0.0	0.0	0.12	0.07	369 <sup>(d)</sup>	1.19 (0.57-2.70)	52
STC 0.5	0.5	0.25	0.08	809 <sup>(d)</sup>	0.62 (0.55-2.00)	69
STC 2.0	2.0	0.43	0.14	1247 <sup>(d)</sup>	0.88 (0.60-2.10)	87
STC 4.0	4.0	0.85	0.26	1837 <sup>(d)</sup>	1.34 (0.90-2.00)	126
STC_NC 0.0*	0.0	-	-	148 <sup>(e)</sup>	-	4
STC_NC 0.5*	0.5	-	-	721 <sup>(e)</sup>	-	31
STC_NC 2.0*	2.0	-	-	1040 <sup>(e)</sup>	-	81
NCC_ISS	0.0	0.19	0.29	742 <sup>(f)</sup>	2.50 (0.85-3.00)	56
NCC_ISS A	1.0	0.29	0.30	991 <sup>(f)</sup>	2.05 (0.75-2.85)	68
NCC_ISAS*	2.0	0.45	0.58	1155 <sup>(g)</sup>	2.40 (1.26-3.00)	95
YP80F	unknown	0.67	0.21	1392 <sup>(d)</sup>	1.55 (0.93-2.00)	92

\* Values (except capacitance) measured from powder samples instead of electrodes

<sup>(a)</sup> Specific pore volume  $V_P$ , specific micropore volume  $V_{\text{micro}}$  (pore size < 2 nm), specific mesopore volume  $V_{\text{meso}}$  (2 nm  $\leq$  pore size < 50 nm)

<sup>(b)</sup> Volume-weighted median of the pore size  $d_{50}$  including the 25<sup>th</sup> and 75<sup>th</sup> percentile of the pore width ( $d_{25}$  and  $d_{75}$ )<sup>186</sup>

<sup>(c)</sup> Specific capacitance measured in an asymmetric cell setup with an oversized activated carbon electrode using 1M CsCl aqueous electrolyte and a scan rate of 1 mV s<sup>-1</sup>

<sup>(d)</sup> Specific surface area calculated from carbon dioxide (at 273 K) and nitrogen (at 77 K) isotherms using HS-NLDFT

<sup>(e)</sup> Specific surface area calculated from nitrogen (at 77 K) isotherms using the BET method

<sup>(f)</sup> Specific surface area calculated from carbon dioxide (at 273 K) and nitrogen (at 77 K) isotherms using QS-NLDFT

<sup>(g)</sup> Specific surface area calculated from nitrogen (at 77 K) isotherms using NLDFT

## 4 Influence of the pore structure on the rate handling capability

In the following three chapters, the results of the electrochemical performance evaluation and in situ scattering experiments are presented.

In this chapter, two hierarchically ordered carbon materials with an inverse mesopore structure are investigated. They are either composed of hexagonally packed nanofibers or cylindrical nanopores arranged on a hexagonal lattice. Both materials are available with different micropore contents as a result of different CO<sub>2</sub> activation treatments. The influence of the pore structure on the capacitance for elevated charging and discharging rates (rate handling capability) was investigated. Large parts of Chapter 4 have already been published in Ref.<sup>142</sup>

### 4.1 Motivation

The capacitance of EDLCs is directly related to the specific surface area of the electrodes. It is well known, that besides the SSA also other parameters crucially influence the performance of a supercapacitor device, such as the size dispersity, tortuosity and the shape of the pores.<sup>186,211</sup> Since EDLCs are often used for applications where high charging and discharging rates are required, global ion transport kinetics between the electrodes and local redistribution within the nanopores of the electrodes also have to be taken into account. While very small and strongly entangled micropores are believed to be advantageous for high capacitance, the optimum pore geometry for improved ion kinetics may look entirely different. In terms of high power density, carbon electrodes containing just ultramicropores (i.e. pores < 0.7 nm)<sup>115</sup> could be disadvantageous due to pore blocking and long diffusion pathways. Theoretical studies have shown that in very narrow pores complex mechanisms may influence the interplay between counterion adsorption and co-ion repulsion.<sup>212</sup> Recent experiments with purely microporous carbons have demonstrated that even at very slow rates the ionic charging shows a non-equilibrium behavior and that the cell design itself, as well as the ion mobility and concentration can significantly influence the charge storage mechanism.<sup>21</sup>

Different types of carbon materials with hierarchical porosity were investigated in terms of their ability to handle high charging and discharging rates. These

materials not only show promising rate handling capability but also high specific capacitance.<sup>183,191,213-215</sup> The basic idea of using hierarchical macro-meso-microporous carbons is that the long-range transport of the ions proceeds via macro- and mesopores, while the charge is predominantly stored within micropores and ultramicropores, which are closely connected to the mesopores. In this way, small micropores with a high degree of geometric confinement would be responsible for a high energy density by efficiently screening the counterion charge,<sup>34,173</sup> and macro- and mesopores would provide “ion-highways” for the fast and efficient transport of ions towards and away from the micropores. Although there is recent experimental evidence that very subtle “solvent dilution effects” may in some cases hamper this concept,<sup>216</sup> it is widely accepted that pore hierarchy should be generally beneficial for faster ion transport in EDLCs.

To further analyze this concept, two hierarchically porous carbon materials were investigated, with structural features on the mesopore length scale that can be described as an inverse replication of each other, i.e. hexagonally packed nanofibers versus cylindrical mesopores arranged on a 2D hexagonal lattice. Both samples exhibit a hierarchical macro/meso/microporous structure with the macroporosity being formed by a network of struts in the micrometer range. In addition, both samples were subjected to different CO<sub>2</sub> activation treatments with the goal to create a similar micropore size distribution and arrangement. The first material is based on a soft templating route (soft templated carbon, STC) following the approach by Hasegawa et al.,<sup>177</sup> which results in cylindrical mesopores with narrow diameter distribution arranged on a 2D hexagonal lattice. This material resembles closely the well-known silica based SBA-15 material.<sup>184</sup> The second material is based on a hard templating route applying a hierarchically porous monolithic silica material comprising 2D hexagonally arranged mesopores as the mold.<sup>192,193</sup> Casting of the cylindrical mesopores of this mold results in a monolithic structure with a cellular macroporous network build-up of hexagonally ordered carbon nanofibers (nanocast carbon, NCC), leaving mesopores where the silica walls in the mold used to be. Similar types of mesoporous carbon was first synthesized in form of a powder by Jun et al.<sup>189</sup> and are known as CMK-3 type material. Consequently, the two carbon materials investigated in this chapter exhibit an inverted mesopore structure, namely isolated cylindrical mesopores in the STC and a three-dimensional interconnected network of elongated mesopores between the carbon nanofibers in the NCC materials with a strongly different tortuosity due to the high aspect ratio (see Figure 4.1).

In this chapter, a thorough structural analysis of the STC and NCC materials by electron microscopy, gas adsorption analysis and X-ray scattering techniques is provided. Simon Rumswinkel (University of Salzburg, Austria) performed the synthesis of the materials, electron microscopy and gas adsorption analysis.

Cyclic voltammetry and electrochemical impedance spectroscopy on electrodes soaked with 1M CsCl aqueous electrolyte was conducted in order to determine relevant electrochemical performance parameters, such as the specific capacitance and the rate handling capability of the two materials. A detailed comparison with a purely microporous activated carbon reference sample is also given.

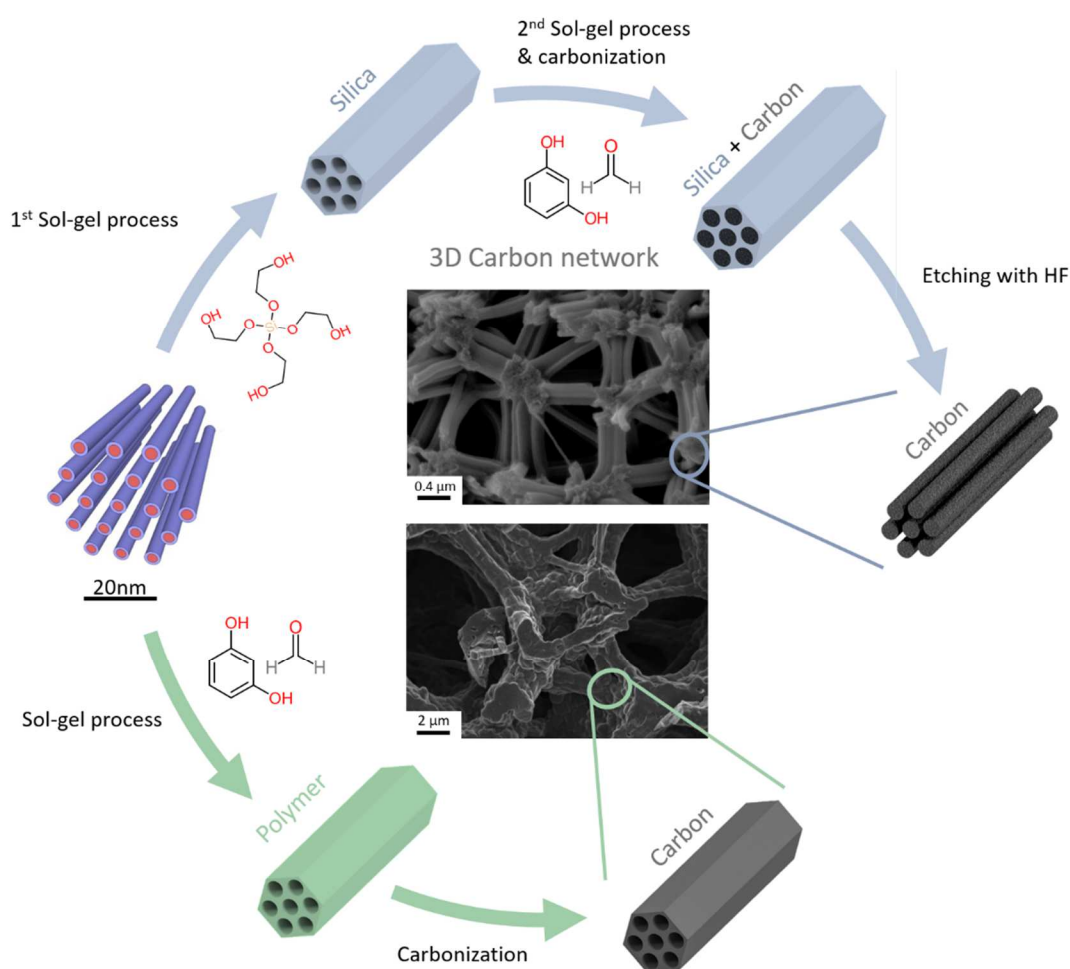


Figure 4.1: Schematic representation of the two different synthesis routes to obtain hierarchically structured monolithic carbons. In the middle a SEM image of the NCC and STC sample is given. Upper route: nanocasting approach (NCC). Lower route: soft-templating route (STC). Reprinted with permission from Ref.<sup>142</sup> Copyright 2019 American Chemical Society



## 4.2 Structural analysis

### 4.2.1 Sample preparation and measurement techniques

**Materials:** Simon Rumswinkel (University of Salzburg, Austria) synthesized the STC and NCC materials. The synthesis route is described schematically in Figure 4.1, and in more detail in Ref.<sup>142</sup> The reference material is a purely microporous activated carbon (YP80F) and is a commercial product (Kuraray Chemical Co., Japan).

**Gas adsorption analysis:** Gas adsorption measurements of the pure carbon material and the electrodes were done by Simon Rumswinkel and Miralem Salihovic (University of Salzburg, Austria) using N<sub>2</sub> and CO<sub>2</sub> in a Micromeritics ASAP 2420 device. Data analysis was done with the built-in software package using the HS-NLDFT model for carbon slit pores with surface roughness at 77 K for N<sub>2</sub>-data<sup>119</sup> and the NLDFT model for carbon at 273 K with CO<sub>2</sub>.

**Small-angle X-ray scattering:** SAXS experiments were performed on electrodes containing 10 mass% of PTFE binder. The electrodes have a well-defined thickness leading to the same irradiated volume for all samples. SAXS measurements were performed at the Austrian SAXS beamline at the synchrotron radiation facility Elettra in Trieste,<sup>208</sup> employing a monochromatic X-ray beam with a wavelength  $\lambda = 0.077$  nm. The SAXS patterns were recorded with a Pilatus3 1M (Dectris) area detector. The transmitted X-ray beam intensity, as well as the intensity of the primary beam, were recorded using a photodiode mounted on the beam-stop in front of the detector, and an ionization chamber in front of the sample, respectively. The 2D SAXS images were azimuthally integrated using the software package Fit2D,<sup>217</sup> leading to the scattered intensity as a function of the scattering vector  $q$  (see Chapter 2.5). The intensity of each of the resulting scattering curves was normalized to the corresponding transmission value.

**X-ray diffraction:** X-ray diffraction (XRD) measurements were performed with a D8 Advance Eco (Bruker AXS) using a Cu-K X-ray tube ( $\lambda = 0.154$  nm) and an energy sensitive detector (LYNXEYE-XE). The angular range ( $2\theta$ ) was 5 – 100° using a step size of 0.05° and an exposure time of 10 s/step. All measurements were performed on electrodes containing 10 mass% of PTFE binder on a zero background sample holder (Sil'tronix Silicon Technologies).

### 4.2.2 Structural analysis: results

The synthesis routes shown in Figure 4.1 result in two types of carbon materials with inverted mesopore structures. Both, NCC and STC can be prepared as monoliths (Figure 4.2a and Figure 4.2d) and show a similar morphology on the micrometer scale with a cellular macroporous network of carbon struts (Figure 4.2b and Figure 4.2e). It should be note however that the size of the structures in the STC material is noticeably larger. It was found that synthetic parameters, such as temperature differences in the sample during gelation as well as concentration inhomogeneities have a strong impact on the phase separation process. In addition, a strong syneresis during aging was observed, resulting in structural differences in the core of the samples in comparison to the external surface. This inherently causes a quite heterogeneous macropore morphology over the cross section of the monoliths, ranging from  $\sim 1.5$  to 5 times the size observed in the NCC material. Therefore, further processing of the material to electrodes as a powder was advantageous since inhomogeneities are averaged.

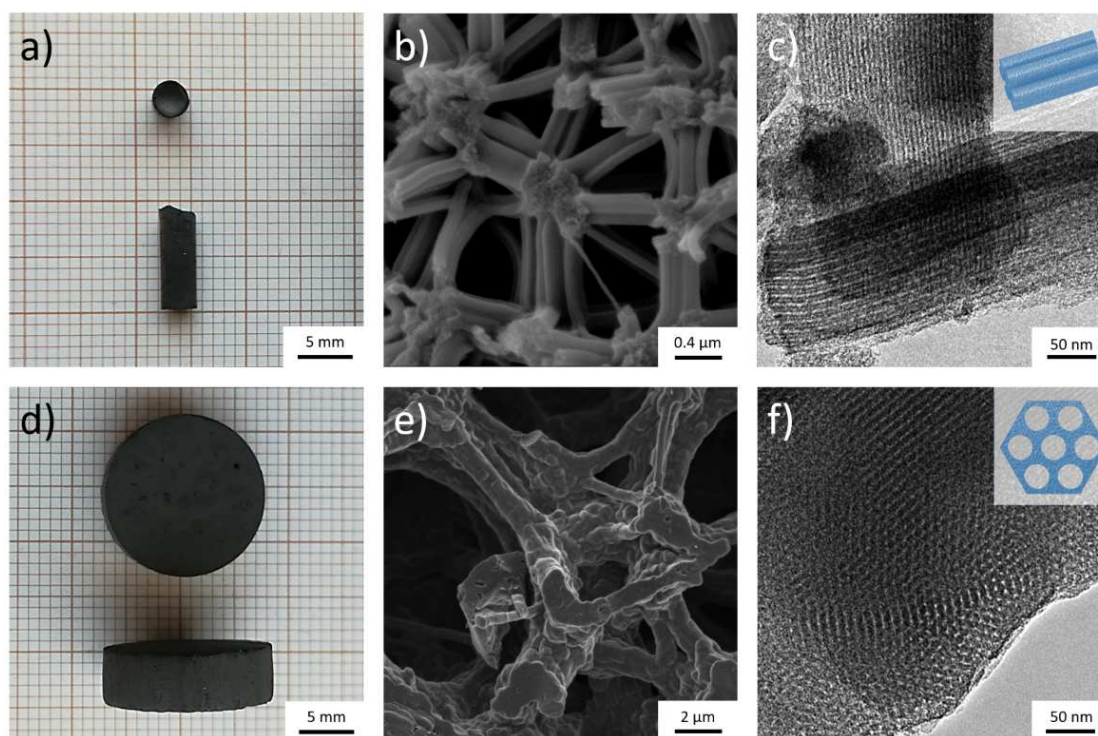


Figure 4.2: Representation of the different levels of hierarchy of NCC (upper row) and STC (lower row) materials, shown by photographs of the monoliths (a,d), SEM images of the macroporous strut network (b,e) and TEM images of the ordered mesopore structure (c,f). Reprinted with permission from Ref.<sup>142</sup> Copyright 2019 American Chemical Society

For the nanocast materials the struts consist of 2D-hexagonally arranged carbon nanorods, with mesopores in between the nanorods, as schematically shown in Figure 4.2c. The rods themselves contain micropores, with their amount depending on the activation time. The STC material features 2D hexagonally ordered cylindrical mesopores aligned along the long axis of the approximately 4  $\mu\text{m}$  long carbon struts (Figure 4.1 and Figure 4.2f). Again, the carbon mesopore walls contain micropores as a consequence of the carbonization and activation process. The data for the structural characterization from GSA are given for the electrode samples in Table 4.1.

Table 4.1: Sample properties derived from gas adsorption analysis of the electrodes containing 10 mass% PTFE binder.

Sample	Activation time <sup>(a)</sup> (h)	$V_P$ <sup>(a)</sup> ( $\text{cm}^3 \text{g}^{-1}$ )	$V_{\text{micro}}$ <sup>(a)</sup> ( $\text{cm}^3 \text{g}^{-1}$ )	$V_{\text{meso}}$ <sup>(a)</sup> ( $\text{cm}^3 \text{g}^{-1}$ )	$S_{\text{DFT}}$ <sup>(b)</sup> ( $\text{m}^2 \text{g}^{-1}$ )	$d_{50}$ ( $d_{25}$ - $d_{75}$ ) <sup>(c)</sup> (nm)
NCC 0.0	0.0	0.55	0.20	0.35	558	2.44 (1.61-3.99)
NCC 0.5	0.5	0.73	0.25	0.48	744	2.54 (1.67-3.91)
NCC 2.0	2.0	0.90	0.35	0.55	1072	2.40 (1.24-3.40)
NCC 4.0	4.0	1.16	0.46	0.7	1364	2.44 (1.21-3.50)
STC 0.0	0.0	0.19	0.12	0.07	369	1.19 (0.57-2.70)
STC 0.5	0.5	0.33	0.25	0.08	809	0.62 (0.55-2.00)
STC 2.0	2.0	0.57	0.43	0.14	1247	0.88 (0.60-2.10)
STC 4.0	4.0	1.11	0.85	0.26	1837	1.34 (0.90-2.00)
YP80F	not known	0.88	0.67	0.21	1392	1.55 (0.93-2.00)

<sup>(a)</sup>  $\text{CO}_2$  activation was performed at 925°C

<sup>(b)</sup> Specific pore volume  $V_P$ , specific micropore volume  $V_{\text{micro}}$  (pore size < 2 nm), specific mesopore volume  $V_{\text{meso}}$  (2 nm  $\leq$  pore size < 50 nm)

<sup>(c)</sup> Specific surface area  $S_{\text{DFT}}$  obtained from gas adsorption analysis via DFT calculations for electrodes with different activation times.

<sup>(d)</sup> Volume-weighted median of the pore size  $d_{50}$  (see Figure 4.4) including the 25<sup>th</sup> and 75<sup>th</sup> percentile of the pore width ( $d_{25}$  and  $d_{75}$ )<sup>186</sup>, see Figure 4.4a and Figure 4.4b.

Adsorption isotherms for carbon dioxide and nitrogen are shown for NCC and STC electrodes in Figure 4.3. The nitrogen adsorption isotherms of the NCC electrodes (Figure 4.3c) show the well-known characteristics of CMK-3 type micro-mesoporous carbons.<sup>117</sup> In contrast, the isotherms of the STC electrodes (Figure 4.3d) show a different shape, suggesting that these materials are mainly microporous. However, there is also a slight indication of a capillary condensation

event around  $p/p_0 = 0.5$ , which becomes more pronounced for increasing activation time, providing evidence for the presence of mesopores.

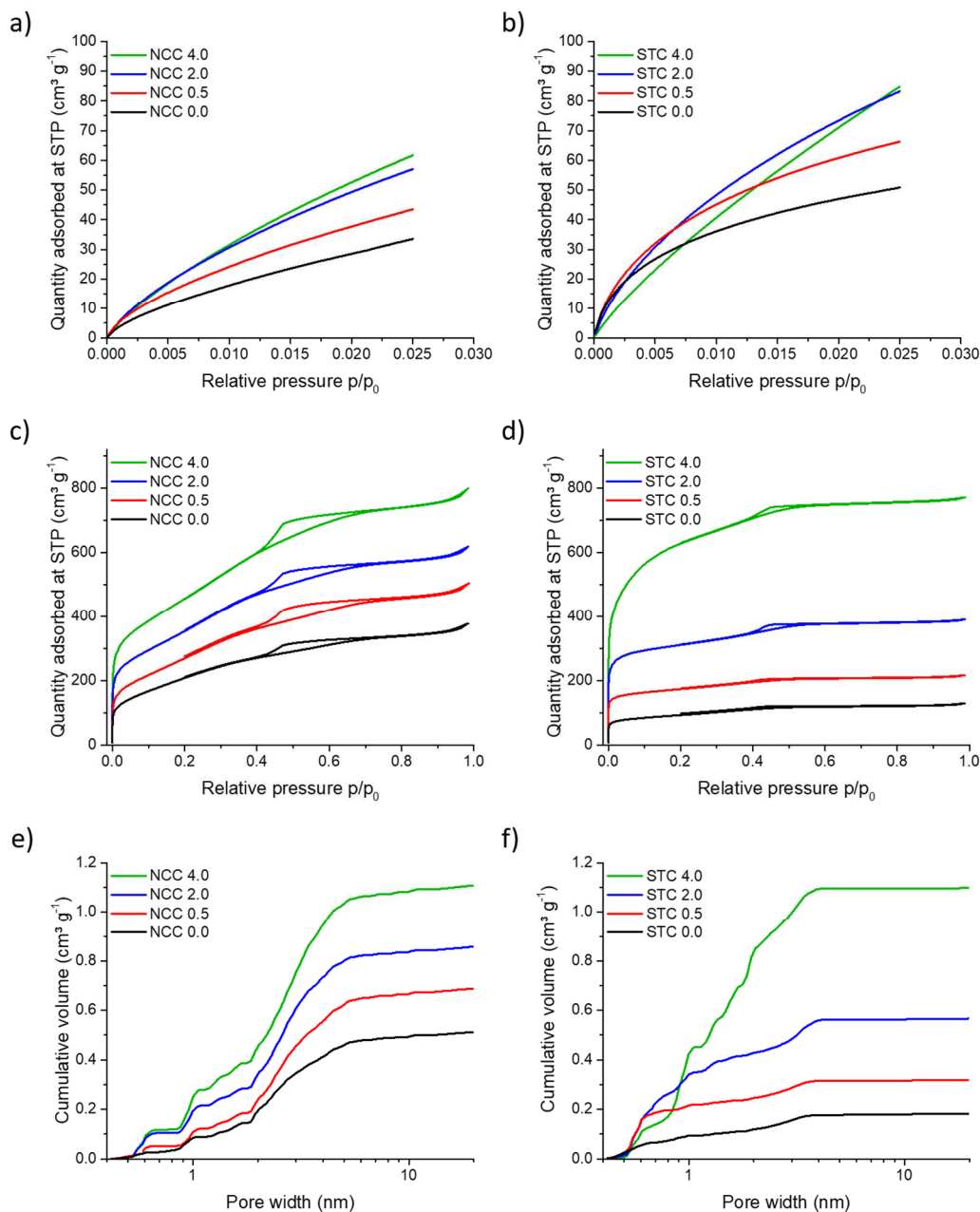


Figure 4.3: Carbon dioxide isotherms at 273 K from the NCC (a) and STC (b) electrodes containing 10 mass% PTFE binder. Nitrogen adsorption isotherms for the same NCC (c) and STC (d) electrodes recorded at 77 K. Cumulative pore volume as a function of the pore size calculated from carbon dioxide at 273 K (up to  $\sim 0.6$  nm) and nitrogen at 77 K (above  $\sim 0.6$  nm) adsorption isotherms for NCC (e) and STC (f) electrodes. Reprinted with permission from Ref.<sup>142</sup> Copyright 2019 American Chemical Society

Both types of samples show a clear increase in specific pore volume and specific surface area for increasing CO<sub>2</sub> activation time. The cumulative pore size distributions calculated from the nitrogen adsorption isotherms (Figure 4.3c and Figure 4.3d) and carbon dioxide adsorption isotherms (Figure 4.3a and Figure 4.3b) using NLDFIT<sup>119</sup> are shown in Figure 4.3e and Figure 4.3f, and the structural parameters are summarized in Table 4.1.

Obviously, all samples contain a substantial amount of micropores, even when no activation was performed (37% and 63% of the pore volume for NCC and STC, respectively, see Table 4.1). Activation treatment increases both, the specific pore volume and surface area moderately for the NCC materials, and strongly for the STC materials. The volume-weighted median of the pore size (Table 4.1) stays nearly constant for the NCC samples with most of the total pore volume being contributed by pores between 2 nm and 5 nm in width. In contrast, for all the STC samples most of the pore volume consists of micropores (< 2 nm). With increasing activation an initial increase in ultra-microporosity in STC is followed by pore widening leading to an increase of the median pore size  $d_{50}$  for the longest duration of activation the treatments (Figure 4.4).

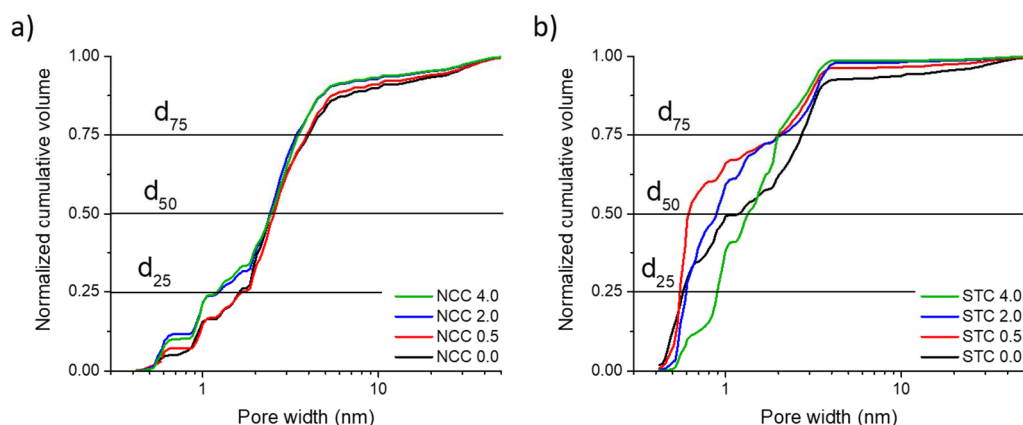


Figure 4.4: Normalized cumulative pore size distribution for NCC (a) and STC (b) electrodes calculated from carbon dioxide at 273 K (up to  $\sim 0.6$  nm) and nitrogen at 77 K (above  $\sim 0.6$  nm) adsorption isotherms for NCC and STC electrodes containing 10 mass% PTFE binder. The horizontal lines determine the pore sizes  $d_{25}$ ,  $d_{50}$  and  $d_{75}$  listed in Table 4.1. Reprinted with permission from Ref.<sup>142</sup> Copyright 2019 American Chemical Society

Figure 4.5 shows the nitrogen adsorption isotherm and the normalized cumulative pore size distribution for the commercial activated carbon material (YP80F). This material shows the expected nearly purely microporous behavior and is therefore an ideal reference material.

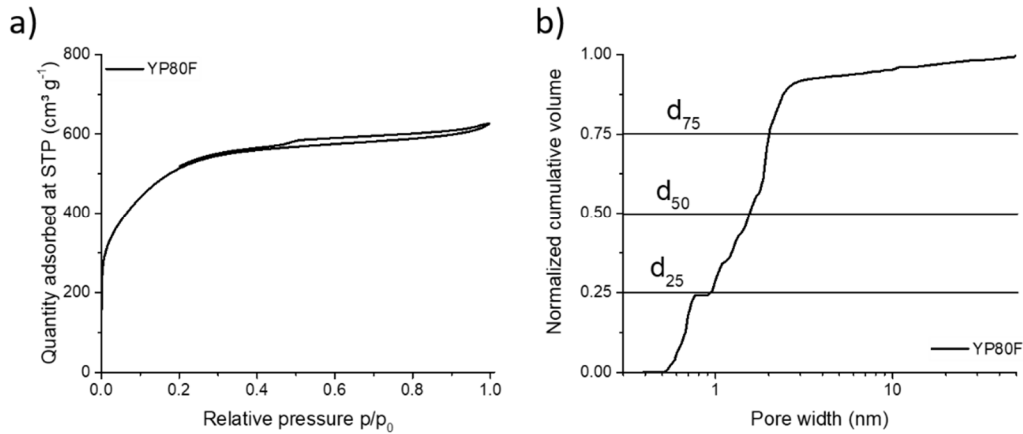


Figure 4.5: Nitrogen adsorption isotherms for YP80F electrode containing 10 mass% PTFE binder recorded at 77 K (a) and normalized cumulative pore size distribution for YP80F electrodes calculated from nitrogen adsorption (b). The horizontal lines determine the pore sizes  $d_{25}$ ,  $d_{50}$  and  $d_{75}$  listed in Table 4.1. Reprinted with permission from Ref.<sup>142</sup> Copyright 2019 American Chemical Society

Pore characteristics (specific surface area and specific pore volume) for the pure carbon materials deviate from the electrodes towards higher values (Table 4.2), which correlates with the absence of the nonporous binder.

Table 4.2: Sample properties derived from gas adsorption analysis of the pure carbon.

Sample	Activation time (h)	$V_P$ <sup>(a)</sup> ( $\text{cm}^3 \text{g}^{-1}$ )	$V_{\text{micro}}$ <sup>(a)</sup> ( $\text{cm}^3 \text{g}^{-1}$ )	$S_{\text{DFT}}$ <sup>(b)</sup> ( $\text{m}^2 \text{g}^{-1}$ )	$d_{50}$ ( $d_{25}$ - $d_{75}$ ) <sup>(c)</sup> (nm)
NCC 0.0 pure	0.0	0.67	0.27	759	2.30 (1.35-3.33)
NCC 0.5 pure	0.5	0.97	0.36	1167	2.39 (1.38-3.30)
NCC 2.0 pure	2.0	1.17	0.47	1502	2.35 (1.00-3.23)
NCC 4.0 pure	4.0	1.44	0.60	1748	2.29 (0.99-3.20)
STC 0.0 pure	0.0	0.22	0.14	408	0.85 (0.65-2.36)
STC 0.5 pure	0.5	0.40	0.30	989	0.62 (0.58-2.08)
STC 2.0 pure	2.0	0.74	0.55	1602	0.87 (0.63-2.00)
STC 4.0 pure	4.0	1.23	0.92	2103	1.31 (0.86-2.01)

<sup>(a)</sup> Specific pore volume  $V_P$ , specific micropore volume  $V_{\text{micro}}$  (pore size < 2 nm),

<sup>(b)</sup> Specific surface area  $S_{\text{DFT}}$  obtained from gas adsorption analysis via HS-NLDFT calculations from nitrogen adsorption isotherms

<sup>(c)</sup> Volume-weighted median of the pore size  $d_{50}$  (see Figure 4.4 and Figure 4.5b) including the 25<sup>th</sup> and 75<sup>th</sup> percentile of the pore width ( $d_{25}$  and  $d_{75}$ )<sup>186</sup>

The reduced surface area of the electrode compared to the pure carbon is expected because of the included nonporous binder (~10 mass%) in the electrode. The fiber morphology of the used PTFE binder (Figure 2.45) is not expected to cause extensive pore blocking, similar to YP80F using 10 mass% of PTFE binder.<sup>20</sup> Nevertheless, the SSA reduction of the electrodes compared to the pure carbon exceeds the expected 10%, leading to the assumption that some pores are blocked by the binder phase.

From GSA it is known that the micropore structure is strongly influenced by the CO<sub>2</sub> activation treatment for both sample types. The macropore system on the other hand is left unchanged, even for the longest activation time (Figure 4.6).

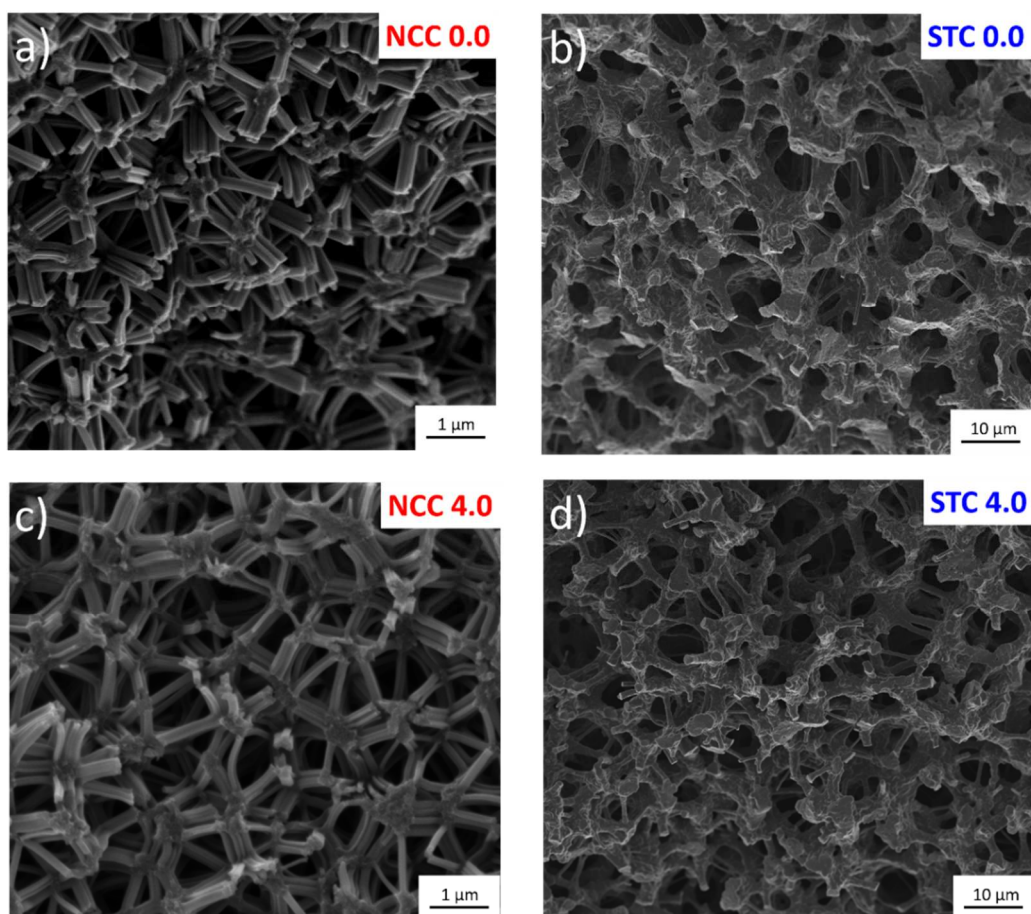


Figure 4.6: SEM images of the not-activated NCC (a) and STC (b) materials, as well as the four hours activated NCC (c) and STC (d) samples. The activation process does not change the macroporosity of the material for either the STC or NCC materials. Even after four hours of CO<sub>2</sub> treatment, no change of the macropore structure can be seen. Reprinted with permission from Ref.<sup>142</sup> Copyright 2019 American Chemical Society

The XRD measurements (Figure 4.7b and Figure 4.7d) reveal the well-known structure expected for a carbon material prepared from a “hard carbon” precursor

such as resorcinol/formaldehyde. It is characterized by “turbostratic” stacking of graphene sheets,<sup>218</sup> leading to in-plane reflections (hk) and to stacking reflections (00l). It can be observed that in particular the intensity and width of the (002) peak is strongly affected by the activation. This suggests that the activation preferentially reduces the number of turbostratic carbon sheets within a stack. The (10) peak, on the other hand, stays nearly unchanged even after a four hour CO<sub>2</sub> activation treatment. This indicates that the in-plane order of the graphene layers stays largely intact during activation. The width of the Bragg reflections from the atomic carbon structure (Figure 4.7b and Figure 4.7d) can be used to determine the average crystallite size  $L$  using the Scherrer equation,

$$L = K \frac{2\pi}{FWHM} \quad (4.1)$$

where  $FWHM$  is the full width at half maximum of the Bragg peak. After background subtraction using splines, the stacking height  $L_c$  and the in-plane size  $L_a$  were calculated using  $K = 0.91$  for  $L_c$  and  $K = 1.84$  for  $L_a$  (Table 4.3).<sup>219,220</sup>

Table 4.3: Structural parameters obtained from XRD.

Sample	$a^{(a)}$ (nm)	$c^{(a)}$ (nm)	$L_c^{(b)}$ (nm)	$L_a^{(b)}$ (nm)	$N^{(c)}$	$\rho_{\text{skel}}^{(d)}$ (g cm <sup>-3</sup> )
NCC 0.0	0.24	0.78	0.95	3.89	3.46	2.05
NCC 0.5	0.24	0.79	0.89	3.72	3.22	2.01
NCC 2.0	0.24	0.81	0.80	3.65	2.97	2.01
NCC 4.0	0.24	0.88	0.73	3.54	2.77	1.97
STC 0.0	0.24	0.77	0.89	3.55	3.27	2.04
STC 0.5	0.24	0.80	0.88	3.42	3.25	2.03
STC 2.0	0.24	0.81	0.87	3.26	3.13	1.95
STC 4.0 <sup>(e)</sup>	0.24	-	-	3.54	-	-

<sup>(a)</sup> In-plane and out-of-plane lattice parameters ( $a$  and  $c$ );

<sup>(b)</sup> Stacking height ( $L_c$ ), in plane crystallite size ( $L_a$ ) calculated using the the Scherrer equation

<sup>(c)</sup> Average number of graphene stacks ( $N$ )

<sup>(d)</sup> Carbon skeletal density ( $\rho_{\text{skel}}$ ) calculated from XRD measurements

<sup>(e)</sup> For STC 4.0 the stacking parameters  $c$  and  $L_c$  could not be reliably estimated from the XRD data because of the weak (002) reflection. Therefore, for the corresponding calculations of the skeletal density the value of STC 2.0 was used for the following calculations

From the position of the (002) peak the average layer distance  $d_{002} = 2\pi/q_{002}$  is calculated, and the average number of stacked graphene layers  $N = 1 + L_c/d_{002}$  is determined (Table 4.3). In addition the dimensions  $a$  and  $c$  of the “graphite-like” unit cell allow estimating the skeletal carbon density:



$$\rho_{skel} = \frac{8m_c}{\sqrt{3}ca^2} \quad (4.2)$$

with  $m_c$  being the mass of a single carbon atom. All parameters are listed in Table 4.3 and are in good agreement with values from literature.<sup>96,221</sup>

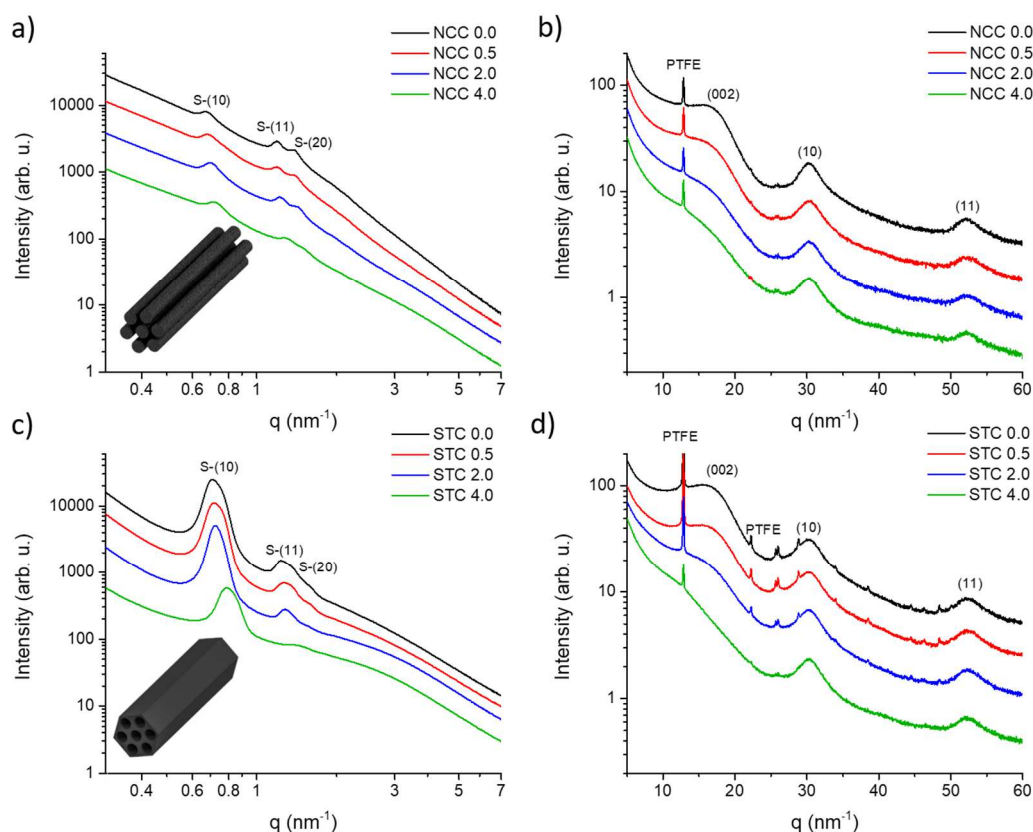


Figure 4.7: SAXS (left) and XRD (right) patterns of the NCC (a, b) and STC (c, d) electrodes for different CO<sub>2</sub> activation durations. The curves are shifted vertically for clarity. The Bragg peaks in the SAXS patterns arising from the hexagonal pore lattice are denoted by a prefix “S” in order to distinguish them from the Bragg peaks of the turbostratic carbon seen in XRD. The sharp peaks in the XRD patterns arise from the crystalline PTFE binder. Reprinted with permission from Ref.<sup>142</sup> Copyright 2019 American Chemical Society

It is shown in Table 4.3 that the activation process causes a reduction of the average number of graphene sheets from  $\sim 3.5$  to  $\sim 2.8$ , while the skeletal carbon density  $\rho_{skel}$  shows only minor changes with a tendency towards lower values. We note that the NCC and STC samples show similar changes in the atomic order with activation. This is not surprising, since both types of material are synthesized using the same precursor followed by identical heat-treatments.

From the TEM images (Figure 4.2c and Figure 4.2f) it is obvious that the samples have an ordered nanostructure. This is confirmed by the SAXS profiles (Figure 4.7a and Figure 4.7c), which show well-resolved Bragg reflections arising from the 2D hexagonal lattice of pores or fibers with lattice constant  $a_{meso}$ :

$$a_{meso} = \frac{2\pi}{q_{S-(10)}} \frac{2}{\sqrt{3}} \quad (4.3)$$

The most prominent change with activation is a shift of the position of the S-(10) peak to higher  $q$  values, which implies a reduction of the lattice spacing  $a_{meso}$  with activation (Table 4.4). This shift is more pronounced for the NCC samples. It is also quite small for short activation times and becomes obvious for the four hour activated samples. Apart from the Bragg peaks arising from the ordered mesopores/fibers, the SAXS patterns show additionally a significant diffuse scattering from the disordered micropores. This diffuse scattering shows clear differences between the NCC and the STC samples, and also exhibits changes with activation. For a better illustration, a so-called Kratky plot (Intensity $\cdot q^2$  vs.  $q$ ) of the SAXS data is shown in Figure 4.8, highlighting the differences in the diffuse “background” scattering between the two sample types as well as its changes during the activation process more clearly.

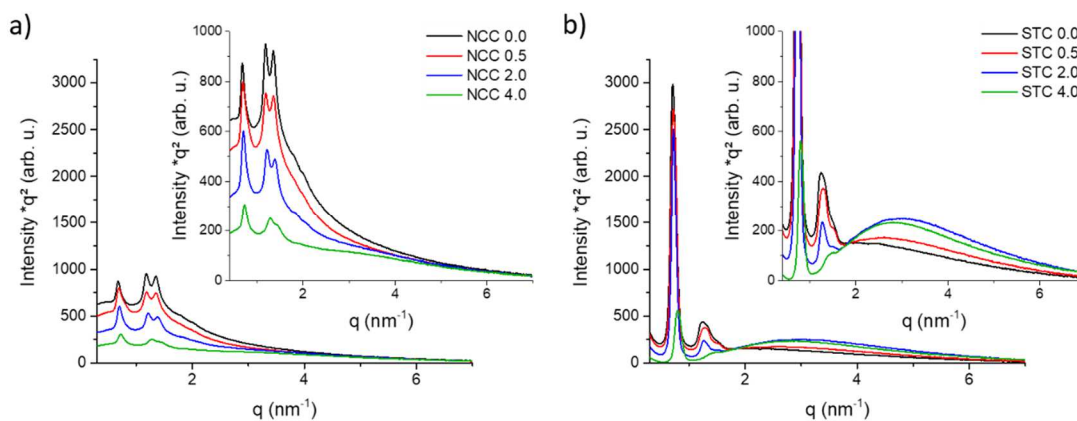


Figure 4.8: Kratky plot for NCC (a) and STC (b) materials after subtracting the constant background and the electron density fluctuation contribution. The insets show a magnification. Reprinted with permission from Ref.<sup>142</sup> Copyright 2019 American Chemical Society

While the Bragg peaks arise from the ordered mesopores, the diffuse scattering comes mainly from the (disordered) micropores. The diffuse scattering is mostly located directly below the Bragg peaks for the NCC samples. For the STC samples, it is clearly shifted to higher  $q$  values. This means that the STC samples contain

considerably smaller micropores as compared to the NCC material, which is fully consistent with the pore size distributions obtained from nitrogen adsorption (Figure 4.3e and Figure 4.3f).

Table 4.4: Structural parameters obtained from SAXS.

Sample	$a_{\text{meso}}$ <sup>(a)</sup> (nm)	$t$ <sup>(b)</sup> (nm)	$l_{\text{carbon}}$ <sup>(b)</sup> (nm)	$l_{\text{pore}}$ <sup>(b)</sup> (nm)	$\phi$ <sup>(c)</sup>	$\phi_{\text{micro}}$ <sup>(d)</sup>	$S_{\text{SAXS}}$ <sup>(e)</sup> (m <sup>2</sup> g <sup>-1</sup> )
NCC 0.0	10.01	1.40	2.65	2.99	0.53	0.29	736
NCC 0.5	9.95	1.34	2.24	3.30	0.60	0.33	884
NCC 2.0	9.93	1.07	1.65	2.99	0.64	0.41	1204
NCC 4.0	8.99	0.82	1.17	2.68	0.70	0.48	1730
STC 0.0	10.47	1.21	4.34	1.68	0.28	0.20	451
STC 0.5	10.11	0.98	2.46	1.63	0.40	0.34	800
STC 2.0	10.17	0.69	1.31	1.46	0.53	0.46	1561
STC 4.0	9.93	0.62	0.90	1.95	0.68	0.63	2276

<sup>(a)</sup> Lattice parameter of the 2D hexagonal pore lattice ( $a_{\text{meso}}$ ) calculated from the position of peak S-(10)

<sup>(b)</sup> Average chord length ( $t$ ) and average chord lengths of the carbon phase ( $l_{\text{carbon}}$ ) and the pore phase ( $l_{\text{pore}}$ ) calculated from integral SAXS parameters

<sup>(c)</sup> The porosity  $\phi$  is calculated from the specific pore volume (Table 4.1) and the skeletal density (Table 4.3) by  $\phi = \frac{\rho V_p}{1 + \rho V_p}$

<sup>(d)</sup> The microporosity  $\phi_{\text{micro}}$  is calculated from the specific micropore volume (Table 4.1) and the skeletal density (Table 4.3) by  $\phi_{\text{micro}} = \frac{\rho V_{\text{micro}}}{1 + \rho V_{\text{micro}}}$ ;

<sup>(e)</sup> The specific surface area ( $S_{\text{SAXS}}$ ) is calculated using Equation 4.4.

Generally, the SAXS patterns provide an independent and complementary approach to better understand the changes of the pore systems with activation by calculating average pore characteristics from integral SAXS parameters. Since the used NCC and STC samples deviate from the ideal behavior of a two-phase system with sharp edges, the evaluation of the SAXS data was performed following the approach in Refs.<sup>94,95,99</sup> Before calculating structural parameters from the SAXS data it is necessary to subtract the fluctuation contribution. From fitting Equation 2.46 to the measured scattering intensity in the  $q$  range from 5 nm<sup>-1</sup> to 7 nm<sup>-1</sup>,  $P$ ,  $B$  and  $C$  were obtained. The parameter  $l$  (Equation 2.45), which is also necessary to determine the intensity contribution of the electron density fluctuation, cannot be calculated directly from the fit. In Ref.<sup>95</sup> this parameter was chosen between the lowest value to appropriately fit the high  $q$ -range and the maximum value that does not exceed the measured total intensity. This procedure is not applicable here because the scattering contribution from the mesopores can mask the limiting value.<sup>94</sup> Therefore, the lateral correlation length

$l$ , was set equal to the average in-plane crystallite size  $L_a$  obtained from the width of the (10) peak in the XRD patterns. Using  $l = L_a$  it is now possible to calculate the fluctuation contribution (Equation 2.45) and subtract it from the measured SAXS curves together with the constant  $C$  obtained from the fit at large  $q$ . After the subtraction of the fluctuation term, it is possible to calculate the surface to volume ratio according to Equation 2.43. From dividing this value by the filling density  $\rho = (1 - \varphi)\rho_{skel}$  the specific surface area is calculated from integral SAXS parameters:

$$S_{SAXS} = \frac{\pi\varphi P}{\rho_{skel} \bar{I}} \quad (4.4)$$

with the skeletal density  $\rho_{skel}$  calculated from XRD, and the porosity  $\varphi$  calculated from the specific pore volume taken from the N<sub>2</sub> adsorption isotherms:

$$\varphi = \frac{\rho_{skel} V_p}{1 + \rho_{skel} V_p} \quad (4.5)$$

From the porosity  $\varphi$  and the average chord length  $t$  (Equation 2.47) and it is possible to calculate the average chord length of the carbon phase  $l_{carbon}$  and the pores  $l_{pore}$ .<sup>98</sup>

$$t = \varphi l_{carbon} = (1 - \varphi) l_{pore} \quad (4.6)$$

These quantities allow determining structural parameters without an assumption of the size and shape. Even though their absolute values are not directly comparable to, e.g., average pore sizes obtained from the evaluation of adsorption isotherms using specific assumptions about the pore shape, the general trends should be similar. The specific surface area  $S_{SAXS}$  is obtained without any a priori assumption about the shape of the pores. It just requires the knowledge of the skeletal carbon density derived from XRD (Table 4.3) and the specific pore volume from gas adsorption analysis (Table 4.1), both being very reliable quantities. The comparison confirms a similar trend and a fair quantitative agreement for the surface areas obtained from SAXS (Table 4.4) and DFT (Table 4.1).

In addition, from the integral SAXS parameters the average chord length  $t$  of the two-phase carbon-pore system was calculated (Equation 2.47). The mean chord length  $t$  is measure for the mean length of uninterrupted straight lines in one of the two phases (pore or carbon) averaged over all directions (Figure 2.19).<sup>82</sup> Table 4.4 shows that  $t$  decreases with activation for both, STC and NCC in a

similar manner. Generally, this is expected since activation creates more micropores. However, the interpretation of  $t$  is not unique, since it contains both, the chord length of the pores and the chord length of the carbon phase. Combining  $t$  with the porosity obtained from the specific pore volume (Table 4.1) and the skeletal density (Table 4.3), the average chord lengths of the two phases,  $l_{pore}$  and  $l_{carbon}$  can be calculated via Equation 4.6. Table 4.4 shows that the pore chord-length is considerably larger for NCC than for STC, underlining again the much smaller micropore size in the STC series. Interestingly, the chord length of the pores changes only slightly (10-15%) as a consequence of activation, while the chord length of the carbon phase decreases strongly (more than a factor of 2 for NCC and almost a factor of 5 for STC). This can be understood by the fact, that CO<sub>2</sub> activation process not only creates new (small) micropores, but also enlarges existing micropores and mesopores. On the other hand, the CO<sub>2</sub> etching process removes carbon so the thickness of the carbon walls separating the micropores must become smaller in any case. Hence, these parameters contain very detailed and useful information on the hierarchical carbon-pore system complementary to the structural data obtained from adsorption analysis.

### 4.2.3 Inhomogeneity in different NCC series

The STC samples show significant size changes of the structures over the cross section of the monoliths. For the NCC samples, such behavior could not be observed. Although all NCC samples used in this thesis were produced using the same synthesis route, the scattering curves deviate for different sample series. Some NCC samples show significant difference in the scattering curves, depending on the measurement position. Figure 4.9 shows SAXS measurements for different positions on two cut in half NCC monolith fragments from an early NCC sample series not used for other experiments. It can be seen that, depending on the position of the measurements, the S-(10) peak height is reduced or can even totally vanish, while the S-(11) and S-(20) peaks are still visible. The diffuse scattering contribution is only slightly changed possibly due to inhomogeneous distribution of the micropores in the system. These changes in micropore scattering alone however cannot cause the drastic reduction of the peak intensity.

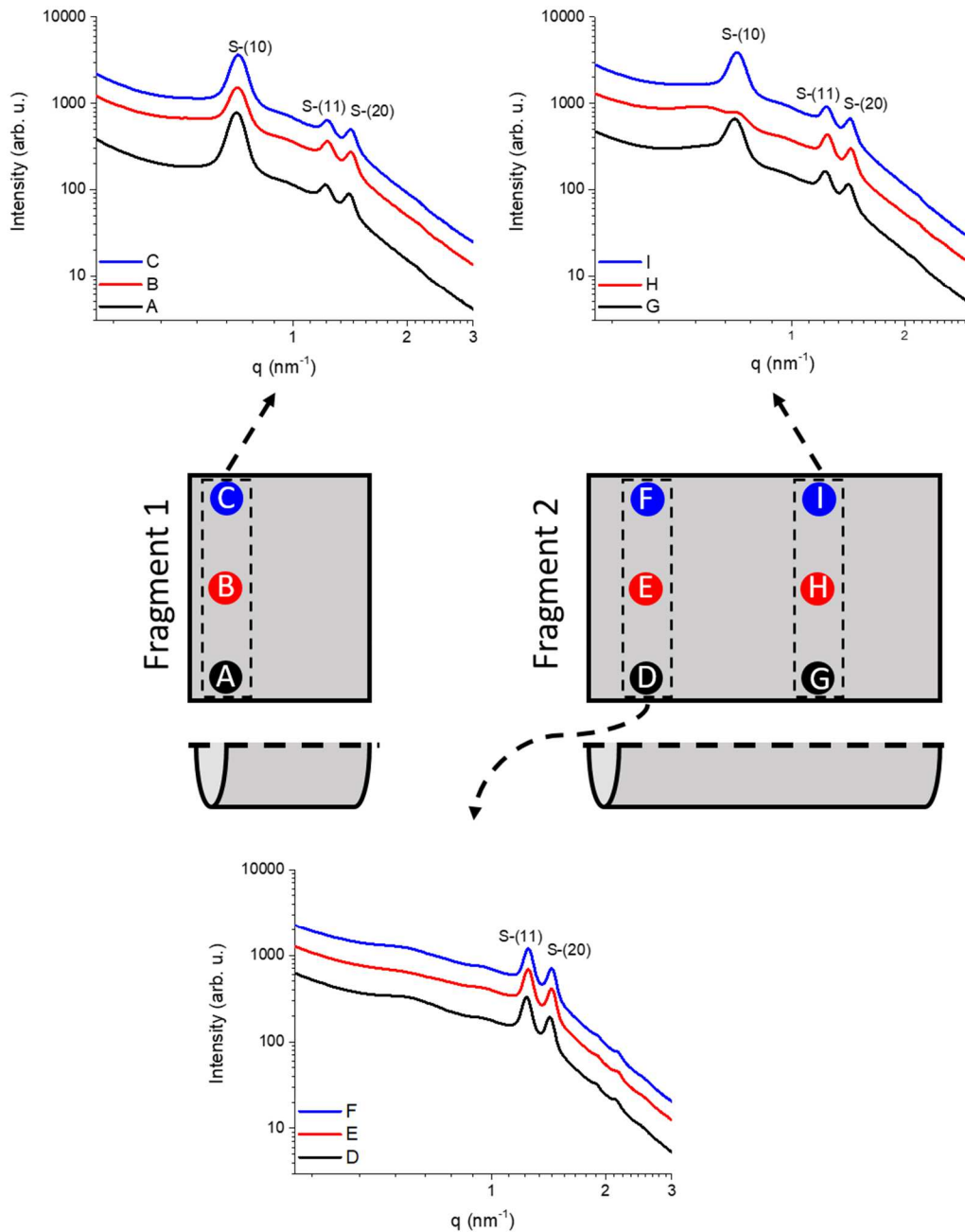


Figure 4.9: SAXS curves from two cut in half monoliths taken from the same sample series. A clear difference depending on the measurement position can be seen.

Besides the change of the S-(10) peak, in some curves (Figure 4.9, curves D-F and H), also additional shoulder can be observed at  $q \sim 0.6 \text{ nm}^{-1}$ . These peaks cannot be linked to the 2D hexagonal structure of the NCC sample. Hofmann et al.<sup>222</sup> observed a similar behavior during adsorption experiments of fluorinated pentane in SBA-15. The additional peak in the filled SBA-15 structure was

explained by the formation of bubbles in the cylindrical mesopores. These bubbles are believed to create an additional periodic structure along the pore axis, with a similar periodicity the pore distance.<sup>222</sup> A comparable effect could also happen in the carbon nanorods. The additional periodic structure could be formed from void space in the (not ideally cylindrical) carbon nanorods created during the synthesis procedure.

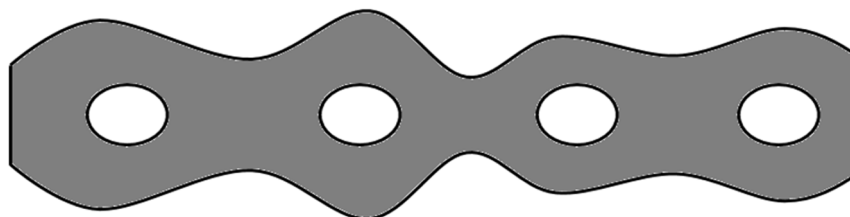


Figure 4.10: Schematic representation of periodic structures created via void spaces inside the nanorods.

### 4.3 Electrochemical performance

All electrochemical measurements were done with an aqueous 1M CsCl solution as electrolyte as in several previous studies on EDLCs.<sup>20,21,34,173,199</sup> Cyclic voltammetry (CV) measurements were carried out using the symmetric cell setup for scan rates ranging from  $0.5 \text{ mV s}^{-1}$  up to  $500 \text{ mV s}^{-1}$  in a cell voltage ranging between 0 V and 1.0 V. In addition, also CV measurements of the asymmetric setup were done in a potential window  $\pm 0.6 \text{ V}$  against an oversized quasi-reference. The results of the asymmetric setups did not differ noticeably from those of the symmetric setup. Electrochemical impedance spectroscopy (EIS) measurements were performed at 0 V with 5 mV rms amplitude in a frequency range between 10 mHz and 100 kHz using the asymmetric setup.

#### 4.3.1 Performance evaluation

The influence of the  $\text{CO}_2$  activation treatment on the electrochemical performance was investigated with cyclic voltammetry. In Figure 4.11, CV curves of the NCC and STC samples without  $\text{CO}_2$  treatment as well as the 4 hours activated samples are shown for different scan rates (symmetric setup). The CVs at low scan rates have a nearly rectangular shape, indicating a pure EDLC behavior. The capacitance decreases with increasing scan rate as expected, and

the deviation from the rectangular shape due to a serial resistive contribution becomes obvious. This effect is much more pronounced for the STC samples.

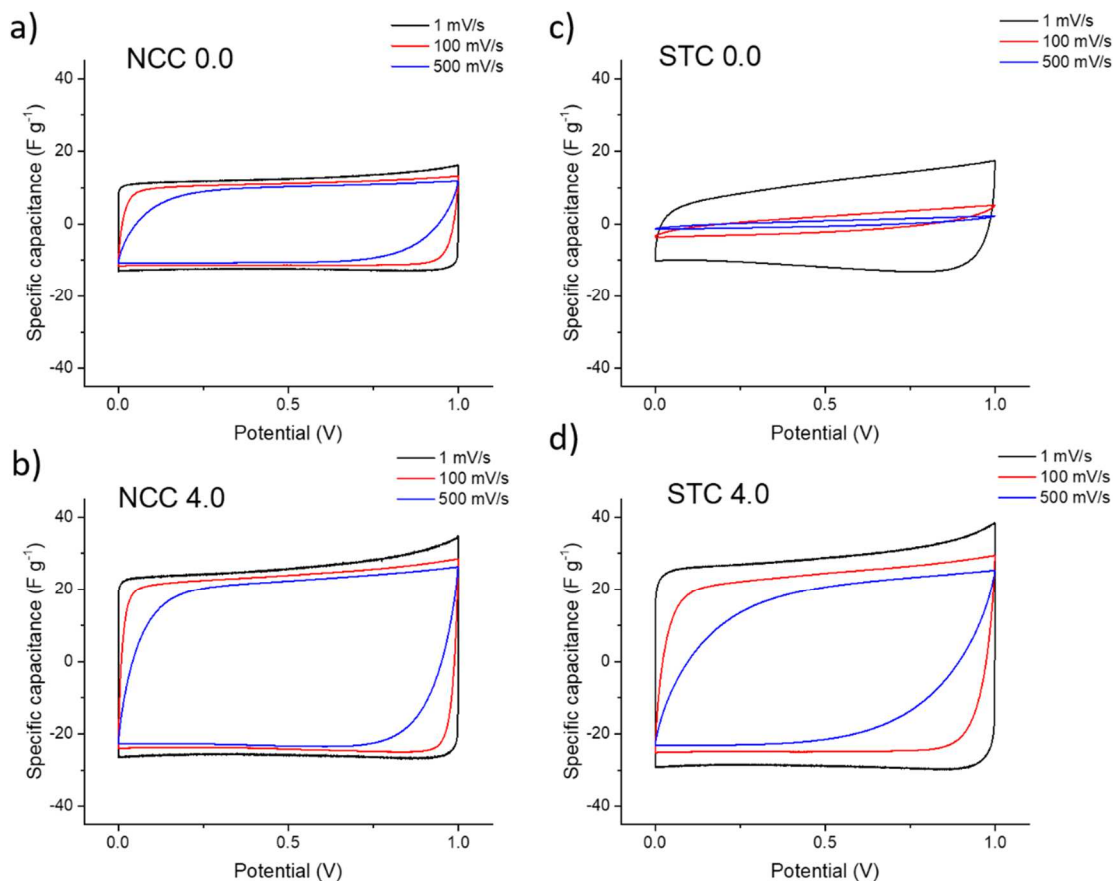


Figure 4.11: Cyclic voltammograms of symmetrical devices (normalized to the combined mass of both electrodes) using untreated (a) and 4 hour activated (b) NCC samples, as well as the untreated (c) and 4 hour activated (d) STC samples. Reprinted with permission from Ref.<sup>142</sup> Copyright 2019 American Chemical Society

Comparing the untreated (Figure 4.11a and Figure 4.11c) and the 4 hours activated (Figure 4.11b and Figure 4.11d) samples, it can be clearly seen that the capacitance is significantly increased upon activation for both material types. This is not surprising, since the activation process also increases the specific surface area (Table 4.1 and Table 4.4). The capacitance shows an almost perfect correlation with the specific surface area (Figure 4.12), only the increase of the NCC for the 0.5 h activated sample is more pronounced than the other samples.



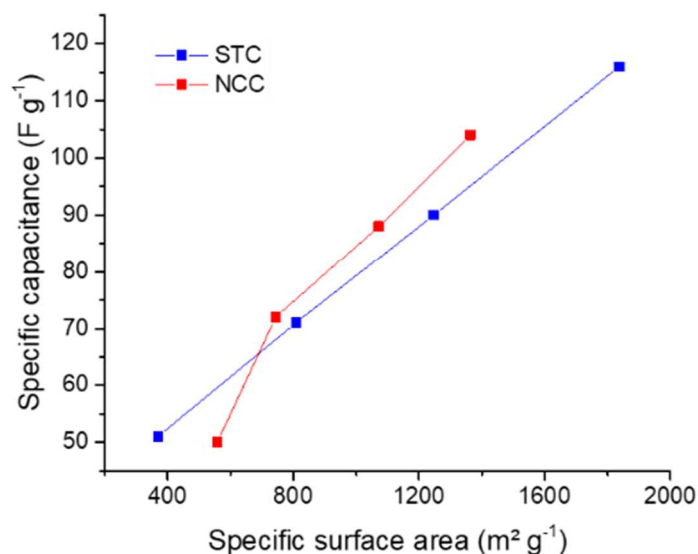


Figure 4.12: Specific capacitance (from CV with  $0.5 \text{ mV s}^{-1}$ ) vs. specific surface area (DFT) shows linear behavior for most samples. Only the non-activated NCC sample deviates from this linear behavior.

To evaluate the rate handling capability, the specific capacitance  $C$  was calculated from CV measurements using scan rates in the range between  $0.5$  and  $500 \text{ mV s}^{-1}$ , according to Equation 2.13. The specific capacitance is shown in Figure 4.13 as a function of the scan rate for different activation times. The superior rate handling capability of NCC compared to the reference material can be best seen for the half-hour activated sample (Figure 4.13a). For low scan rates the NCC 0.5 sample has a lower capacitance compared to the reference material, but for scan rates above  $200 \text{ mV s}^{-1}$  this is reversed. The two-hour activated sample already outperforms the reference at  $20 \text{ mV s}^{-1}$ , and the four-hour activated sample shows a higher initial capacitance as well as better stability than the reference. For the STC material, the situation is different. Only the four-hour activated sample shows higher capacitance than the reference material, and the rate handling capability of STC is overall similar to the reference sample. The STC 4.0 sample has the highest absolute value for the specific capacitance of all investigated samples at very low scan rate ( $0.5 \text{ mV s}^{-1}$ ), which is expected because this sample also has the highest specific surface area (Table 4.1 and Table 4.4).

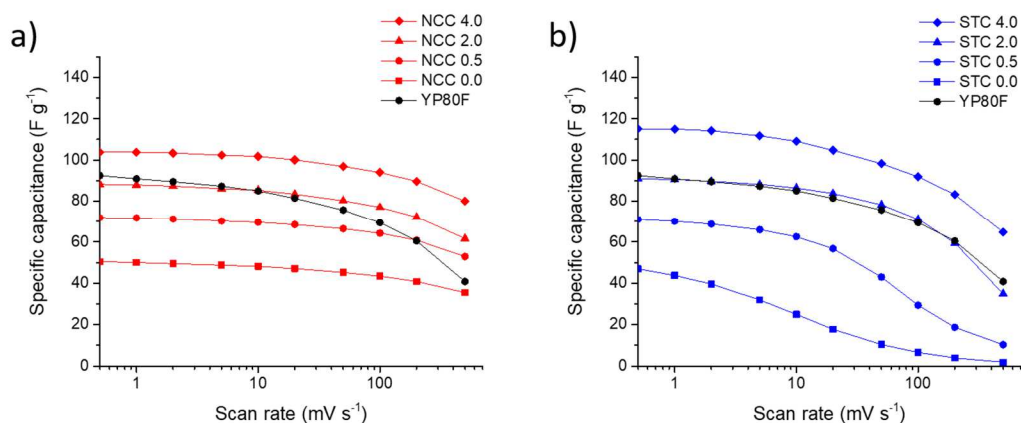


Figure 4.13: Specific capacitance (calculated from cyclic voltammograms) vs. scan rate for the activated NCC (a, red curves) and STC (b, blue curves) samples measured with a symmetric cell setup. The black curve represents the reference material (activated carbon YP80F). Reprinted with permission from Ref.<sup>142</sup> Copyright 2019 American Chemical Society

The measurements performed with a half-cell setup (Figure 4.14) show the same trend as the measurements using a symmetric cell setup. Although, it is worth noting that from the used half-cell setups (with YP80F as quasi-reference) the rate handling capability cannot be evaluated as reliable as from a symmetric cell setup. This can be explained by the fact that the activated carbon reference also experiences a capacitance decrease for elevated scan rates (Figure 4.13). Therefore, the capacitance ratio between the WE and the CE changes, which also affects the measured capacitance of the sample (Equation 2.8). If the investigated material is more stable compared to the reference electrode, the rate handling capability is underestimated and vice versa. Equation 2.8, which describes the capacitance of two serial capacitors, can easily explain this. The reduced capacitance of the reference electrode (under the assumption of an unchanged WE) will change the capacitance ratio of the WE and the CE and therefore reduces the measured capacitance even if the capacitance of the WE does not change. This results in an underestimation of the rate handling capability. If the reference electrode is more stable compared to the working electrode, the rate handling capability is overestimated due to a continuous increase of the CE capacitance compared to the WE. As a result, the measured rate handling capability is partly determined by the reference electrode in a half-cell setup.

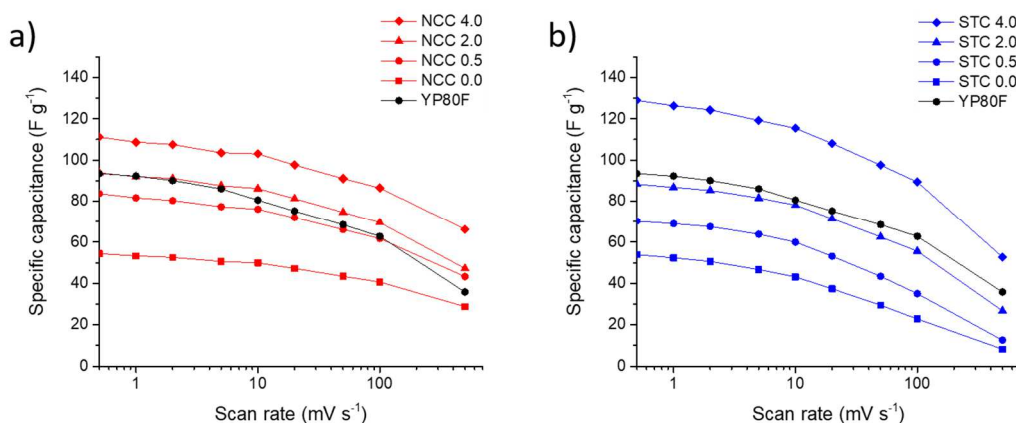


Figure 4.14: Specific capacitance (calculated from cyclic voltammograms) vs. scan rate for the activated NCC (a, red curves) and STC (b, blue curves) samples measured with a half-cell design with using an oversized CE. The black curve represents the reference material (activated carbon YP80F).

Using electrochemical impedance spectroscopy, it is possible to study electrochemical processes in a wide span of time ranges from milliseconds up to hours.<sup>57,74,223</sup> The Nyquist plots (Figure 4.15) show a significantly different behavior of the two material types. While for NCC the curves are only slightly different, the STC material is strongly influenced by the CO<sub>2</sub> activation treatment.

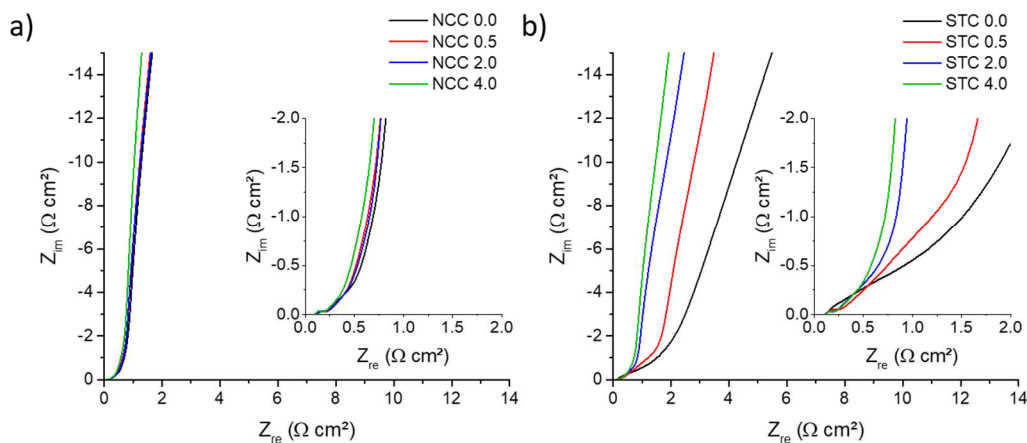


Figure 4.15: Nyquist impedance plot of NCC (a) and STC (b) samples for different CO<sub>2</sub> activation treatments using a half cell setup. The insets show the magnification of the first part. Reprinted with permission from Ref.<sup>142</sup> Copyright 2019 American Chemical Society

The equivalent serial resistance (ESR), originating from the intra- and interparticle resistance, as well as from electrode/current collector resistance, wiring, etc.,<sup>73</sup> is similar for both material types and is not strongly affected by the activation process (Table 4.5). Only the sample NCC 4.0 has a slightly lower ESR. The similar ESR values for all the measured samples is expected because the cell

design, the carbon precursor and the heat treatment temperatures are similar for all samples.

The equivalent distributed resistance (EDR), corresponding to the 45° part (Figure 4.15) of a Warburg impedance<sup>74</sup>, is also listed in Table 4.5. The EDR decrease slightly for the NCC materials with increasing activation. For the STC samples, however, the EDR is much higher for the non-activated and the 0.5 h activated sample, and reaches similar values as the NCC and the reference materials for the highest activation times. This suggests that the low-activated STC materials exhibit significantly different diffusive properties.

Table 4.5: Electrical properties.

Sample	$C_{0.5}$ <sup>(a)</sup> (F g <sup>-1</sup> )	ESR <sup>(b)</sup> (Ω cm <sup>2</sup> )	EDR <sup>(b)</sup> (Ω cm <sup>2</sup> )
NCC 0.0	50	0.12	0.59
NCC 0.5	72	0.12	0.53
NCC 2.0	88	0.12	0.55
NCC 4.0	104	0.10	0.52
STC 0.0	51	0.12	1.71
STC 0.5	71	0.12	1.29
STC 2.0	90	0.12	0.57
STC 4.0	116	0.12	0.55
YP80F	92	0.11	0.54

<sup>(a)</sup>  $C_{0.5}$  specific capacitance calculated from CV at a scan rate of 0.5 mV s<sup>-1</sup>

<sup>(b)</sup> Equivalent serial resistance (*ESR*) and equivalent distributed resistance (*EDR*) from Nyquist plot

### 4.3.2 STC sample without calcination

The STC samples described in the previous chapters were calcined at 523 K in air for 30 minutes.<sup>142</sup> From comparing samples with and without this calcination step it turned out that this is an important step in terms of the electrochemical performance (capacitance and rate handling capability) of the material.

Figure 4.16 shows that the not calcined soft templated carbon (STC\_NC) exhibits a significantly reduced capacitance even at very low cycling rates. The overall capacitance is significantly lower compared to the calcined samples, especially for the not- and short time activated carbon. After a two-hour CO<sub>2</sub> activation the capacitance of the not calcined sample (STC\_NC 2.0), for low scan rates, is comparable to its calcined counterpart (STC 2.0).

In terms of rate handling capability, the not calcined samples exhibit a drastically reduced capacitance for elevated scan rates. This results in a capacitance loss of ~80% (for the not- and 0.5 h activated materials) when increasing the scan rate from 0.5 to 10  $\text{mV s}^{-1}$ . Only after a two-hour  $\text{CO}_2$  treatment, the not calcined sample reached a specific capacitance, for high scan rates, comparable to the calcined (but not activated) version.

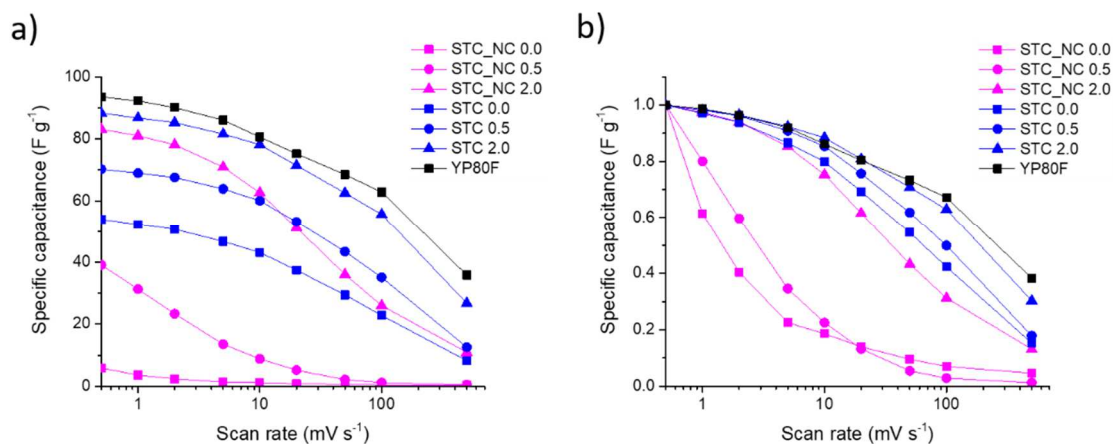


Figure 4.16: Specific capacitance (calculated from cyclic voltammograms) vs. scan rate for the activated STC\_NC and STC samples (a). Relative specific capacitance (normalized to the capacitance at 0.5  $\text{mV s}^{-1}$ ) versus scan rate for STC\_NC and STC samples (b). The black curve represents the reference material (activated carbon YP80F). All measurements were done using an oversized counter electrode as a quasi-reference. Reprinted with permission from Ref.<sup>142</sup> Copyright 2019 American Chemical Society

This behavior may be tentatively explained by a (meso)pore blocking during the carbonization procedure caused by remaining surfactants. The activation process could open up blocked pores and remove surface groups. As a result, the accessible surface area is increased, which also increases the electrochemical performance of the material. However, no further attempts were undertaken to quantify this hypothesis with the help of detailed structural analysis.

### 4.3.3 Electro-wetting

Before the actual electrochemical measurements are made, several CV cycles were performed. During these “conditioning” experiments, one sample behaved rather different. The not activated (but calcined) STC sample showed a continuous increase of its capacitance over many cycles. As seen in Figure 4.17a, the capacitance value after 5 cycles is rather low and increases dramatically after

additional 40 cycles. This material reached its maximum capacitance only after more than 100 CV cycles. After the conditioning, the capacitance was comparable to the not activated NCC material. This drastic increase in capacitance was only observed in the not activated STC material.

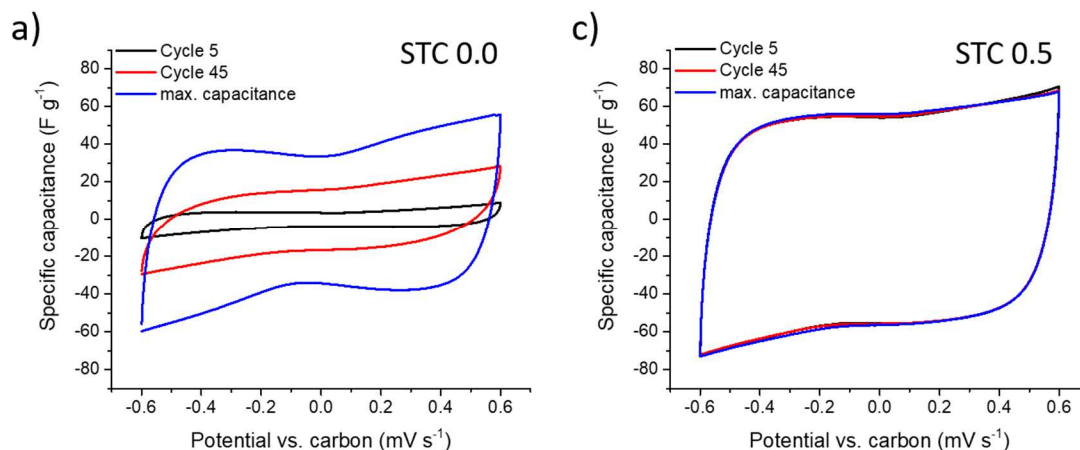


Figure 4.17: Cyclic voltammograms of the not-activated (a) and 30 minutes activated (b) STC samples. The not activated sample drastically increases the overall capacitance with the cycling until it reaches a maximum value. The STC 0.5 reaches nearly its maximum capacitance already after 5 cycles. All measurements were done using an oversized counter electrode as a quasi-reference at a scan rate of 20 mV s<sup>-1</sup>.

The drastic increase in capacitance can be explained by a (slow) wetting of the electrode itself. If the electrode is not fully infiltrated with the electrolyte, the available surface area is reduced, which also reduces the capacitance. The applied potential can cause wetting of hydrophobic parts of the electrode. It is known that the contact angle of an electrolyte can be reduced if a potential is applied, which is caused by the formation of an electrical double layer at the electrode/electrolyte interface, leading to a reduction of the surface tension.<sup>224</sup>

Another result of this electro wetting effect is the increase of the capacitance at higher potentials, seen by the deviation from an ideal rectangular shape (“butterfly wings”) shown in Figure 4.17a. The link between electro wetting and the deviation of the CV curves from the ideal rectangular shape has already been investigated for organic electrolytes. This deviation can be explained by the fact that a higher potential leads to a higher accessible surface area (caused by electro wetting).<sup>225,226</sup>

Both effects, the strong increase of the capacitance upon cycling and the rather pronounced “butterfly wings” in the CV curve are only visible for the not-activated soft templated sample. The 30 minutes activated STC 0.5 electrode on

the other hand immediately reaches its full capacitance and the CV curves are closer to an ideal rectangular shape (Figure 4.17b). This could be explained by a change of the (micro)pore surface chemistry during the high temperature CO<sub>2</sub> activation process.

In contrast to the STC material, the NCC electrodes show no increase of the capacitance during the conditioning procedure. Even the not activated sample reaches its maximum capacitance immediately (Figure 4.18). In addition, the CV curves are almost ideally rectangular without the pronounced butterfly wings.

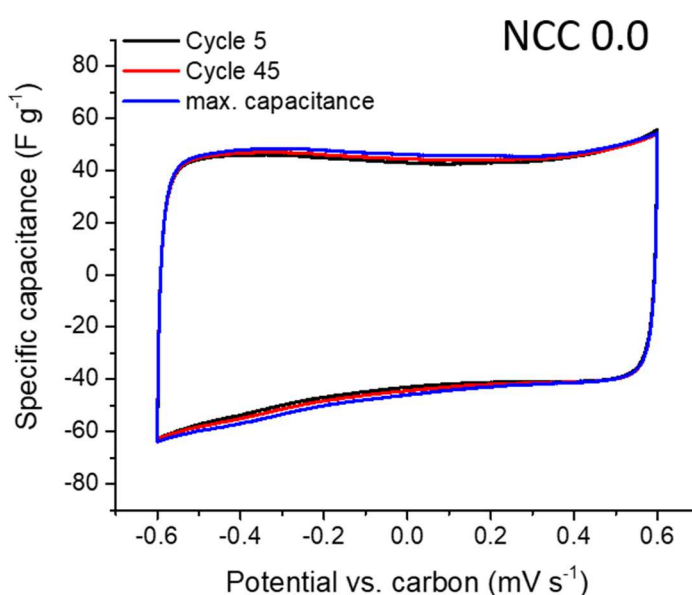


Figure 4.18: Cyclic voltammograms of the not-activated NCC sample. It reaches nearly its maximum capacitance already after 5 cycles. All measurements were done using an oversized counter electrode as a quasi-reference at a scan rate of 20 mV s<sup>-1</sup>.

## 4.4 Discussion

In Figure 4.12 it was shown that the specific capacitance increases with activation time for both, the NCC and the STC materials, in a similar manner. The rate handling capability, however, was found to depend differently on the activation time, being generally superior for NCC as compared to STC. This is visualized more clearly in Figure 4.19a-c, where the specific capacitance for each scan rate was normalized to the capacitance at the lowest scan rate. The NCC samples show a superior behavior over the reference sample for all activation times and even for the non-activated sample. The CO<sub>2</sub> activation leads to only a slight

improvement of the rate handling capability in this material type. The STC material after a four-hour  $\text{CO}_2$  activation shows the highest absolute value of the specific capacitance for low scan rates ( $C_{0.5}$ , see Table 4.5). However, this material exhibits a significantly poorer rate handling capability when no or only a short-time  $\text{CO}_2$  activation was performed. The rate handling capability improves during the activation (Figure 4.19b), and reaches, after four hours of activation, a similar performance as the reference material YP80F.

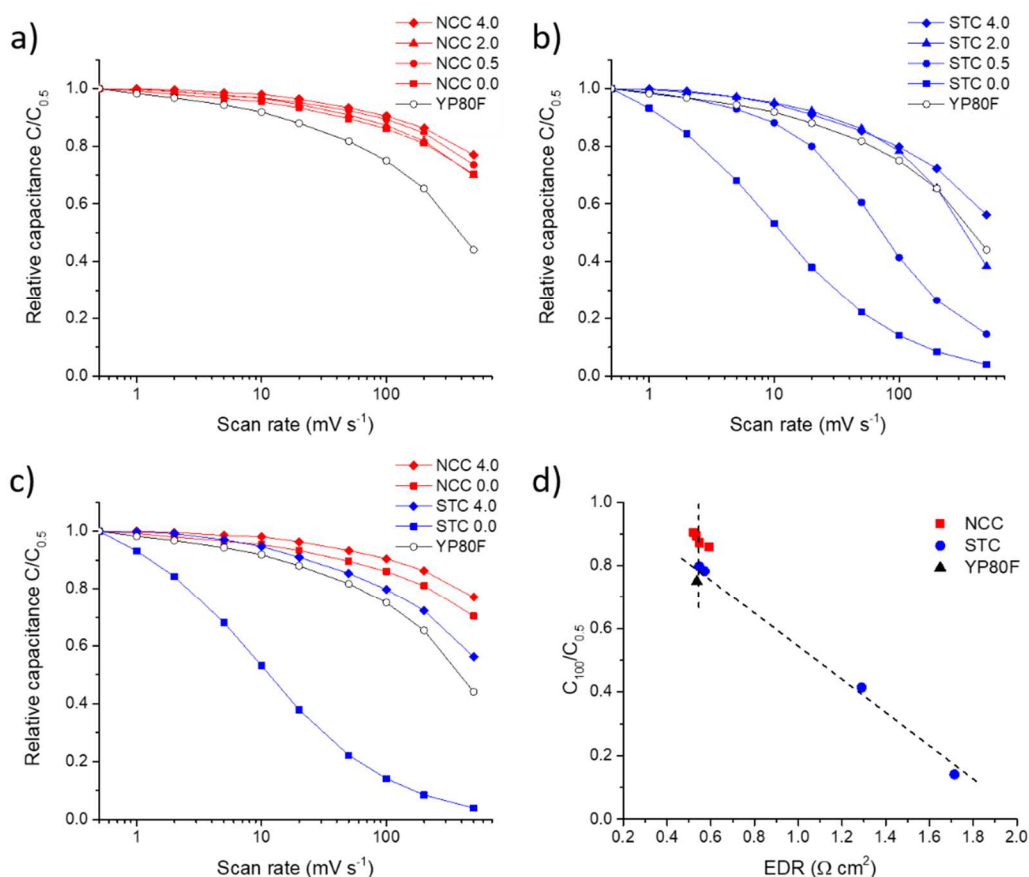


Figure 4.19: Relative specific capacitance (normalized to the capacitance at  $0.5 \text{ mV s}^{-1}$ ) vs. scan rate for NCC (a) and STC (b) samples as well as for the reference material (YP80F). (c) Relative capacitance (normalized to the capacitance measured at  $0.5 \text{ mV s}^{-1}$ ) vs. scan rate for the untreated and 4 hour activated NCC (red) and STC (blue) samples as well as the reference materials (black). (d) Relative capacitance at  $100 \text{ mV s}^{-1}$  ( $C_{100}/C_{0.5}$ ) vs. EDR. Reprinted with permission from Ref.<sup>142</sup> Copyright 2019 American Chemical Society

From EIS (Figure 4.15 and Table 4.5) it is found that the equivalent serial resistance (ESR) is nearly the same for all materials, but the equivalent distributed resistance (EDR) is not. As seen in Table 4.5, the NCC materials show only minor EDR changes with activation, but the activation process drastically



reduces the EDR of the STC samples. Figure 4.19d shows a plot of the relative capacitance  $C_{100}/C_{0.5}$  vs. the EDR. There seem to be two regimes: one in which the EDR decreases strongly and a second one where the EDR remains constant.

The EDR is related to ion transport into the pores of the electrode and can be influenced by ion diffusion velocity and the length of the diffusion pathways.<sup>74,227</sup> Therefore, it is necessary to consider the structural differences of the two different material types as well as their changes during the activation process in some more detail. First, the capacitance is mostly determined by the micropores, since they make up the major part of the specific surface area. Second, the different mesopore structures of the two carbon materials (see Figure 4.1) result in major differences concerning the accessibility of the micropores. The carbon rod structure of the NCC materials represent a highly interconnected mesopore space in three dimensions, which consequently allows for a fast ion transport within these pores towards the micropores located in the nanorods (Figure 4.20a). Also for the STC materials the electrolyte can access the micropores via the cylindrical mesopores. However, ion transport towards the micropores within the mesopore walls in this case is only possible via a one-dimensional transport of ions along the cylindrical mesopores. The struts forming the macropores (see Figure 4.2b and Figure 4.2e) have a quite high length to thickness aspect ratio, and are strongly interconnected. Hence, the accessibility in the STC material is possible either via micropores or via very long one-dimensional mesopore channels, leading to either lower diffusion velocity or longer diffusion pathways. Therefore, the much better rate handling capability of NCC as compared to STC material, particularly for the non-activated samples or for low activation times, is naturally explained by the poor connectivity of the micropore network and the long 1D mesopore diffusion paths in STC.

There may however be several other factors influencing the rate handling capability. Not only the mesopore connectivity, but also their specific volume is quite different for the NCC and STC samples (Table 4.1). Besides, providing faster diffusion, the mesopores also constitute an ion reservoir illustrated in Figure 4.20b. During the charging process, ions from the mesopores can diffuse into the micropores without the need to diffuse all the way from the macropores or bulk electrolyte in the separator. Since the specific mesopore volume of the NCC samples is considerably larger than the one of the STC samples (Table 4.1), a better rate handling capability of NCC would be expected due to this fact.

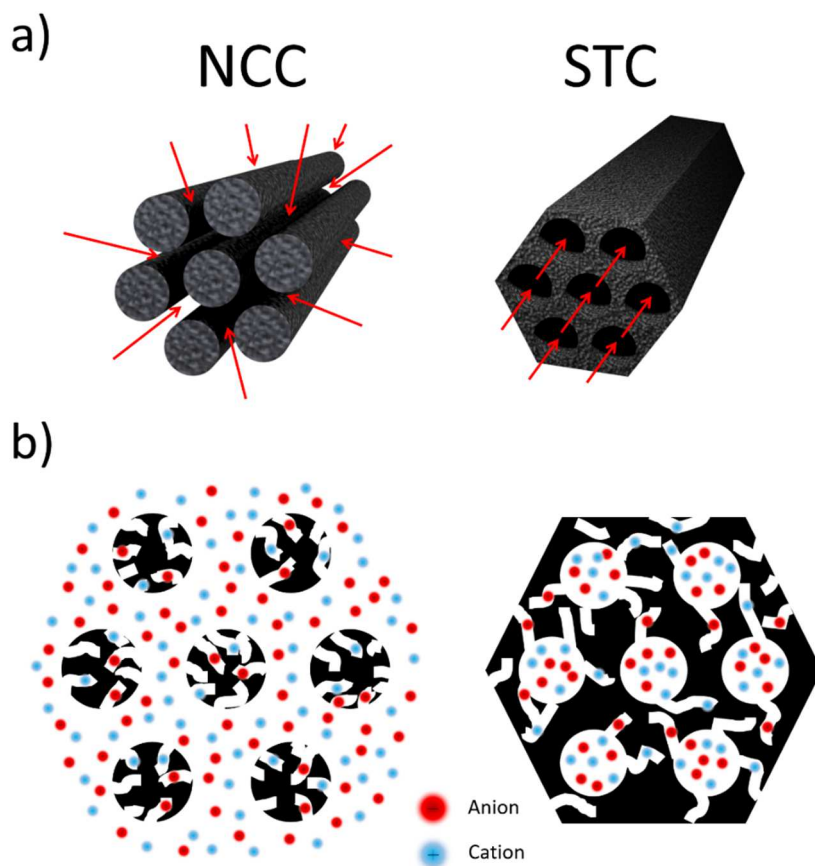


Figure 4.20: Schematic representation of ion transport in the used materials with the red arrows indicating the ion diffusion paths in the mesopores (a), and the ion reservoir located in the mesopores (b). Reprinted with permission from Ref.<sup>142</sup> Copyright 2019 American Chemical Society

The CO<sub>2</sub> activation process influences the mesopore connectivity in different ways. In the NCC samples, the activation introduces micropores within the carbon nanorods but leaves the mesopore network essentially unchanged except, for the increase in specific mesopore volume. This explains qualitatively why for the NCC samples the rate handling capability does not markedly depend on the activation. In the STC materials, however, the micropores are located in the continuous carbon phase surrounding the cylindrical mesopores. Upon CO<sub>2</sub> activation the specific micropore volume increases strongly which can be expected to influence the connectivity of the micropore network as discussed in the following based on the nanostructural data.

The mean chord-length of the carbon phase  $l_{carbon}$  is 4.34 nm for the non-activated STC sample (Table 4.4). Considering that the mean micropore size is smaller than 1 nm (see Figure 4.3f) and the microporosity is only about 20% (Table 4.4), it is very unlikely that the micropores can form a continuous network

within the solid carbon phase. This situation is completely changed for the four-hour activated sample. Here, the mean carbon chord-length  $l_{carbon}$  is 0.9 nm, which is in the same range as the micropore size, and the microporosity is larger than 60%. Hence, in this case it is most likely that the micropores form an open network within the mesopore walls. Consequently, if the (faster, but much longer) ion transport through the cylindrical mesopores is outperformed by the (slower, but shorter) transport through the micropore network in the STC, the mesopores will not play a decisive role anymore. This should finally result in a three-dimensional access of all pores via the micropore network, which should then be comparable to the (purely microporous) activated carbon reference material. This is indeed the case for the two- and four-hours activated STC material, which show an almost identical rate handling capability as the YP80F reference material (see Figure 4.19b).

Concerning the macropore structure, we believe that the different strut thickness seen in the STC and NCC samples at the macropore level (Figure 4.2) has only a limited impact on the rate handling performance for the non-activated and short-time activated samples. The small amount of micropores can be expected to lead to a not well-connected micropore network, which is therefore better accessible via the cylindrical mesopores. After a longer activation time the micropore network is well connected and therefore, the behavior is comparable to activated carbon materials with a grain size of several micrometer.

Finally, when comparing the four-hours activated STC and NCC samples, it is obvious that only for the NCC material the optimum benefit from the hierarchical pore structure is obtained, since only this structure enables fast transport via a 3D mesopore network and very short diffusion pathways from these mesopores into the micropores, which eventually determine the absolute capacitance of the system.

## 4.5 Conclusion

Two hierarchically organized carbon materials with comparable cellular networks of macropores and a nanostructure that can be described as an inverse replication of each other were characterized. The soft templated carbon material (STC) features cylindrical mesopores arranged on a 2D hexagonal lattice similar to the SBA-15 type silica, with micropores within the mesopore walls. In contrast, the nanocast carbon (NCC) materials exhibit bundles of periodically arranged nanofibers with an inverted mesopore structure compared to the STC materials.

CO<sub>2</sub> activation was performed to increase the amount of micropores within the mesopore walls. Both materials outperform a purely microporous activated carbon reference material in terms of specific capacitance and rate handling capability, demonstrating that a hierarchical pore geometry is beneficial for the electrochemical performance. The NCC material showed a significantly better rate handling capability than the STC material, particularly for short activation times. This is attributed to the 3D interconnected mesopores in NCC allowing fast ion diffusion through the mesopore space into the micropores within the carbon nanorods. In the STC materials the mesopores are not interconnected but long parallel cylinders, leading to substantially longer 1D diffusion paths for ions coming from outside the mesopores. The activation process increases the microporosity of the mesopore walls, generating eventually a percolating micropore network which improves the rate handling capability. In conclusion, for better rate handling capability, it is not sufficient to just realize a hierarchical pore network, but the performance strongly depends on the type of hierarchy.

## 5 Electrosorption induced electrode expansion

In this chapter, electrosorption induced dimensional changes in supercapacitor electrodes, made of ordered mesoporous carbon, are discussed. By using a combination of electrochemical dilatometry and in situ small-angle X-ray scattering it was possible to track electrode expansion and shrinkage on the nanometer and the macroscopic scale. Large parts of Chapter 5 have already been published in Ref.<sup>199</sup>

### 5.1 Motivation

An important side effect caused by ion electrosorption is the volumetric expansion of the carbon electrodes during operation. Although electrode deformation is usually much smaller as compared to batteries,<sup>228</sup> repeated expansion and contraction of the electrode may contribute towards electrode degradation. Moreover, this deformation must not necessarily be unwanted, as it opens a facile way to build highly efficient bilayer actuators of astonishing simplicity.<sup>229,230</sup> So far, dimensional changes of electrodes in EDLCs were analyzed using in situ dilatometry or atomic force microscopy.<sup>35,141,231–234</sup> In situ dilatometry was even proposed as a method of choice to investigate ion transport in and out of the electrode pores to gain insight on ion-size effects and optimized electrolyte/electrode combinations.<sup>141</sup> However, studies trying to relate volume changes unambiguously to ion concentration and ion-size related steric effects are contradicting.<sup>232</sup> In Li-ion battery electrode swelling, Li intercalation plays by far the dominant role. In contrast, in porous supercapacitor electrodes, several contributions may be of the same order of magnitude, including electronic effects on the surface carbon atoms caused by electrosorbed ions.<sup>232,235,236</sup> In order to exploit the full potential of in situ dilatometry for studying ion charge storage and transport phenomena, those contributions have to be identified and understood in detail.

X-ray scattering is considered advantageous in studying electrosorption-induced pore swelling in EDLCs, as it can probe concurrently the microscopic strain of the carbon and the ion location within the nanopores. For disordered nanoporous carbons the crystalline order is usually too low to enable X-ray diffraction for the quantitative study of expansion/contraction processes. In the small-angle scattering regime, pore swelling is a second order effect which is hardly extractable

from the data.<sup>20</sup> Therefore, a tailored carbon material with an ordered mesoporous structure, giving rise to sharp Bragg reflections from the mesopore lattice in the SAXS regime was used, comparable to the NCC material described in Chapter 4. This material allows analyzing the electrosorption induced strain at the mesopore level via the shift of a distinct diffraction peak. In this chapter, an in situ approach of studying the microscopic (by in situ SAXS) and macroscopic (by in situ dilatometry) swelling behavior of carbon based supercapacitor electrodes with ordered mesopores and different amounts of disordered micropores is presented.

## 5.2 Materials characterization

Two nanocast carbon materials were used for this experiment: a not activated sample (NCC\_ISS) and a one-hour CO<sub>2</sub> activated sample (NCC\_ISS A). Table 5.1 lists the structural parameters of the used samples.

Table 5.1: Structural parameters and specific capacitance of the used as synthesized (NCC\_ISS) and activated (NCC\_ISS A) sample. All values obtained from electrodes containing 10 mass% PTFE binder.

Sample	$S_{\text{Total}}^{(a)}$ (m <sup>2</sup> g <sup>-1</sup> )	$S_{0.63-1.3}^{(a)}$ (m <sup>2</sup> g <sup>-1</sup> )	$V_{\text{pore}}^{(b)}$ (cm <sup>3</sup> g <sup>-1</sup> )	$V_{\text{micro}}^{(b)}$ (cm <sup>3</sup> g <sup>-1</sup> )	$V_{\text{meso}}^{(b)}$ (cm <sup>3</sup> g <sup>-1</sup> )	$d^{(c)}$ (nm)	$C^{(d)}$ (F g <sup>-1</sup> )
NCC_ISS	742	113	0.48	0.19	0.29	8.34	56
NCC_ISS A	991	250	0.59	0.29	0.30	8.34	68

<sup>(a)</sup> Total specific surface area  $S_{\text{Total}}$  and specific surface area for pores in the range between 0.63 nm and 1.3 nm  $S_{0.63-1.3}$  calculated from N<sub>2</sub> and CO<sub>2</sub> adsorption isotherms using QSDFT assuming slit pores.

<sup>(b)</sup> Total pore volume  $V_{\text{pore}}$  calculated at relative pressure 0.95 p/p<sub>0</sub>. Micropore volume for pores smaller 2 nm  $V_{\text{micro}}$ . Mesopore volume for pores in the range between 2 nm and 30 nm  $V_{\text{meso}}$

<sup>(c)</sup> Lattice spacing  $d$  was calculated from the non-electrolyte-filled (empty) electrode.

<sup>(d)</sup> Capacitance values were obtained from cyclic voltammetry at 1 mV s<sup>-1</sup> with 1M CsCl in the range of ±0.6 V vs. carbon.

### 5.2.1 Gas adsorption analysis

Gas adsorption analysis experiments were performed by Nicolas Jäckel (INM Saarbrücken, Germany) using an Autosorb iQ system (Quantachrome) with liquid nitrogen (77 K). The electrodes were degassed at 102 Pa and 423 K for 10 h. Isotherms were recorded at relative pressures (p/p<sub>0</sub>) from 5 · 10<sup>-7</sup> to 1.0 in 58 steps. The specific surface area was calculated with the ASiQwin-software using the

quenched-solid density function theory SSA (QSDFT-SSA) assuming slit pores. Values for the total pore volume correspond to  $p/p_0 = 0.95$ . Carbon dioxide sorption was carried out at 0 °C in the relative pressure range from  $1 \cdot 10^{-4}$  to  $1 \cdot 10^{-2}$  in 40 steps. SSA (Table 5.1) and pore size distribution (PSD, Figure 5.1) were calculated for pore sizes between 0.3 nm and 1 nm with the ASiQwin software using nonlocal density functional theory (NLDFT). The total PSD from 0.3 nm to 30 nm was incremented by a linear approximation of the calculated pore volume (CO<sub>2</sub>-sorption-derived PSD was used up to a pore size of 0.9 nm and N<sub>2</sub>-sorption-derived PSD for pores larger than 0.9 nm) to an equidistant point density of 0.1 nm in the range 0.3-5.0 nm and a point-to-point distance of 1 nm for pores larger than 5 nm.

The differential PSD of the NCC\_ISS material shows two distinct peaks, one in the micropore region at ~0.5 nm and one in the mesopore region at ~3 nm. Activation increased the amount of the smallest pores, and an additional micropore population at ~1 nm appeared, while the amount of mesopores remained essentially unchanged.

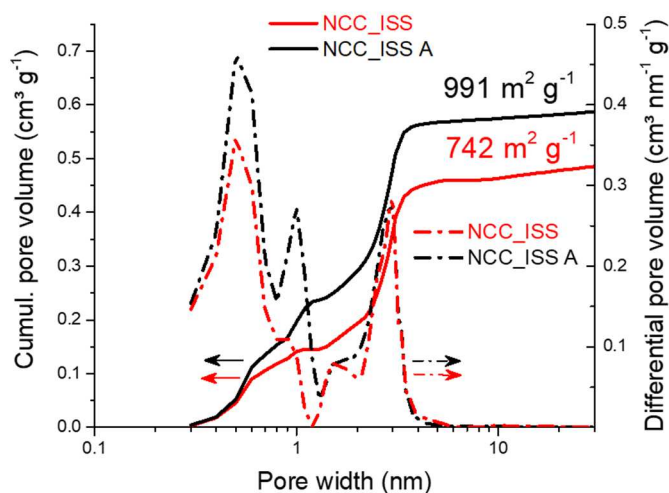


Figure 5.1: Cumulative specific pore volume and differential pore size distribution of the carbon electrodes containing 10 mass% PTFE binder, determined from CO<sub>2</sub> and N<sub>2</sub> sorption isotherms. Reprinted with permission from Ref.<sup>199</sup> Copyright 2017 American Chemical Society

## 5.2.2 Electrochemical characterization

Cyclic voltammetry of the NCC\_ISS and the NCC\_ISS A electrodes was performed in 1M CsCl and 1M LiCl aqueous electrolyte using the in situ supercapacitor cell (Figure 3.2). All measurements were done with an asymmetric cell setup using an oversized activated carbon counter electrode as a quasi-reference (half-cell design, see Chapter 2.2). Figure 5.2 shows the typical behavior of a pure EDLC device without any pseudo-capacitive contributions. As expected, the mass-specific capacitance of the NCC\_ISS A electrode is higher than the one of the MC electrode due to the increased SSA (Table 5.1).

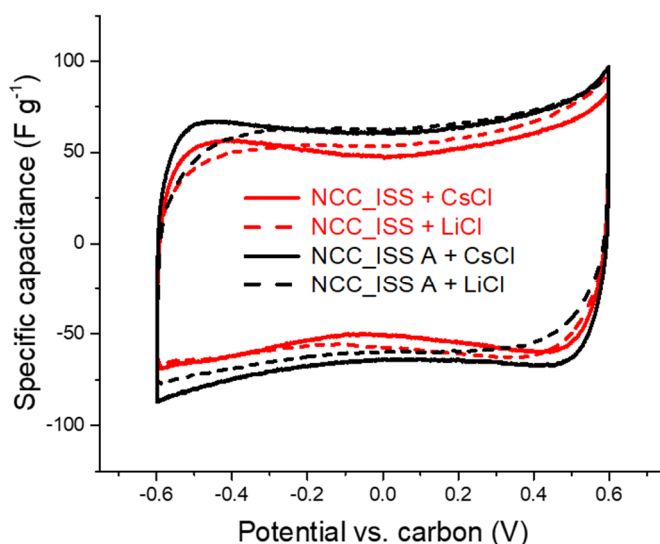


Figure 5.2: Cyclic voltammetry measurement of both electrode materials with  $1 \text{ mV s}^{-1}$  scan rate in 1 M CsCl and 1 M LiCl aqueous electrolyte using a half cell design. Reprinted with permission from Ref.<sup>199</sup> Copyright 2017 American Chemical Society

## 5.2.3 In situ electrochemical dilatometry

Electrochemical dilatometry was performed by Nicolas Jäckel (who published these results in his PhD thesis<sup>237</sup>) using an ECD-2-nano dilatometer (EL-CELL). The cell uses an oversized counter electrode as a quasi-reference, similar to the setup used for in situ SAXS measurements. The working electrode was loaded with a constant force of 1 N and the strain was tracked with a DP1S displacement transducer (Solartron Metrology, accuracy  $\pm 15 \text{ nm}$ ).



## 5.3 In situ SAXS

### 5.3.1 SAXS data evaluation

Figure 5.3 shows the well resolved Bragg reflections in the SAXS curve necessary for the evaluation of the electrosorption induced volume change. The main reflection corresponding to a lattice spacing of  $d = 8.34$  nm which did not change upon activation, although the Bragg peak from the activated sample became broader indicating that the mesopore order is somewhat reduced by the activation process. The diffuse scattering below the Bragg peak originates from the disordered micropores. The increase of the intensity at large  $q$  as a consequence of activation (Figure 5.3), being proportional to the increase in SSA via Porod's law,<sup>82</sup> is in good agreement with gas sorption analysis Table 5.1.

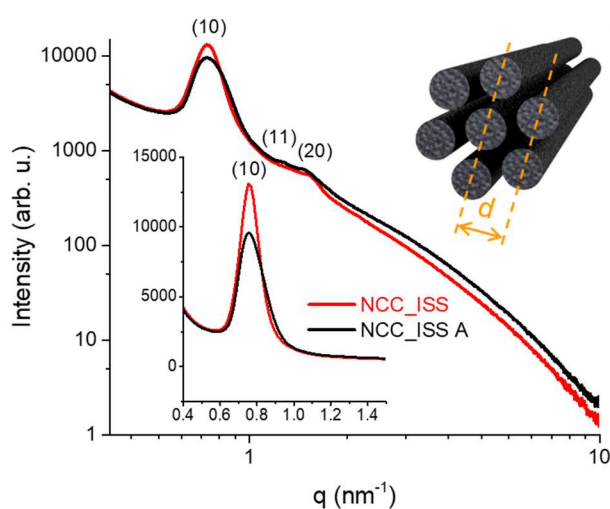


Figure 5.3: SAXS curves of the dry electrodes and schematic drawing of the carbon rods with lattice spacing  $d$  calculated from the (10) Bragg peak position. Reprinted with permission from Ref.<sup>199</sup> Copyright 2017 American Chemical Society

Fitting of the first order Bragg peak (10) for the different applied voltages was done as follows: In the first step the constant background, which changes due to the change of ion concentration, was determined in the  $q$ -range from  $7 \text{ nm}^{-1}$  to  $9 \text{ nm}^{-1}$  by employing Porod's law.<sup>82</sup> In the second step, the sum of a lognormal distribution and a power law were fitted to the data between  $0.5 \text{ nm}^{-1}$  and  $2.0 \text{ nm}^{-1}$ , where the power law captured the changes of the diffuse scattering from the micropores. The Bragg-peak position was determined from the maximum position

$q_0$  of the fitted log-normal function. Strain as a function of applied voltage was determined by calculating the relative shift of this peak position with respect to its position at 0 V. To reduce the noise level, the peak positions from 10 consecutive SAXS curves were averaged. All data treatments were done with the software package Igor Pro 6.37 (WaveMetrics).

### 5.3.2 Beam stability

Since the volumetric changes in supercapacitor electrodes are extremely small, it is necessary to guarantee stable experimental conditions. The evaluation of the strain for example relies on the exact determination of the beam center. If the beam center is not accurately determined, the azimuthal integration leads to a shift and broadening of the peak. Therefore, the position of the X-ray beam has to be stable during the entire experiment. In one of the experiments, the position of the X-ray beam was not stable enough. As a result, it was not possible to accurately evaluate the strain of the electrode during charging and discharging. Figure 5.4 shows significant drops of the calculated peak positions because of the shifted beam.

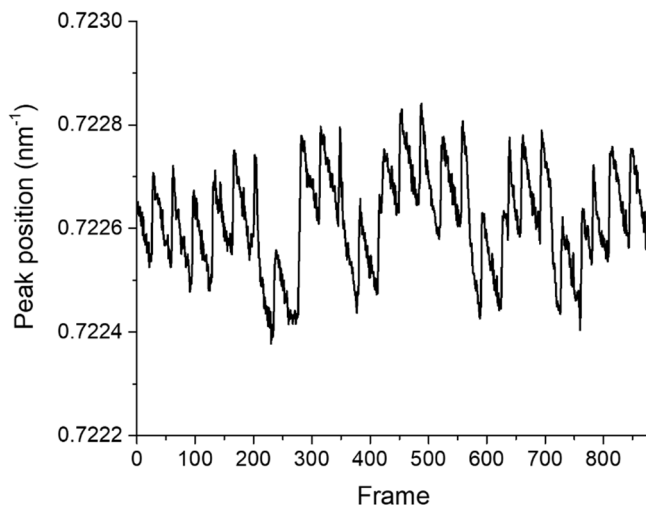


Figure 5.4: Peak position of the (10) peak in a not-activated NCC sample during a CV measurement.

In a first attempt to evaluate these shifts, it was tested to determine the beam center for each measured frame before azimuthally integrate the frame. Therefore, the beam center was determined using the (10) ring (Figure 5.5) originating from the ordered structure of the carbon nanorods. Due to the setup, not the whole

ring was visible, reducing the accuracy with which the position of the beam center could be evaluated. The (11) ring and the (20) ring were too weak to adequately fit the beam center. Therefore, it was not possible to accurately analyze the data.

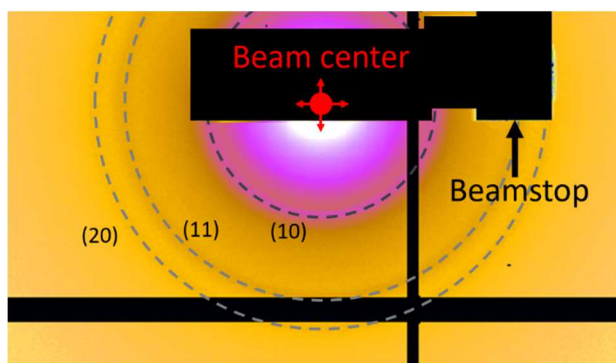


Figure 5.5: Magnification of the detector image during an in situ experiment. The dashed circles marks the position of the (10), (11) and (20) peaks of the hexagonally ordered structure of carbon nanorods in a NCC sample.

In an additional experiment the beam center position was tracked using silver behenate (AgBeh).<sup>238</sup> Since AgBeh has more (sharp) peaks in the SAXS regime compared to the used NCC sample, the beam center can be calculate very precisely. For future measurements, it could be helpful to place an AgBeh sample behind the measured sample to keep track of the beam position.

Fortunately, for the measurements shown in this chapter, it was not necessary to calculate the position of the beam center for each frame individually, because its position was very stable during entire the experiments.

### 5.3.3 Measurements with a lab source

In addition to the experiments performed at the Austrian SAXS beamline, it was also tried to measure the electrosorption induced electrode deformation with a lab instrument (Nanostar, Bruker AXS). This instrument is equipped with a Cu  $K_{\alpha}$  microfocus X-ray source and a Vantec 2000 detector. The detector is movable and was set to a distance of 105 cm away from the sample. This guarantees a good resolution in the peak range. The experimental setup is shown in Figure 5.6.

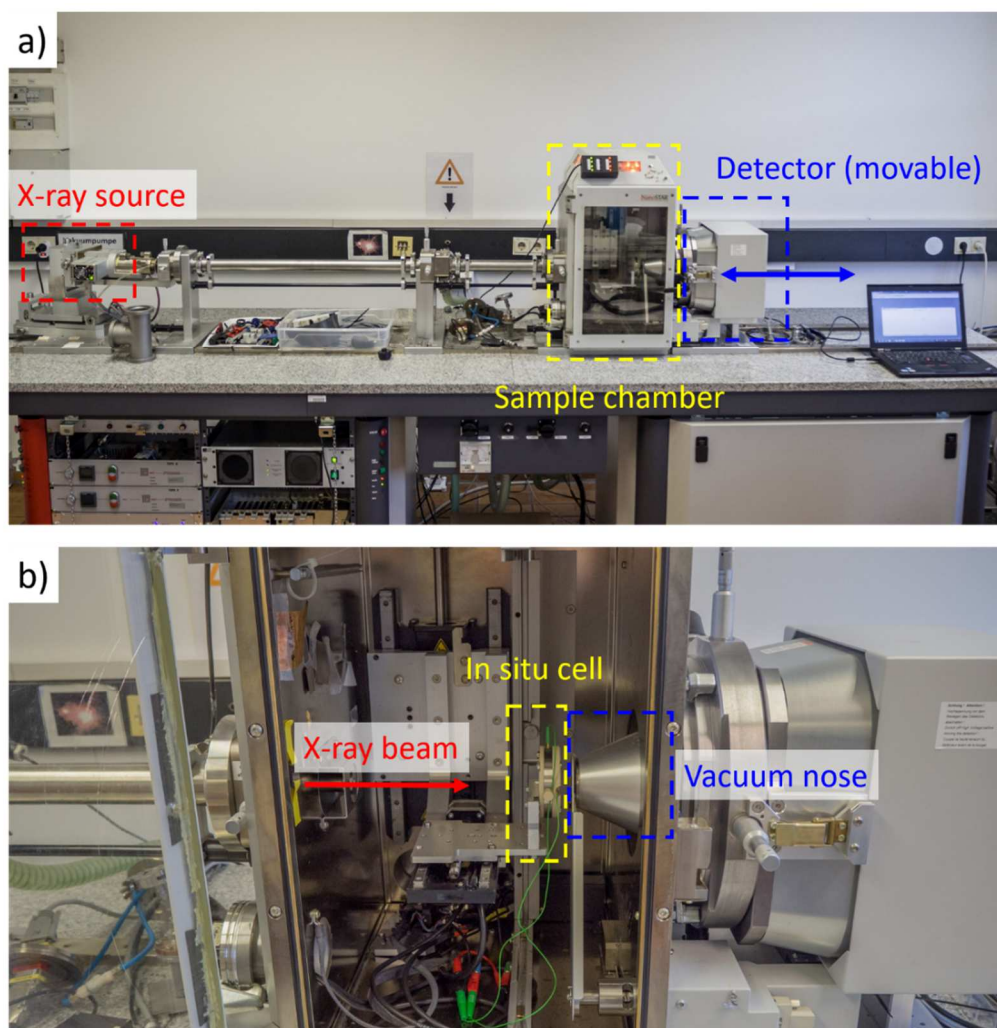


Figure 5.6: (a) Measurement setup for the in situ measurements using a Nanostar (Bruker, AXS) lab instrument. (b) Setup inside the sample chamber. The vacuum nose is necessary to enable measurements under ambient conditions.

The strain vs. potential curve obtained from this experiment (Figure 5.7) suggests an asymmetric expansion behavior for positive and negative potentials and proves that it is in principle possible to track electrode deformation with this instrument. This method has significant drawbacks compared to experiments performed at a synchrotron radiation facility. Due to the reduced photon flux of the lab sources (several orders of magnitude lower), the time resolution is in the range of 15 minutes (compared to a time resolution in the range of seconds at the Austrian SAXS beamline). In addition, the achievable statistic is limited. As a result, these measurements are limited to preparation measurements for the actual experiments performed at a synchrotron radiation facility.

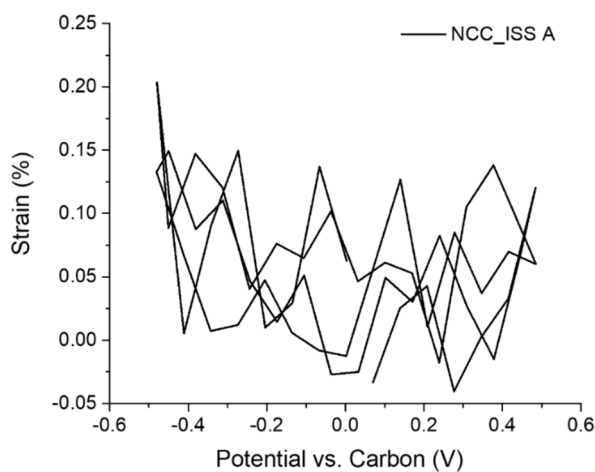


Figure 5.7: Strain vs. potential of the NCC\_ISS A sample during a CV measurement with a scan rate of  $0.2 \text{ mV s}^{-1}$  using a 1M CsCl aqueous electrolyte (measured with a lab instrument)

### 5.3.4 Electrode wetting

To perform an in situ SAXS experiment on an operating supercapacitor, it is important that the electrode is entirely filled with electrolyte. This was the case for the NCC\_ISS and NCC\_ISS A samples. For the not-calcined STC samples, the situation was different. In a disassembled in situ cell it was observed that the electrode showed a dry area (Figure 5.8). As a result, there was no electrolyte inside the irradiated electrode volume. Therefore, it was not possible to perform in situ SAXS and X-ray transmission measurements with this sample.

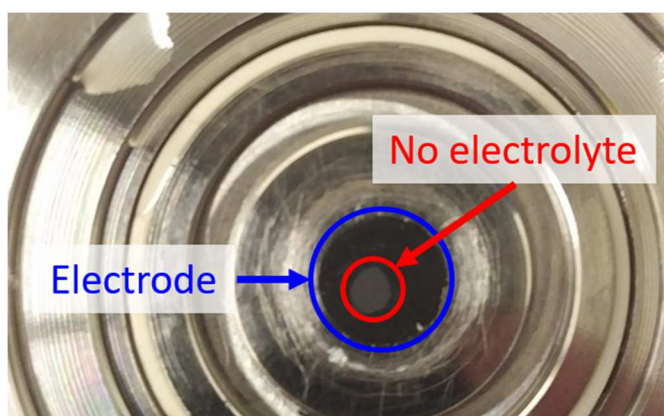


Figure 5.8: Disassembled in situ cell with a not-calcined STC electrode. The area inside the red circle is not soaked with electrolyte.

## 5.4 Results

In order to quantify the volumetric changes of the working electrode during charging and discharging, the change of the peak position (Figure 5.9) was measured in situ, providing the lattice strain as a function of the applied voltage.

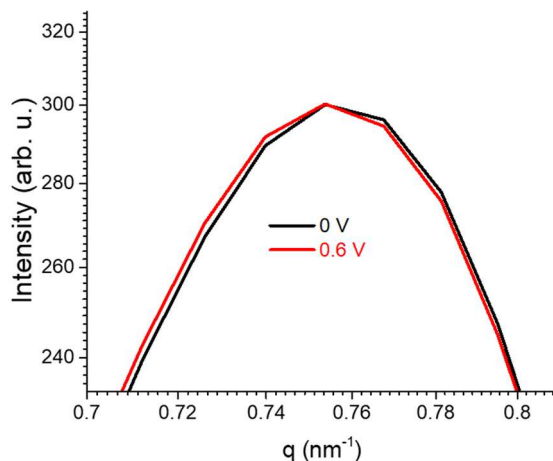


Figure 5.9: Visualization of the (10) peak position for 0 V and 0.6 V for NCC\_ISS A with aqueous 1M CsCl. Reprinted with permission from Ref.<sup>199</sup> Copyright 2017 American Chemical Society

These “nanoscopic” strains from the swelling of the mesopore lattice were compared to macroscopic strains derived from in situ electrochemical dilatometry performed on electrodes made from the same material. The results are shown in Figure 5.10 for two different aqueous electrolytes (1M CsCl and 1M LiCl). As the electron densities of the cations in these two salts are different, this approach represents a kind of contrast variation. A similar approach (although with other salts) turned out suitable to systematically analyze the changes in disordered carbons during in situ SAXS.<sup>20</sup> As shown in Figure 5.10a and Figure 5.10b, for the NCC sample, there is a good correspondence between the SAXS and the dilatometry measurements for both electrolytes. Both methods show slightly asymmetric curves with higher strain at negative potentials, which is already known from literature<sup>232,233,235,239</sup> and is in good agreement with measurements performed with the lab instrument (Figure 5.7). The good qualitative and reasonable quantitative agreement between strains from SAXS and dilatometry suggests that the tiny peak shifts (Figure 5.9) are in this case not obscured by contrast induced changes of the SAXS curves due to the rearrangement of ions.<sup>20</sup>

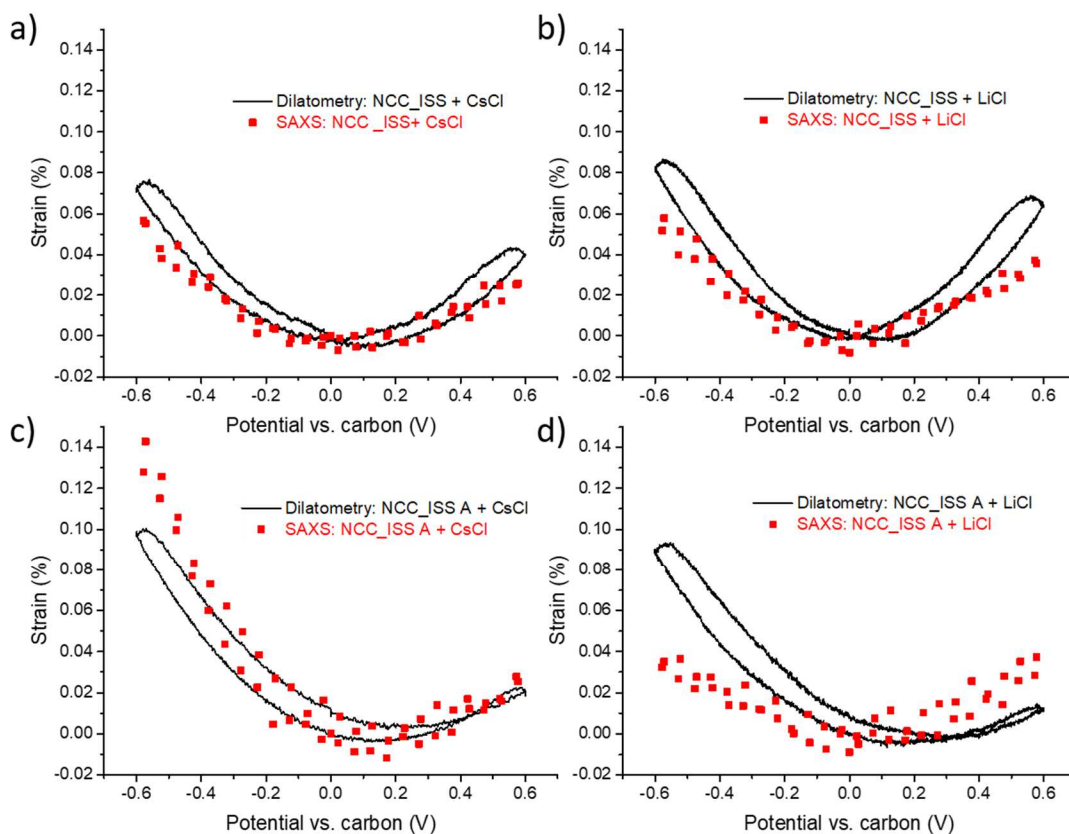


Figure 5.10: Strain vs. potential from in situ SAXS (red) and in situ dilatometry (black) for NCC\_ISS with aqueous 1M CsCl (a), NCC\_ISS with aqueous 1M LiCl (b), NCC\_ISS A with 1M CsCl (c), and NCC\_ISS A with 1M LiCl (d). All strain curves were recorded with a scan rate of  $1 \text{ mV s}^{-1}$ . Reprinted with permission from Ref.<sup>199</sup> Copyright 2017 American Chemical Society

The agreement is less satisfactory for the NCC\_ISS A sample shown in Figure 5.10c and Figure 5.10d. The strain curves measured with dilatometry are pronouncedly asymmetric, but similar for the two electrolytes. In the strain curves obtained from SAXS, a distinct dependence on the used electrolyte can be observed. For aqueous 1M CsCl, the SAXS curve is highly asymmetric, even exceeding the asymmetry of the dilatometry curve. For aqueous 1M LiCl however, the shape of the SAXS curve is almost symmetric. To be more precise, for positive applied voltage, the strain curves from SAXS are similar for both electrolytes and qualitatively consistent with the findings from dilatometry. For negative potential and aqueous 1M CsCl, the maximum SAXS strain exceeds the one from dilatometry by almost a factor of 1.5, while for LiCl the situation is reversed. It is possible that these differences are caused by contrast effects due to local ion rearrangement,<sup>34</sup> since upon charging counter-ions will accumulate near the carbon strut surface and within the micropores. At negative polarization, the carbon

pores are populated dominantly by  $\text{Cs}^+$  and  $\text{Li}^+$ , respectively, whose electron densities are strongly different. Therefore, we expect so-called “pseudostrains” influencing the measured peak shift.<sup>240</sup> The deviation from the macroscopic strain measured by dilatometry depends on the counter-ion electron density and the amount of micropores within the carbon struts. Considering additionally a higher strain at negative voltage as compared to positive voltage in the NCC\_ISS A sample as suggested from dilatometry, the data become qualitatively consistent.

## 5.5 Discussion

An asymmetric shape with higher strains for cation electrosorption as compared to anion electrosorption has been reported for in situ dilatometry studies on carbon electrodes before.<sup>141,241</sup> Using in situ SAXS and carbon materials with an ordered mesopore structure, it is shown here experimentally that this strain unambiguously originates from the micro-/mesopore scale by evaluating the shift of a Bragg reflection from the ordered mesopore lattice. The magnitude and the asymmetry of the strain with respect to the sign of the applied voltage was found to depend on the amount of micropores within the otherwise identical carbon nanorods of the model material. Therefore, ion size effects can be rejected to be exclusively responsible for the asymmetry, implying that the overall strain must be a combination of at least two individual effects. First, an increase in the total (cation plus anion) concentration upon electrode charging,<sup>20</sup> either globally (in all micro- and mesopores) or locally (only in sites with high degree of confinement<sup>34</sup>), would lead to a positive osmotic pressure and thus to an expansion for both, positive and negative polarizations.<sup>35,239</sup> A second effect being in the right order of magnitude is the variation of the C-C bond length. Electron/hole doping during electrode charging influences the band structure and hence the length of the C-C bonding.<sup>235,242</sup> Applying a negative potential elongates the bonding, which in consequence leads to an expansion, and vice versa. Such effects have been explicitly calculated for a simple model of the axial elongation of cylindrical nanopores with an ionic liquid as electrolyte, and have been successfully compared with experiments.<sup>239</sup>

Adding to this, here it is shown that an increase of microporosity (corresponding to an increase of the relative amount of surface carbon atoms) strongly enhances this asymmetry, being in good agreement with previous studies on different carbon materials.<sup>232</sup> A simple estimation of two strain contributions (symmetric and asymmetric) supports the prediction that asymmetric swelling is a surface related



effect and caused by electron/hole doping. Comparing the two carbons investigated in this chapter reveals a just slightly changed symmetric strain contribution (osmotic pressure) and roughly a doubling of the asymmetric contribution (electron/hole doping) in the micropore rich carbon (Figure 5.11). This corresponds roughly to the doubling of the micropore surface area in the pore size range between 0.63 nm and 1.3 nm (where the biggest change occurs) due to the activation process (Table 5.1). This is indeed expected since the influence of electron/hole doping should roughly scale with the surface area.

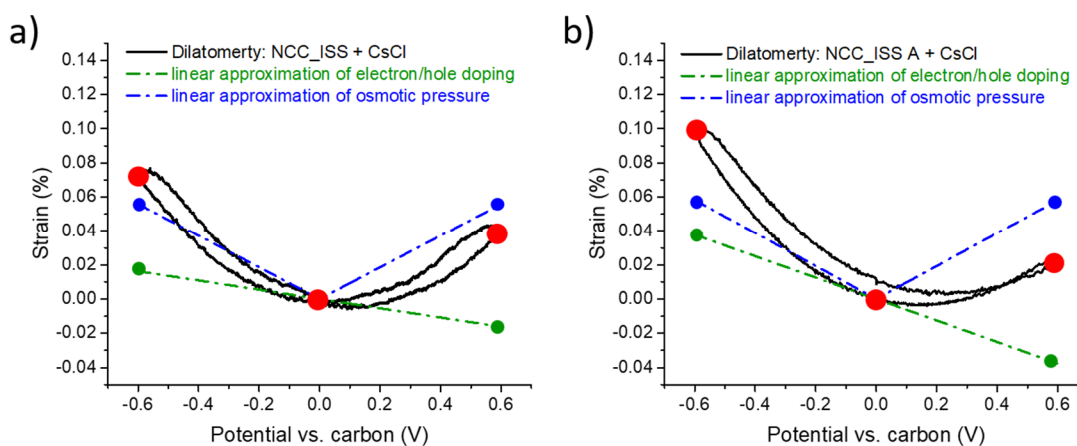


Figure 5.11: Linear strain approximation of the two main contributions electron/hole (green dots) doping and osmotic pressure (blue dots) for the NCC\_ISS (a) and the NCC\_ISS A (b). The red dots show the sum of the two contributions. The dashed lines do not show fitted curves

## 5.6 Conclusion

It was demonstrated that hierarchical carbons with hexagonally ordered carbon nanorods are useful model materials to investigate dimensional changes of supercapacitor electrodes during operation. The unique combination of a tailored material and novel in situ techniques makes the pore strain accessible on different length scales. The use of different electrolytes containing ions with different electron densities represents a contrast variation approach, which allowed to qualitatively separate X-ray contrast effects from real strains. By also performing in situ electrochemical dilatometry, it was possible to compare macroscopic swelling with dimensional changes on the length scale of the ordered mesopores. The investigation of two materials with different PSDs revealed that the amount of micropores inside the carbon nanorods considerably influences the polarization dependent magnitude of dimensional changes during operation.

## 6 Ion specific concentration change analyzed by ASAXS

In this chapter, in situ anomalous small-angle X-ray scattering (ASAXS) is evaluated as a method to extract both, real-time structural and ion-specific chemical information from one single experiment. Large parts of Chapter 6 have been submitted for publication.

### 6.1 Motivation

The most crucial requirement for the further improvement of EDLC electrodes is a comprehensive understanding of processes taking place in the complex nanopore space, and their impact on the electrochemical performance. For instance, a generally still unanswered question are the factors determining different ion storage mechanisms such as counter-ion adsorption, co-ion expulsion, or ion exchange.<sup>21,243</sup> Answering this question demands for high-resolution experimental techniques that not only allow comprehensive characterization of the nanopore structure beyond size distributions based on pore shape assumptions, but also the in situ monitoring of the local and global kinetics of the ions within the pore space and their preferred adsorption sites. Nuclear magnetic resonance (NMR),<sup>36</sup> electrochemical quartz crystal microbalance (eQCM),<sup>244</sup> and X-ray transmission (XRT)<sup>21</sup> have been employed for in situ studies within the recent years, providing crucial experimental data for the validation of theoretical predictions and numerical simulations.<sup>32,245-247</sup> eQCM and XRT, being sensitive to the mass and the X-ray absorption coefficient of the electrode, respectively, can only detect the net concentration of both, cations and anions. Therefore, complementary information, e.g. on the overall accumulated charge, is necessary to calculate cation and anion concentration changes separately as a function of an applied potential.<sup>20,244</sup> In addition, possible accompanying volume changes in the electrode material due to electrosorption induced deformation (see Chapter 5) and/or concentration changes of the solvent must either be known or be negligible to achieve interpretable results.<sup>20,36,244</sup> In contrast to eQCM and XRT, spectroscopic techniques like NMR are highly element-specific and provide local information on whether a specific ion type is preferentially adsorbed. However, they do not provide structural information comparable to SAXS measurements. Combinations of eQCM or XRT with NMR appear to be difficult, because

different cell geometries and different electrode volumes hamper a direct comparison of the results.<sup>21</sup>

Here, in situ anomalous small-angle X-ray scattering (in situ ASAXS) is presented as a powerful approach that fully utilizes the advantages of SAXS, and at the same time eliminates its main drawback concerning the lack of element sensitivity. In situ ASAXS provides simultaneous real-time structural and chemical information by combining SAXS with the principle of absorption spectroscopy by utilizing the change of the scattering power of a resonant element near its adsorption edge.

## 6.2 In situ ASAXS

### 6.2.1 Material characterization

**Material:** For all measurements shown in this chapter, an ordered mesoporous carbon material produced via nanocasting with an additional CO<sub>2</sub> activation procedure (2 hours at 925°C) was used (NCC\_ISAS). The electrode preparation was done according to Chapter 3.1. The structural parameters are shown in Table 3.1 and Table 6.1.

Table 6.1: Characterization information of the sample used for all ASAXS studies

Activation time (h)	S <sub>DFT</sub> <sup>(a)</sup> (m <sup>2</sup> g <sup>-1</sup> )	V <sub>micro</sub> <sup>(b)</sup> (cm <sup>3</sup> g <sup>-1</sup> )	V <sub>meso</sub> <sup>(b)</sup> (cm <sup>3</sup> g <sup>-1</sup> )	d <sub>50</sub> (d <sub>25</sub> -d <sub>75</sub> ) <sup>(c)</sup> (nm)	C <sup>(d)</sup> (F g <sup>-1</sup> )
2.0	1155	0.45	0.58	2.40 (1.26-3.00)	95

<sup>(a)</sup> Specific surface area obtained from NLDFIT using nitrogen adsorption isotherms

<sup>(b)</sup> Micro- ( $V_{micro}$ , pores < 2 nm) and mesopore volume ( $V_{meso}$ , 2 nm < pores < 30 nm)

<sup>(c)</sup> Volume-weighted median of the pore size  $d_{50}$  including the 25<sup>th</sup> and 75<sup>th</sup> percentile of the pore width ( $d_{25}$  and  $d_{75}$ ),<sup>186</sup>

<sup>(d)</sup> Capacitance values were obtained from cyclic voltammetry at 0.5 mV s<sup>-1</sup> with 1M RbBr in the range of ±0.6 V vs. carbon.

**Electrochemical characterization:** Figure 6.1 shows cyclic voltammetry measurements for two different scan rates (0.5 mV s<sup>-1</sup> and 2 mV s<sup>-1</sup>). It can be seen that the capacitance is higher for negative potential. This can be tentatively explained by a smaller (bare) ion size of Rb<sup>+</sup> compared to Br<sup>-</sup> leading higher accessible surface area for the Rb<sup>+</sup> ion.<sup>129,248</sup>

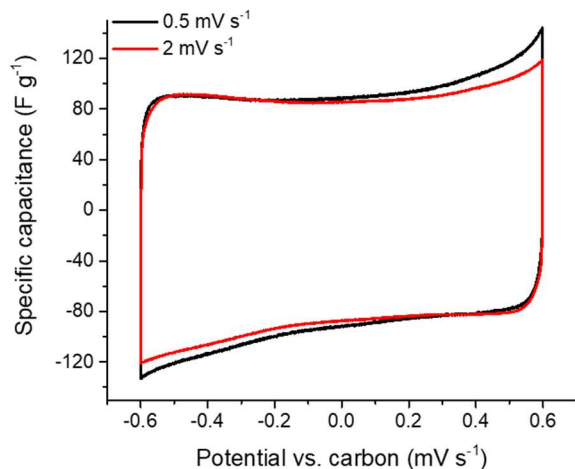


Figure 6.1: Cyclic voltammety for  $0.5 \text{ mV s}^{-1}$  and  $0.5 \text{ mV s}^{-1}$  scan rates using  $1 \text{ M RbBr}$  as electrolyte. Measurements were performed with an oversized CE as a quasi-reference

### 6.2.2 In situ ASAXS

ASAXS utilizes the energy dependence of the atomic scattering factor  $f$  of a specific element near its absorption edge (Equation 2.49) to obtain element specific information in systems containing more than two mesoscopic phases.<sup>100,107</sup> Figure 6.2a shows the anomalous scattering factors of Bromine (Br) and Rubidium (Rb),<sup>249</sup> which are present in the used electrolyte ( $1\text{M RbBr}$ ). The imaginary part  $f''$  is related to the X-ray absorption coefficient and is essentially constant at energies below the absorption edges (dashed vertical lines). The effective number of electrons of the resonant ion is however reduced in this region. Consequently, several SAXS measurements at different photon energies below the absorption edge of the resonating ion (indicated by black circles in Figure 6.2a) allow to change its effective electron number by roughly 10% (considering that  $\text{Br}^-$  and  $\text{Rb}^+$  having the same number of electrons,  $f_0 = 36$ ).

The ASAXS measurements were performed at four different energies below the Br and the Rb edge (Figure 6.2). For measurements at the Rb edge fluorescence contributions and the change of  $f'_{\text{Br}}$  can significantly influence the result of the data separation. To reduce these influences, only the three measurements closest to the absorption edge were used for data evaluation.

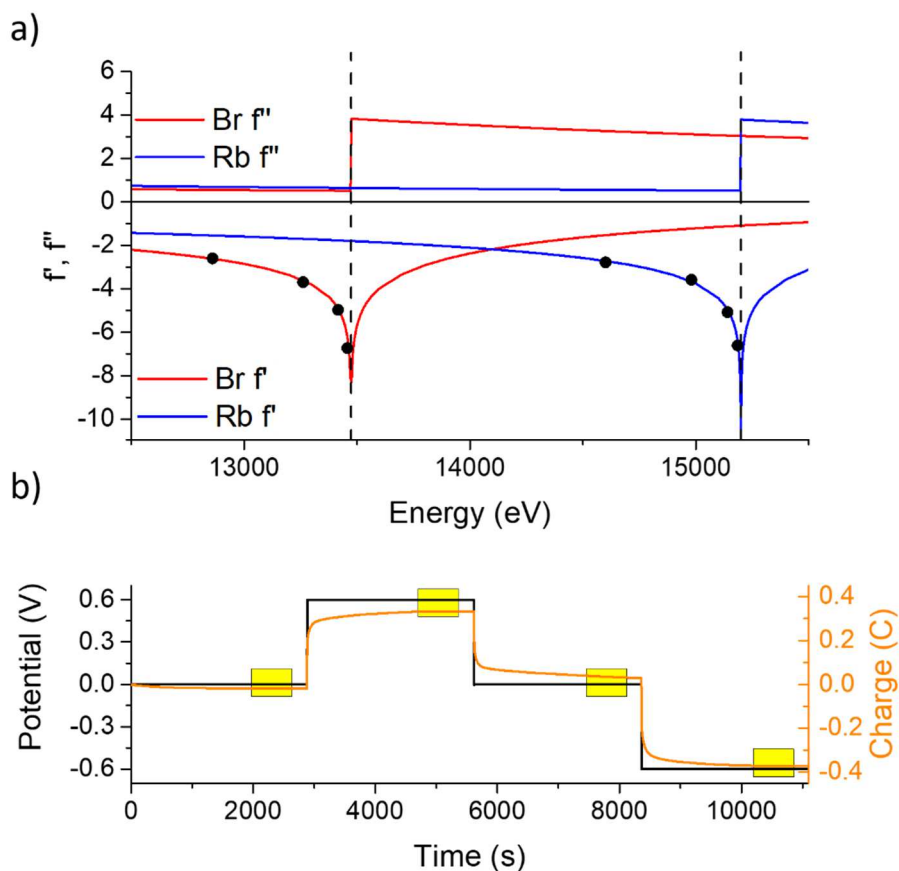


Figure 6.2: (a) Real- ( $f'$ ) and imaginary ( $f''$ ) parts of the energy dependent anomalous scattering factor as a function of the photon energy for Br and Rb.<sup>103</sup> The vertical dashed lines mark the absorption edges (Br: 13474 eV; Rb: 15200 eV) and the black dots are the energies of the performed ASAXS experiments. (b) Chronoamperometry measurements with the yellow boxes indicating the time period needed to perform the ASAXS measurements at the 8 different energies marked in (a). The accumulated charge for positive applied potentials is lower than for negative potentials. This is consistent with CV measurements (Figure 6.1).

## 6.3 Data evaluation

### 6.3.1 Effective $f'$ and $f''$ values

The position of the absorption edge, as well as  $f'$  and  $f''$ , necessary for the data analysis, are tabulated for all elements.<sup>103</sup> As seen in Equation 2.55, the measured scattering intensity strongly depends on the real and imaginary part of the scattering factor. Instrumental shifts (in particular regarding absolute energy calibration of the monochromator) as well as a chemical shift of the absorption edge lead to deviations from the theoretical calculations. For the evaluation of

ASAXS measurements the exact position of the absorption edge as well as the resulting shifts of the  $f'$  and  $f''$  function have to be taken into account. The measurements of the absorption edge revealed a shift of 3 eV for both ion species (Br<sup>-</sup> and Rb<sup>+</sup>) contained in the used electrolyte. If not corrected, this shift leads to wrong values of  $f'$  and  $f''$  and in further consequence to an error in the data analysis. In addition to this shift, the monochromator at ID02 has a limited energy resolution of  $\frac{\Delta E}{E} = 2 \cdot 10^{-4}$ .

The effective values  $f'_{eff}$  and  $f''_{eff}$  were calculated by weighting the shift corrected theoretical curves of  $f'$  and  $f''$  by a Gaussian energy distribution (Table 6.2).<sup>250</sup> For all data evaluation procedures corrected values  $f'_{eff}$  and  $f''_{eff}$  were used.

These corrections only slightly influence the measurements far away from the absorption edge, but need definitely to be taken into account in the close proximity of the absorption edge.

Table 6.2: Original and effective scattering factors

Energy (eV)	$\Delta E^{(a)}$ (eV)	$f'$	$f'_{eff}$	$f''$	$f''_{eff}$
12871	Br -600	-2.636	-2.640	0.551	0.550
13271	Br -200	-3.683	-3.696	0.521	0.520
13431	Br -40	-5.231	-5.306	0.509	0.509
13463	Br -8	-6.730	-7.130	0.508	0.529
14997	Rb -200	-3.741	-3.756	0.525	0.525
15157	Rb -40	-5.295	-5.370	0.515	0.515
15189	Rb -8	-6.790	-7.220	0.518	0.578

<sup>(a)</sup> Energy difference with respect to the measured Rb and Br absorption edge

### 6.3.2 Data separation

For experiments performed below the Br edge, the absence of any (energy dependent) fluorescence radiation allows a straightforward separation of the three scattering contributions using Equation 2.56. The calculation of the resonant scattering curve was performed by using all four energies as well as each possible subset of three different energies. The resulting set of four curves was then averaged to obtain the final resonant scattering curve (Figure 6.3).

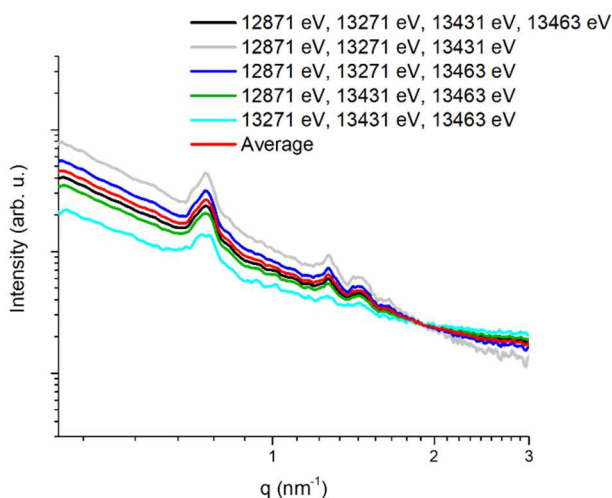


Figure 6.3: Resonant scattering calculated from measurements at different energies.

The fact that the Rb edge is quite close to the Br absorption edge (Figure 6.2) leads to a significant contribution of Br-fluorescence for the ASAXS experiments at the Rb edge, as shown in Figure 6.4. This additional  $q$ -independent, but energy dependent contribution in the SAXS data can dramatically change the calculated resonant scattering contribution. The voltage dependent scattering intensity from anion and cation concentration changes, together with the unknown voltage and energy dependent fluorescence from Br<sup>-</sup> ions in the electrode prevents an exact solution of Equation 2.56.<sup>107</sup>

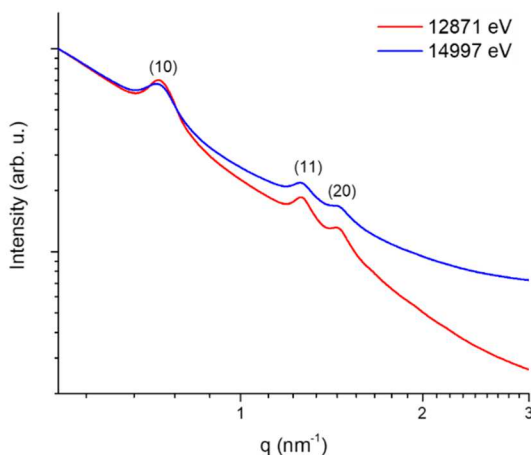


Figure 6.4: Scattering curves measured below (red curve) and above the absorption edge (blue curve) of Br. It can be seen that the fluorescence plays a big role for higher  $q$  values. In the range of the (10) peak the constant background from fluorescence is small compared to the scattering intensity. Both curves are normalized to 1 at  $q=0.5$  for better visibility of the fluorescence background.

The influence of the fluorescence on the calculation of the resonant scattering contribution will be discussed using the quadratic fit method (Equation 2.57) for a single set of intensities measured at the Rb edge.

The overall value of the fluorescence has no impact on the calculated resonant scattering curve, the change of the fluorescence contribution on the other hand can have a substantial impact on the solution of Equations 2.56 and 2.57. If a constant contribution is added to or subtracted from each measured point, it results only in an increase or decrease of the non-resonant contribution (Equation 2.57). This is shown in Figure 6.5, where from each point of a measured data set (black squares) an artificial fluorescence value (corresponding to the estimated fluorescence level at  $q = 8 \text{ nm}^{-1}$ ) is subtracted (red triangles). The calculated resonant intensity  $F_R^2$  is not affected. Only the value of  $F_0^2$  is reduced by this subtraction, which is expected from Equation 2.57. If the fluorescence value is not constant, but scales (e.g. linear) with the energy, there is also a change of the calculated resonant intensity  $F_R^2$ . This is illustrated in Figure 6.5: the blue triangles show a fluorescence background that decreases (artificially) linear with increasing energy. It can be clearly seen that in this case not only the non-resonant term  $F_0^2$ , but also the cross term and the resonant term  $F_R^2$  change.

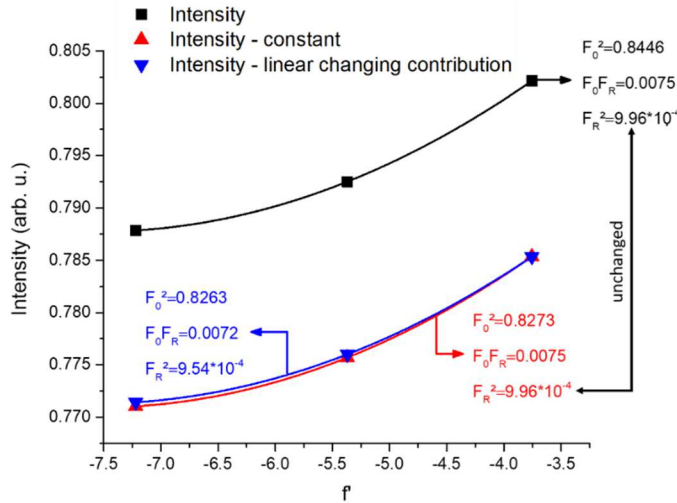


Figure 6.5: Representation of the influence of Br fluorescence subtraction on the calculated resonant scattering contribution at the Rb edge for  $q=0.31 \text{ nm}^{-1}$ . When a constant value is subtracted from the measured intensities (black squares), only the non-resonant contribution  $F_0^2$  changes (red triangles). In reality, the fluorescence is energy depended. The blue curve shows the result under the assumption of a linear (with energy) decreasing fluorescence contribution. It can be seen that this deviation from the ideal case leads to a change of the calculated resonant contribution. This effect is more pronounced for high  $q$ -values.



In reality, the fluorescence is energy depended, and only if the fluorescence radiation remains essentially constant within the energy window chosen for the ASAXS experiment, a reliable separation of the non-resonant and resonant scattering is possible. To keep the Br-fluorescence level for the ASAXS measurements at the Rb edge as constant as possible, a strongly reduced energy range of 192 eV with only three energies (as compared to 592 eV at the Br edge, with four energies) was used. Because of the reduced number of energies used and the fluorescence contribution, data obtained at the Rb edge are much noisier and have therefore been smoothed (adjacent averaging). The results obtained from the measurements at the Rb absorption edge are therefore not as reliable as the ones from the Br edge where no fluorescence contribution is present. It has to be noted, that in addition to the fluorescence radiation from Br, also the anomalous scattering factor  $f'$  of Br is not perfectly constant in the chosen energy interval, leading to a similar effect as the fluorescence. All calculations in this chapter were performed using Equation 2.56 under the assumption of a constant fluorescence.

### 6.3.3 Radiation damage

Radiation damage is a well-known issue when performing X-ray scattering experiments at high brilliance synchrotron radiation sources like the ESRF.<sup>251,252</sup> To estimate the possible influence of radiation damage during the ASAXS experiment, repeated measurements after different irradiation times with the synchrotron beam have been compared to the initial measurements. Figure 6.6 shows the initial SAXS curve (red line) as well as an advanced measurement (~372 seconds irradiated) at the same voltage (blue line). It was observed that the damage causes two major changes in the SAXS curve: an intensity drop by a  $q$ -independent factor proportional to the irradiation dose as well as a slight increase of the constant background with irradiation. The exposure dose between the shown curves is ~100 times higher than between the ASAXS measurements performed at each individual potential step and twice the dose between two potential steps. Therefore, within an individual ASAXS energy scan, the impact of radiation damage can be neglected.

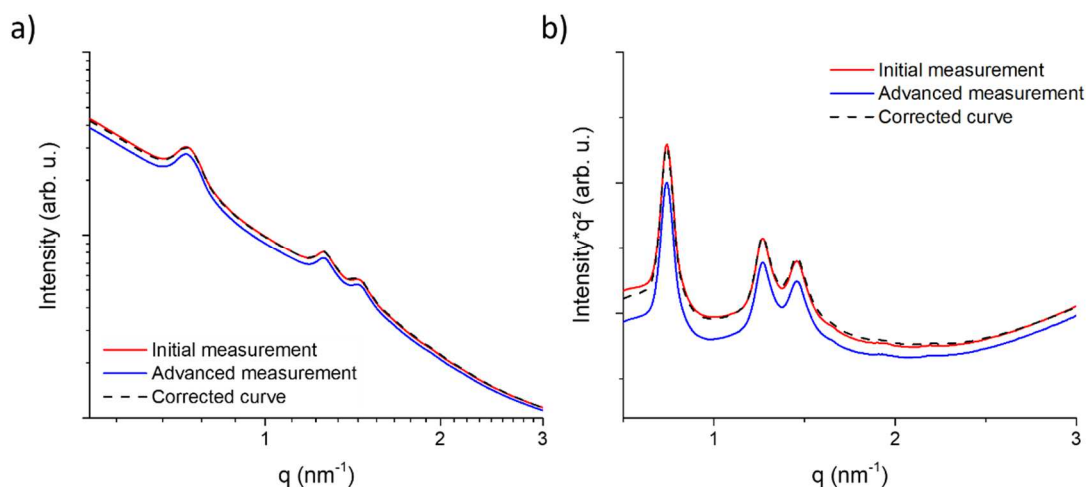


Figure 6.6: Radiation damage: (a) the red line shows the initial measurement and the blue line represents the same sample after a long exposure time. With a simple combination of a constant background increase and an intensity drop by a constant factor, the radiation damage can be nearly compensated (dashed black line). (b) Kratky plot for the measured curves as well as the corrected curve.

To evaluate the influence of the radiation damage on the results from different ASAXS experiment at different applied potentials, it is helpful to look at Equation 2.57 again. Similar to the fluorescence contribution, an increased constant background has no influence on the resonant scattering intensity. The intensity drop due to radiation damage on the other hand will change both, the resonant and the non-resonant scattering intensity by the same percentage. Since the intensity decreases roughly linearly with irradiation dose, the accumulated dose being known for each measured SAXS pattern from the accumulated monitor signal at the beamline, all results shown could be corrected for radiation damage under his assumption.

## 6.4 Results and discussion

The SAXS data at a given energy (Figure 6.7a) show an increase of the intensity at +0.6V and a corresponding decrease at -0.6 V as compared to the neutral case at 0 V, with some  $q$ -dependent differences. If we recall that  $\text{Br}^-$  and  $\text{Rb}^+$  have the same number of electrons ( $f_0 = 36$ ), and the anomalous contributions are small at this energy, a pure ion replacement mechanism is not compatible with these changes.

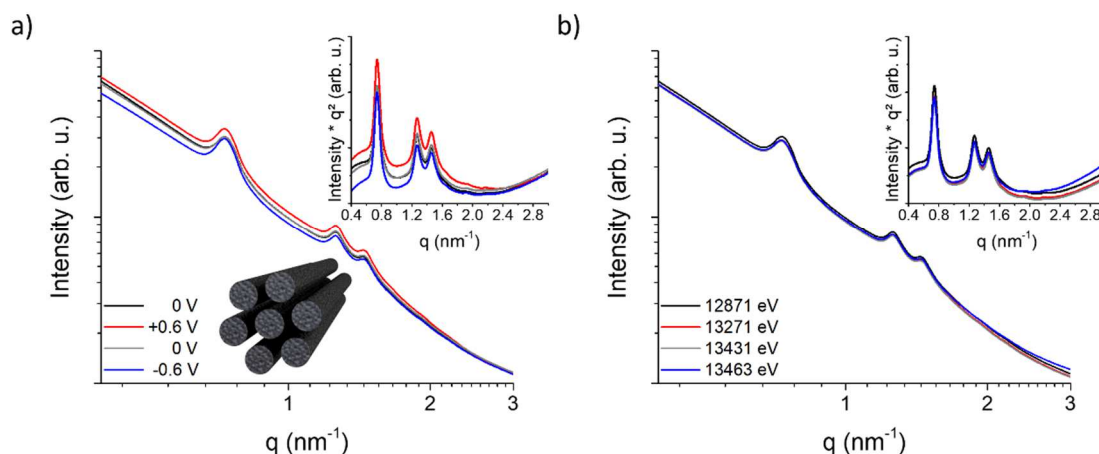


Figure 6.7: SAXS profiles from the working electrode at different applied potentials and a photon energy of 12871 eV (a), and at different photon energies close to the Br edge at a potential of 0 V (b). For a better visualization of the Bragg peaks insets showing Kratky plots<sup>82</sup> ( $I(q) \cdot q^2$  versus  $q$ ) are included. The peaks originate from the hexagonally ordered carbon nanorods, which are shown schematically in (a)

In previous work on disordered microporous carbon electrodes, a strategy was developed how to evaluate such data towards the local ion configuration within the micropore network with the aid of real space pore models combined with Monte Carlo simulations.<sup>34</sup> However, the global ion concentration was an experimental input parameter (obtained from XRT).<sup>21</sup> Therefore, the voltage dependent global concentration for each ion species via ASAXS is highly desirable. The SAXS experiments at different energies (Figure 6.7b) show a small but systematic dependency of the scattering intensity on the photon energy.

The separation of the non-resonant and the resonant scattering contribution was performed by solving a linear system of equations,<sup>104</sup> as already described in Chapter 2.6.1. The non-resonant scattering intensity (Figure 6.8 black curve) contains the usual SAXS information from all species within the irradiated volume, i.e., anions, cations, the solvent, and the electrode material itself. In contrast, the resonant scattering curve (Figure 6.8 red curve) contains information on the spatial arrangement of the resonant ion only, as illustrated schematically in the corresponding inset. First, it should be noted that the magnitude of the resonant term is about two orders of magnitude smaller than the one of the non-resonant term, which gives an indication on the high demands with respect to the required data quality for an ASAXS experiment. Second, the shapes of the resonant and non-resonant scattering curves are in general quite similar (Figure 2.21 shows a direct comparison of the non-resonant and resonant scattering intensity of this sample). Therefore, the focus in this thesis is first on the total (integrated)

intensity changes of the resonant scattering curves with applied potential and not on the attempt to evaluate the details of the resonant scattering curves.

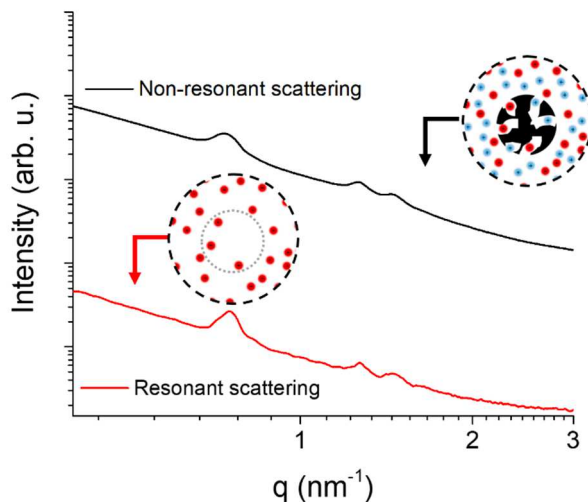


Figure 6.8: Non-resonant (black) and resonant (red) ASAXS intensity at the Br edge and a potential of 0 V. The insets show schematic representations of the respective scattering contributions (black: carbon, red: Br<sup>-</sup>, blue: Rb<sup>+</sup>; the solvent water would also be contributing to the non-resonant scattering, but is not shown for clarity).

For Br (Figure 6.9a) the resonant scattering curves show a significantly stronger intensity decrease for negative potential (-0.6 V), as compared to the intensity increase for positive potential (+0.6 V). There is also a slight change from the first to the second measurement at 0 V, which was performed to have an internal monitor for possible radiation damage due to the high primary photon flux of the synchrotron beam.

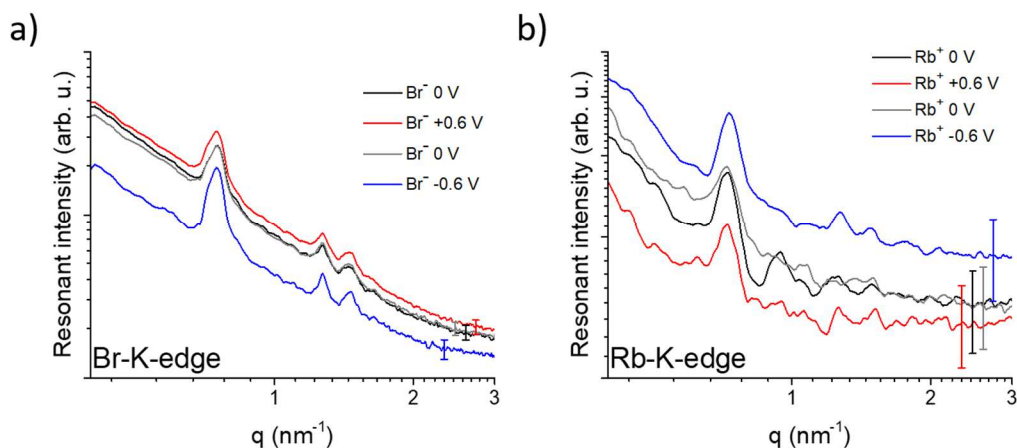


Figure 6.9: Resonant ASAXS curves for Br (a) and Rb (b), at different applied potentials.

The resonant intensity curves from the Rb-edge are considerably more noisy as compared to those from the Br-edge. Yet, a noteworthy different change of the resonant  $\text{Rb}^+$  scattering curves with the applied potential is obvious in Figure 6.9b. The intensity increases for negative and decreases for positive potential in this case as expected, but in contrast to  $\text{Br}^-$ , there is no evident asymmetry with respect to 0 V for  $\text{Rb}^+$ .

The integrated intensity of a two-phase system (e.g. pores in carbon) is proportional to  $\phi(1 - \phi)\Delta\rho^2$ , where  $\phi$  is the porosity and  $\Delta\rho^2$  the effective electron density contrast between pores and carbon.<sup>82</sup> Similarly, for the resonant scattering curves, the mean effective electron density level in the pores is determined by the concentration of the corresponding resonant ion species. Assuming negligible (effective) porosity changes,<sup>20</sup> the square root of the integrated intensity change is therefore proportional to the resonant ion concentration change (Figure 6.10a). The amount of  $\text{Br}^-$  ions is higher and the amount of  $\text{Rb}^+$  ions is lower at positive potential as compared to 0 V, and the opposite holds true for negative potential. Interestingly, the  $\text{Br}^-$  ions clearly show a different behavior for positive and negative potentials. At positive potential, the concentration of anions increases slightly, while it is significantly reduced at negative potential. In contrast, the behavior of the cations ( $\text{Rb}^+$ ) appears to be symmetric around 0 V. It should be kept in mind that the data for the  $\text{Rb}^+$  ions show a considerably larger experimental uncertainty than the  $\text{Br}^-$  data, and a possible slight asymmetry for the cations cannot unambiguously be excluded. Yet, the data in Figure 6.10a suggest that there are two different charging mechanisms present, depending on the applied potential: ion replacement for negative applied potential, and a combination of co-ion expulsion and ion replacement for positive potential. Interestingly, the asymmetry in the cation and anion concentration changes goes along with a slight asymmetry in the observed specific capacitance. Co-ion expulsion has recently been observed in electrodes with organic electrolyte using in situ NMR,<sup>36</sup> and in the initial state of charging in disordered activated carbon electrodes with aqueous  $\text{RbBr}$  using in situ XRT.<sup>21</sup> Two possible reasons for the observed behavior are considered. First, differences in ion size (bare and hydrated), hydration enthalpy, or mobility<sup>21,174</sup> (Table 6.3), might cause ion-specific interactions with the carbon confinement and thus asymmetric concentration changes. Second, specifically adsorbed  $\text{Br}^-$  ions at 0 V, possibly cause a negative potential of zero charge, resulting in a saturation of adsorbed  $\text{Br}^-$  ions at positive potentials.<sup>253,254</sup> The data given in Figure 6.10a do not directly contain this information, since only the relative intensity change with respect to

the intensity at 0 V is given. Detailed atomistic simulations and additional experiments are needed to fully understand the origin of the different ion behavior, which is beyond the scope of this work.

Table 6.3: Ion radii and mobility

Ion	Bare ion radius <sup>248</sup> (nm)	Hydrated radius <sup>248</sup> (nm)	Mobility <sup>255</sup> ( $10^{-8} \text{ m}^2 \text{ V}^{-1} \text{ s}^{-1}$ )	Diffusion coefficient <sup>255</sup> ( $10^{-9} \text{ m}^2 \text{ s}^{-1}$ )	Hydration enthalpy <sup>57</sup> (kJ mol <sup>-1</sup> )
Br <sup>-</sup>	0.195	0.330	7.20	1.85	-17.9
Rb <sup>+</sup>	0.148	0.329	7.70	1.98	-18.5

The integrated intensity provides information on the element-specific cation and anion concentration changes within the range of length scales covered by the  $q$ -range in the SAXS data ( $\pi/q \approx 1 \text{ nm} - 7 \text{ nm}$ ). Since this range covers essentially the entire micro-/mesopore sizes of the investigated carbon, these changes can be interpreted as *global ion concentration* changes. Additional information on possible *local ion-specific re-arrangement*<sup>20,34,173</sup> may be obtained from the  $q$ -dependent changes of the resonant SAXS profiles. The following discussion is restricted to the anions only, because of the large scatter of the resonant scattering data from the Rb edge.

While the diffuse scattering in Figure 6.9a does not exhibit noticeable  $q$ -dependent intensity variations, the three Bragg reflections from the ordered mesopore arrangement do show peak-dependent changes with the applied potential. This is visualized in Figure 6.10b, where the diffuse scattering contribution was subtracted from each resonant Br<sup>-</sup> SAXS profile. A similar trend as for the integrated intensity, i.e., a peak intensity decrease for negative potential and an increase for positive potential was observed. However, there are obvious differences for the three Bragg peaks as indicated by the relative Bragg-peak areas in Figure 6.10b. The first order Bragg-peak decrease at negative potential is less than the increase at positive potential, just opposite to the integrated intensity (Figure 6.10a). This is a clear sign of a local redistribution of the Br<sup>-</sup> ions within the micro- and mesopores. Indeed, such diffraction-peak intensity changes are known to be very sensitive to the form-factor of the ordered mesopore structure, which is affected by the adsorption of guest species at or within the mesopore walls.<sup>84</sup>

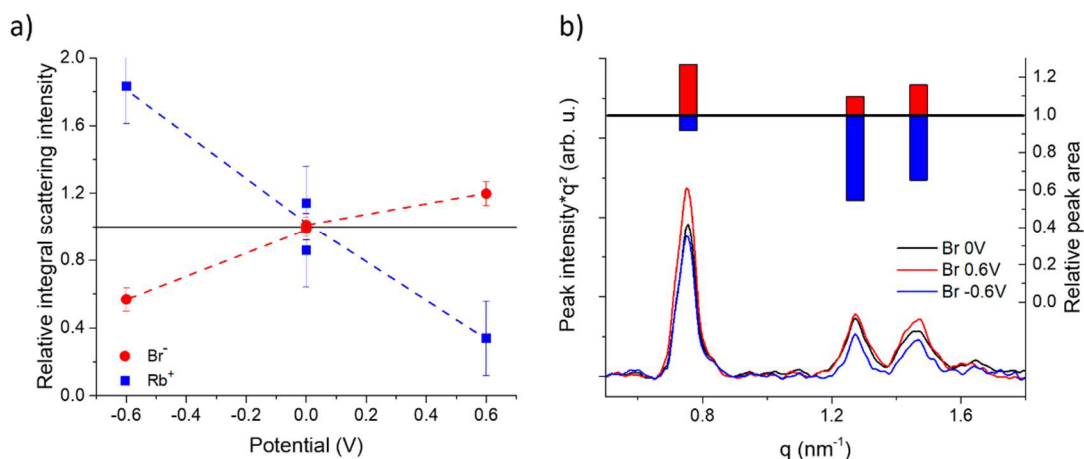


Figure 6.10: (a) Integrated intensity of the resonant scattering curves versus applied potential for Rb<sup>+</sup> (blue) and Br<sup>-</sup> (red). The dashed lines are guides for the eye. (b) Kratky plot of the Bragg-peaks (after subtraction of the diffuse scattering) and relative peak area for different applied potentials.

A future quantification attempt requires detailed information on the nanopore structure (such as the activation induced microporosity gradient within the carbon nanorods), and sufficiently large changes of the Bragg-peaks to set-up a detailed form-factor model. The ASAXS capabilities of element specificity, together with improved model carbons with more clearly separated micro- and mesopore distributions, can thus enable unimagined details of ion re-arrangement in hierarchical pore spaces. It has to be emphasized that compared to previous in situ SAXS studies,<sup>20,21,34,173</sup> no additional electrochemical data are necessary for in situ ASAXS, as it is both, structure- and element sensitive. This fact may not be of academic interest only, as electrochemical data include the whole electrode, while the SAXS (and XRT) measurements cover typically a much smaller electrode volume hit by the X-ray beam. Therefore, such experiments would enable also position sensitive ASAXS measurements at different electrode locations, and would for instance allow studying the influence of the cell design on the local ion storage mechanism.

### 6.4.1 Fluorescence data

During the ASAXS experiment it was possible to perform additional in situ fluorescence measurements at the same instrument (ID02, ESRF). The intensity change of the emitted fluorescence radiation is proportional to the change of the total ion concentration in the irradiated volume. In contrast to XRT

experiments,<sup>20,21</sup> there is no additional data from electrochemical measurements needed to analyze the concentration change of each individual ion species.

Figure 6.11 shows the applied potential and the corresponding fluorescence detector image of a measurement just above the Rb absorption edge (15250 eV). In the detector image, it can be seen that the Br and Rb fluorescence lines behave differently. At maximum positive potential, the Rb fluorescence shows a minimum and the Br fluorescence shows a maximum. For the maximum negative potential, this is reversed, as expected.

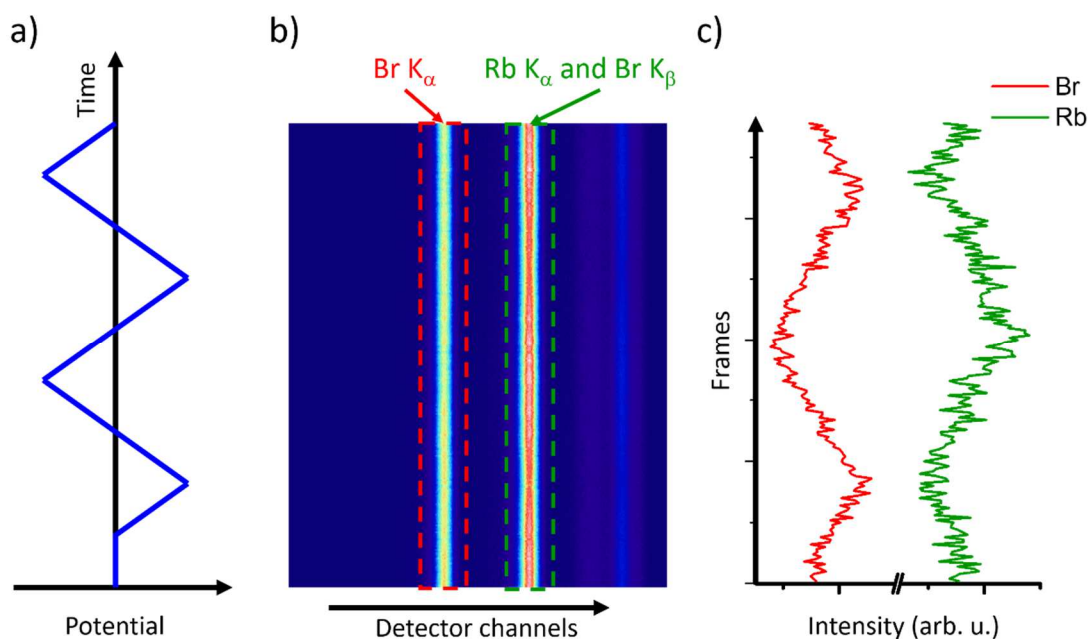


Figure 6.11: Schematic representation of the applied potential (a), the corresponding fluorescence detector image (b) and intensity of the Br and Rb fluorescence (c). The intensity change of the fluorescence signal is proportional to the concentration change of the corresponding ion species.

To calculate ion concentration changes as a function of the applied potential, it is necessary to calculate the intensity of the Br K<sub>α</sub> and the Rb K<sub>α</sub> signal. From the Br K<sub>α</sub> signal it is possible to directly calculate the relative concentration change of Br ions. The case is a little bit more complicated for the Rb ions. The reason is that the Rb K<sub>α</sub> (13395 eV) line is close to the Br K<sub>β</sub> (13292 eV) line<sup>256</sup> and cannot be resolved separately (Figure 6.12). As a result, the measured intensity does not represent the change of Rb ions directly, but is a combination of both ion species. To accurately calculate the change of the Rb ion concentration, it is necessary to subtract the Br K<sub>β</sub> contribution.



To evaluate the Br  $K_{\beta}$  contribution, a measurement below the Rb absorption edge was performed (Figure 6.12) to calculate the relation between the Br  $K_{\alpha}$  and Br  $K_{\beta}$  intensities. It was found that the intensity of the Br  $K_{\beta}$  signal is  $\sim 25\%$  of the Br  $K_{\alpha}$  signal.

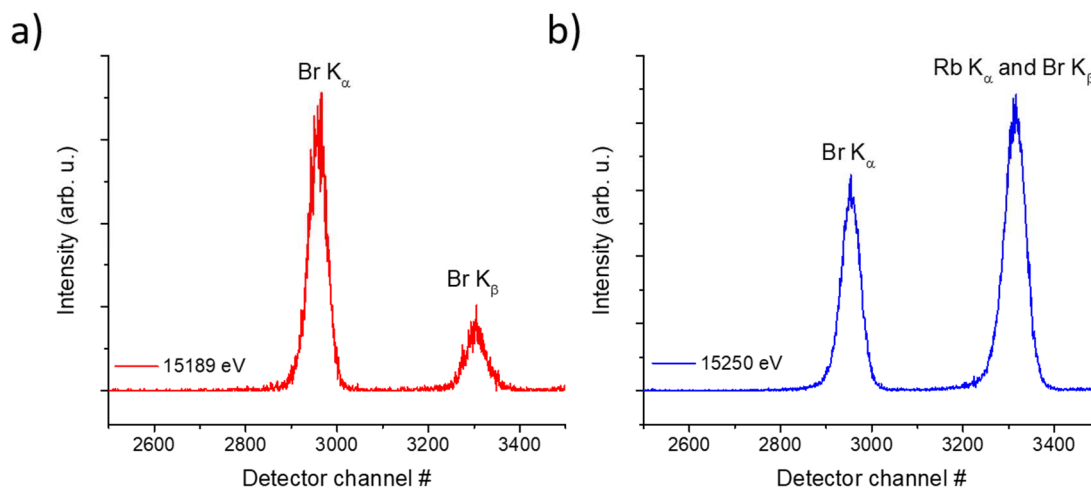


Figure 6.12: Fluorescence measurements below (a) and above (b) the Rb absorption edge. It can be clearly seen that the Br  $K_{\beta}$  and the Rb  $K_{\alpha}$  cannot be resolved separately but merge to a single peak.

After subtracting the Br  $K_{\beta}$  contribution ( $\sim 25\%$  of the Br  $K_{\alpha}$  signal), to obtain the “pure” Rb  $K_{\alpha}$  signal can be used to calculate the concentration changes of the Rb ions. The change of the (corrected) peak area is directly proportional to change of the concentration of each individual ion species. It has to be mentioned that no calibration of the fluorescence detector was performed. Therefore, the results obtained from this experiments are rough estimations to give the trends. Although, the ion concentration change shown in Figure 6.13b is in good agreement with previous studies using XRT methods.<sup>20,21</sup> Additionally, it can be seen that the difference between cation and anion change is higher for negative than for positive potentials. This fits the CV data, where a higher capacitance for negative potentials was observed (Figure 6.13a). Interestingly, the results of the fluorescence experiments differ from the results obtained from ASAXS. This can be explained by the different electrochemical testing methods. While the ASAXS measurement was performed in a nearly equilibrium state (chronoamperometry with  $\sim 2000$  seconds equilibration time), the fluorescence measurements were performed during cyclic voltammetry with a scan rate of  $2 \text{ mV s}^{-1}$ . It is already known from previous studies that these two measurements (and even a change of the scan rate) can influence the charging behavior in an ECLC.<sup>21</sup>

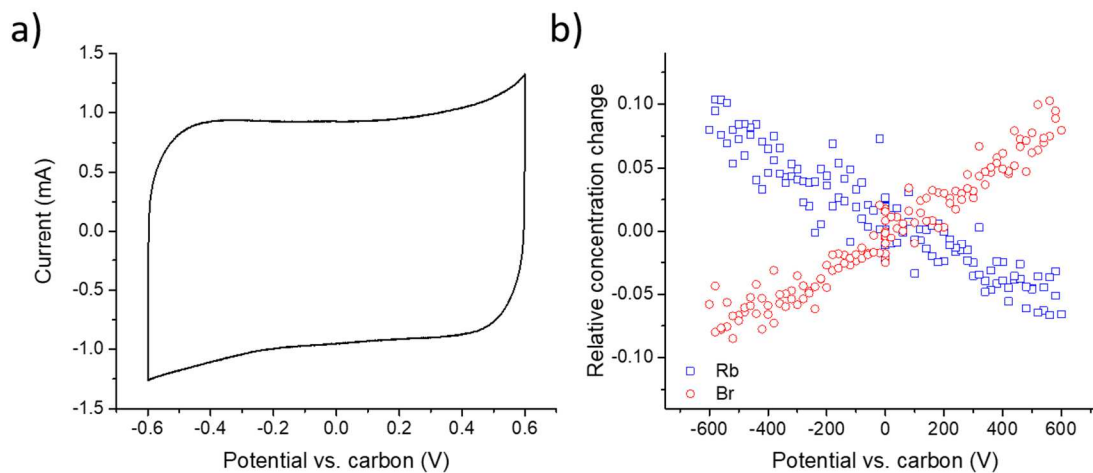


Figure 6.13: (a) Cyclic voltammogram recorded with an in situ cell at  $2 \text{ mV s}^{-1}$  during the fluorescence measurement. (b) Calculated ion concentration change as a function of the applied potential.

## 6.5 Conclusion

It was shown that in situ ASAXS is a powerful new method providing access to real-time ion-specific structural information in an aqueous nanoporous carbon-based supercapacitor cell. Different relative global- and local concentration changes of anions and cations were shown to occur for positive and negative applied potentials in an activated carbon electrode with ordered mesopores. This proof-of-principle experiment sets the basis to exploit the full potential of in situ ASAXS for contributing to the elucidation of further unknown details of ion electrosorption in nanoporous carbons. For instance, the recent advanced SAXS data analysis method to synergistically combine SAXS with atomistic Monte Carlo simulations<sup>34,173</sup> can easily be extended to element-specific ASAXS. More generally, the lack of suitable structure-sensitive in situ techniques critically impedes progress in increasingly complex electrochemical systems for energy storage and conversion beyond supercapacitors and CDI. In situ ASAXS has the potential to contribute substantially to fill this gap in the future. However, its future widespread use relies on highest data quality, further experimental and theoretical development, a wide accessible energy range, and access to specialized beamlines dedicated for ASAXS. With the combination of cyclic voltammetry and fluorescence measurements it was possible to confirm results from previous studies using a combination of X-ray transmission and electrochemical data.<sup>20,21</sup>

## 7 Summary and outlook

The main goal of this thesis was to increase the understanding of electrode and ion behavior during charging and discharging of an operating carbon based supercapacitor device, as well as the development and improvement of measurement techniques suitable to achieve this goal.

Three main questions treated in this thesis:

1. How does the pore structure influence the charging behavior?
2. How does the charging influence the electrode material and can the electrode expansion be linked to the pore structure?
3. Is it possible to study ion charging behavior with ASAXS without the need of additional data (from electrochemical measurements) or ambiguous simplifications and assumptions necessary to interpret the data?

To answer these questions, a set of two different hierarchically ordered mesoporous carbon materials was used. These materials are either composed of hexagonally packed nanofibers or cylindrical nanopores arranged on a hexagonal lattice. With different additional CO<sub>2</sub> activation treatments it was possible to tune the pore size distribution and increase the specific surface area. As a result, two structures, essentially representing the negative of each other were available. These materials allowed the development and improvement of experiments and data analysis tools to (at least partly) answer the three above mentioned questions (see Chapters 4-6).

It was shown that the pore structure of the electrode has a significant impact on the rate handling capability of a supercapacitor device. However, that does not mean that the charging and discharging processes are now fully understood. Additional measurements, numerical simulations and theoretical calculations are needed to gain a detailed understanding of the ion and electrode behavior:

First, a detailed understanding of the structure of the carbon materials is necessary. The characterization studies have shown that the hexagonally ordered mesostructure definitely survives the activation treatment, although the order is reduced upon during this process. However, there are still some open questions. Where exactly are the micropores located? In the NCC materials they have to be located in the carbon nanorods, in the STC they have to be in the mesopore walls, but how are they distributed? How exactly does the activation process

change the structure? To answer these questions a detailed structural model is necessary. In addition to the structural changes, it is also important to understand how the surface chemistry is influenced by the activation treatment. A detailed knowledge of the materials and the changes occurring during the activation process can help to further evaluate charging processes and expansion behavior.

As it was shown in Chapter 5, the pore structure has an influence on the volumetric change of a supercapacitor electrode. To examine the influence of the micropores in more detail, additional experiments and theoretical calculations of the influence of electron/hole doping are necessary. The measurement of samples with different CO<sub>2</sub> activation treatments as well as the use of soft templated carbons (containing hexagonally ordered cylindrical mesopores) could be a step in the right direction. Both experiments have been performed, but suffered from major issues: the position of the X-ray beam was not as stable (see Chapters 5.3.2). As a result, it was not possible to adequately analyze the data. The used not-calcined STC samples investigated turned out to be not suitable for the in situ experiments because of their hydrophobic nature (see Chapter 5.3.4). The calcined samples did not show this behavior and should be suitable to perform in situ SAXS measurements. Unfortunately the calcined samples were not available for this experiment and should be considered for future investigations. In addition to the pore structure, also the surface chemistry could influence the expansion behavior, a fact that was not taken into account at all up to now.

The shown ASAXS experiments have been designed as a proof-of-concept study. It was possible to show that ASAXS can be used to study behavior of individual ions without any additional (electrochemical) data need for the interpretation. It is known from earlier work that the behavior of the used electrolyte (containing RbBr) is somewhat different compared to others.<sup>20,21</sup> Due to the limited photon energy range available for ASAXS experiments, RbBr is the only possible electrolyte with a monovalent cation and anion with an absorption edge for both species in the energy range of ID02. To get a detailed understanding of the ion behavior it would be of interest to exchange the cation and anion (using RbCl and CsBr).

Fluorescence radiation can be a major issue when performing ASAXS experiments, especially in systems containing components with absorption edges near the edge of the investigated species. An optimized setup and the integration of the fluorescence detector can help evaluate the fluorescence contribution in the scattering pattern and help to improve the results obtained from ASAXS experiments.

The presented ASAXS experiment is a first step towards a “dream” experiment: simultaneously measuring the concentration changes and structural changes of each species in the sample

In situ (anomalous) small-angle X-ray scattering experiments can play help to gain a detailed understanding of the ion and electrode behavior in carbon based supercapacitor devices. These techniques can be used to study charging mechanisms as well as parameters influencing them. This information can help to identify crucial effects and material characteristics to improve the electrochemical performance of future supercapacitor devices.

In conclusion: although there are still a lot of open questions needed to be answered, ordered mesoporous carbon materials in combination with electrochemical characterization and in situ scattering experiments proved to be a step towards a better understanding of charging processes in supercapacitors.

## 8 Bibliography

- (1) Delpla, I.; Jung, A.-V.; Baures, E.; Clement, M.; Thomas, O. Impacts of climate change on surface water quality in relation to drinking water production. *Environment international* **2009**, *35*, 1225–1233, DOI: 10.1016/j.envint.2009.07.001.
- (2) Kanae, S. Global Warming and the Water Crisis. *J. Health Sci.* **2009**, *55*, 860–864, DOI: 10.1248/jhs.55.860.
- (3) Shope, R. Global climate change and infectious diseases. *Environmental health perspectives* **1991**, *96*, 171–174, DOI: 10.1289/ehp.9196171.
- (4) Botkin, D. B.; Saxe, H.; Araújo, M. B.; Betts, R.; Bradshaw, R. H. W.; Cedhagen, T.; Chesson, P.; Dawson, T. P.; Etterson, J. R.; Faith, D. P.; Ferrier, S.; Guisan, A.; Hansen, A. S.; Hilbert, D. W.; Loehle, C.; Margules, C.; New, M.; Sobel, M. J.; Stockwell, D. R. B. Forecasting the Effects of Global Warming on Biodiversity. *BioScience* **2007**, *57*, 227–236, DOI: 10.1641/B570306.
- (5) Pounds, J. A.; Bustamante, M. R.; Coloma, L. A.; Consuegra, J. A.; Fogden, M. P. L.; Foster, P. N.; La Marca, E.; Masters, K. L.; Merino-Viteri, A.; Puschendorf, R.; Ron, S. R.; Sánchez-Azofeifa, G. A.; Still, C. J.; Young, B. E. Widespread amphibian extinctions from epidemic disease driven by global warming. *Nature* **2006**, *439*, 161–167, DOI: 10.1038/nature04246.
- (6) Chowdhury, F. R.; Nur, Z.; Hassan, N.; Seidlein, L. von; Dunachie, S. Pandemics, pathogenicity and changing molecular epidemiology of cholera in the era of global warming. *Annals of clinical microbiology and antimicrobials* **2017**, *16*, 10, DOI: 10.1186/s12941-017-0185-1.
- (7) Garcia-Solache, M. A.; Casadevall, A. Global warming will bring new fungal diseases for mammals. *mBio* **2010**, *1*, DOI: 10.1128/mBio.00061-10.
- (8) Hartelt, K.; Pluta, S.; Oehme, R.; Kimmig, P. Spread of ticks and tick-borne diseases in Germany due to global warming. *Parasitology research* **2008**, *103 Suppl 1*, S109-16, DOI: 10.1007/s00436-008-1059-4.
- (9) Meinshausen, M.; Meinshausen, N.; Hare, W.; Raper, S. C. B.; Frieler, K.; Knutti, R.; Frame, D. J.; Allen, M. R. Greenhouse-gas emission targets for limiting global warming to 2 degrees C. *Nature* **2009**, *458*, 1158–1162, DOI: 10.1038/nature08017.
- (10) Agnew, S.; Dargusch, P. Effect of residential solar and storage on centralized electricity supply systems. *Nature Clim Change* **2015**, *5*, 315–318, DOI: 10.1038/NCLIMATE2523.

- 
- (11) Trancik, J. E. Renewable energy: Back the renewables boom. *Nature* **2014**, *507*, 300–302, DOI: 10.1038/507300a.
- (12) Braff, W. A.; Mueller, J. M.; Trancik, J. E. Value of storage technologies for wind and solar energy. *Nature Clim Change* **2016**, *6*, 964–969, DOI: 10.1038/NCLIMATE3045.
- (13) Hittinger, E.; Whitacre, J. F.; Apt, J. What properties of grid energy storage are most valuable? *J. Power Sources* **2012**, *206*, 436–449, DOI: 10.1016/j.jpowsour.2011.12.003.
- (14) Evans, A.; Strezov, V.; Evans, T. J. Assessment of utility energy storage options for increased renewable energy penetration. *Renew. Sust. Energ. Rev.* **2012**, *16*, 4141–4147, DOI: 10.1016/j.rser.2012.03.048.
- (15) Beguin, F.; Presser, V.; Balducci, A.; Frackowiak, E. Carbons and electrolytes for advanced supercapacitors. *Adv. Mater. (Weinheim, Ger.)* **2014**, *26*, 2219–51, 2283, DOI: 10.1002/adma.201304137.
- (16) Dubal, D. P.; Ayyad, O.; Ruiz, V.; Gomez-Romero, P. Hybrid energy storage: the merging of battery and supercapacitor chemistries. *Chem. Soc. Rev.* **2015**, *44*, 1777–1790, DOI: 10.1039/c4cs00266k.
- (17) Fathabadi, H. Novel fuel cell/battery/supercapacitor hybrid power source for fuel cell hybrid electric vehicles. *Energy* **2018**, *143*, 467–477, DOI: 10.1016/j.energy.2017.10.107.
- (18) Yu, Z.; Zinger, D.; Bose, A. An innovative optimal power allocation strategy for fuel cell, battery and supercapacitor hybrid electric vehicle. *J. Power Sources* **2011**, *196*, 2351–2359, DOI: 10.1016/j.jpowsour.2010.09.057.
- (19) Simon, P.; Gogotsi, Y.; Dunn, B. Materials science. Where do batteries end and supercapacitors begin? *Science* **2014**, *343*, 1210–1211, DOI: 10.1126/science.1249625.
- (20) Prehal, C.; Weingarth, D.; Perre, E.; Lechner, R. T.; Amenitsch, H.; Paris, O.; Presser, V. Tracking the structural arrangement of ions in carbon supercapacitor nanopores using in situ small-angle X-ray scattering. *Energy Environ. Sci.* **2015**, *8*, 1725–1735, DOI: 10.1039/c5ee00488h.
- (21) Prehal, C.; Koczwar, C.; Amenitsch, H.; Presser, V.; Paris, O. Salt concentration and charging velocity determine ion charge storage mechanism in nanoporous supercapacitors. *Nat. Commun.* **2018**, *9*, 4145, DOI: 10.1038/s41467-018-06612-4.
- (22) Simon, P.; Gogotsi, Y. Materials for electrochemical capacitors. *Nat. Mater.* **2008**, *7*, 845–854, DOI: 10.1038/nmat2297.

- (23) Raviv, U.; Laurat, P.; Klein, J. Fluidity of water confined to subnanometre films. *Nature* **2001**, *413*, 51–54, DOI: 10.1038/35092523.
- (24) Meissner, J.; Prause, A.; Findenegg, G. H. Secondary Confinement of Water Observed in Eutectic Melting of Aqueous Salt Systems in Nanopores. *J. Phys. Chem. Lett.* **2016**, *7*, 1816–1820, DOI: 10.1021/acs.jpcllett.6b00756.
- (25) Rasaiah, J. C.; Garde, S.; Hummer, G. Water in nonpolar confinement: from nanotubes to proteins and beyond. *Annual review of physical chemistry* **2008**, *59*, 713–740, DOI: 10.1146/annurev.physchem.59.032607.093815.
- (26) Salanne, M. Ionic Liquids for Supercapacitor Applications. *Topics in current chemistry (Journal)* **2017**, *375*, 63, DOI: 10.1007/s41061-017-0150-7.
- (27) Reber, D.; Kühnel, R.-S.; Battaglia, C. High-voltage aqueous supercapacitors based on NaTFSI. *Sustainable Energy Fuels* **2017**, *1*, 2155–2161, DOI: 10.1039/C7SE00423K.
- (28) Dai, Z.; Peng, C.; Chae, J. H.; Ng, K. C.; Chen, G. Z. Cell voltage versus electrode potential range in aqueous supercapacitors. *Scientific reports* **2015**, *5*, 9854, DOI: 10.1038/srep09854.
- (29) Augustyn, V.; Simon, P.; Dunn, B. Pseudocapacitive oxide materials for high-rate electrochemical energy storage. *Energy Environ. Sci.* **2014**, *7*, 1597, DOI: 10.1039/c3ee44164d.
- (30) Brousse, T.; Bélanger, D.; Long, J. W. To Be or Not To Be Pseudocapacitive? *J. Electrochem. Soc.* **2015**, *162*, A5185-A5189, DOI: 10.1149/2.0201505jes.
- (31) Merlet, C.; Rotenberg, B.; Madden, P. A.; Taberna, P.-L.; Simon, P.; Gogotsi, Y.; Salanne, M. On the molecular origin of supercapacitance in nanoporous carbon electrodes. *Nat. Mater.* **2012**, *11*, 306–310, DOI: 10.1038/NMAT3260.
- (32) Forse, A. C.; Merlet, C.; Griffin, J. M.; Grey, C. P. New Perspectives on the Charging Mechanisms of Supercapacitors. *JACS* **2016**, *138*, 5731–5744, DOI: 10.1021/jacs.6b02115.
- (33) Merlet, C.; Pean, C.; Rotenberg, B.; Madden, P. A.; Daffos, B.; Taberna, P.-L.; Simon, P.; Salanne, M. Highly confined ions store charge more efficiently in supercapacitors. *Nat. Commun.* **2013**, *4*, DOI: 10.1038/ncomms3701.
- (34) Prehal, C.; Koczwara, C.; Jäckel, N.; Schreiber, A.; Burian, M.; Amenitsch, H.; Hartmann, M. A.; Presser, V.; Paris, O. Quantification of ion confinement and desolvation in nanoporous carbon supercapacitors with modelling and in situ X-ray scattering. *Nat. Energy* **2017**, *2*, 16215, DOI: 10.1038/nenergy.2016.215.
- (35) Hantel, M. M.; Presser, V.; McDonough, J. K.; Feng, G.; Cummings, P. T.; Gogotsi, Y.; Kotz, R. In Situ Electrochemical Dilatometry of Onion-Like



- Carbon and Carbon Black. *J. Electrochem. Soc.* **2012**, *159*, A1897-A1903, DOI: 10.1149/2.006212jes.
- (36) Griffin, J. M.; Forse, A. C.; Tsai, W.-Y.; Taberna, P.-L.; Simon, P.; Grey, C. P. In situ NMR and electrochemical quartz crystal microbalance techniques reveal the structure of the electrical double layer in supercapacitors. *Nat. Mater.* **2015**, *14*, 812–819, DOI: 10.1038/NMAT4318.
- (37) Deschamps, M.; Gilbert, E.; Azais, P.; Raymundo-Pinero, E.; Ammar, M. R.; Simon, P.; Massiot, D.; Beguin, F. Exploring electrolyte organization in supercapacitor electrodes with solid-state NMR. *Nat. Mater.* **2013**, *12*, 351–358, DOI: 10.1038/nmat3567.
- (38) Prehal, C. Ion electrosorption in nanoporous carbons. Dissertation, Montanuniversität Leoben, Leoben, 2017.
- (39) Morak, R. Sorptionsinduzierte Verformung hierarchisch poröser Materialien: Untersuchungen mittels in-situ Röntgen und Neutronen Kleinwinkelstreuung. Dissertation, Montanuniversität Leoben, Leoben, 2017.
- (40) Erko, M. Water properties in confined geometry. Dissertation, Montanuniversität Leoben, Leoben, 2012.
- (41) Horn, M.; MacLeod, J.; Liu, M.; Webb, J.; Motta, N. Supercapacitors: A new source of power for electric cars? *Economic Analysis and Policy* **2019**, *61*, 93–103, DOI: 10.1016/j.eap.2018.08.003.
- (42) González, A.; Goikolea, E.; Barrena, J. A.; Mysyk, R. Review on supercapacitors: Technologies and materials. *Renew. Sust. Energ. Rev.* **2016**, *58*, 1189–1206, DOI: 10.1016/j.rser.2015.12.249.
- (43) Chen, G. Z. Understanding supercapacitors based on nano-hybrid materials with interfacial conjugation. *Progress in Natural Science: Materials International* **2013**, *23*, 245–255, DOI: 10.1016/j.pnsc.2013.04.001.
- (44) Huang, J.; Sumpter, B. G.; Meunier, V. A universal model for nanoporous carbon supercapacitors applicable to diverse pore regimes, carbon materials, and electrolytes. *Chemistry (Weinheim an der Bergstrasse, Germany)* **2008**, *14*, 6614–6626, DOI: 10.1002/chem.200800639.
- (45) Huang, J.; Sumpter, B. G.; Meunier, V. Theoretical model for nanoporous carbon supercapacitors. *Angewandte Chemie (International ed. in English)* **2008**, *47*, 520–524, DOI: 10.1002/anie.200703864.
- (46) Feng, G.; Qiao, R.; Huang, J.; Sumpter, B. G.; Meunier, V. Ion distribution in electrified micropores and its role in the anomalous enhancement of capacitance. *ACS nano* **2010**, *4*, 2382–2390, DOI: 10.1021/nn100126w.

- (47) Lin, Z.; Goikolea, E.; Balducci, A.; Naoi, K.; Taberna, P. L.; Salanne, M.; Yushin, G.; Simon, P. Materials for supercapacitors: When Li-ion battery power is not enough. *Mater. Today* **2018**, DOI: 10.1016/j.mattod.2018.01.035.
- (48) Presser, V.; Dennison, C. R.; Campos, J.; Knehr, K. W.; Kumbur, E. C.; Gogotsi, Y. The Electrochemical Flow Capacitor: A New Concept for Rapid Energy Storage and Recovery. *Adv. Energy Mater.* **2012**, *2*, 895–902, DOI: 10.1002/aenm.201100768.
- (49) Wang, W.; Luo, Q.; Li, B.; Wei, X.; Li, L.; Yang, Z. Recent Progress in Redox Flow Battery Research and Development. *Adv. Funct. Mater.* **2013**, *23*, 970–986, DOI: 10.1002/adfm.201200694.
- (50) Chmiola, J.; Yushin, G.; Dash, R.; Gogotsi, Y. Effect of pore size and surface area of carbide derived carbons on specific capacitance. *J. Power Sources* **2006**, *158*, 765–772, DOI: 10.1016/j.jpowsour.2005.09.008.
- (51) Gong, Y.; Li, D.; Fu, Q.; Pan, C. Influence of graphene microstructures on electrochemical performance for supercapacitors. *Progress in Natural Science: Materials International* **2015**, *25*, 379–385, DOI: 10.1016/j.pnsc.2015.10.004.
- (52) Stoller, M. D.; Ruoff, R. S. Best practice methods for determining an electrode material's performance for ultracapacitors. *Energy Environ. Sci.* **2010**, *3*, 1294, DOI: 10.1039/c0ee00074d.
- (53) Lee, J.; Jäckel, N.; Kim, D.; Widmaier, M.; Sathyamoorthi, S.; Srimuk, P.; Kim, C.; Fleischmann, S.; Zeiger, M.; Presser, V. Porous carbon as a quasi-reference electrode in aqueous electrolytes. *Electrochim. Acta* **2016**, *222*, 1800–1805, DOI: 10.1016/j.electacta.2016.11.148.
- (54) Widmaier, M.; Krüner, B.; Jäckel, N.; Aslan, M.; Fleischmann, S.; Engel, C.; Presser, V. Carbon as Quasi-Reference Electrode in Unconventional Lithium-Salt Containing Electrolytes for Hybrid Battery/Supercapacitor Devices. *J. Electrochem. Soc.* **2016**, *163*, A2956-A2964, DOI: 10.1149/2.0421614jes.
- (55) Liu, R.-S. *Electrochemical technologies for energy storage and conversion: Volume 1&2*; John Wiley & Sons: Hoboken, 2012.
- (56) Hantel, M. M. *Graphite oxide and graphene oxide based electrode materials for electrochemical double layer capacitors*.
- (57) *Supercapacitors: Materials, systems, and applications*; Beguin, F.; Frackowiak, E., Eds.; Materials for sustainable energy and development; Wiley: Weinheim, 2013.
- (58) Laheäär, A.; Przygocki, P.; Abbas, Q.; Béguin, F. Appropriate methods for evaluating the efficiency and capacitive behavior of different types of

- supercapacitors. *Electrochem. Commun.* **2015**, *60*, 21–25, DOI: 10.1016/j.elecom.2015.07.022.
- (59) Khomenko, V.; Frackowiak, E.; Béguin, F. Determination of the specific capacitance of conducting polymer/nanotubes composite electrodes using different cell configurations. *Electrochim. Acta* **2005**, *50*, 2499–2506, DOI: 10.1016/j.electacta.2004.10.078.
- (60) Kostoglou, N.; Koczwara, C.; Prehal, C.; Terziyska, V.; Babic, B.; Matovic, B.; Constantinides, G.; Tampaxis, C.; Charalambopoulou, G.; Steriotis, T.; Hinder, S.; Baker, M.; Polychronopoulou, K.; Doumanidis, C.; Paris, O.; Mitterer, C.; Rebholz, C. Nanoporous activated carbon cloth as a versatile material for hydrogen adsorption, selective gas separation and electrochemical energy storage. *Nano Energy* **2017**, *40*, 49–64, DOI: 10.1016/j.nanoen.2017.07.056.
- (61) Reitz, C.; Breitung, B.; Schneider, A.; Di Wang; Lehr, M. von der; Leichtweiss, T.; Janek, J.; Hahn, H.; Brezesinski, T. Hierarchical Carbon with High Nitrogen Doping Level: A Versatile Anode and Cathode Host Material for Long-Life Lithium-Ion and Lithium-Sulfur Batteries. *ACS Appl. Mater. Interfaces* **2016**, *8*, 10274–10282, DOI: 10.1021/acsami.5b12361.
- (62) Cottrell, F. G. Der Reststrom bei galvanischer Polarisation, betrachtet als ein Diffusionsproblem. *Zeitschrift für Physikalische Chemie* **1903**, *42U*, DOI: 10.1515/zpch-1903-4229.
- (63) Saveant, J. M.; Vianello, E. Potential-sweep chronoamperometry: Kinetic currents for first-order chemical reaction parallel to electron-transfer process (catalytic currents). *Electrochim. Acta* **1965**, *10*, 905–920, DOI: 10.1016/0013-4686(65)80003-2.
- (64) Bard, A. J.; Faulkner, L. R. *Electrochemical methods: Fundamentals and applications*, 2. ed.; Wiley: New York, 2001.
- (65) Arbizzani, C.; Mastragostino, M.; Meneghello, L. Characterization by impedance spectroscopy of a polymer-based supercapacitor. *Electrochim. Acta* **1995**, *40*, 2223–2228, DOI: 10.1016/0013-4686(95)00167-D.
- (66) Bardé, F.; Taberna, P. L.; Tarascon, J. M.; Palacín, M. R. Evidence for electronic and ionic limitations at the origin of the second voltage plateau in nickel electrodes, as deduced from impedance spectroscopy measurements. *J. Power Sources* **2008**, *179*, 830–836, DOI: 10.1016/j.jpowsour.2008.01.045.
- (67) Zhang, X.; Wang, X.; Jiang, L.; Wu, H.; Wu, C.; Su, J. Effect of aqueous electrolytes on the electrochemical behaviors of supercapacitors based on

- hierarchically porous carbons. *J. Power Sources* **2012**, *216*, 290–296, DOI: 10.1016/j.jpowsour.2012.05.090.
- (68) Segalini, J.; Daffos, B.; Taberna, P. L.; Gogotsi, Y.; Simon, P. Qualitative Electrochemical Impedance Spectroscopy study of ion transport into sub-nanometer carbon pores in Electrochemical Double Layer Capacitor electrodes. *Electrochim. Acta* **2010**, *55*, 7489–7494, DOI: 10.1016/j.electacta.2010.01.003.
- (69) Taberna, P. L.; Simon, P.; Fauvarque, J. F. Electrochemical Characteristics and Impedance Spectroscopy Studies of Carbon-Carbon Supercapacitors. *J. Electrochem. Soc.* **2003**, *150*, A292, DOI: 10.1149/1.1543948.
- (70) *Impedance spectroscopy: Theory, experiment, and applications*; Barsoukov, E.; Macdonald, J. R., Eds., Second edition; Wiley-Interscience a John Wiley & Sons Inc. publication: Hoboken, New Jersey, 2005.
- (71) Xie, Y.; Du, H. Electrochemical capacitance of a carbon quantum dots–polypyrrole/titania nanotube hybrid. *RSC Adv.* **2015**, *5*, 89689–89697, DOI: 10.1039/C5RA16538E.
- (72) Fletcher, S.; Black, V. J.; Kirkpatrick, I. A universal equivalent circuit for carbon-based supercapacitors. *J Solid State Electrochem* **2014**, *18*, 1377–1387, DOI: 10.1007/s10008-013-2328-4.
- (73) Kötz, R.; Carlen, M. Principles and applications of electrochemical capacitors. *Electrochim. Acta* **2000**, *45*, 2483–2498, DOI: 10.1016/S0013-4686(00)00354-6.
- (74) Cericola, D.; Spahr, M. E. Impedance Spectroscopic Studies of the Porous Structure of Electrodes containing Graphite Materials with Different Particle Size and Shape. *Electrochim. Acta* **2016**, *191*, 558–566, DOI: 10.1016/j.electacta.2016.01.121.
- (75) Paasch, G.; Micka, K.; Gersdorf, P. Theory of the electrochemical impedance of macrohomogeneous porous electrodes. *Electrochim. Acta* **1993**, *38*, 2653–2662, DOI: 10.1016/0013-4686(93)85083-B.
- (76) Keiser, H.; Beccu, K. D.; Gutjahr, M. A. Abschätzung der porenstruktur poröser elektroden aus impedanzmessungen. *Electrochim. Acta* **1976**, *21*, 539–543, DOI: 10.1016/0013-4686(76)85147-X.
- (77) Oz, A.; Hershkovitz, S.; Belman, N.; Tal-Gutelmacher, E.; Tsur, Y. Analysis of impedance spectroscopy of aqueous supercapacitors by evolutionary programming: Finding DFRT from complex capacitance. *Solid State Ionics* **2016**, *288*, 311–314, DOI: 10.1016/j.ssi.2015.11.008.

- 
- (78) Als-Nielsen, J.; Des McMorrow. *Elements of modern X-ray physics*, Second edition; Wiley: Chichester, 2011.
- (79) Sivia, D. S. *Elementary scattering theory: For X-ray and neutron users*; Oxford Univ. Press: Oxford, 2011.
- (80) Melnichenko, Y. B. *Small-Angle Scattering from Confined and Interfacial Fluids: Applications to Energy Storage and Environmental Science*, 1st ed. 2016; Springer: Cham, 2016.
- (81) Kittel, C. *Introduction to solid state physics*, 8. ed.; Wiley: Hoboken, NJ, 2005.
- (82) *Small angle X-ray scattering*; Glatter, O.; Kratky, O., Eds.; Acad. Pr: London, 1982.
- (83) *Neutron, x-ray and light scattering: Introduction to an investigative tool for colloidal and polymeric systems*; Lindner, P.; Zemb, T., Eds.; Delta series; North-Holland: Amsterdam, New York, 1991.
- (84) Zickler, G. A.; Jähnert, S.; Wagermaier, W.; Funari, S. S.; Findenegg, G. H.; Paris, O. Physisorbed films in periodic mesoporous silica studied by in situ synchrotron small-angle diffraction. *Phys. Rev. B* **2006**, *73*, 17, DOI: 10.1103/PhysRevB.73.184109.
- (85) Förster, S.; Timmann, A.; Konrad, M.; Schellbach, C.; Meyer, A.; Funari, S. S.; Mulvaney, P.; Knott, R. Scattering curves of ordered mesoscopic materials. *J. Phys. Chem. B* **2005**, *109*, 1347–1360, DOI: 10.1021/jp0467494.
- (86) Feigin, L. A.; Svergun, D. I.; Taylor, G. W. *Structure Analysis by Small-Angle X-Ray and Neutron Scattering*; Springer US: Boston, MA, 1987.
- (87) Hecht, E. *Optics*, 5 ed/fifth edition, Global edition; Pearson global edition; Pearson: Boston, Columbus, Indianapolis, 2017.
- (88) Gommès, C. J. Small-angle scattering and scale-dependent heterogeneity. *J. Appl. Crystallogr.* **2016**, *49*, 1162–1176, DOI: 10.1107/S1600576716007810.
- (89) Gommès, C. J.; Prieto, G.; Jongh, P. E. de. Small-Angle Scattering Analysis of Empty or Loaded Hierarchical Porous Materials. *J. Phys. Chem. C* **2016**, *120*, 1488–1506, DOI: 10.1021/acs.jpcc.5b09556.
- (90) Fratzl, P.; Gupta, H. S.; Paris, O.; Valenta, A.; Roschger, P.; Klaushofer, K. Diffracting “stacks of cards” - some thoughts about small-angle scattering from bone. *Scattering Methods and the Properties of Polymer Materials*; Springer Berlin Heidelberg: Berlin, Heidelberg, 2005; pp 33–39.
- (91) Ruland, W. Small-angle scattering of two-phase systems: determination and significance of systematic deviations from Porod's law. *J. Appl. Crystallogr.* **1971**, *4*, 70–73, DOI: 10.1107/S0021889871006265.

- (92) Perret, R.; Ruland, W. The microstructure of PAN-base carbon fibres. *J. Appl. Crystallogr.* **1970**, *3*, 525–532, DOI: 10.1107/S0021889870006805.
- (93) Perret, R.; Ruland, W. X-ray small-angle scattering of non-graphitizable carbons. *J. Appl. Crystallogr.* **1968**, *1*, 308–313, DOI: 10.1107/S0021889868005558.
- (94) Jafta, C. J.; Petzold, A.; Risse, S.; Clemens, D.; Wallacher, D.; Goerigk, G.; Ballauff, M. Correlating pore size and shape to local disorder in microporous carbon: A combined small angle neutron and X-ray scattering study. *Carbon* **2017**, *123*, 440–447, DOI: 10.1016/j.carbon.2017.07.046.
- (95) Härk, E.; Petzold, A.; Goerigk, G.; Ballauff, M.; Kent, B.; Keiderling, U.; Palm, R.; Vaas, I.; Lust, E. The effect of a binder on porosity of the nanoporous RP-20 carbon. A combined study by small angle X-ray and neutron scattering. *Microporous Mesoporous Mater.* **2019**, *275*, 139–146, DOI: 10.1016/j.micromeso.2018.08.022.
- (96) Härk, E.; Kardjilov, N.; Hilger, A.; Petzold, A.; Risse, S.; Vaas, I.; Goerigk, G.; Jafta, C.; Ballauff, M.; Lust, E. The Nanoporous RP-20 Carbon Electrode as a Model for Energy Storage and Conversion Systems – Studied with  $\mu$ CT, SAXS and SANS Techniques. *ECS Trans.* **2017**, *77*, 1133–1144, DOI: 10.1149/07711.1133ecst.
- (97) Petzold, A.; Juhl, A.; Scholz, J.; Ufer, B.; Goerigk, G.; Fröba, M.; Ballauff, M.; Mascotto, S. Distribution of Sulfur in Carbon/Sulfur Nanocomposites Analyzed by Small-Angle X-ray Scattering. *Langmuir* **2016**, *32*, 2780–2786, DOI: 10.1021/acs.langmuir.5b04734.
- (98) Smarsly, B.; Antonietti, M.; Wolff, T. Evaluation of the small-angle x-ray scattering of carbons using parametrization methods. *The Journal of Chemical Physics* **2002**, *116*, 2618–2627, DOI: 10.1063/1.1433463.
- (99) Härk, E.; Petzold, A.; Goerigk, G.; Risse, S.; Tallo, I.; Härmas, R.; Lust, E.; Ballauff, M. Carbide derived carbons investigated by small angle X-ray scattering: Inner surface and porosity vs. graphitization. *Carbon* **2019**, DOI: 10.1016/j.carbon.2019.01.076.
- (100) Stuhrmann, H. B. Resonance scattering in macromolecular structure research. In *Characterization of Polymers in the Solid State II: Synchrotron Radiation, X-ray Scattering and Electron Microscopy*; Kausch, H. H., Zachmann, H. G., Eds.; Advances in Polymer Science 67; Springer: Berlin, Heidelberg, 1985; pp 123–163.

- 
- (101) Cromer, D. T.; Liberman, D. Relativistic Calculation of Anomalous Scattering Factors for X Rays. *The Journal of Chemical Physics* **1970**, *53*, 1891–1898, DOI: 10.1063/1.1674266.
- (102) Cromer, D. T.; Liberman, D. A. Anomalous dispersion calculations near to and on the long-wavelength side of an absorption edge. *Acta Cryst A* **1981**, *37*, 267–268, DOI: 10.1107/S0567739481000600.
- (103) Brennan, S.; Cowan, P. L. A suite of programs for calculating x-ray absorption, reflection, and diffraction performance for a variety of materials at arbitrary wavelengths. *Review of Scientific Instruments* **1992**, *63*, 850–853, DOI: 10.1063/1.1142625.
- (104) Sztucki, M.; Cola, E.; Narayanan, T. Anomalous small-angle X-ray scattering from charged soft matter. *The European Physical Journal Special Topics* **2012**, *208*, 319–331, DOI: 10.1140/epjst/e2012-01627-x.
- (105) Jusufi, A.; Ballauff, M. Correlations and Fluctuations of Charged Colloids as Determined by Anomalous Small-Angle X-Ray Scattering. *Macromol. Theory Simul.* **2006**, *15*, 193–197, DOI: 10.1002/mats.200500084.
- (106) Haas, S.; Fenger, R.; Fertitta, E.; Rademann, K. Cascade catalysis of highly active bimetallic Au/Pd nanoclusters: structure–function relationship investigation using anomalous small-angle X-ray scattering and UV–Vis spectroscopy. *J. Appl. Crystallogr.* **2013**, *46*, 1353–1360, DOI: 10.1107/S0021889813018190.
- (107) Haas, S.; Hoell, A.; Wurth, R.; Rüssel, C.; Boesecke, P.; Vainio, U. Analysis of nanostructure and nanochemistry by ASAXS: Accessing phase composition of oxyfluoride glass ceramics doped with Er<sup>3+</sup>/Yb<sup>3+</sup>. *Phys. Rev. B* **2010**, *81*, 161, DOI: 10.1103/PhysRevB.81.184207.
- (108) Dingenouts, N.; Merkle, R.; Guo, X.; Narayanan, T.; Goerigk, G.; Ballauff, M. Use of anomalous small-angle X-ray scattering for the investigation of highly charged colloids. *J. Appl. Crystallogr.* **2003**, *36*, 578–582, DOI: 10.1107/S0021889803000256.
- (109) Sztucki, M.; Di Cola, E.; Narayanan, T. New opportunities for Anomalous Small-Angle X-Ray Scattering to characterize Charged Soft Matter Systems; p 12004.
- (110) Stuhmann, H. B.; Notbohm, H. Configuration of the four iron atoms in dissolved human hemoglobin as studied by anomalous dispersion. *Proc. Natl. Acad. Sci. U.S.A.* **1981**, *78*, 6216–6220, DOI: 10.1073/pnas.78.10.6216.

- (111) Sztucki, M.; Di Cola, E.; Narayanan, T. Instrumental developments for anomalous small-angle X-ray scattering from soft matter systems. *J. Appl. Crystallogr.* **2010**, *43*, 1479–1487, DOI: 10.1107/S002188981003298X.
- (112) Ballauff, M.; Jusufi, A. Anomalous small-angle X-ray scattering: analyzing correlations and fluctuations in polyelectrolytes. *Colloid and polymer science* **2006**, *284*, 1303–1311, DOI: 10.1007/s00396-006-1516-5.
- (113) Brunauer, S.; Emmett, P. H.; Teller, E. Adsorption of Gases in Multimolecular Layers. *J. Am. Chem. Soc.* **1938**, *60*, 309–319, DOI: 10.1021/ja01269a023.
- (114) Thommes, M. Physical Adsorption Characterization of Nanoporous Materials. *Chemie Ingenieur Technik* **2010**, *82*, 1059–1073, DOI: 10.1002/cite.201000064.
- (115) Thommes, M.; Kaneko, K.; Neimark, A. V.; Olivier, J. P.; Rodriguez-Reinoso, F.; Rouquerol, J.; Sing, K. S.W. Physisorption of gases, with special reference to the evaluation of surface area and pore size distribution (IUPAC Technical Report). *Pure and Applied Chemistry* **2015**, *87*, 160, DOI: 10.1515/pac-2014-1117.
- (116) Jagiello, J.; Thommes, M. Comparison of DFT characterization methods based on N<sub>2</sub>, Ar, CO<sub>2</sub>, and H<sub>2</sub> adsorption applied to carbons with various pore size distributions. *Carbon* **2004**, *42*, 1227–1232, DOI: 10.1016/j.carbon.2004.01.022.
- (117) Gor, G. Y.; Thommes, M.; Cychosz, K. A.; Neimark, A. V. Quenched solid density functional theory method for characterization of mesoporous carbons by nitrogen adsorption. *Carbon* **2012**, *50*, 1583–1590.
- (118) Zdravkov, B.; Čermák, J.; Šefara, M.; Janků, J. Pore classification in the characterization of porous materials: A perspective. *Open Chemistry* **2007**, *5*, 269, DOI: 10.2478/s11532-007-0017-9.
- (119) Jagiello, J.; Olivier, J. P. Carbon slit pore model incorporating surface energetical heterogeneity and geometrical corrugation. *Adsorption* **2013**, *19*, 777–783, DOI: 10.1007/s10450-013-9517-4.
- (120) Jäckel, N.; Rodner, M.; Schreiber, A.; Jeongwook, J.; Zeiger, M.; Aslan, M.; Weingarh, D.; Presser, V. Anomalous or regular capacitance? The influence of pore size dispersity on double-layer formation. *J. Power Sources* **2016**, *326*, 660–671, DOI: 10.1016/j.jpowsour.2016.03.015.
- (121) Centeno, T. A.; Sereda, O.; Stoeckli, F. Capacitance in carbon pores of 0.7 to 15 nm: a regular pattern. *Phys. Chem. Chem. Phys.* **2011**, *13*, 12403–12406, DOI: 10.1039/c1cp20748b.



- (122) Naguib, M.; Mashtalir, O.; Carle, J.; Presser, V.; Lu, J.; Hultman, L.; Gogotsi, Y.; Barsoum, M. W. Two-dimensional transition metal carbides. *ACS nano* **2012**, *6*, 1322–1331, DOI: 10.1021/nn204153h.
- (123) Lu, X.; Yu, M.; Wang, G.; Tong, Y.; Li, Y. Flexible solid-state supercapacitors: design, fabrication and applications. *Energy Environ. Sci.* **2014**, *7*, 2160, DOI: 10.1039/c4ee00960f.
- (124) Vix-Guterl, C.; Frackowiak, E.; Jurewicz, K.; Friebe, M.; Parmentier, J.; Béguin, F. Electrochemical energy storage in ordered porous carbon materials. *Carbon* **2005**, *43*, 1293–1302, DOI: 10.1016/j.carbon.2004.12.028.
- (125) Ohtaki, H.; Radnai, T. Structure and dynamics of hydrated ions. *Chem. Rev.* **1993**, *93*, 1157–1204, DOI: 10.1021/cr00019a014.
- (126) Bo, Z.; Li, C.; Yang, H.; Ostrikov, K.; Yan, J.; Cen, K. Design of Supercapacitor Electrodes Using Molecular Dynamics Simulations. *Nano-micro letters* **2018**, *10*, 33, DOI: 10.1007/s40820-018-0188-2.
- (127) Mashl, R. J.; Joseph, S.; Aluru, N. R.; Jakobsson, E. Anomalously Immobilized Water: A New Water Phase Induced by Confinement in Nanotubes. *Nano Lett.* **2003**, *3*, 589–592, DOI: 10.1021/nl0340226.
- (128) Senapati, S.; Chandra, A. Dielectric Constant of Water Confined in a Nanocavity. *J. Phys. Chem. B* **2001**, *105*, 5106–5109, DOI: 10.1021/jp011058i.
- (129) Ruiz, V.; Blanco, C.; Santamaría, R.; Juárez-Galán, J. M.; Sepúlveda-Escribano, A.; Rodríguez-Reinoso, F. Carbon molecular sieves as model active electrode materials in supercapacitors. *Microporous Mesoporous Mater.* **2008**, *110*, 431–435, DOI: 10.1016/j.micromeso.2007.06.027.
- (130) Salazar, C. G. de; Sepúlveda-Escribano, A.; Rodríguez-Reinoso, F. Use of immersion calorimetry to evaluate the separation ability of carbon molecular sieves. *Characterisation of Porous Solids V; Studies in Surface Science and Catalysis*; Elsevier, 2000; pp 303–312.
- (131) Kiyono, M.; Koros, W. J.; Williams, P. J. Correlation Between Pyrolysis Atmosphere and Carbon Molecular Sieve Membrane Performance Properties. *Inorganic Polymeric and Composite Membranes - Structure, Function and Other Correlations*; Membrane Science and Technology; Elsevier, 2011; pp 137–173.
- (132) Avraham, E.; Yaniv, B.; Soffer, A.; Aurbach, D. Developing Ion Electroadsorption Stereoselectivity, by Pore Size Adjustment with Chemical Vapor Deposition onto Active Carbon Fiber Electrodes. Case of  $\text{Ca}^{2+}/\text{Na}^{+}$  Separation in Water Capacitive Desalination. *J. Phys. Chem. C* **2008**, *112*, 7385–7389, DOI: 10.1021/jp711706z.

- (133) Porada, S.; Zhao, R.; van der Wal, A.; Presser, V.; Biesheuvel, P. M. Review on the science and technology of water desalination by capacitive deionization. *Progress in Materials Science* **2013**, *58*, 1388–1442, DOI: 10.1016/j.pmatsci.2013.03.005.
- (134) Suss, M. E.; Porada, S.; Sun, X.; Biesheuvel, P. M.; Yoon, J.; Presser, V. Water desalination via capacitive deionization: What is it and what can we expect from it? *Energy Environ. Sci.* **2015**, *8*, 2296–2319, DOI: 10.1039/c5ee00519a.
- (135) Aslan, M.; Weingarh, D.; Jäckel, N.; Atchison, J. S.; Grobelsek, I.; Presser, V. Polyvinylpyrrolidone as binder for castable supercapacitor electrodes with high electrochemical performance in organic electrolytes. *J. Power Sources* **2014**, *266*, 374–383, DOI: 10.1016/j.jpowsour.2014.05.031.
- (136) Ahmadpour, A.; Do, D. D. The preparation of activated carbon from macadamia nutshell by chemical activation. *Carbon* **1997**, *35*, 1723–1732, DOI: 10.1016/S0008-6223(97)00127-9.
- (137) Presser, V.; Heon, M.; Gogotsi, Y. Carbide-Derived Carbons - From Porous Networks to Nanotubes and Graphene. *Adv. Funct. Mater.* **2011**, *21*, 810–833, DOI: 10.1002/adfm.201002094.
- (138) Gu, Y.; Liu, K.; Zhang, X.; Zhang, R. Huge enhancement in electrochemical performance of nano carbide-derived carbon obtained by simply room-temperature soaking treatment in HF and HNO<sub>3</sub> mixed solution. *J Porous Mater* **2019**, *7*, 845, DOI: 10.1007/s10934-019-00724-y.
- (139) Palmer, J. C.; Llobet, A.; Yeon, S.-H.; Fischer, J. E.; Shi, Y.; Gogotsi, Y.; Gubbins, K. E. Modeling the structural evolution of carbide-derived carbons using quenched molecular dynamics. *Carbon* **2010**, *48*, 1116–1123, DOI: 10.1016/j.carbon.2009.11.033.
- (140) Largeot, C.; Portet, C.; Chmiola, J.; Taberna, P.-L.; Gogotsi, Y.; Simon, P. Relation between the ion size and pore size for an electric double-layer capacitor. *J. Am. Chem. Soc.* **2008**, *130*, 2730–2731, DOI: 10.1021/ja7106178.
- (141) Hantel, M. M.; Presser, V.; Kötz, R.; Gogotsi, Y. In situ electrochemical dilatometry of carbide-derived carbons. *Electrochem. Commun.* **2011**, *13*, 1221–1224, DOI: 10.1016/j.elecom.2011.08.039.
- (142) Koczwar, C.; Rumswinkel, S.; Hammerschmidt, L.; Salihovic, M.; Elsaesser, M. S.; Amenitsch, H.; Paris, O.; Huesing, N. Nanofibers versus Nanopores: A Comparison of the Electrochemical Performance of Hierarchically Ordered Porous Carbons. *ACS Appl. Energy Mater.* **2019**, *2*, 5279–5291, DOI: 10.1021/acsaem.9b01035.

- (143) Borboudakis, G.; Stergiannakos, T.; Frysali, M.; Klontzas, E.; Tsamardinos, I.; Froudakis, G. E. Chemically intuited, large-scale screening of MOFs by machine learning techniques. *npj Comput Mater* **2017**, *3*, 2490, DOI: 10.1038/s41524-017-0045-8.
- (144) Furukawa, H.; Cordova, K. E.; O'Keeffe, M.; Yaghi, O. M. The chemistry and applications of metal-organic frameworks. *Science* **2013**, *341*, 1230444, DOI: 10.1126/science.1230444.
- (145) Bonaccorso, F.; Colombo, L.; Yu, G.; Stoller, M.; Tozzini, V.; Ferrari, A. C.; Ruoff, R. S.; Pellegrini, V. 2D materials. Graphene, related two-dimensional crystals, and hybrid systems for energy conversion and storage. *Science* **2015**, *347*, 1246501, DOI: 10.1126/science.1246501.
- (146) Wang, L.; Han, Y.; Feng, X.; Zhou, J.; Qi, P.; Wang, B. Metal-organic frameworks for energy storage: Batteries and supercapacitors. *Coordination Chemistry Reviews* **2016**, *307*, 361–381, DOI: 10.1016/j.ccr.2015.09.002.
- (147) Giancoli, D. C. *Physics for engineers and scientists with modern physics*; Recording for the Blind & Dyslexic: Princeton, N.J., 2008.
- (148) Portet, C.; Taberna, P. L.; Simon, P.; Flahaut, E. Influence of carbon nanotubes addition on carbon-carbon supercapacitor performances in organic electrolyte. *J. Power Sources* **2005**, *139*, 371–378, DOI: 10.1016/j.jpowsour.2004.07.015.
- (149) Sun, L.; Campbell, M. G.; Dincă, M. Electrically Conductive Porous Metal-Organic Frameworks. *Angewandte Chemie (International ed. in English)* **2016**, *55*, 3566–3579, DOI: 10.1002/anie.201506219.
- (150) Wang, L.; Feng, X.; Ren, L.; Piao, Q.; Zhong, J.; Wang, Y.; Li, H.; Chen, Y.; Wang, B. Flexible Solid-State Supercapacitor Based on a Metal-Organic Framework Interwoven by Electrochemically-Deposited PANI. *J. Am. Chem. Soc.* **2015**, *137*, 4920–4923, DOI: 10.1021/jacs.5b01613.
- (151) Naguib, M.; Mochalin, V. N.; Barsoum, M. W.; Gogotsi, Y. 25th anniversary article: MXenes: a new family of two-dimensional materials. *Advanced materials (Deerfield Beach, Fla.)* **2014**, *26*, 992–1005, DOI: 10.1002/adma.201304138.
- (152) Yan, J.; Ren, C. E.; Maleski, K.; Hatter, C. B.; Anasori, B.; Urbankowski, P.; Sarycheva, A.; Gogotsi, Y. Flexible MXene/Graphene Films for Ultrafast Supercapacitors with Outstanding Volumetric Capacitance. *Adv. Funct. Mater.* **2017**, *27*, 1701264, DOI: 10.1002/adfm.201701264.
- (153) Zhu, M.; Huang, Y.; Deng, Q.; Zhou, J.; Pei, Z.; Xue, Q.; Huang, Y.; Wang, Z.; Li, H.; Huang, Q.; Zhi, C. Highly Flexible, Freestanding Supercapacitor

- Electrode with Enhanced Performance Obtained by Hybridizing Polypyrrole Chains with MXene. *Adv. Energy Mater.* **2016**, *6*, 1600969, DOI: 10.1002/aenm.201600969.
- (154) Jäckel, N.; Krüner, B.; van Aken, K. L.; Alhabeib, M.; Anasori, B.; Kaasik, F.; Gogotsi, Y.; Presser, V. Electrochemical in Situ Tracking of Volumetric Changes in Two-Dimensional Metal Carbides (MXenes) in Ionic Liquids. *ACS Appl. Mater. Interfaces* **2016**, *8*, 32089–32093, DOI: 10.1021/acsami.6b11744.
- (155) Iijima, S. Helical microtubules of graphitic carbon. *Nature* **1991**, *354*, 56–58, DOI: 10.1038/354056a0.
- (156) Niu, C.; Sichel, E. K.; Hoch, R.; Moy, D.; Tennent, H. High power electrochemical capacitors based on carbon nanotube electrodes. *Appl. Phys. Lett.* **1997**, *70*, 1480–1482, DOI: 10.1063/1.118568.
- (157) Louie, S. G. Electronic Properties, Junctions, and Defects of Carbon Nanotubes. In *Carbon Nanotubes*; Dresselhaus, M. S., Dresselhaus, G., Avouris, P., Eds.; Topics in Applied Physics; Springer Berlin Heidelberg: Berlin, Heidelberg, 2001; pp 113–145.
- (158) Baughman, R. H.; Zakhidov, A. A.; Heer, W. A. de. Carbon nanotubes—the route toward applications. *Science* **2002**, *297*, 787–792, DOI: 10.1126/science.1060928.
- (159) Zhang, L. L.; Zhao, X. S. Carbon-based materials as supercapacitor electrodes. *Chem. Soc. Rev.* **2009**, *38*, 2520–2531, DOI: 10.1039/b813846j.
- (160) Gao, C.; Guo, Z.; Liu, J.-H.; Huang, X.-J. The new age of carbon nanotubes: an updated review of functionalized carbon nanotubes in electrochemical sensors. *Nanoscale* **2012**, *4*, 1948–1963, DOI: 10.1039/C2NR11757F.
- (161) Pan, H.; Li, J.; Feng, Y. Carbon nanotubes for supercapacitor. *Nanoscale research letters* **2010**, *5*, 654–668, DOI: 10.1007/s11671-009-9508-2.
- (162) Cheng, X.; Gui, X.; Lin, Z.; Zheng, Y.; Liu, M.; Zhan, R.; Zhu, Y.; Tang, Z. Three-dimensional  $\alpha$ -Fe<sub>2</sub>O<sub>3</sub>/carbon nanotube sponges as flexible supercapacitor electrodes. *J. Mater. Chem. A* **2015**, *3*, 20927–20934, DOI: 10.1039/C5TA03635F.
- (163) Jurewicz, K.; Delpeux, S.; Bertagna, V.; Béguin, F.; Frackowiak, E. Supercapacitors from nanotubes/polypyrrole composites. *Chemical Physics Letters* **2001**, *347*, 36–40, DOI: 10.1016/S0009-2614(01)01037-5.
- (164) Afzal, A.; Abuilawi, F. A.; Habib, A.; Awais, M.; Waje, S. B.; Atieh, M. A. Polypyrrole/carbon nanotube supercapacitors: Technological advances and challenges. *J. Power Sources* **2017**, *352*, 174–186, DOI: 10.1016/j.jpowsour.2017.03.128.

- (165) Pan, H.; Poh, C. K.; Feng, Y. P.; Lin, J. Supercapacitor Electrodes from Tubes-in-Tube Carbon Nanostructures. *Chem. Mater.* **2007**, *19*, 6120–6125, DOI: 10.1021/cm071527e.
- (166) Ra, E. J.; Raymundo-Piñero, E.; Lee, Y. H.; Béguin, F. High power supercapacitors using polyacrylonitrile-based carbon nanofiber paper. *Carbon* **2009**, *47*, 2984–2992, DOI: 10.1016/j.carbon.2009.06.051.
- (167) Iijima, S. Direct observation of the tetrahedral bonding in graphitized carbon black by high resolution electron microscopy. *Journal of Crystal Growth* **1980**, *50*, 675–683, DOI: 10.1016/0022-0248(80)90013-5.
- (168) Zeiger, M.; Jäckel, N.; Mochalin, V. N.; Presser, V. Review: Carbon onions for electrochemical energy storage. *J. Mater. Chem. A* **2016**, *4*, 3172–3196, DOI: 10.1039/c5ta08295a.
- (169) McDonough, J. K.; Frolov, A. I.; Presser, V.; Niu, J.; Miller, C. H.; Ubiето, T.; Fedorov, M. V.; Gogotsi, Y. Influence of the structure of carbon onions on their electrochemical performance in supercapacitor electrodes. *Carbon* **2012**, *50*, 3298–3309, DOI: 10.1016/j.carbon.2011.12.022.
- (170) Etzold, B. J. M.; Neitzel, I.; Kett, M.; Strobl, F.; Mochalin, V. N.; Gogotsi, Y. Layer-by-Layer Oxidation for Decreasing the Size of Detonation Nanodiamond. *Chem. Mater.* **2014**, *26*, 3479–3484, DOI: 10.1021/cm500937r.
- (171) Pech, D.; Brunet, M.; Durou, H.; Huang, P.; Mochalin, V.; Gogotsi, Y.; Taberna, P.-L.; Simon, P. Ultrahigh-power micrometre-sized supercapacitors based on onion-like carbon. *Nature nanotechnology* **2010**, *5*, 651–654, DOI: 10.1038/nnano.2010.162.
- (172) Gao, Y.; Zhou, Y. S.; Qian, M.; He, X. N.; Redepenning, J.; Goodman, P.; Li, H. M.; Jiang, L.; Lu, Y. F. Chemical activation of carbon nano-onions for high-rate supercapacitor electrodes. *Carbon* **2013**, *51*, 52–58, DOI: 10.1016/j.carbon.2012.08.009.
- (173) Prehal, C.; Koczwarra, C.; Jäckel, N.; Amenitsch, H.; Presser, V.; Paris, O. A carbon nanopore model to quantify structure and kinetics of ion electrosorption with in situ small-angle X-ray scattering. *Phys. Chem. Chem. Phys.* **2017**, *19*, 15549–15561, DOI: 10.1039/c7cp00736a.
- (174) Forse, A. C.; Griffin, J. M.; Merlet, C.; Carretero-Gonzalez, J.; Raji, A.-R. O.; Trease, N. M.; Grey, C. P. Direct observation of ion dynamics in supercapacitor electrodes using in situ diffusion NMR spectroscopy. *Nat. Energy* **2017**, *2*, 1760, DOI: 10.1038/nenergy.2016.216.
- (175) Phan, T. N.; Gong, M. K.; Thangavel, R.; Lee, Y. S.; Ko, C. H. Enhanced electrochemical performance for EDLC using ordered mesoporous carbons

- (CMK-3 and CMK-8): Role of mesopores and mesopore structures. *Journal of Alloys and Compounds* **2019**, *780*, 90–97, DOI: 10.1016/j.jallcom.2018.11.348.
- (176) Gu, W.; Yushin, G. Review of nanostructured carbon materials for electrochemical capacitor applications: advantages and limitations of activated carbon, carbide-derived carbon, zeolite-templated carbon, carbon aerogels, carbon nanotubes, onion-like carbon, and graphene. *WIREs Energy Environ* **2014**, *3*, 424–473, DOI: 10.1002/wene.102.
- (177) Hasegawa, G.; Kanamori, K.; Kiyomura, T.; Kurata, H.; Abe, T.; Nakanishi, K. Hierarchically Porous Carbon Monoliths Comprising Ordered Mesoporous Nanorod Assemblies for High-Voltage Aqueous Supercapacitors. *Chem. Mater.* **2016**, *28*, 3944–3950, DOI: 10.1021/acs.chemmater.6b01261.
- (178) Lo, A.-Y.; Jheng, Y.; Huang, T.-C.; Tseng, C.-M. Study on RuO<sub>2</sub>/CMK-3/CNTs composites for high power and high energy density supercapacitor. *Applied Energy* **2015**, *153*, 15–21, DOI: 10.1016/j.apenergy.2015.04.050.
- (179) Lu, H.; Kim, K.; Kwon, Y.; Sun, X.; Ryoo, R.; Zhao, X. S. Zeolite-templated nanoporous carbon for high-performance supercapacitors. *J. Mater. Chem. A* **2018**, *6*, 10388–10394, DOI: 10.1039/C8TA00850G.
- (180) Xia, K.; Gao, Q.; Jiang, J.; Hu, J. Hierarchical porous carbons with controlled micropores and mesopores for supercapacitor electrode materials. *Carbon* **2008**, *46*, 1718–1726, DOI: 10.1016/j.carbon.2008.07.018.
- (181) Pal, N.; Bhaumik, A. Soft templating strategies for the synthesis of mesoporous materials: inorganic, organic-inorganic hybrid and purely organic solids. *Advances in Colloid and Interface Science* **2013**, *189-190*, 21–41, DOI: 10.1016/j.cis.2012.12.002.
- (182) Nakanishi, K.; Amatani, T.; Yano, S.; Kodaira, T. Multiscale Templating of Siloxane Gels via Polymerization-Induced Phase Separation †. *Chem. Mater.* **2008**, *20*, 1108–1115, DOI: 10.1021/cm702486b.
- (183) Momčilović, M.; Stojmenović, M.; Gavrilov, N.; Pašti, I.; Mentus, S.; Babić, B. Complex electrochemical investigation of ordered mesoporous carbon synthesized by soft-templating method: charge storage and electrocatalytic or Pt-electrocatalyst supporting behavior. *Electrochim. Acta* **2014**, *125*, 606–614, DOI: 10.1016/j.electacta.2014.01.152.
- (184) Zhao, D.; Feng, J.; Huo, Q.; Melosh, N.; Fredrickson, G. H.; Chmelka, B. F.; Stucky, G. D. Triblock Copolymer Syntheses of Mesoporous Silica with Periodic 50 to 300 Angstrom Pores. *Science* **1998**, *279*, 548–552, DOI: 10.1126/science.279.5350.548.

- (185) Huang, Y.; Cai, H.; Feng, D.; Gu, D.; Deng, Y.; Tu, B.; Wang, H.; Webley, P. A.; Zhao, D. One-step hydrothermal synthesis of ordered mesostructured carbonaceous monoliths with hierarchical porosities. *Chem. Commun.* **2008**, 2641–2643, DOI: 10.1039/b804716b.
- (186) Jäckel, N.; Simon, P.; Gogotsi, Y.; Presser, V. Increase in Capacitance by Subnanometer Pores in Carbon. *ACS Energy Lett.* **2016**, *1*, 1262–1265, DOI: 10.1021/acseenergylett.6b00516.
- (187) Mostazo-López, M. J.; Ruiz-Rosas, R.; Castro-Muñiz, A.; Nishihara, H.; Kyotani, T.; Morallón, E.; Cazorla-Amorós, D. Ultraporous nitrogen-doped zeolite-templated carbon for high power density aqueous-based supercapacitors. *Carbon* **2018**, *129*, 510–519, DOI: 10.1016/j.carbon.2017.12.050.
- (188) Ania, C. O.; Khomenko, V.; Raymundo-Piñero, E.; Parra, J. B.; Béguin, F. The Large Electrochemical Capacitance of Microporous Doped Carbon Obtained by Using a Zeolite Template. *Adv. Funct. Mater.* **2007**, *17*, 1828–1836, DOI: 10.1002/adfm.200600961.
- (189) Jun, S.; Joo, S. H.; Ryoo, R.; Kruk, M.; Jaroniec, M.; Liu, Z.; Ohsuna, T.; Terasaki, O. Synthesis of New, Nanoporous Carbon with Hexagonally Ordered Mesostructure. *J. Am. Chem. Soc.* **2000**, *122*, 10712–10713, DOI: 10.1021/ja002261e.
- (190) Tian, B.; Che, S.; Liu, Z.; Liu, X.; Fan, W.; Tatsumi, T.; Terasaki, O.; Zhao, D. Novel approaches to synthesize self-supported ultrathin carbon nanowire arrays templated by MCM-41. *Chem. Commun.* **2003**, 2726, DOI: 10.1039/B309670J.
- (191) Rose, M.; Korenblit, Y.; Kockrick, E.; Borchardt, L.; Oschatz, M.; Kaskel, S.; Yushin, G. Hierarchical micro- and mesoporous carbide-derived carbon as a high-performance electrode material in supercapacitors. *Small* **2011**, *7*, 1108–1117, DOI: 10.1002/smll.201001898.
- (192) Brandhuber, D.; Torma, V.; Raab, C.; Peterlik, H.; Kulak, A.; Hüsing, N. Glycol-Modified Silanes in the Synthesis of Mesoscopically Organized Silica Monoliths with Hierarchical Porosity. *Chem. Mater.* **2005**, *17*, 4262–4271, DOI: 10.1021/cm048483j.
- (193) Putz, F.; Morak, R.; Elsaesser, M. S.; Balzer, C.; Braxmeier, S.; Bernardi, J.; Paris, O.; Reichenauer, G.; Hüsing, N. Setting Directions: Anisotropy in Hierarchically Organized Porous Silica. *Chem. Mater.* **2017**, *29*, 7969–7975, DOI: 10.1021/acs.chemmater.7b03032.

- (194) Putz, F.; Waag, A.; Balzer, C.; Braxmeier, S.; Elsaesser, M. S.; Ludescher, L.; Paris, O.; Malfait, W. J.; Reichenauer, G.; Hüsing, N. The influence of drying and calcination on surface chemistry, pore structure and mechanical properties of hierarchically organized porous silica monoliths. *Microporous Mesoporous Mater.* **2019**, 109578, DOI: 10.1016/j.micromeso.2019.109578.
- (195) Lukatskaya, M. R.; Dunn, B.; Gogotsi, Y. Multidimensional materials and device architectures for future hybrid energy storage. *Nat. Commun.* **2016**, 7, 12647, DOI: 10.1038/ncomms12647.
- (196) Okubo, M.; Hosono, E.; Kim, J.; Enomoto, M.; Kojima, N.; Kudo, T.; Zhou, H.; Honma, I. Nanosize effect on high-rate Li-ion intercalation in LiCoO<sub>2</sub> electrode. *JACS* **2007**, 129, 7444–7452, DOI: 10.1021/ja0681927.
- (197) Inganäs, O.; Erlandsson, R.; Nylander, C.; Lundström, I. Proton modification of conducting polypyrrole. *Journal of Physics and Chemistry of Solids* **1984**, 45, 427–432, DOI: 10.1016/0022-3697(84)90150-1.
- (198) Dyatkin, B.; Presser, V.; Heon, M.; Lukatskaya, M. R.; Beidaghi, M.; Gogotsi, Y. Development of a green supercapacitor composed entirely of environmentally friendly materials. *ChemSusChem* **2013**, 6, 2269–2280, DOI: 10.1002/cssc.201300852.
- (199) Koczwara, C.; Rumswinkel, S.; Prehal, C.; Jäckel, N.; Elsässer, M. S.; Amenitsch, H.; Presser, V.; Hüsing, N.; Paris, O. In Situ Measurement of Electrosorption-Induced Deformation Reveals the Importance of Micropores in Hierarchical Carbons. *ACS Appl. Mater. Interfaces* **2017**, 9, 23319–23324, DOI: 10.1021/acsami.7b07058.
- (200) Kim, C.; Srimuk, P.; Lee, J.; Fleischmann, S.; Aslan, M.; Presser, V. Influence of pore structure and cell voltage of activated carbon cloth as a versatile electrode material for capacitive deionization. *Carbon* **2017**, 122, 329–335, DOI: 10.1016/j.carbon.2017.06.077.
- (201) Jost, K.; Perez, C. R.; McDonough, J. K.; Presser, V.; Heon, M.; Dion, G.; Gogotsi, Y. Carbon coated textiles for flexible energy storage. *Energy Environ. Sci.* **2011**, 4, 5060, DOI: 10.1039/C1EE02421C.
- (202) Jost, K.; Stenger, D.; Perez, C. R.; McDonough, J. K.; Lian, K.; Gogotsi, Y.; Dion, G. Knitted and screen printed carbon-fiber supercapacitors for applications in wearable electronics. *Energy Environ. Sci.* **2013**, 6, 2698, DOI: 10.1039/c3ee40515j.
- (203) Lee, J.; Krüner, B.; Tolosa, A.; Sathyamoorthi, S.; Kim, D.; Choudhury, S.; Seo, K.-H.; Presser, V. Tin/vanadium redox electrolyte for battery-like



- energy storage capacity combined with supercapacitor-like power handling. *Energy Environ. Sci.* **2016**, *9*, 3392–3398, DOI: 10.1039/c6ee00712k.
- (204) Naoi, K.; Naoi, W.; Aoyagi, S.; Miyamoto, J.-I.; Kamino, T. New generation "nanohybrid supercapacitor". *Accounts of chemical research* **2013**, *46*, 1075–1083, DOI: 10.1021/ar200308h.
- (205) Naoi, K.; Ishimoto, S.; Miyamoto, J.-I.; Naoi, W. Second generation 'nanohybrid supercapacitor': Evolution of capacitive energy storage devices. *Energy Environ. Sci.* **2012**, *5*, 9363, DOI: 10.1039/c2ee21675b.
- (206) Schönmaier, H. In-situ Röntgentransmissionsmessung zur Untersuchung der Ionenkonzentration in nanoporösen, kohlenstoffbasierten Superkondensatoren. Bachelor thesis, Montanuniversität Leoben, Leoben, 2016.
- (207) Weingarth, D.; Zeiger, M.; Jäckel, N.; Aslan, M.; Feng, G.; Presser, V. Graphitization as a Universal Tool to Tailor the Potential-Dependent Capacitance of Carbon Supercapacitors. *Adv. Energy Mater.* **2014**, *4*, 1400316, DOI: 10.1002/aenm.201400316.
- (208) Amenitsch, H.; Rappolt, M.; Kriechbaum, M.; Mio, H.; Laggner, P.; Bernstorff, S. First performance assessment of the small-angle X-ray scattering beamline at ELETTRA. *J. Synchrotron Radiat.* **1998**, *5*, 506–508, DOI: 10.1107/S090904959800137X.
- (209) Narayanan, T.; Sztucki, M.; van Vaerenbergh, P.; Léonardon, J.; Gorini, J.; Claustre, L.; Sever, F.; Morse, J.; Boesecke, P. A multipurpose instrument for time-resolved ultra-small-angle and coherent X-ray scattering. *J. Appl. Crystallogr.* **2018**, *51*, 1511–1524, DOI: 10.1107/S1600576718012748.
- (210) Boesecke, P. Reduction of two-dimensional small- and wide-angle X-ray scattering data. *J. Appl. Crystallogr.* **2007**, *40*, s423-s427, DOI: 10.1107/S0021889807001100.
- (211) Kondrat, S.; Pérez, C. R.; Presser, V.; Gogotsi, Y.; Kornyshev, A. A. Effect of pore size and its dispersity on the energy storage in nanoporous supercapacitors. *Energy Environ. Sci.* **2012**, *5*, 6474, DOI: 10.1039/c2ee03092f.
- (212) Breitsprecher, K.; Holm, C.; Kondrat, S. Charge Me Slowly, I Am in a Hurry: Optimizing Charge-Discharge Cycles in Nanoporous Supercapacitors. *ACS nano* **2018**, *12*, 9733–9741, DOI: 10.1021/acsnano.8b04785.
- (213) Du, J.; Liu, R.; Yu, Y.; Zhang, Y.; Zhang, Y.; Chen, A. N-doped ordered mesoporous carbon prepared by solid–solid grinding for supercapacitors. *J. Mater. Res.* **2018**, *33*, 3408–3417, DOI: 10.1557/jmr.2018.219.

- (214) Herou, S.; Ribadeneyra, M. C.; Madhu, R.; Araullo-Peters, V.; Jensen, A.; Schlee, P.; Titirici, M. Ordered mesoporous carbons from lignin: a new class of biobased electrodes for supercapacitors. *Green Chem.* **2019**, *21*, 550–559, DOI: 10.1039/C8GC03497D.
- (215) Lee, Y.; Kwak, M.-J.; Hwang, C.; An, C.; Song, W.-J.; Song, G.; Kim, S.; Park, S.; Jang, J.-H.; Song, H.-K. Hierarchically Structured Multidimensional Carbon Composite Anchored to a Polymer Mat for a Superflexible Supercapacitor. *ACS Appl. Energy Mater.* **2019**, *2*, 389–397, DOI: 10.1021/acsaem.8b01417.
- (216) Borchardt, L.; Leistenschneider, D.; Haase, J.; Dvoyashkin, M. Revising the Concept of Pore Hierarchy for Ionic Transport in Carbon Materials for Supercapacitors. *Adv. Energy Mater.* **2018**, *8*, 1800892, DOI: 10.1002/aenm.201800892.
- (217) Hammersley, A. P. FIT2D: A multi-purpose data reduction, analysis and visualization program. *J. Appl. Crystallogr.* **2016**, *49*, 646–652, DOI: 10.1107/S1600576716000455.
- (218) *Structure and multiscale mechanics of carbon nanomaterials*; Paris, O., Ed.; CISM courses and lectures / International Centre for Mechanical Science vol. 563; Springer: Wien, Heidelberg, New York, Dordrecht, London, 2016.
- (219) Warren, B. E. X-Ray Diffraction in Random Layer Lattices. *Phys. Rev.* **1941**, *59*, 693–698, DOI: 10.1103/PhysRev.59.693.
- (220) Paris, O.; Zollfrank, C.; Zickler, G. A. Decomposition and carbonisation of wood biopolymers—a microstructural study of softwood pyrolysis. *Carbon* **2005**, *43*, 53–66, DOI: 10.1016/j.carbon.2004.08.034.
- (221) Sevilla, M.; Mokaya, R.; Fuertes, A. B. Ultrahigh surface area polypyrrole-based carbons with superior performance for hydrogen storage. *Energy Environ. Sci.* **2011**, *4*, 2930, DOI: 10.1039/C1EE01608C.
- (222) Hofmann, T.; Wallacher, D.; Perlich, J.; Koyiloth Vayalil, S.; Huber, P. Formation of Periodically Arranged Nanobubbles in Mesopores: Capillary Bridge Formation and Cavitation during Sorption and Solidification in an Hierarchical Porous SBA-15 Matrix. *Langmuir* **2016**, *32*, 2928–2936, DOI: 10.1021/acs.langmuir.5b04560.
- (223) Levi, M. D.; Dargel, V.; Shilina, Y.; Aurbach, D.; Halalay, I. C. Impedance Spectra of Energy-Storage Electrodes Obtained with Commercial Three-Electrode Cells: Some Sources of Measurement Artefacts. *Electrochim. Acta* **2014**, *149*, 126–135, DOI: 10.1016/j.electacta.2014.10.083.

- 
- (224) Zhu, L.; Xu, J.; Xiu, Y.; Sun, Y.; Hess, D. W.; Wong, C.-P. Electrowetting of aligned carbon nanotube films. *J. Phys. Chem. B* **2006**, *110*, 15945–15950, DOI: 10.1021/jp063265u.
- (225) Boukhalfa, S.; Gordon, D.; He, L.; Melnichenko, Y. B.; Nitta, N.; Magasinski, A.; Yushin, G. In situ small angle neutron scattering revealing ion sorption in microporous carbon electrical double layer capacitors. *ACS nano* **2014**, *8*, 2495–2503, DOI: 10.1021/nn406077n.
- (226) Boukhalfa, S.; He, L.; Melnichenko, Y. B.; Yushin, G. Small-angle neutron scattering for in situ probing of ion adsorption inside micropores. *Angewandte Chemie (International ed. in English)* **2013**, *52*, 4618–4622, DOI: 10.1002/anie.201209141.
- (227) Yan, R.; Heil, T.; Presser, V.; Walczak, R.; Antonietti, M.; Oschatz, M. Ordered Mesoporous Carbons with High Micropore Content and Tunable Structure Prepared by Combined Hard and Salt Templating as Electrode Materials in Electric Double-Layer Capacitors. *Adv. Sustainable Syst.* **2018**, *2*, 1700128, DOI: 10.1002/adsu.201700128.
- (228) Nitta, N.; Wu, F.; Lee, J. T.; Yushin, G. Li-ion battery materials: Present and future. *Mater. Today* **2015**, *18*, 252–264, DOI: 10.1016/j.mattod.2014.10.040.
- (229) Torop, J.; Palmre, V.; Arulepp, M.; Sugino, T.; Asaka, K.; Aabloo, A. Flexible supercapacitor-like actuator with carbide-derived carbon electrodes. *Carbon* **2011**, *49*, 3113–3119, DOI: 10.1016/j.carbon.2011.03.034.
- (230) Torop, J.; Arulepp, M.; Leis, J.; Punning, A.; Johanson, U.; Palmre, V.; Aabloo, A. Nanoporous Carbide-Derived Carbon Material-Based Linear Actuators. *Materials* **2010**, *3*, 9–25, DOI: 10.3390/ma3010009.
- (231) Black, J. M.; Feng, G.; Fulvio, P. F.; Hillesheim, P. C.; Dai, S.; Gogotsi, Y.; Cummings, P. T.; Kalinin, S. V.; Balke, N. Strain-Based In Situ Study of Anion and Cation Insertion into Porous Carbon Electrodes with Different Pore Sizes. *Adv. Energy Mater.* **2014**, *4*, 1300683, DOI: 10.1002/aenm.201300683.
- (232) Hantel, M. M.; Weingarh, D.; Kötz, R. Parameters determining dimensional changes of porous carbons during capacitive charging. *Carbon* **2014**, *69*, 275–286, DOI: 10.1016/j.carbon.2013.12.026.
- (233) Ruch, P. W.; Kötz, R.; Wokaun, A. Electrochemical characterization of single-walled carbon nanotubes for electrochemical double layer capacitors using non-aqueous electrolyte. *Electrochim. Acta* **2009**, *54*, 4451–4458, DOI: 10.1016/j.electacta.2009.03.022.

- (234) Kaasik, F.; Tamm, T.; Hantel, M. M.; Perre, E.; Aabloo, A.; Lust, E.; Bazant, M. Z.; Presser, V. Anisometric charge dependent swelling of porous carbon in an ionic liquid. *Electrochem. Commun.* **2013**, *34*, 196–199, DOI: 10.1016/j.elecom.2013.06.011.
- (235) Hahn, M.; Barbieri, O.; Campana, F. P.; Kötz, R.; Gallay, R. Carbon based double layer capacitors with aprotic electrolyte solutions: The possible role of intercalation/insertion processes. *Appl. Phys. A* **2006**, *82*, 633–638, DOI: 10.1007/s00339-005-3403-1.
- (236) Hahn, M.; Barbieri, O.; Gallay, R.; Kötz, R. A dilatometric study of the voltage limitation of carbonaceous electrodes in aprotic EDLC type electrolytes by charge-induced strain. *Carbon* **2006**, *44*, 2523–2533, DOI: 10.1016/j.carbon.2006.05.002.
- (237) Jäckel, N. Structure and Properties of Supercapacitor and Lithium-Ion Battery Electrodes: The Role of Material, Electrolyte, Binder and Additives. Dissertation, Universität des Saarlandes, Saarbrücken, 2018.
- (238) Huang, T. C.; Toraya, H.; Blanton, T. N.; Wu, Y. X-ray powder diffraction analysis of silver behenate, a possible low-angle diffraction standard. *J. Appl. Crystallogr.* **1993**, *26*, 180–184, DOI: 10.1107/S0021889892009762.
- (239) Rochester, C. C.; Pruessner, G.; Kornyshev, A. A. Statistical Mechanics of ‘Unwanted Electroactuation’ in Nanoporous Supercapacitors. *Electrochim. Acta* **2015**, *174*, 978–984, DOI: 10.1016/j.electacta.2015.04.064.
- (240) Prass, J.; Müter, D.; Erko, M.; Paris, O. Apparent lattice expansion in ordered nanoporous silica during capillary condensation of fluids. *J. Appl. Crystallogr.* **2012**, *45*, 798–806, DOI: 10.1107/S0021889812025058.
- (241) Shao, L.-H.; Biener, J.; Kramer, D.; Viswanath, R. N.; Baumann, T. F.; Hamza, A. V.; Weissmüller, J. Electrocapillary maximum and potential of zero charge of carbon aerogel. *Phys. Chem. Chem. Phys.* **2010**, *12*, 7580–7587, DOI: 10.1039/b916331j.
- (242) Sun, G.; Kürti, J.; Kertesz, M.; Baughman, R. H. Dimensional Changes as a Function of Charge Injection in Single-Walled Carbon Nanotubes. *J. Am. Chem. Soc.* **2002**, *124*, 15076–15080, DOI: 10.1021/ja020616j.
- (243) Salanne, M.; Rotenberg, B.; Naoi, K.; Kaneko, K.; Taberna, P.-L.; Grey, C. P.; Dunn, B.; Simon, P. Efficient storage mechanisms for building better supercapacitors. *Nat. Energy* **2016**, *1*, 16070, DOI: 10.1038/nenergy.2016.70.
- (244) Levi, M. D.; Salitra, G.; Levy, N.; Aurbach, D.; Maier, J. Application of a quartz-crystal microbalance to measure ionic fluxes in microporous carbons for energy storage. *Nat. Mater.* **2009**, *8*, 872–875, DOI: 10.1038/nmat2559.

- 
- (245) Kondrat, S.; Kornyshev, A. Charging Dynamics and Optimization of Nanoporous Supercapacitors. *J. Phys. Chem. C* **2013**, *117*, 12399–12406, DOI: 10.1021/jp400558y.
- (246) Lee, A. A.; Kondrat, S.; Oshanin, G.; Kornyshev, A. A. Charging dynamics of supercapacitors with narrow cylindrical nanopores. *Nanotechnology* **2014**, *25*, 315401, DOI: 10.1088/0957-4484/25/31/315401.
- (247) Kondrat, S.; Georgi, N.; Fedorov, M. V.; Kornyshev, A. A. A superionic state in nano-porous double-layer capacitors: insights from Monte Carlo simulations. *Phys. Chem. Chem. Phys.* **2011**, *13*, 11359–11366, DOI: 10.1039/c1cp20798a.
- (248) Nightingale, E. R. Phenomenological Theory of Ion Solvation. Effective Radii of Hydrated Ions. *J. Phys. Chem.* **1959**, *63*, 1381–1387, DOI: 10.1021/j150579a011.
- (249) Brenner, A. M.; Adkins, B. D.; Spooner, S.; Davis, B. H. Porosity by small-angle X-ray scattering (SAXS): comparison with results from mercury penetration and nitrogen adsorption. *Journal of Non-Crystalline Solids* **1995**, *185*, 73–77, DOI: 10.1016/0022-3093(94)00669-5.
- (250) Patel, M.; Rosenfeldt, S.; Ballauff, M.; Dingenouts, N.; Pontoni, D.; Narayanan, T. Analysis of the correlation of counterions to rod-like macroions by anomalous small-angle X-ray scattering. *Phys. Chem. Chem. Phys.* **2004**, *6*, 2962, DOI: 10.1039/b402155j.
- (251) Meisburger, S. P.; Warkentin, M.; Chen, H.; Hopkins, J. B.; Gillilan, R. E.; Pollack, L.; Thorne, R. E. Breaking the radiation damage limit with Cryo-SAXS. *Biophysical journal* **2013**, *104*, 227–236, DOI: 10.1016/j.bpj.2012.11.3817.
- (252) Kirby, N.; Cowieson, N.; Hawley, A. M.; Mudie, S. T.; McGillivray, D. J.; Kusel, M.; Samardzic-Boban, V.; Ryan, T. M. Improved radiation dose efficiency in solution SAXS using a sheath flow sample environment. *Acta crystallographica. Section D, Structural biology* **2016**, *72*, 1254–1266, DOI: 10.1107/S2059798316017174.
- (253) Golub, D.; Oren, Y.; Soffer, A. Electro adsorption, the electrical double layer and their relation to dimensional changes of carbon electrodes. *Carbon* **1987**, *25*, 109–117, DOI: 10.1016/0008-6223(87)90047-9.
- (254) Kosmulski, M. *Surface Charging and Points of Zero Charge*; CRC Press, 2009.

- (255) Koneshan, S.; Rasaiah, J. C.; Lynden-Bell, R. M.; Lee, S. H. Solvent Structure, Dynamics, and Ion Mobility in Aqueous Solutions at 25 °C. *J. Phys. Chem. B* **1998**, *102*, 4193–4204, DOI: 10.1021/jp980642x.
- (256) Brunetti, A.; Sanchez del Rio, M.; Golosio, B.; Simionovici, A.; Somogyi, A. A library for X-ray–matter interaction cross sections for X-ray fluorescence applications. *Spectrochimica Acta Part B: Atomic Spectroscopy* **2004**, *59*, 1725–1731, DOI: 10.1016/j.sab.2004.03.014.

## 9 List of publications

This thesis is based on the content of publications 1 to 3

- 1 **C. Koczwar**a, C. Prehal, S. Haas, P. Boesecke, N. Hüsing, O. Paris, Towards Real-time Ion-specific Structural Sensitivity in Nanoporous Carbon Electrodes using In Situ Anomalous Small Angle X-ray Scattering (submitted)
- 2 **C. Koczwar**a, S. Rumswinkel, L. Hammerschmidt, M. Salihovic, M. S. Elsässer, H. Amenitsch, O. Paris, N. Hüsing, Nanofibers versus Nanopores: A Comparison of the Electrochemical Performance of Hierarchically Ordered Porous Carbons *ACS Applied Energy Materials* **2** (2019), 5279–5291
- 3 **C. Koczwar**a, S. Rumswinkel, C. Prehal, N. Jäckel, M. S. Elsässer, H. Amenitsch, V. Presser, N. Hüsing, O. Paris, In Situ Measurement of Electrosorption-Induced Deformation Reveals the Importance of Micropores in Hierarchical Carbons. *ACS Applied Materials and Interfaces*. **9** (2017), 23319-23324
- 4 N. Natter, N. Kostoglou, **C. Koczwar**a, C. Tampaxis, T. Steriotis, R. Gupta, O. Paris, C. Rebholz, C. Mitterer, Plasma-Derived Graphene-Based Materials for Water Purification and Energy Storage. *C* **5** (2019)
- 5 C. Prehal, **C. Koczwar**a, H. Amenitsch, V. Presser, O. Paris, Salt concentration and charging velocity determine ion charge storage mechanism in nanoporous supercapacitors. *Nature communications* **9** (2018), 4145
- 6 C. Prehal, **C. Koczwar**a, N. Jäckel, A. Schreiber, M. Burian, H. Amenitsch, M. A. Hartmann, V. Presser, O. Paris, Quantification of ion confinement and desolvation in nanoporous carbon supercapacitors with modelling and in situ X-ray scattering. *Nature Energy*. **2** (2017),16215
- 7 C. Prehal, **C. Koczwar**a, N. Jäckel, H. Amenitsch, V. Presser, O. Paris, A carbon nanopore model to quantify structure and kinetics of ion electrosorption with in situ small-angle X-ray scattering. *Physical chemistry, chemical physics: PCCP*. **19** (2017),15549-15561

- 8 N. Kostoglou, **C. Koczwar**a, C. Prehal, V. Terziyska, B. Babic, B. Matovic, G. Constantinides, C. Tampaxis, G. Charalambopoulou, T. Steriotis, S. Hinder, M. A. Baker, K. Polychronopoulou, C. C. Doumanidis, O. Paris, C. Mitterer, C. Rebholz, Nanoporous activated carbon cloth as a versatile material for hydrogen adsorption, selective gas separation and electrochemical energy storage. *Nano Energy*. **40** (2017), 49-64.